Nonlinear Analysis and Control of Standalone, Parallel DC-DC, and Parallel Multi-Phase PWM Converters

by

Sudip K. Mazumder

Dissertation submitted to the Faculty of the
Virginia Polytechnic Institute and State University
in partial fulfillment of the requirements for the degree of

DOCTOR OF PHILOSOPHY
in
Electrical and Computer Engineering

Ali H. Nayfeh, Co-Chair	Dushan Boroyevich, Co-Chair
Hugh VanLandingham	Jason Lai
William T. Baumann	

July 30, 2001
Blacksburg, Virginia

Keywords: Power Electronics, DC-DC Converters, Multi-Phase Converters, Parallel Converters, Modeling, Stability Analysis, Nonlinear Control, Bifurcation Theory, Floquet Theory, Sliding Surface, Differential Inclusion, Lyapunov's Method

Nonlinear Analysis and Control of Standalone, Parallel DC-DC, and Parallel Multi-Phase PWM Converters

Sudip K. Mazumder

(ABSTRACT)

Applications of distributed-power systems are on the rise. They are already used in telecommunication power supplies, aircraft and shipboard power-distribution systems, motor drives, plasma applications, and they are being considered for numerous other applications. The successful operation of these multi-converter systems relies heavily on a stable design. Conventional analyses of power converters are based on averaged models, which ignore the fast-scale instability and analyze the stability on a reduced-order manifold. As such, validity of the averaged models varies with the switching frequency even for the same topological structure.

The prevalent procedure for analyzing the stability of switching converters is based on linearized smooth averaged (small-signal) models. Yet there are systems (in active use) that yield a non-smooth averaged model. Even for systems for which smooth averaged models are realizable, small-signal analyses of the nominal solution/orbit do not provide anything about three important characteristics: region of attraction of the nominal solution, dependence of the converter dynamics on the initial conditions of the states, and the post-instability dynamics. As such, converters designed based on small-signal analyses may be conservative. In addition, linear controllers based on such analysis may not be robust and optimal. Clearly, there is a need to analyze the stability of power converters from a di®erent perspective and design nonlinear controllers for such hybrid systems.

In this Dissertation, using bifurcation analysis and Lyapunov's method, we analyze the stability and dynamics of some of the building blocks of distributed-power systems, namely standalone, integrated, and parallel converters. Using analytical and experimental results, we show some of the di®erences between the conventional and new approaches for stability

analyses of switching converters and demonstrate the shortcomings of some of the existing results. Furthermore, using nonlinear analyses we attempt to answer three fundamental questions: when does an instability occur, what is the mechanism of the instability, and what happens after the instability?

Subsequently, we develop nonlinear controllers to stabilize parallel dc-dc and parallel multi-phase converters. The proposed controllers for parallel dc-dc converters combine the concepts of multiple-sliding-surface and integral-variable-structure control. They are easy to design, robust, and have good transient and steady-state performances. Furthermore, they achieve a constant switching frequency within the boundary layer and hence can be operated in interleaving or synchronicity modes. The controllers developed for parallel multi-phase converters retain many of the above features. In addition, they do not require any communication between the modules; as such, they have high redundancy. One of these control schemes combines space-vector modulation and variable-structure control. It achieves constant switching frequency within the boundary layer and a good compromise between the transient and steady-state performances.

ACKNOWLEDGEMENTS

I am deeply indebted to Drs. Ali H. Nayfeh and Dushan Boroyevich for agreeing to co-advise me on an area of power electronics, which is challenging and of immense importance. During my candidacy as a Doctoral student, they have been constant sources of invaluable guidance, support, encouragement, and motivation. I want to specially thank Dr. Nayfeh for his words of advice on issues related not only to academics but, to life in general.

Let me express my sincerest gratitude to Drs. Hugh VanLandingham, Jason Lai, and William T. Baumann for accepting to serve as a member of my committee. I am also thankful to Dr. Fred C. Lee for providing me with opportunities to work with him on some challenging multi-phase converter projects. I would also like to thank Dr. Vadim I. Utkin (formerly with Institute of Control Sciences, Moscow) for some of our conceptual discussions on variable-structure control. Thanks also goes to Dr. Pushkin Kachroo for useful discussions regarding hybrid control.

Let me take this opportunity to extend a special thanks to Dr. Kam Ng (the O±ce of Naval Research) for his words of encouragement and support.

Particular acknowledgments go to all of my colleagues at the Center for Power Electronics Systems and at the Nonlinear Dynamics Laboratory at Virginia Polytechnic Institute and State University. Their valuable comments and continuous encouragement are greatly appreciated. I will always cherish the moments I had with Peter Barbosa, Francisco Canales, and Waleed Faris.

I am grateful to my extended family, whose love and support have enabled me to ¯nish this work. During thick and thin, my wife (Paromita) and daughter (Soumyaa), my sister (Jayati), my brother-in-law (Dr. Subho Mozumdar), and my father-in-law (Dr. Purnendu Bhattacharjee) have been a constant source of encouragement, support, and joy for me. I shall always cherish the enthusiasm with which my father (Dr. Somendra K. Mazumder) discussed with me problems on °uid mechanics and hydrodynamic stability. I believe that

his enthusiasm and scienti¯c prowess has always inspired me to constantly challenge myself and strive hard to achieve the best. I am grateful to my mother (Sumitra), without whose blessings I could not have achieved whatever little I have today.

Finally, let me express my deepest gratitude to God for His blessings.

To The Omniscient, my family, and to all of those unknown and known geniuses whose lives and words of advice have in°uenced me positively

GRANT INFORMATION

This work was supported by the O±ce of Naval Research under Grant No. N00014-96-1-1123 and made use of the ERC Shared Facilities supported by the National Science Foundation under Award Number EEC-9731677.

Contents

List of Tables

List of Figures

Chapter 1

Introduction

We start with a brief motivation for our work and the objectives of this dissertation. We then provide a literature review of the existing work in related areas. Finally, we outline the objectives of the present work and provide a brief description of the accomplishments in the subsequent chapters.

1.1 Motivation and Objectives

With increasing demand for higher power, reliability, modularity, higher efficiency, reconfigurability of power converters, reduced voltage and current ripples, reduced cost, and fast dynamic responses, the need for integrated and parallel converters is on the rise (Carsten, 1987; Hingorani, 1990 and 1993; Sable et al., 1991; Siri, 1991; Patil et al., 1992; Tabisz et al., 1992; Wildrick et al., 1992; Wildrick, 1993; Burns et al., 1994; Hua et al., 1994; Huynh, 1994; Kassakian and Perreault, 1994; Needham et al., 1994; Rostek, 1994; Wills, 1994; Lee, 1995, 2000a,b; Petry, 1995; Watson et al., 1995; White, 1995; Gholdston et al., 1996; Hingorani and Gyugyi, 1996; Thottuvelil, 1996; Xing, et al., 1996; Belkhayat, 1997; Lee et al., 1997; Panov et al., 1997; Thandi, 1997; Glennon, 1998; Luo et al., 1998; Nayfeh, 1998; ODDR&E

and EPRI, 1998; Zhang, 1998; Alfayyoumi, 1999; Batham et al., 1999; Drobnik et al., 1999; Feng et al., 1999; Khan, 1999; Thunes et al., 1999; Tolbert et al., 1999; Watson and Lee, 1999; Zhu et al., 1999; Alderfer et al., 2000; Barbosa et al., 2000; Chandrasekaran, 2000; Hur and Nam, 2000; Jensen et al., 2000; Mazumder et al., 2000b; Sun, 2000; Tuladhar et al., 2000; Ye, 2000; Bowman and Young, C., 2001; Liu et al., 2001; Mazumder et al., 2001a, b, d, f). There are many organizations, including the Office of Naval Research (ONR), Rockwell, Lockheed Martin, Raytheon, Boeing, United Technologies, Intel, General Motors, Allison Electric Drive, Microlinear, which are either supporting or intend to support the realization of such distributed power systems for specific applications. The areas of application of such distributed power systems are numerous. Figure 1.1 shows a Power-Electronics-Building-Block (PEBB) based shipboard dc distributed power system (Lee et al., 1997; Thandi, 1997; Nayfeh, 1998; Xing et al., 1998 and 1999; Thandi et al. 1999). The heart of the large-scale power-electronic system is a high-voltage (800 V) distributed dc bus to which various high-power source and sink (load) converters are connected. In Figure 1.1, the source converters are bidirectional boost converters, which interface three-phase generators to the dc bus. The load converters are dc-dc converters and multi-phase dc-ac inverters. Typical loads for the system could include motors, a secondary utility bus, pulsating loads, and nonlinear loads like uninterruptable power supplies (UPS).

Figure 1.2 shows a typical dc distributed power system for a telecommunication power supply (Lee, 1995). The architecture of the power systems evolves around a primary dc bus (regulated at 400 V) and a secondary dc bus (regulated at 48 V). The power to the primary dc bus is typically fed by boost converters, which interface to a multi-phase utility. The high voltage on the primary bus is stepped down using front-end converters and their output is connected to the secondary dc bus. The secondary bus serves as the source of power for all the loads. Figure 1.2 also shows that the front-end converters are connected to a current-sharing bus. This bus enables the even distribution of load power among the N modules. Comparing Figures 1.1 and 1.2, we observe that although the overall architectures of the two power systems are not much different, the applications of these two systems are

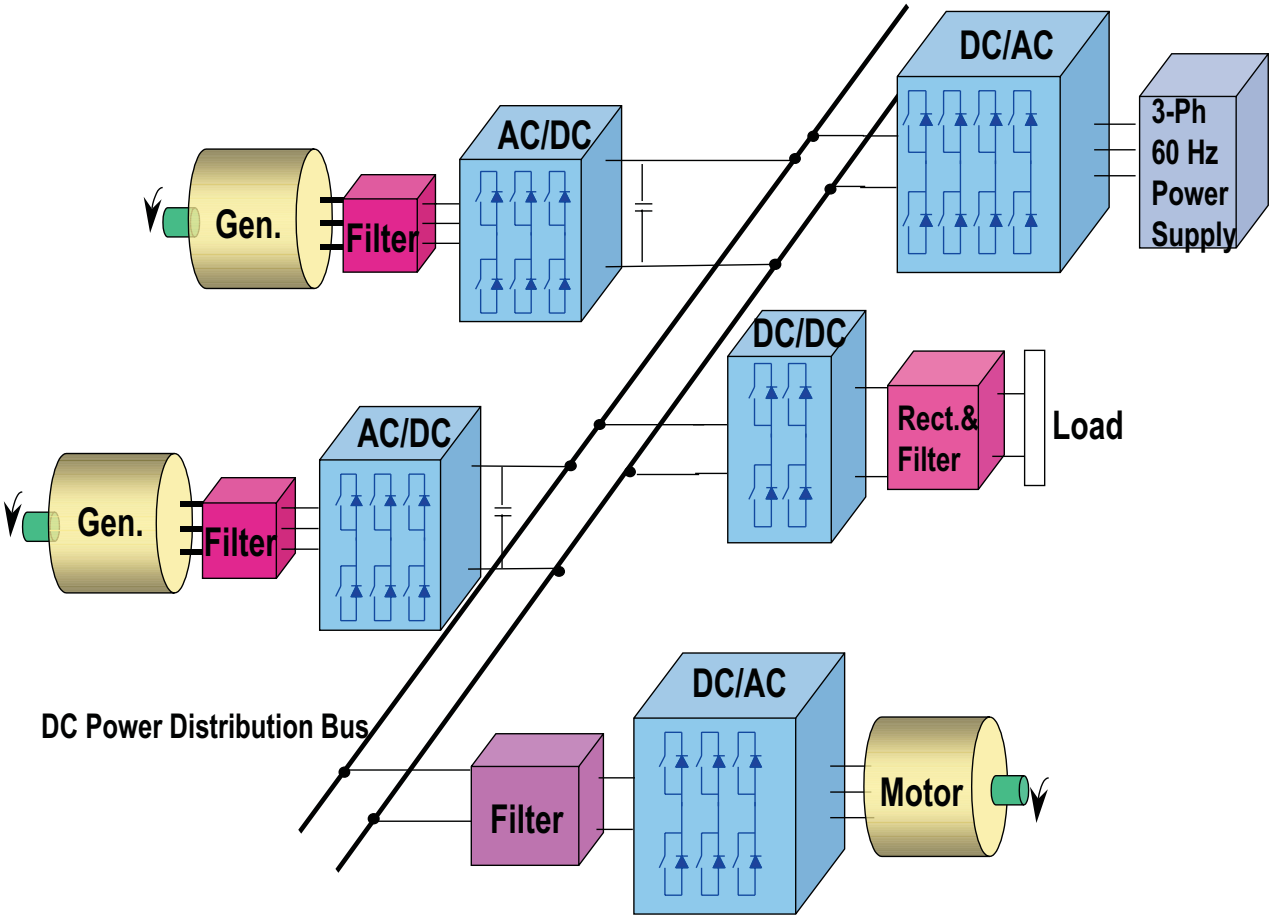

Figure 1.1: A PEBB-based shipboard dc distributed power system.

vastly different. The power system shown in Figure 1.1 deals with a much higher power and voltage as compared to the one shown in Figure 1.2.

Next, we illustrate in Figure 1.3 a baseline power distribution system for a typical next generation transport aircraft (Chandrasekaran, 2000). The power distribution is built around a dual 270V/500kW dc bus with an auxiliary power unit (APU) and a battery-backup auxiliary bus. The starter/generator units (500 kW each) generate three-phase ac power at 110V and 400Hz. The bidirectional power converters (BDC) between a starter/generator unit and the corresponding dc distribution bus tightly regulate the bus at 270V even under feedforward and feedback disturbances. Typical loads that the dc bus has to supply include electric actuators, environmental control systems, and negative-impedance avionics etc.

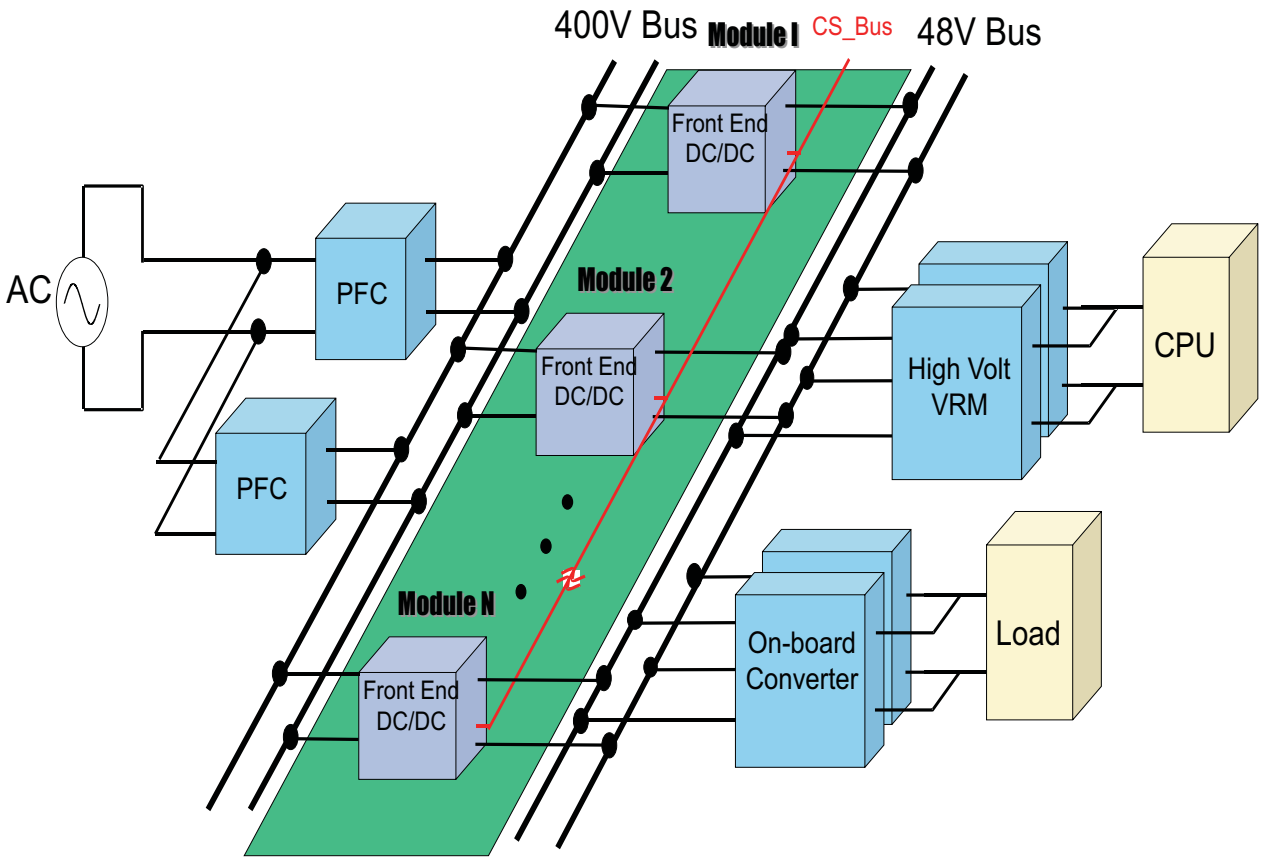

Figure 1.2: A dc distributed power system for a telecommunication power supply.

The concept of a distributed power system has also been applied to the areas of multi-axis drives, electric vehicles, and flexible ac transmission systems (FACTS). With all of the advantages of these systems come increasing complexities related to their design, stability, and control (Hingorani, 1990 and 1993; Lee 1995 and 2000a; Lee et al., 1997; Xing, 1998 and 1999; Alfayyoumi, 1999; Xing et al., 1999; Ye, 2000; Mazumder et al., 2001a, b, d, f). The major challenges regarding the stability of these systems are related to the even distribution of power, the circulation energy, nonlinearities due to system interactions, and the nonlinearities of the individual closed-loop converter modules. In addition, many of these systems drive nonlinear loads. As such, there is growing feeling that simplistic linear models of many of these complex nonlinear hybrid systems (Witsenhausen, 1966; Tavernini, 1987; Gollu, A. and Varaiya, 1989; Kourjanski and Varaiya, 1995; Michel, 1997; Branicky,

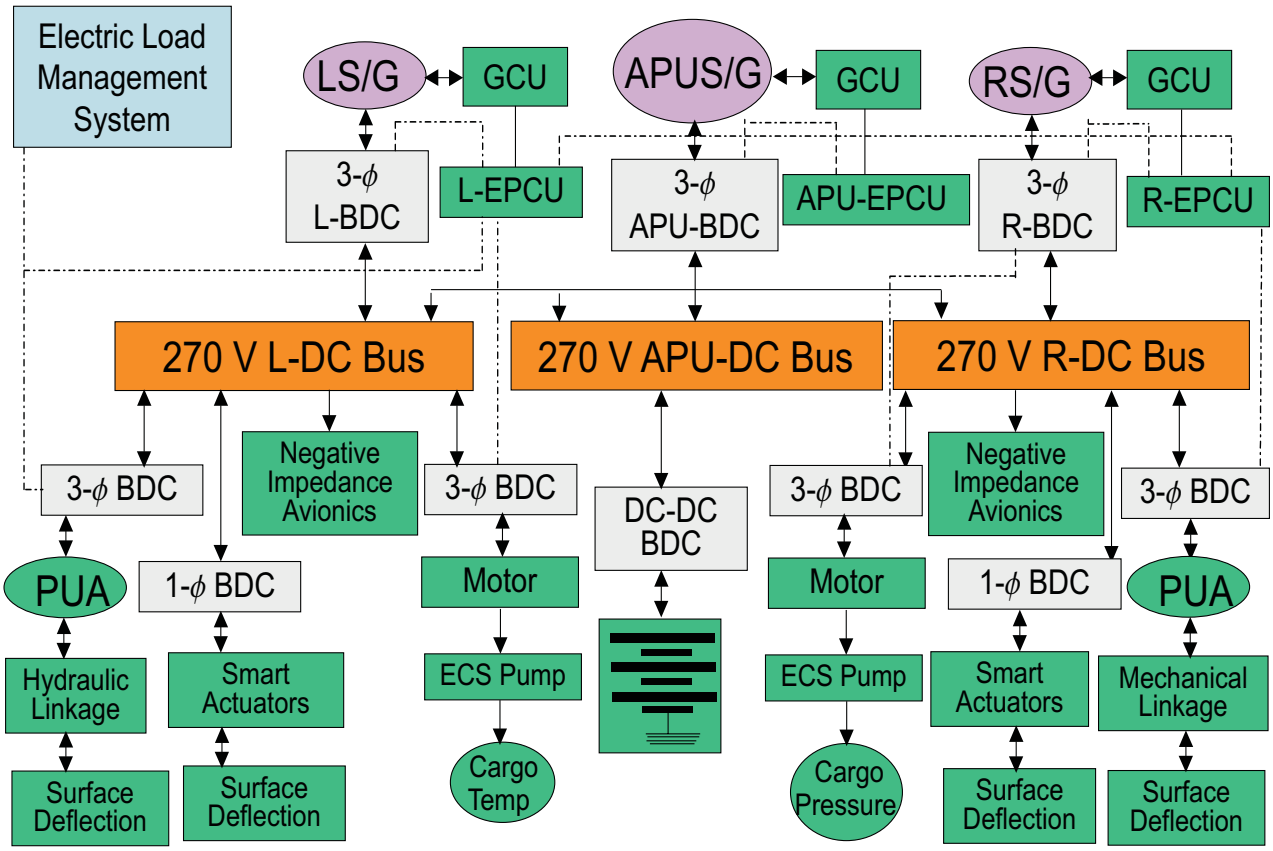

Figure 1.3: A baseline power distribution system for a next generation transport aircraft.

1998; Aubin, 1999; DeCarlo et al., 2000) may not be a viable solution (Balestrino et al., 1974; Lee et al., 1979; Erickson et al., 1982; Gelig and Churilov, 1987; Hamill and Jefferies, 1988; Kipnis, 1989 and 1991; Sira-Ramirez, 1989; Wood, 1989; Krein and Bass, 1989 and 1990; Sanders, 1989; Tymerski et al., 1989; Tse and Adams, 1990 and 1991; Abed et al., 1992; Hamill and Deane, 1992; Sanders, 1993; Tse, 1994a-c; Wolf et al., 1994; Wolf and Sanders, 1994; Belkhayat et al., 1995; Hamill, 1995; Fossas and Olivar, 1996; Banerjee et al., 1997; Chau et al., 1997; Alfayyoumi, 1998; Gelig and Churilov, 1998; Poddar et al., 1998; Alfayyoumi et al., 1999 and 2000; Fang and Abed, 1999; Chandrasekaran et al., 1999 and 2000; Chen et al.; 2000; Lyshevski, 2000; Mazumder et al., 2000a; Banerjee and Verghese, 2001; Mazumder et al., 2001a-f; Mazumder and Nayfeh, 2001; Nayfeh and Mazumder, 2001). This Dissertation is an attempt to address some of these concerns and to propose solutions

for such nonlinear systems in the form of better modeling, analysis, and control techniques. The specific objectives of this Dissertation are the following:

- Modeling and stability analysis of standalone, integrated, and parallel dc-dc pulsewidth modulation (PWM) converters and extending these methodologies to multi-phase PWM converters.
- Nonlinear control and stabilization of parallel dc-dc and parallel non-isolated multi-phase (and multi-stage) PWM converters.

1.2 Literature Review

In this section, we review the state-of-the-art of stability analysis and control of standalone, integrated, and parallel dc-dc and parallel multi-phase PWM converters.

1.2.1 Modeling and Stability Analysis of Standalone DC-DC and Multiphase PWM Converters

Switching-mode power-electronic converters are nonlinear dynamical systems. The nonlinearities arise primarily due to switching, power devices, and passive components, such as transformers, inductors, and parasitics. As shown in Fig 1.4, historically, there have been four major approaches to the modeling and analysis of the switching nonlinearity in dc-dc converters. The most widely used approach is a small-signal analysis based on state-space averaging (Middlebrook and Cuk, 1977; Cuk and Middlebrook, 1977), circuit averaging (Wester and Middlebrook, 1972), and using the PWM switch model (Vorperian, 1990a, b; Tymerski et al., 1988). Simple analytical expressions in terms of the circuit components were derived to characterize the low-frequency response of such systems. Middlebrook and Cuk (1977) generalized the above technique by introducing the state-space averaging method.

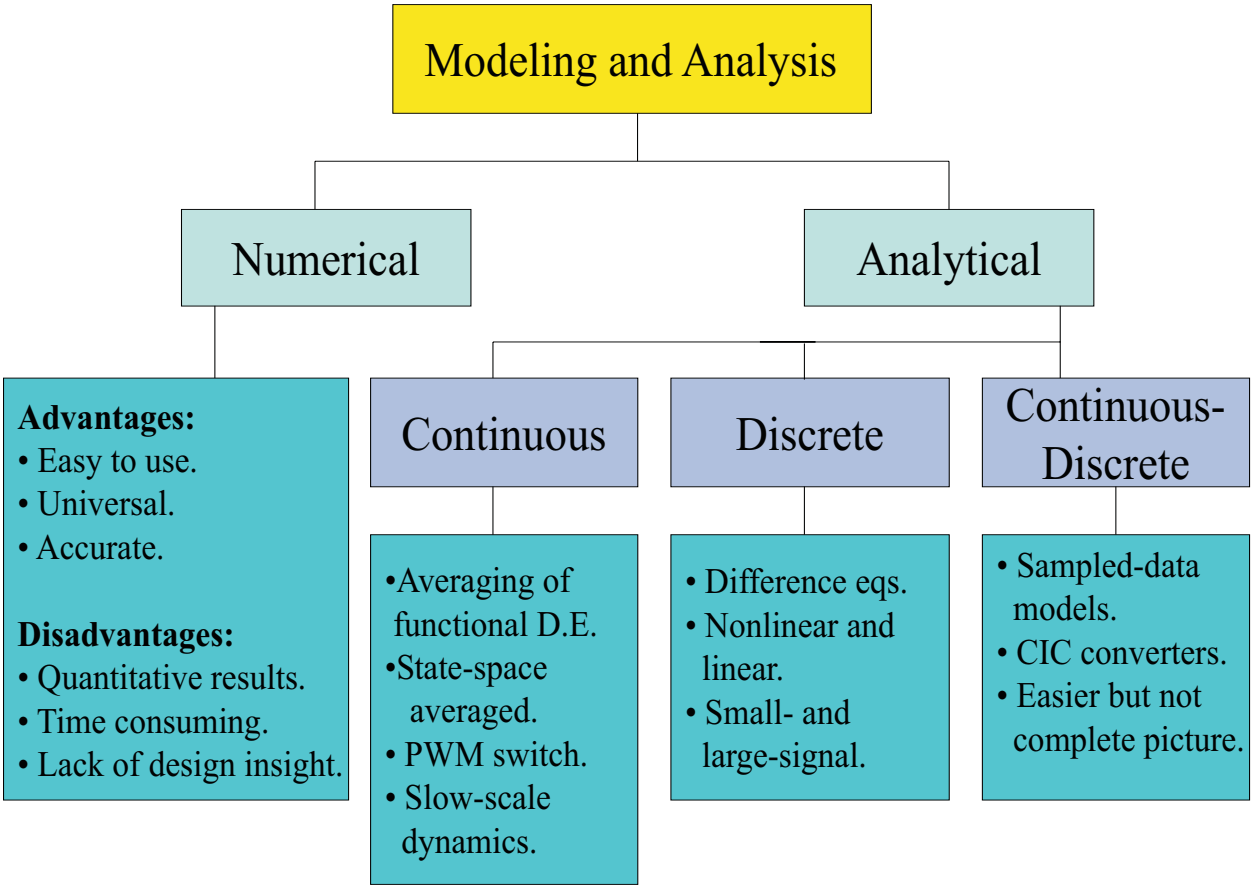

Figure 1.4: A survey of various modeling methods.

They replaced the state-space description of the switched network by a single state-space description, hence eliminating the switching process from consideration and representing the average effect of the switched networks in one cycle of operation. By means of state-space averaging, the original nonlinear discrete system was simplified into a nonlinear continuous system. This system was further simplified by perturbing the averaged system around an operating point and then linearizing the resulting perturbed equations. After a considerable amount of matrix manipulations, the system characteristics, such as input impedance, output impedance, line-to-output transfer function, and control-to-output characteristics, were obtained.

Vorperian (1990a, b) presented a circuit-oriented approach to the analysis of PWM con-

verters. His method relies on the identification of a three-terminal nonlinear device, called the PWM switch, which consists of the active and passive switches in a PWM converter. Once the invariant properties of the PWM switch were determined, an average equivalent circuit model was derived, and dc and small-signal characteristics of the converter were obtained by a simple replacement of the PWM switch with its equivalent circuit model.

Continuous techniques make certain assumptions in order to achieve the final simplified averaged model. The first simplifying assumption is the linear ripple approximation or the straight line approximation, which approximates the matrix exponentials appearing in the solutions of linear systems by the first two terms of their Taylor series expansions. This approximation is valid when the natural frequencies of the converter are all well below the switching frequency such that the solutions are approximately linear. This is the case for a well-designed PWM converter. The second approximation is in effect an averaging of the output or the duty ratio function, which is less justified. Note that, in a closed-loop regulator system, the output is responsible for generating the duty-ratio function. This approximation effectively eliminates a sampler, and hence may be expected to affect the accuracy of the averaging methods at frequencies approaching one-half the switching frequency, known as the high-frequency regime or the fast-scale dynamics.

In some of the recent works (Lehman and Bass, 1996a, b; Sakharuk et al., 2000), averaged models of dc-dc converters have been developed by first modeling the converters as functional differential equations and then applying the averaging operator to these equations. This approach, which is similar to the earlier works of Bainov and Milusheva (1981) and Balachandra and Sethna (1975), results in enhanced accuracy as compared to the results obtained by state-space averaging methods. An alternate approach, which generalizes the Krylov-Bogoliubov-Mitropolsky (KBM) method (Bogoliubov and Mitropolski, 1961; Nayfeh, 1973; Sanders, 1985), has been used by other researchers (Sanders, 1989; Sanders et al., 1991; Bass and Sun, 1998; Sun et al., 1998; Sun 2000; Sun and Mehrotra, 2001) to obtain more accurate averaged models. Although these averaged models enhance the accuracy of the state-space averaging methods, they do not predict the fast-scale dynamics due to the

switching behavior of the regulator; they can only capture the slow-scale dynamics (Aubin and Cellina, 1984; Utkin, 1992; Hamill, 1995; Alfayyoumi et al., 1999, 2000; Mazumder et al., 2000a; Mazumder and Nayfeh, 2001; Mazumder et al., 2001c-f). Besides, the accuracy of these models degrades as the switching frequency of the converter decreases. It is also not clear how these methodologies can be applied to complex hybrid power-electronic systems. Furthermore, the algebraic complexity of these methods is more than that of state-space averaging methods. As such, a numerical simulator is a necessity, which takes away the physical insight obtained using state-space averaged models.

Exact discrete modeling techniques (Capel et al., 1975; Prajoux et al., 1976; Lee et al., 1979) make no simplifying assumptions as those made by state-space averaging techniques. The switched continuous system is replaced by a discrete system that describes the state of the system at the switching frequency. Hence, these modeling techniques can predict the fast-scale dynamics. Prajoux et al. (1976) presented a discrete approach, which is capable of accurately describing the dynamics of a system with varying structures within a given period by a linearized discrete time-domain model. It was used to model a boost converter operating in the continuous conduction mode. Capel et al. (1975) applied this method to multi-loop buck and boost regulators in both types of conduction modes. Lee et al. (1979) extended this analysis to the three types of converters: buck, boost, and buck boost.

The third approach describes the switched-mode power supply using a typical continuous time model of the form $\dot{\psi} = f(\psi, u, t)$, where the right-hand side is discontinuous due to abrupt changes in the control (PWM for example). This class of models is one of the hardest to study (Aubin and Cellina, 1984; Fillipov, 1988; Utkin, 1992). Besides, the existence of solutions for this class of systems is not always well-defined. So far analysis using switching models has relied completely upon numerical simulations. Such simulations could be extremely time consuming for many applications and often run into convergence problems. On the other hand, switching models are the most accurate of all of the models because they can describe the dynamics of any switching converter in saturated as well as unsaturated regions (Mazumder et al. 2001a, b, e).

Because of the complexity of switching models, more simplified techniques that combine both continuous and discrete models were developed (Brown and Middlebrook, 1981; Shortt and Lee, 1983; Ridley, 1991). Brown and Middlebrook (1981) developed a new modeling approach combining continuous and discrete techniques. Their model did not treat the duty ratio as a smooth, slowly time-varying wave, but as a waveform of discrete pulses. The power stage model was still based on averaging techniques. Shortt and Lee (1983), on the other hand, developed a discrete-averaged model by combining the aforementioned averaging and discrete techniques. The model used the averaged state-space form of the averaging technique and determined the output by a discrete sampler. Ridley (1991) presented a new small-signal model for pulse-width-modulated converters operating with current-mode control. Sampled-data modeling was applied to the current-mode cell, which is common to all converters, and the results obtained were simplified to give a model for analysis and design. Because these hybrid methods include the effects of the sampling action caused by the switching in one way or another, they succeed where averaged models fail in predicting the boundaries of fast-scale instabilities.

Recently, dc-dc switching regulators were observed to behave in a chaotic manner. More interesting nonlinear behaviors, such as subharmonics and a period-doubling route to chaos, were also encountered. To explore these interesting phenomena, one needs discrete models. Chaos and subharmonic instabilities in dc-dc converters were observed and described by Brockett and Wood (1984), Wood (1989), Jefferies et al. (1989), Deane and Hamill (1990), Deane (1992), Hamill et al. (1992), and Fossas and Olivar (1996). These works illustrate how chaos can occur in simple voltage-mode PWM dc-dc buck converters operating in the continuous conduction mode. Chaos was also studied for a current-programmed boost PWM dc-dc switching converter operating in the continuous conduction mode by Hamill and Jefferies (1988), Krein and Bass (1989, 1990), Zafrany and Ben-Yaakov (1995), Chan and Tse (1996a, b), Marrero et al. (1996), and in the discontinuous conduction mode by Tse and Adams (1990) and Tse (1994a, b). Chaos due to a border collision bifurcation, which (commonly) occurs in dc-dc switching regulators when the error signal hits the ramp signal either

at the bottom or at the top, was explained recently by Banerjee et al. (1997) and Banerjee and Grebogi (1999). Earlier works on border-collision bifurcations in other fields were reported by Feigin (1974, 1995) and Nusse and York (1992). In a recent study, Alfayyoumi (1998) and Alfayyoumi et al. (1999, 2000) took a more systematic approach to the modeling and stability analysis of standalone dc-dc converters operating with duty-ratio control in the unsaturated region.

Next, we investigate the area of standalone multi-phase converters, which, like the standalone dc-dc converters, is a field that has been explored by many researchers. We start with single-phase converters and then consider multi-phase converters.

One of the most common single-phase applications is the boost power-factor-correction (PFC) circuit. PFC circuits are widely used in power electronics. One of the most common circuits used to achieve unity power factor is the time-varying boost PFC circuit. The operation of such converters was analyzed in detail by many researchers (Mohan et al., 1984; Henze and Mohan, 1986; Ridley, 1989; Williams, 1989; Zhou et al., 1990, 1992; Huliehel et al., 1992; Simonetti et al., 1995; Sun et al., 1998). However, very few have even attempted to properly analyze the stability of these systems. The system of equations for the boost PFC circuit involves discontinuity in control and non-differentiability in state and time. These features, in addition to the time-varying nature of the converter, make the analysis of the boost PFC circuit difficult.

Some researchers analyzed the stability of this time-varying system using a smooth linearized small-signal model. Mohan et al. (1984) used the concept of quasi-static analysis to analyze the current-loop stability of boost PFC circuits operating with hysteretic control. Ridley (1989) and Williams (1989) developed small-signal models to facilitate the design of an output-voltage compensator for resistive and constant-power loads. A more concrete small-signal analysis is given by Huliehel et al. (1992); they justify their analysis by replacing the time-varying input voltage with a nonlinear feedforward control. They developed a small-signal model for the boost PFC circuit, operating with a constant switching frequency,

for the design and analysis of the voltage and current loops. Zhou and Jovanović (1992) demonstrated the occurrence of current-loop instabilities in the boost PFC circuit operating with peak-current-mode control and with average-current-mode control.

The boost PFC circuit has been extended to areas of application that require bidirectional power flow, such as drives, UPS, and propulsion systems (Uher, 1979; Stihi and Ooi, 1988; Chang et al. 1990; Thiyagarajah, 1991; Miyashita et al., 1994; Malesani et al., 1996). The basic analyses of such systems, however, remain similar to those of unidirectional converters with the exception that all of the states (assuming ideal switches) are now continuous. Using a simple linearized averaged model, Stihi and Ooi (1988) showed how sn improper design and an incorporation of a low-pass filter (used to eliminate the impact of switching effect) can result in a feedback instability.

Pan and Chen (1993) proposed a step-up/down single-phase ac-dc power converter without a current sensor. The power converter adopts a front-end diode rectifier so that only one active switch is required. They extended the familiar state-space averaging technique for discontinuous mode dc-dc power converters to model the proposed ac-dc converter. Unlike existing models, which are valid only for a very low-frequency range, below the line frequency, their proposed model is applicable up to half the switching frequency.

A common assumption in most of the above references is that the input voltage, the line parameters, or the load of multi-phase converter is balanced. This may not be always the case. Jacobina et al. (1999) employed a vector modeling approach to represent the transient and steady-state behaviors of unbalanced single-phase PWM converters. They introduced a fictitious second single-phase system to obtain a vector model and used it to develop current controllers to stabilize the unbalanced system (Jacobina et al., 1999, 2001).

Another concept, known as dynamic phasors, has been recently put forward by Stankovic et al. (1998) to model and analyze single- and multi-phase converters. The concept of dynamic phasors follows from the theory of generalized averaging (Sanders, 1991). Dynamic phasors provide a compromise between detailed time-domain models and simple frequency-

domain procedures and hence are well suited for fast numerical simulations. Using dynamic phasors, balanced and unbalanced and single-phase and poly-phase systems have been analyzed (Stankovic et al., 1998, 2000).

We now shift our focus to converters that have three or more phases. Although, there are publications on two-phase converters, in general they are uncommon. The first comprehensive approach to modeling three-phase PWM converters was published by Ngo (1984). Subsequently, Ngo (1986), Wu et al. (1991), Bauer and Klaassens (1993), Hiti and Borojevic (1994), and Hiti (1995) published papers on switching models of three-phase converters, and averaging, transformation (in the synchronous frame), and linearization of these models. While the procedure to develop switching models using discontinuous switching functions remains the same as that used for dc-dc converters, application of averaging methods to multi-phase converters is different. This is because multi-phase converters have two fundamental frequencies and hence a state-space averaging method may not be sufficient. Ngo (1984), Rim (1990), Wu et al. (1990), and Bauer and Klaassens (1993) have proposed averaging by replacing the switching network by sets of ideal transformers. This averaged model is valid only if both the dc port and ac terminals of three-phase converters are either current or voltage controlled; a condition that holds only if parasitic resistances are zero (Hiti, 1994). Sanders (1989) and Sanders et al. (1991) proposed a more comprehensive approach to obtain averaged and generalized averaged models of multi-phase converters. However, it is not apparent how the methodology can be extended to multi-phase systems, which incorporate continuous conduction mode (CCM) and discontinuous conduction mode (DCM). Recently, using an averaged modeling method, Chandrashekaran (2000) extended the impedance matching criterion proposed by Middlebrook (1976) to three-phase ac-dc converters with an input filter and developed sufficient conditions for the stability of the linearized filter-converter system.

Most of the above references assume that the input voltage, the line parameters, or the load of multi-phase converter are balanced. When this is not the case, zero components can emerge in a three-phase system (Enjeti et al., 1990, 1991; Rioual and Pouliquen, 1993;

Campos et al., 1994; Ojo and Bhat, 1994; Vincenti and Jin, 1994; Xing et al., 1998; Ye, 2000). Enjeti et al. (1990, 1991) and Campos et al. (1994) showed that, due to an unbalanced input voltage, undesired low-frequency harmonics appear in the dc output voltage and ac input currents if standard modulation techniques are applied. Ojo and Bhat (1994) analyzed the impact of the zero component on the small-signal transfer functions of buck rectifiers and concluded that this impact is negligible. Operation of a boost rectifier under unbalanced conditions was studied by Rioual and Pouliquen (1993). A voltage compensator was designed to suppress the undesired low-frequency harmonics in the closed-loop systems.

Recently, the dynamic phasor modeling technique has been used to analyze unbalanced multi-phase power systems (Stankovic et al., 1998, 2000). The proposed technique, which builds upon the generalized averaging method proposed by Sanders et al. (1991), is a polyphase generalization of the dynamic phasor approach, and it is applicable to nonlinear power system models. In steady state, the dynamic phasors reduce to standard phasors from ac circuit theory.

In an alternate approach, Jacobina et al. (1999 and 2001) have proposed the concept of a vector model to analyze the transient and steady-state behaviors of polyphase systems operating under balanced and unbalanced conditions. For a three-phase three-wire (four wire) system, the vector model is obtained by using an appropriate coordinate transformation of the system of equations from stationary coordinates to *dq* (*dqo*) coordinates. Using these vector models, they have proposed positive- and negative-sequence controllers to control unbalanced polyphase converters when the unbalancing results from supply voltages and parametric variations (Jacobina et al., 1999, 2001).

Recently, Ryan (1997) and Zhang (1998a) have addressed the modeling, analysis, and control issues of four-legged voltage source power converters by developing averaged models for a four-legged inverter in both the *abc* and *dqo* coordinates. Using the linearized averaged model, they devised control schemes, which stabilize a four-legged converter even when it is driving unbalanced and nonlinear loads as long as the control bandwidth of the linearized

system is high.

There are some common shortcomings in all of the above analyses. First, they assume that a discontinuous system can be always represented by a simple smooth model. Second, they do not take into account the impact of initial conditions on the dynamics of the system. Third, many of these analyses do not recognize that some of the averaged models can be nonlinear and nonsmooth.

1.2.2 Stability Analysis and Control of Parallel DC-DC PWM Converters

Hedel (1980) published one of the earliest papers on a basic parallel dc-dc converters where he proposed an isolated topology based on interleaving and outlined the design methodology for these converters. Since then parallel dc-dc converters have found extensive application in distributed power-supply systems. They have many desirable features: increased reliability, expandability, and hot plug-in capability. However, the analyses, design, and control of such converters are not simple (Ridley, 1986; Siri, 1991; Kohama et al., 1994; Wu et al., 1994; Chen, 1995; Panov et al., 1996; Rajagopalan et al., 1996; Thottuvelil and Verghese, 1996 and 1998; Perreault et al., 1997; Zafrany and Yaakov, 1998; Mazumder et al., 2000b, 2001a, d, f). In general, the modules of parallel converters are not identical. This may be due to component tolerances, non-identical characteristics of elecrical conductors connecting converters to the shared load, and non-identical changes in the characteristics of the components due to their uneven aging or being subjected to different physical conditions. As such, two stable standalone systems may not share the load equally when connected in parallel. This unequal load sharing may increase the thermal stress of one or more units, thereby reducing the reliability of the system considerably (Jordan, 1991; Glaser and Witulski, 1992; Mammano, 1993; Batarseh et al., 1994a; Perkinson; 1995).

One way of making such converters have approximately equal output currents is through

the droop method (Glaser, 1992; Jamerson and Mullett, 1993, 1994; Batarseh et al., 1994b) where the output impedance of each converter is made large enough to ensure current sharing despite small differences in their output voltages. The droop method is easy to implement because no connection is required between the modules. As such, the overall system has high modularity and reliability. However, the method has poor output voltage regulation and requires trimming of the references for individual converters so that they match each other closely. Glaser and Witulski (1992) and Batarseh et al. (1994b) have outlined simple procedures to ascertain proper load sharing among converter modules. However, none of these analyses has focussed on the overall stability of the system beyond the linear regime.

Recently, Tuladhar and Jin (1998) have proposed a control technique, which allows paralleled dc-dc power converters to share the load in a distributed power-supply system. The control technique, which is a variation of the droop method, does not require interconnections among the modules and automatically compensates for variations in the parameters of the power converter and line impedance. The basic idea of the control scheme is to let each converter inject a small ac voltage to the system as a control signal. Then, the frequency of the injected control signal is drooped as a function of the output current of the unit. As such, the frequency of the control signal of each unit is different if the load sharing is uneven. This difference in frequency integrates over time and causes the circulation of a small real power, which is measured and used to adjust the output voltage of each unit. The trade-off of the proposed methodology is the complexity added to the circuit since one now has to deal with a small injected signal. Another downside of the method is the small ripples introduced at the output. In addition, the performance of the states of the converters, especially under transient conditions, is far from satisfactory.

The inherent drawbacks in the droop method have paved the way for active current-sharing techniques (Hirschberg, 1985; Ridley, 1986; Small, 1988; Choi et al., 1990; Lee et al., 1991; Jordan, 1991; Siri et al., 1991 and 1992a, b; Wu et al., 1991; Choi, 1992 and 1998; Wu et al., 1992a, b; Batarseh et al., 1994a; Kohama et al., 1994; Wu et al., 1994; Banda and Siri, 1995; Chen, 1995; Siri and Banda, 1995; Huth, 1996; Jovanovic, 1996;

Panov et al., 1996; Perreault et al., 1996a,b; Thottuvelil and Verghese, 1996; Garabandic, 1998; Schuellein, 1998; Siri and Truong, 1998; Tomescu and Vanlandingham, 1998; Wu et al.; 1998). The literature on active current-sharing methods is vast. Fundamentally, however, there are two types of methodologies, which have been the focus of research so far: one uses average-current techniques and another uses master-slave current methods. Depending on how the averaging is done or whether the master and slave are fixed or dynamic, there are many variations even for these two control methodologies. Further variations are possible, depending on how the output of the current-sharing processor is utilized by each module of a parallel converter. For example, the output of a current-sharing processor could be a part of an inner or an outer loop of a multi-loop feedback control scheme.

Figure 1.5 shows a simplified block diagram of a general current-sharing scheme for a parallel converter having N modules. The symbols $T_1(s)$, $T_2(s)$, $\cdots$, $T_N(s)$ represent the transfer functions of the amplifiers. The reference signals for the current (i.e., i_{r1}, i_{r2}, $\cdots$, i_{rN}) are generated using the weighting functions β_1, β_2, $\cdots$, β_N and α_1, α_2, $\cdots$, α_N, respectively. By comparing the references for the currents with the output current of each module error signals are generated, which are then fed to the adjustment amplifiers. The output of the amplifiers (v_{err1}, v_{err2}, $\cdots$, v_{errN}) are typically used to adjust either the references for the bus voltage or the inner current loop of each converter. The regelation schemes for the former and latter cases are referred to as outer- and inner-loop regulation.

If α_1, α_2, $\cdots$, α_N are equal to unity and each of β_1, β_2, $\cdots$, β_N is each proportional to the current rating of each module of the parallel converter, then such a current-sharing scheme is known as average-current method (Small, 1988; Siri and Lee, 1990; Batarseh and Siri, 1994; Kohama et al., 1994; Wu et al., 1994; Siri and Banda, 1995; Huth, 1996; Jovanovic, 1996; Thottuvelil and Verghese, 1996; Tomescu and Vanlandingham, 1998). The average-current method enables precise current sharing. It requires a single sharing bus for interconnection among the modules and has high noise immunity. Although the reliability of average-current methods is less than desirable, they are dominant and widely used in the industry. Moreover, unlike master-slave method low-frequency noise does not cause failure of the sharing control

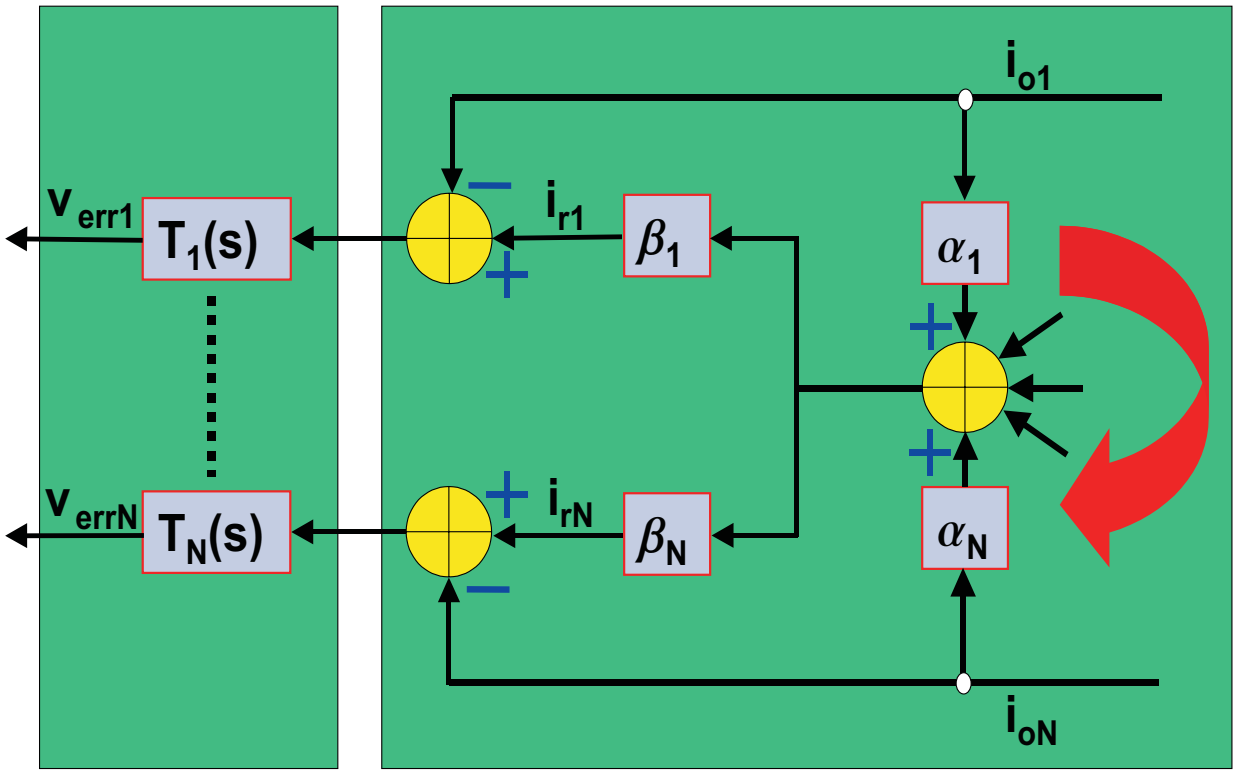

Figure 1.5: A simplified block diagram, which illustrates the basic concept of current sharing.

in average-current methods.

To improve the fault-tolerance capability of the average-current method, Perreault et al. (1996) proposed a frequency-based current-sharing method. The basic idea is a modified version of the averaged-current method. However, unlike the traditional method, the current sharing (for one of their schemes) is achieved using frequency encoding. As such, there is no need for a dedicated bus, which enhances the fault-tolerance capability and reliability of the system. A potential problem of this scheme is the high cost due to the use of complicated circuits and techniques. It is also not clear how the scheme will be affected if the load current has not only a dc component but also low-frequency components. Moreover, the performance of this new scheme has not been demonstrated for nonminimum-phase systems, for systems whose modules have parametric variations, and for systems where the cable impedance has a significant effect. Furthermore, the dynamic performance of the new scheme needs to be

demonstrate under conditions when a fault and a feedforward or a feedback transient occur simultaneously.

Recently, López et al. (1998) developed a variable-structure controller, which uses the averaged-current method for current sharing, to stabilize a parallel dc-dc buck converter. However, the interleaving scheme works only for three parallel modules. Besides, this paper does not give any details regarding the existence and stability of the sliding manifolds. Furthermore, the steady-state performance of the system and the impact of the feedforward disturbance due to the change in the input voltage on its dynamic performance are not shown. In addition, they do not show how to extend it to nonminimum-phase systems, such as boost converters. The zero dynamics of such systems are difficult to stabilize. However, it is a step in the right direction because it recognizes that closed-loop parallel dc-dc converters are nonlinear systems. Almost all of the existing controllers, which use the average-current method, are linear and are based on the small-signal analysis.

Next, we review the literature on current-sharing techniques using the master-slave concept. Historically, there are three types of master-slave methods: dedicated master, rotating master, and democratic master. In Figure 1.4, if $\alpha_1 = \alpha_2 \cdots = \alpha_N = 1$, $\beta_1 = 1$, and $\beta_2 = \beta_3 \cdots = \alpha_N = 0$, then the current-sharing technique is known as dedicated master-slave method (Tanaka, 1988; Siri and Lee, 1990; Wu et al., 1991; Siri et al., 1992; Siri and Banda, 1995; Panov et al., 1997). It enables stable output-voltage regulation but has poor redundancy because the scheme uses a dedicated master. As such, if the master fails, then the entire system breaks down.

Petruzziello et al. (1990) proposed the rotating-master method, which is an improvement over the dedicated-master method. Unlike the latter method, the rotating master method ensures that the α (in Figure 1.4) are not always equal to one; instead the new method ensures that the α, corresponding to each block, is equal to one in turn. As such, each module has the capability and the chance of becoming a master. Thus, the rotating-master method enhances the reliability of the system. However, the implementation of the system

is complex. Moreover, the output voltage may fluctuate due to continuous reassignment of the master module.

Jordan (1991) proposed the democratic-master method, which combines some of the advantages of the average-current and dedicated-master methods. In this scheme, a module that carries the highest output current automatically becomes the master; the other modules operate as slaves. As such, the fault tolerance of this scheme is high. Besides, the implementation of this scheme requires a single bus, which interconnects all of the modules. Thus, the proposed scheme is reliable. However, the democratic-master method has some limitations. First, under transient conditions, the sharing of the output current among the modules is not always satisfactory and a start-up circuit may be needed. Second, there is a possibility of failure in the feedback control because of a continual fight among the modules to become the master. Third, the democratic-master method is sensitive to noise, which can cause fight for the master. As such, proper layout and grounding is essential.

While most of the publications have focussed primarily on the architectures of the control schemes, there have been some publications on the modeling and analysis of these parallel converters. However, most of these analyses have relied on linearized small-signal analyses to determine the local stability. Next, we discuss the pros and cons of existing active current-sharing control schemes and then explore the literature on modeling and stability analyses of closed-loop converters, which use such control schemes.

Ridley (1986) developed a small-signal model for a parallel buck converter based on state-space averaging and showed that a multiple power-converter module system can be reduced to an equivalent single-module system to facilitate its analysis and design. However, in his analysis, he assumed that the parameters of all of the modules are the same. In addition, the stability of the system under transient condition is not discussed.

Kohama et al. (1994) used state-space averaging to obtain a small-signal model of a parallel dc-dc converter with two modules. Using the root-locus method, they demonstrated the instability of the parallel system when the two modules have different circuit parameters.

They also discussed the dynamic stability of the system, which however does not follow from their analysis.

Wu et al. (1994) evaluated the performance of a central-limit control (CLC) scheme by taking into account the converter cable resistance and using large-signal simulations. They also used the large- and small-signal frequency response of the current-sharing loop gains for different cable resistance values. However, the proposed controller is developed using a linear loop-gain analysis, and as such the impact of the circuit parameters and the initial conditions on the large-signal stability of the system is unknown.

Chen (1995) used a small-signal analysis to investigate the stability of a load-sharing parallel dc-dc converter using a model that includes the effect of the resistances of the cables and battery. Using this slightly detailed model, he showed that the effects of the battery and cable are to lower the amplitude of the loop gain and to slow down the response of the system; they have no effect on the stability of the system.

Panov et al. (1996) proposed a systematic approach for assessing the small-signal stability and dynamic performance of parallel modules operating with master-slave current-sharing control. The approach is based on the interface stability concept and allows a straightforward design of a current-sharing loop compensator. The suggested approach is general and can be applied to any number of parallel modules.

Thottuvelil and Verghese (1996) developed a method for assessing the small-signal stability of parallel dc-dc converters operating with active current-sharing control. The generalized methodology can be applied to any number of converters, which may be different or identical. For identical converters, the method results in a particularly simple stability criterion.

Zafrany and Yaakov (1998) used a linearized averaged model to analyze the small-signal stability of a parallel dc-dc buck converter. They also introduced the concept of "folded model" to lump N parallel modules into a single unit, which reduces the simulation time. Apparently, this idea is similar to that proposed by Ridley (1986). This paper also reports a result on the global stability of the system. However, no (theoretical) large-signal stability

analysis has been done.

A collection of works on the stability analysis of parallel dc-dc PWM converters (using small-signal analysis) for spacecraft applications is also provided by Lee (1990). All of these analyses are based primarily on linearized averaged (small-signal) models, the deficiencies of all of which are outlined in Section 1.2.1. Obviously, linear controllers designed for such systems can not always give robust solutions and optimum performance.

1.2.3 Control of Parallel Nonisolated Multi-Phase PWM Converters

Multi-phase power converters, operating in a parallel configuration, are being increasingly used in applications, such as motor drives, power-factor-correction equipments, and UPS (Ogasawara, 1987; Takahashi and Yamane, 1986; Kawabata and Higashino, 1988; Dixon and Ooi, 1989; Komatsuzaki, 1994). These systems have several advantages, such as the capability to handle high power, modularity, high reliability, reduced voltage or current ripple, and fast-dynamic response. Traditionally, a parallel multi-phase converter either has a transformer at the ac side (Dixon and Ooi, 1989; Zhang and Ooi, 1993; Meyer and Sonnenmoser, 1993; Komatsuzaki, 1994) or uses separate power supplies (Kawabata and Higashino, 1988). As such, the converters are not coupled and can be designed individually. This approach, however, results in a bulky and expensive system because of the line-frequency transformer and additional power supplies. With the significant improvement in the integrated power-module technology, it has now become possible and feasible to directly connect three-phase converters in parallel.

There have been numerous works regarding the design, operation, and control of multi-phase PWM rectifiers (Marple, 1979; Gauger, 1986; Dixon and Ooi, 1988; Prasad et al., 1989; Enjeti and Ziogas, 1990; Hingorani, 1990, 1993; Enjeti and Choudhury, 1991; Habetler, 1991; Rioual et al., 1993; Sabanovic et al., 1993; Hiti et al., 1994; Hingorani and Gyugyi, 1996;

Julian et al., 1996; Vlatkovic et al., 1996; Mazumder, 1997; Escobar et al., 1998; Mattavelli et al., 2001). However, only a few papers discussed the issues of paralleling non-isolated multi-phase converters (Matakas and Masada, 1993, 1995; Matakas et al., 1995; Burlacu and Masada, 1996; Burlacu et al., 1997). For example, in a balanced three-phase system, the control is usually implemented in a synchronous reference frame. Such a controller usually controls the currents on the dq axes only because the zero-axis current is negligible for the balanced system. However, when two or more three-phase PWM modules are directly connected, circulating currents can exist in all of the phases (Xing et al., 1999; Xing, 2000). However, the zero-axis current is not reflected on the dq axes and hence a synchronous-frame controller (in the dq axes) has no effect on the zero-axis current.

There are several ways to reduce the cross-current between the modules (Matsui, 1985; Takahashi and Yamane, 1986; Ogasawara, 1987; Sato and Kataoka, 1995). Recently, using linearized averaged models, Xing et al. (1999, 2000) developed linear control schemes for two standardized three-phase modules to reduce the cross-current using a linear controller and space-vector modulation schemes that do not use the zero vectors. The advantage of such schemes is that the communication among the modules is minimal. However, there is no published result on the dynamic response and the impact of the zero-axis disturbance on the stability of the overall system. Korondi et al. (Korondi et al., 1991) developed a controller for a three-phase standalone inverter, which is capable of operating with an unbalanced load. The controller operates in the $\alpha\beta$ frame. To ensure sinusoidal output waves, the $\alpha\beta$ components are controlled non-ideally using a hysteresis relay with an additional zero-phase-sequence elimination. By incorporating the effect of the zero-sequence current in an existing dq model (Hiti, 1995), Ye et al. (2000) put forward an idea, similar to that proposed by Korondi et al. (1991), to control a PTBC instead of a standalone converter. Using this modified model, they have demonstrated the impact of small-signal interactions among the modules and devised a control scheme that minimizes the zero-sequence current on a reduced-order manifold. The linear control scheme is simple and minimizes the zero-sequence current under steady-state conditions by simply varying the duration of the zero

space vector. However, if the system saturates, the control scheme will not work effectively, even under steady-state conditions. This is because, when the system saturates, the zero vector can not be applied (Holtz, 1992). Furthermore, the performance of the system under dynamic conditions has not been demonstrated (Ye, 2000; Ye et al., 2000). Finally, the implementation of this scheme requires that the duration of the zero vectors of one of the modules of the PTBC is fixed (Ye, 2000; Ye et al., 2000).

1.3 Outline and Contributions of This Dissertation

The main emphasis of this Dissertation is on developing methodologies for analyzing the stability and dynamics of switching converters by treating them as discontinuous and nonlinear systems and on controlling the dynamics of parallel converters using robust and nonlinear controllers. Based on this work, a few papers have been published (Lee et al., 1997; Xing et al., 1998, 1999; Ye et al., 1998; Mazumder et al., 2000a, b, 2001a-f). We believe, the new approaches to the analyses of the stability and dynamics and design of controllers, outlined in this Dissertation, will lead to improved stability, performance, and design of power-electronic systems.

We begin, by investigating the fast- and slow-scale instabilities of a standalone dc-dc converter using a nonlinear map. Using bifurcation analysis and Floquet theory, we develop analytic criteria for predicting the stability of the period-one and higher-order orbits of the map. Such an approach enables the determination of the post-instability dynamics, the effect of initial conditions of the states of the converter on its stability, and the dynamics and the region of attraction of the nominal solution. Comparing the results of the map with those of the averaged model shows the shortcomings of the latter in predicting fast-scale instabilities.

Subsequently, we extend some of the fundamental methodologies to analyze more complex standalone and parallel converters. First of all, we consider an integrated filter-converter system. We show the shortcomings of a well-known linear criterion, which is used to predict

instabilities due to sub-system interaction, in integrated systems. Second, we analyze the stability of a single-phase boost PFC circuit using a hybrid model. The stability analysis of this converter is one of the hardest because the model of the boost PFC involves discontinuity in control and non-differentiability in state and time. Using concepts of discontinuous systems and Lyapunov's method, we develop conditions for global and local existence of a closed-loop boost PFC. Using these conditions and the concept of equivalent control, we derive conditions for the onset of instabilities in such systems. Subsequently, we develop a second-order Poincare map and outline the procedure to determine the instability mechanisms and the post-instability dynamics. Third, we outline the techniques to extend the nonlinear analysis to multilevel dc-dc and single-phase bidirectional converters. The analysis of these converters shows how the fundamental techniques can be extended to more complex multi-switch power-electronic systems. For both converters, we outline a procedure to obtain maps, which describe their dynamics. For the multilevel converter, we formulate an analytic stability condition using the derived map. For a single-phase bidirectional converter, using a first-order Poincare map, we show how a stable system undergoes torus breakdown and ultimately enters a chaotic state when a bifurcation parameter is changed. This kind of instability, which occurs on the fast scale, can not be predicted by existing averaged models (Chandrasekaran, 2000). Fourth, we analyze the stabilty and dynamics of N parallel dc-dc converters. We develop stability criteria based on nonlinear maps and switching and averaged models. Using bifurcation theory and Lyapunov's method, we investigate the stability of a parallel dc-dc converter under saturated and unsaturated conditions and show that there is a significant difference in the prediction of the instabilities based on switching and discrete models as compared to averaged models. To investigate the post-instability dynamics using a map, we also develop a discrete normal form.

Detailed stability analyses of standalone, integrated, and parallel switching converters brings out some of the key deficiencies of the existing methodologies, which are based on averaged models. As such, controllers that are designed based on these methodologies may be conservative and may not stabilize the closed-loop systems. To overcome these deficiencies,

we develop nonlinear controllers, which stabilize parallel dc-dc and multi-phase switching converters.

We begin, by developing robust controllers (for parallel dc-dc converters), which combine the concepts of integral-variable-structure and multiple-sliding-surface control. These control schemes have several advantages. First, they are easy to design because each sliding surface is independently controlled. Second, the controllers yield good transient responses even under parametric variations. Third, the controllers eliminate the bus-voltage error and the error between the line currents of the converter modules under steady-state conditions. Fourth, the integrators in the control schemes reduce the impact of very high-frequency dynamics due to parasitics on an experimental closed-loop system. Fifth, the control schemes within the boundary layer enable operation of the converters with a finite switching frequency. Sixth, using these controllers, the converter modules can be operated in interleaving or synchronous modes.

Next, we propose three different control schemes to stabilize parallel multi-phase converters and compare them with existing control schemes. None of these schemes requires any communication among the modules and hence they have high redundancy. Furthermore, they can operate even if the switchings of the modules are not synchronized, the switching frequencies are different, and the parameters of the modules vary. Two of the proposed control schemes are developed in the continuous domain, whereas the third scheme is developed in the discrete domain. We find that the dynamic performances of all of the proposed control schemes are better than the existing schemes. The discrete-control scheme achieves the best compromise between steady-state and transient responses. This is because this scheme combines space-vector modulation and nonlinear control. We believe that this is the first time such a scheme has been developed to control a parallel multi-phase converter.

Chapter 2

Modeling and Stability Analyses. I. Fundamental Theory for Basic Standalone DC-DC PWM Converters

Using an exact formulation based on nonlinear maps, we develop a systematic method to model dc-dc converters operating with static or dynamic feedback control. We use this methodology to investigate the fast-scale instabilities of a high-frequency dc-dc voltage-mode buck converter that employs dynamic-feedback control for voltage regulation and operates in the CCM. The basic idea can, however, be easily extended to other classes of dc-dc converters. We validate experimentally the theoretical results. We compare the results obtained with the exact formulation with those obtained using state-space averaged models and point out the shortcoming of averaged models in predicting fast-scale instabilities. Currently, most of the commercial dc-dc converters operate at 100 kHz or above. At such high frequencies the effects of parasitic elements can not be ignored as has been done in the past by most investigators. In this chapter we also demonstrate the impact of very high-frequency dynamics, due to parasitics and device nonlinearities, on the onset of chaos by developing a high-frequency model. The parasitic parameters for this model are obtained using a finite-element analy-

sis package based on the actual printed-circuit board (PCB) of the experimental converter. The analyses in this chapter are based on systems that are close to dc-dc converters used in practice, and hence the results should be of interest to practicing engineers. The present results indicate that nonlinear analyses of power converters lead to a better understanding of their dynamics. With these analyses, one can clearly demarcate the boundaries of instabilities (without resorting to time consuming numerical simulations) and demonstrate the fast-scale and slow-scale instabilities. This may lead to converters that have better design and performance.

2.1 Modeling and Analysis

Initially, we assume that the nonlinearities due to the power device and parasitics are negligible. Then, we demonstrate their effect through a high-frequency model. The converter is clocked at a rate equal to the switching frequency. Moreover, the controller is designed in such a way that, once a change of state is latched, it can be reset only by the next clock. This effectively eliminates the possibility of multiple pulses. We analyze the closed-loop buck converter (without the filter) first and then extend it for the integrated system. The buck converter operating under the CCM and duty ratio control is a piecewise smooth system. The multi-topological system, shown in Figure 2.1, is in the on-state (for duration T_1) when u is closed and in the off-state (for duration T_2) when u is open. If we represent the two states, the inductor current $[i_L(t)]$ and the output capacitor voltage $[v_c(t)]$ of the open-loop converter, by $X(t)$, then we write the system of equations governing the two states as

$$\begin{aligned} \tfrac{dX(t)}{dt} &= A_1^o X(t) + B_1^o v_{in} \\ v_{dc}(t) &= C_1^o X(t) \end{aligned} \tag{2.1}$$

for $0 \leq t < T_1$ and

$$\begin{aligned} \tfrac{dX(t)}{dt} &= A_2^o X(t) + B_2^o v_{in} \\ v_{dc}(t) &= C_2^o X(t) \end{aligned} \tag{2.2}$$

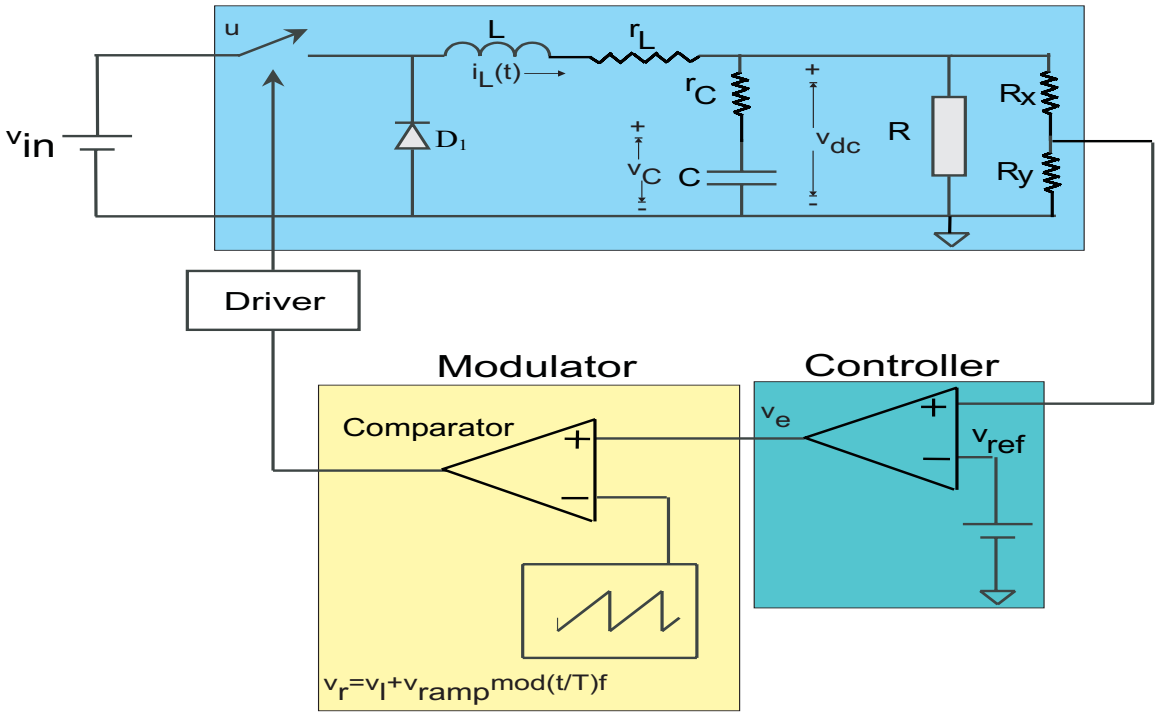

Figure 2.1: A closed-loop buck converter.

for $T_1 \leq t < T_2$ where

$$T = T_1 + T_2. \tag{2.3}$$

In (2.1) and (2.2), $v_{dc}(t)$ is the sum of $v_c(t)$ and the voltage drop across r_C. The matrices $A_1^o, A_2^o, B_1^o, B_2^o, C_1^o$, and C_2^o in (2.1) and (2.2) are given by

$$\begin{aligned}
A_1^o &= \begin{bmatrix} -\frac{r_L}{L} - \frac{r_C R}{(R+r_C)L} & -\frac{R}{(R+r_C)L} \\ \frac{R}{(R+r_C)C} & -\frac{1}{(R+r_C)C} \end{bmatrix}, \quad B_1^o = \begin{bmatrix} \frac{1}{L} \\ 0 \end{bmatrix}, \quad C_1^o = \begin{bmatrix} \frac{r_C R}{R+r_C} & \frac{R}{R+r_C} \end{bmatrix} \\
A_2^o &= \begin{bmatrix} -\frac{r_L}{L} - \frac{r_C R}{(R+r_C)L} & -\frac{R}{(R+r_C)L} \\ \frac{R}{(R+r_C)C} & -\frac{1}{(R+r_C)C} \end{bmatrix}, \quad B_2^o = \begin{bmatrix} 0 \\ 0 \end{bmatrix}, \quad C_3^o = \begin{bmatrix} \frac{r_C R}{R+r_C} & \frac{R}{R+r_C} \end{bmatrix}
\end{aligned} \tag{2.4}$$

Using (2.1) and (2.2), we derive the open-loop state-space averaged model by taking the average of the states in the on- and off-intervals. This yields the following large-signal

time-varying continuous system:

$$\begin{aligned}\frac{d\overline{X(t)}}{dt} &= \left(A_1^o d + A_2^o \overline{d}\right)\overline{X(t)} + \left(B_1^o d + B_2^o \overline{d}\right)\overline{v_{in}} \\ \overline{v_{dc}(t)} &= \left(C_1^o d + C_2^o \overline{d}\right)\overline{X(t)}\end{aligned} \tag{2.5}$$

where the duty ratio $d = T_1/T$.

Next, we derive the exact solution of the open-loop system by stacking the consecutive solutions of (2.1) and (2.2) over a switching period. The resulting discrete-time difference equation can be written in state-space form as

$$\begin{aligned}X_{k+1} &= f_1^o\left(X_k, d_k, v_{in}\right) = \Phi\left(d_k\right) X_k + \Gamma\left(d_k\right) v_{in} \\ v_{dc_{k+1}} &= f_2^o\left(X_k, d_k, v_{in}\right) = C_2^o X_{k+1}\end{aligned} \tag{2.6}$$

where

$$\Phi\left(d_k\right) = \Phi_2\left(1 - d_k\right)\Phi_1\left(d_k\right), \qquad \Phi_i\left(\tau\right) = e^{A_i^o \tau} \tag{2.7}$$

$$\Gamma\left(d_k\right) = \Phi_2\left(1 - d_k\right)\int_0^{d_k T} \Phi_1\left(\tau\right) B_1^o d\tau + \int_0^{(1-d_k T)} \Phi_2\left(\tau\right) B_2^o d\tau. \tag{2.8}$$

Using

$$\int_0^t e^{A_i^o \tau} B_i^o d\tau = \left[e^{A_i^o t} - I\right]\left(A_i^o\right)^{-1} B_i^o \tag{2.9}$$

and (2.7) and (2.8), we simplify the expression for X_{k+1} in (2.6a) to

$$\begin{aligned}X_{k+1} = f_1^o\left(X_k, d_k, v_{in}\right) &= e^{A_2^o(1-d_k)T} e^{A_1^o d_k T} X_k + e^{A_2^o(1-d_k)T}\left[e^{A_1^o d_k T} - I\right]\left(A_1^o\right)^{-1} B_1^o v_{in} \\ &\quad + \left[e^{A_2^o(1-d_k)T} - I\right]\left(A_2^o\right)^{-1} B_2^o v_{in}.\end{aligned} \tag{2.10}$$

To derive a model for the closed-loop system, we assume that the mth-order, linear, time-invariant error amplifier (shown in Figure 2.1) can be modeled as

$$\begin{aligned}\frac{d\xi(t)}{dt} &= A_c \xi(t) + B_c v_{in} + B_{rc} v_{ref} \\ v_e(t) &= H_c \xi(t)\end{aligned} \tag{2.11}$$

where $\xi(t)$ is a $m \times 1$ state vector representing the states of the controller, A_c is a constant matrix, B_c and B_{rc} are $1 \times m$ row vectors, H_c is a $1 \times m$ row vector, v_{ref} is the reference voltage, and $v_e(t)$ is the output of the error amplifier. Using (2.1), (2.2), and (2.11), we obtain the following equations for the closed-loop converter system:

$$\begin{aligned} \tfrac{d\Psi(t)}{dt} &= A_1\Psi(t) + B_1 v_{in} + B_{r1} v_{ref} \\ v_{dc}(t) &= C_1\Psi(t) \\ v_e(t) &= P_1\Psi(t) \end{aligned} \tag{2.12}$$

for $0 \le t < T_1$ and

$$\begin{aligned} \tfrac{d\Psi(t)}{dt} &= A_2\Psi(t) + B_2 v_{in} + B_{r2} v_{ref} \\ v_{dc}(t) &= C_2\Psi(t) \\ v_e(t) &= P_2\Psi(t) \end{aligned} \tag{2.13}$$

for $T_1 \le t < T$. In (2.13), $\Psi(t)$ represents the combined states of the controller and the power stage. The matrices $A_1, A_2, B_1, B_2, B_{r1}, B_{r2}, C_1$, and C_2 in (2.12) and (2.13) are given by

$$\begin{aligned} A_1 &= \begin{bmatrix} A_1^o & 0 \\ SC_1^o & A_c \end{bmatrix}, \; B_1 = \begin{bmatrix} B_1^o \\ 0 \end{bmatrix}, \; B_{r1} = \begin{bmatrix} 0 \\ B_{rc} \end{bmatrix}, \; C_1 = \begin{bmatrix} C_1^o & 0 \end{bmatrix}, \; H_1 = \begin{bmatrix} H_c & 0 \end{bmatrix} \\ A_2 &= \begin{bmatrix} A_2^o & 0 \\ SC_2^o & A_c \end{bmatrix}, \; B_2 = \begin{bmatrix} B_2^o \\ 0 \end{bmatrix}, \; B_{r2} = \begin{bmatrix} 0 \\ B_{rc} \end{bmatrix}, \; C_2 = \begin{bmatrix} C_2^o & 0 \end{bmatrix}, \; H_2 = \begin{bmatrix} H_c & 0 \end{bmatrix}. \end{aligned} \tag{2.14}$$

Using (2.12) and (2.13), we obtain the following state-space averaged model for the closed-loop system:

$$\begin{aligned} \tfrac{d\overline{\Psi(t)}}{dt} &= \left[A_1 d + A_2 \overline{d}\right] \overline{\Psi}(t) + \left[B_1 d + B_2 \overline{d}\right] \overline{v_{in}} + \left[B_{r1} d + B_{r2} \overline{d}\right] v_{ref} \\ \overline{v}_{dc}(t) &= \left(C_1 d + C_2 \overline{d}\right) \overline{\Psi}(t). \end{aligned} \tag{2.15}$$

Similarly, we can write an exact discrete model for the closed-loop system in the form

$$\begin{aligned}
\Psi_{k+1} &= f_1\left(\Psi_k, d_k, v_{in}\right) \\
&= e^{A_2(1-d_k)T} e^{A_1 d_k T} \Psi_k \\
&\quad + \left[e^{A_2(1-d_k)T}\left(e^{A_1 d_k T} - I\right)\left(A_1\right)^{-1} B_1 + \left(e^{A_2(1-d_k)T} - I\right)\left(A_2\right)^{-1} B_2\right] v_{in} \\
&\quad + \left[e^{A_2(1-d_k)T}\left(e^{A_1 d_k T} - I\right)\left(A_1\right)^{-1} B_{r1} + \left(e^{A_2(1-d_k)T} - I\right)\left(A_2\right)^{-1} B_{r2}\right] v_{ref} \\
v_{dc_{k+1}} &= f_2\left(\Psi_k, d_k, v_{in}\right) = C_2 \Psi_{k+1}.
\end{aligned} \tag{2.16}$$

The auxiliary equation for the switching condition of the closed-loop feedback system is

$$\sigma\left(\Psi_k, d_k, v_{in}\right) = \varphi \cdot \left[e^{A_1 d_k T}\Psi_k + \left(e^{A_1 d_k T} - I\right)\left(A_1\right)^{-1}\left(B_1 v_{in} + B_{r1} v_{ref}\right)\right] - v_{ramp} d_k = 0. \tag{2.17}$$

In (2.17), the term φ represents the feedback controller and v_{ramp} is the magnitude of the ramp shown in Figure 2.1. For example, for a lag-lead controller with an integrator,

$$\varphi = \omega_m \begin{pmatrix} 0 & 0 & \omega_{z1}\omega_{z2} & \omega_{z1} + \omega_{z2} & 1 \end{pmatrix}. \tag{2.18}$$

The transfer function of the controller is

$$G_c(s) = \frac{\omega_I}{s} \frac{\left(s + \omega_{z1}\right)\left(s + \omega_{z2}\right)}{\left(s + \omega_{p1}\right)\left(s + \omega_{p2}\right)} = \frac{\omega_m}{s} \frac{\left(\frac{s}{\omega_{z1}} + 1\right)\left(\frac{s}{\omega_{z2}} + 1\right)}{\left(\frac{s}{\omega_{p1}} + 1\right)\left(\frac{s}{\omega_{p2}} + 1\right)} \tag{2.19}$$

where ω_I is the integrator gain and ω_{z1}, ω_{z2}, ω_{p1}, and ω_{p2} are the zeros and poles of the controller.

2.2 Period-One Responses and Their Stability

The fixed points Ψ_k of (2.16) correspond to period-one limit cycles of the closed-loop regulator. They can be obtained by using the constraint $\Psi_{k+1} = \Psi_k = \Psi_s$. Letting $V_{in} = v_{in}$

and $D = d_k$ in (2.16), we find that the fixed points are given by

$$\Psi_s = \left[I - e^{A_2(1-D)T}e^{A_1DT}\right]^{-1}\left[\begin{array}{c}\left(\begin{array}{c}e^{A_2(1-D)T}\left(e^{A_1DT}-I\right)(A_1)^{-1}B_1+\\ \left(e^{A_2(1-D)T}-I\right)(A_2)^{-1}B_2\end{array}\right)V_{in}+\\ \left(\begin{array}{c}e^{A_2(1-D)T}\left(e^{A_1DT}-I\right)(A_1)^{-1}B_{r1}+\\ \left(e^{A_2(1-D)T}-I\right)(A_2)^{-1}B_{r2}\end{array}\right)v_{ref}\end{array}\right] \tag{2.20}$$

Substituting (2.20) into (2.17), we obtain

$$\begin{aligned}\sigma\left(\Psi_s, D, V_{in}\right) &= \varphi\left[e^{A_1DT}\left(\begin{array}{c}\left(e^{A_2(1-D)T}e^{A_1DT}\right)^{-1}\\ \left(\begin{array}{c}e^{A_2(1-D)T}\left(e^{A_1DT}-I\right)(A_1)^{-1}B_1+\\ \left(e^{A_2(1-D)T}-I\right)(A_2)^{-1}B_2\end{array}\right)V_{in}+\\ \left(\begin{array}{c}e^{A_2(1-D)T}\left(e^{A_1DT}-I\right)(A_1)^{-1}B_{r1}+\\ \left(e^{A_2(1-D)T}-I\right)(A_2)^{-1}B_{r2}\end{array}\right)v_{ref}\end{array}\right)+\right.\\ &\quad\left.\left(e^{A_1DT}-I\right)(A_1)^{-1}\left(B_1V_{in}+B_{r1}v_{ref}\right)\right]\\ &- v_{ramp}D = 0.\end{aligned} \tag{2.21}$$

The transcendental equation (2.21) is solved numerically using a combination of the bisection and secant methods to determine the fixed points.

To ascertain the stability of a given fixed point, we perturb the nominal values $(\Psi_s, D, V_{in}, V_{dc})$ as

$$\Psi = \Psi_s + \hat{\Psi}, \qquad d = D + \hat{d}, \qquad v_{in} = V_{in} + \hat{v}_{in}, \qquad v_{dc} = V_{dc} + \hat{v}_{dc}. \tag{2.22}$$

Substituting (2.22) into (2.16) and (2.17), expanding the results in Taylor series, and keeping first-order terms, we obtain

$$\hat{\Psi}_{k+1} \approx \frac{\partial f_1}{\partial \Psi}\hat{\Psi}_k + \frac{\partial f_1}{\partial d}\hat{d}_k + \frac{\partial f_1}{\partial v_{in}}\hat{v}_{in} \tag{2.23}$$

$$\hat{v}_{dc_{k+1}} \approx \frac{\partial f_2}{\partial \Psi}\hat{\Psi}_k + \frac{\partial f_2}{\partial d}\hat{d}_k + \frac{\partial f_2}{\partial v_{in}}\hat{v}_{in} \tag{2.24}$$

$$0 \approx \frac{\partial \sigma}{\partial \Psi}\hat{\Psi}_k + \frac{\partial \sigma}{\partial d}\hat{d}_k + \frac{\partial \sigma}{\partial v_{in}}\hat{v}_{in}. \tag{2.25}$$

It follows from (2.25) that

$$\hat{d}_k = -\left[\frac{\partial \sigma}{\partial d}\right]^{-1}\left[\frac{\partial \sigma}{\partial \Psi}\ \hat{\Psi}_k + \frac{\partial \sigma}{\partial v_{in}}\hat{v}_{in}\right]. \tag{2.26}$$

Substituting (2.26) into (2.23) and (2.24) yields

$$\begin{aligned}\hat{\Psi}_{k+1} &\approx \left[\frac{\partial f_1}{\partial \Psi} - \frac{\partial f_1}{\partial d}\left(\frac{\partial \sigma}{\partial d}\right)^{-1}\frac{\partial \sigma}{\partial \Psi}\right]\hat{\Psi}_k + \left[\frac{\partial f_1}{\partial v_{in}} - \frac{\partial f_1}{\partial d}\left(\frac{\partial \sigma}{\partial d}\right)^{-1}\frac{\partial \sigma}{\partial v_{in}}\right]\hat{v}_{in} \\ &= H_1\hat{\Psi}_k + H_2\hat{v}_{in}\end{aligned} \tag{2.27}$$

$$\begin{aligned}\hat{v}_{dc_{k+1}} &\approx \left[\frac{\partial f_2}{\partial \Psi} - \frac{\partial f_2}{\partial d}\left(\frac{\partial \sigma}{\partial d}\right)^{-1}\frac{\partial \sigma}{\partial \Psi}\right]\hat{\Psi}_k + \left[\frac{\partial f_2}{\partial v_{in}} - \frac{\partial f_2}{\partial d}\left(\frac{\partial \sigma}{\partial d}\right)^{-1}\frac{\partial \sigma}{\partial v_{in}}\right]\hat{v}_{in} \\ &= H_3\hat{\Psi}_k + H_4\hat{v}_{in}.\end{aligned} \tag{2.28}$$

The stability of a given fixed point can be ascertained by the eigenvalues (Floquet multipliers) of H_1 (Nayfeh and Mook, 1979; Wolf et al., 1994; Nayfeh and Balachandran, 1995). For asymptotic stability, all of the Floquet multipliers must be within the unit circle. As a control parameter, such as the input voltage, is varied, we found that the fixed point loses stability by one of two scenarios. In the first scenario, a Floquet multiplier exits the unit circle in the complex plane through -1. The post-instability response is a period-two limit cycle and the bifurcation is a flip or a period-doubling bifurcation (Nayfeh and Balachandran, 1995; Wolf et al ,1994). The bifurcation may be supercritical or subcritical, depending on whether the created period-two fixed point is stable or unstable. For supercritical bifurcations, the created period-two fixed point coexists with the unstable period-one fixed point. On the other hand, for subcritical bifurcations, the created period-two fixed point coexists with the stable period-one fixed point. In the second scenario, two complex conjugate Floquet multipliers exit the unit circle away from the real axis. The post-instability response

is two-period quasi periodic and the bifurcation is a Hopf bifurcation (Nayfeh and Mook, 1979; Wolf et al., 1994; Nayfeh and Balachandran, 1995). The normal form of the Hopf bifurcation can be used to determine whether it is subcritical or supercritical. Alternatively, for supercritical bifurcations, the created quasiperiodic response coexists with the unstable period-one response; whereas for subcritical bifurcations, the created quasiperiodic response coexists with the stable period-one response.

2.3 Period-Two Fixed Points and Their Stability

To investigate the behavior of the period-doubled response, we construct a second-order map by imposing the constraint $\Psi_{k+2} = \Psi_k = \Psi_{2s}$. Using a methodology similar to that used in the period-one case, we construct the second-order map

$$\begin{aligned}\Psi_{2s} &= \left[I - e^{A_2(1-D_2)T}e^{A_1D_2T}e^{A_2(1-D_1)T}e^{A_1D_1T}\right]^{-1}\cdot \\ &\left[\begin{array}{c} e^{A_2(1-D_2)T}e^{A_1D_2T}\cdot \\ \left(\begin{array}{c}\left(e^{A_2(1-D_1)T}\left(e^{A_1D_2T}-I\right)(A_1)^{-1}B_1+\left(e^{A_2(1-D_1)T}-I\right)(A_2)^{-1}B_2\right)V_{in}+ \\ \left(e^{A_2(1-D_1)T}\left(e^{A_1D_2T}-I\right)(A_1)^{-1}B_{r1}+\left(e^{A_2(1-D_1)T}-I\right)(A_2)^{-1}B_{r2}\right)v_{ref}\end{array}\right)+ \\ \begin{array}{c}\left(e^{A_2(1-D_2)T}\left(e^{A_1D_2T}-I\right)(A_1)^{-1}B_1+\left(e^{A_2(1-D_2)T}-I\right)(A_2)^{-1}B_2\right)V_{in}+ \\ \left(e^{A_2(1-D_2)T}\left(e^{A_1D_2T}-I\right)(A_1)^{-1}B_{r1}+\left(e^{A_2(1-D_2)T}-I\right)(A_2)^{-1}B_{r2}\right)v_{ref}\end{array}\end{array}\right] \end{aligned} \quad (2.29)$$

$$\begin{aligned}\Psi_{1s} &= e^{A_2(1-D_1)T}e^{A_1D_1T}\Psi_{2s}+ \\ &\left(e^{A_2(1-D_1)T}\left(e^{A_1(1-D_1)T}-I\right)(A_1)^{-1}B_1+\left(e^{A_2(1-D_1)T}-I\right)(A_2)^{-1}B_2\right)V_{in}+ \\ &\left(e^{A_2(1-D_1)T}\left(e^{A_1(1-D_1)T}-I\right)(A_1)^{-1}B_{r1}+\left(e^{A_2(1-D_1)T}-I\right)(A_2)^{-1}B_{r2}\right)v_{ref}\end{aligned} \quad (2.30)$$

where D_1, D_2, Ψ_{1s}, and Ψ_{2s} are the duty ratios and states corresponding to the period-two fixed points. The switching conditions are

$$\sigma_1(\Psi_{1s}, D_1, V_{in}) = \varphi\cdot\left[e^{A_1D_1T}\Psi_{1s}+\left(e^{A_1D_1T}-I\right)(A_1)^{-1}(B_1V_{in}+B_{r1}v_{ref})\right]-v_{ramp}D_1=0 \quad (2.31)$$

$$\sigma_2(\Psi_{2s}, D_2, V_{in}) = \varphi\cdot\left[e^{A_1D_2T}\Psi_{2s}+\left(e^{A_1D_2T}-I\right)(A_1)^{-1}(B_1V_{in}+B_{r1}v_{ref})\right]-v_{ramp}D_2=0. \quad (2.32)$$

The procedure for determining D_1, D_2, Ψ_{1s}, and Ψ_{2s} is the same as that used for the period-one fixed point except that we need two initial guesses for the duty ratios. Guessing D_1 and D_2, we determine Ψ_{1s} and Ψ_{2s} using (2.29) and (2.30) and then correct D_1 and D_2 using (2.31) and (2.32).

The stability of the period-two fixed points can be determined as before by perturbing them and forming the linearized variational equations

$$\hat{\Psi}_{k+2} = H_5\hat{\Psi}_k + H_6\hat{v}_{in} \tag{2.33}$$

$$\hat{v}_{dc_{k+2}} = H_7\hat{\Psi}_k + H_8\hat{v}_{in}. \tag{2.34}$$

Again the stability of the period-two orbit can be determined by calculating the Floquet multipliers of H_5, which can be shown to be

$$H_5 = \left[\frac{\partial f_1}{\partial \Psi_2} - \frac{\partial f_1}{\partial d_2}\left(\frac{\partial \sigma}{\partial d_2}\right)^{-1}\frac{\partial \sigma}{\partial \Psi_2}\right]\left[\frac{\partial f_1}{\partial \Psi_1} - \frac{\partial f_1}{\partial d_1}\left(\frac{\partial \sigma}{\partial d_1}\right)^{-1}\frac{\partial \sigma}{\partial \Psi_1}\right]. \tag{2.35}$$

For stability, all of the Floquet multipliers of H_5 must be within the unit circle. So when the period-one orbit loses stability, the stability of the period-two orbit determines whether the period-doubling bifurcation is supercritical or subcritical. For the Hopf bifurcation, two complex conjugate multipliers leave the unit circle away from the real axis. The determination of whether the bifurcation is subcritical or supercritical can be done by calculating the normal form of the bifurcation. An alternate method is to find out whether there exists a periodic response with a period close to $\frac{2\pi}{Im(\lambda_{Hopf})}$ (where λ_{Hopf} is the complex multiplier exiting the unit circle) in the neighborhood of the bifurcation point as the bifurcation parameter is increased. If so, then the Hopf bifurcation is supercritical. If not then, we can reduce the bifurcation parameter slowly and find out whether there are more than one stable solution by perturbing the period-one solution. If multiple stable solutions coexist, the Hopf bifurcation is subcritical. Of the multiple solutions one is the period-one solution. The others are global solutions.

2.4 Stability Analysis using the Linearized Averaged Model

For the averaged model, determination of the stability of the period-one solution can be performed using the loop gain T_v of the voltage loop (Lee, 1990). The loop gain of the closed-loop buck converter can be determined using

$$T_v(s) = G_d(s)H(s)(FM)(A) \tag{2.36}$$

where $FM(= \frac{1}{v_{ramp}})$ is the modulator gain, $A(= \frac{R_x}{R_x+R_y})$ is the sensor gain, $G_d(s)$ is the control to the output transfer function

$$G_d(s) = \left(\frac{R}{r_L+R}\right) v_{in} \frac{1 + sr_C C}{s^2 LC\left(\frac{R+r_C}{R+r_L}\right) + s\left(\frac{r_L R + r_L r_C + r_C R}{R+r_L} + \frac{L}{r_L+R}\right) + 1} \tag{2.37}$$

and $H_c(s)$ is the controller transfer function. The phase margin of T_v determines the stability of the closed-loop system.

2.5 Effect of Parasitics

In the above model for the closed-loop system, the impact of device nonlinearities and parasitic dynamics was neglected. In conventional commercial converters, the switching frequency is equal to or greater than 100 kHz. At these high frequencies, the parasitics become very important and analyses based on nominal models may not be accurate. If the switching speed of the device (particularly the diode) is fast enough (for example using a Schottky diode), the impact of the device nonlinearity is reduced to some extent as long as the duty ratio of the system is not very small. However, the parasitic parameters vary from board to board, and hence the parasitic dynamics are hard to control even with a well-designed PCB. To conduct the sensitive experiments reported in this chapter, we had

to design the board four times and make special arrangements to reduce the common-mode noise.

The impact of these very high-frequency dynamics (commonly called noise by practicing engineers) can be lumped into a stochastic recursion relation (Crutchfield et al., 1981; Crutchfield and Huberman, 1980):

$$\Psi_{k+1} = f_1\left(\Psi_k, d_k, v_{in}\right) + \Omega_k \chi. \tag{2.38}$$

The quantity Ω_k is a random variable controlled by an even distribution of unit width and χ is a variable that controls the width (or amplitude) of the noise. Equation (2.38) is identical to the first map in (2.16) in the case of a deterministic quantity Ω_k.

This approach for studying the effect of external noise on the transition to chaos for maps has been done in the past by physicists (Crutchfield et al., 1981; Crutchfield and Huberman, 1980). However, the assumption of a Gaussian distribution is not always valid in power-electronic systems. This is because the distribution is skewed, primarily due to glitches in the power-converter response, and hence the mean and the median of the distribution are not the same. We consider a more direct approach here. We extract the parameters of the high-frequency model (based on the actual PCB layout) using the INCA software and high-speed design data books (Zhang, 1998a). The INCA software is a finite-element analysis package and gives the self inductance associated with a trace and the mutual inductances associated with the coupling between traces. We, however, neglect the mutual inductances because they are smaller than the self inductances by at least three orders of magnitude. As the switching frequency increases to the mega Hertz range, the mutual inductance will become more prominent. Once the parameters have been extracted, we use the SABER software to simulate the higher-order system (Figure 2.2). The snubber placed across the diode helps with very high-frequency ringing, with the response dynamics being faster than the switching frequency dynamics by three orders of magnitude. Therefore, we include the snubber in the high-frequency model. The power devices used in the simulation are actual

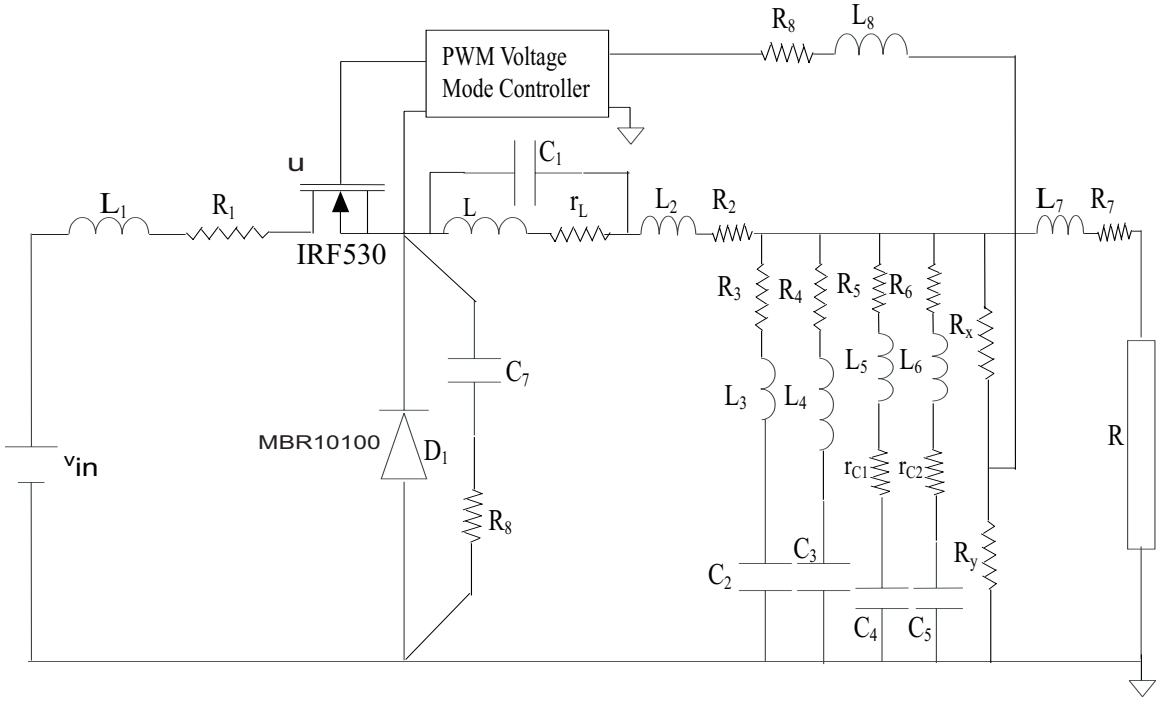

Figure 2.2: A high-frequency model of the closed-loop buck converter.

models; they are used to account for the reverse recovery effect and junction capacitances associated with the devices.

2.6 Results

We present a bifurcation analysis of the closed-loop buck converter. We compare these results with those obtained by using the averaged model. Then, we present experimental results that we obtained with the buck converter shown in Figure 2.3. We use an active load (in resistance mode) to study the influence of load resistance. Then, we show the impact of the very high-frequency dynamics associated with parasitics and device nonlinearities on the onset of chaos.

The values of the parameters of the nominal model are $r_L = 0.021\ \Omega$, $r_C = 0.021\ \Omega$, $L = 50\ \mu$H, $C = 4400\ \mu$F, $v_{ref} = 2.0$ V, $R = 1\ \Omega$ - $5\ \Omega$, $v_l = 1.8$ V, $v_{ramp} = 3.0$ V, and

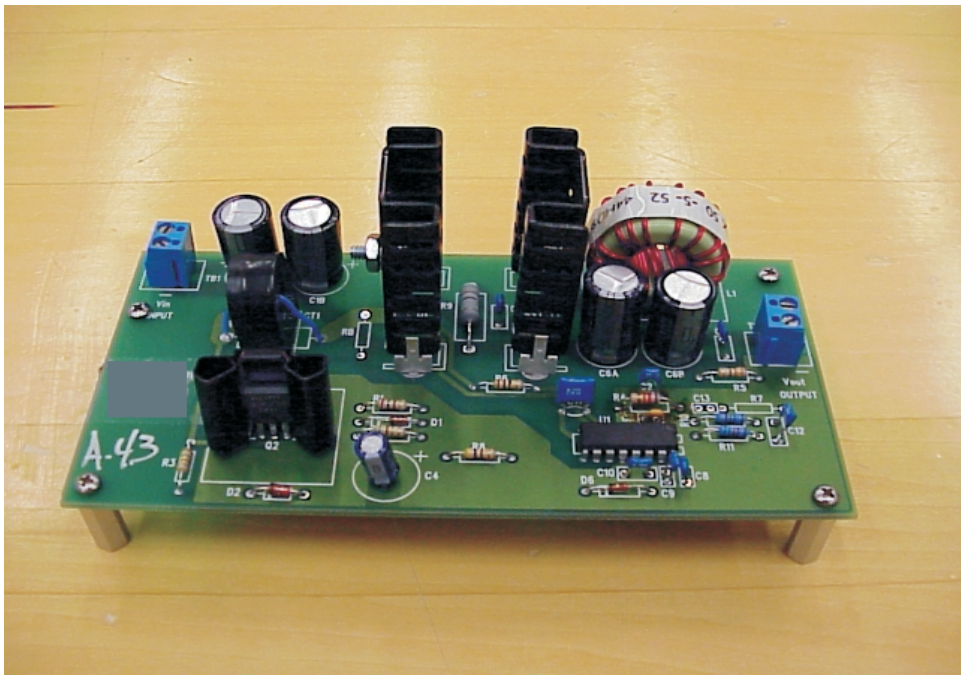

Figure 2.3: Experimental closed-loop buck converter.

$f = \frac{1}{T} = 100$ kHz. The converter we have chosen has a low output voltage and a wide variation in the input voltage. This is a typical scenario in a telecommunication application with a nominal input voltage of 48 volts. As such, the nominal duty ratio can be very low.

In Figure 2.4, we present the frequency-response function obtained with the averaged model for the loop gain of a voltage-mode buck converter. The controller for the closed-loop system has the form $G_c(s) = \frac{\omega_I}{s}\frac{(s+\omega_{z1})(s+\omega_{z2})}{(s+\omega_{p1})(s+\omega_{p2})}$. The worst phase margin is 20°, and hence the converter is stable according to the small-signal averaged model.

In Figure 2.5, we show a theoretical bifurcation diagram for this closed-loop system. The load is kept at one ohm, and the input voltage, which is the bifurcation parameter, is varied between 20 to 62 volts in increments of 0.1 volt. The bifurcation diagram is constructed using the exact method and numerical techniques. The exact method works for v_{in} less than 55 volts. Beyond that the system saturates and hence (2.17) is indeterminate. To carry on, we use numerical methods. The bifurcation analysis clearly shows a fast-scale instability,

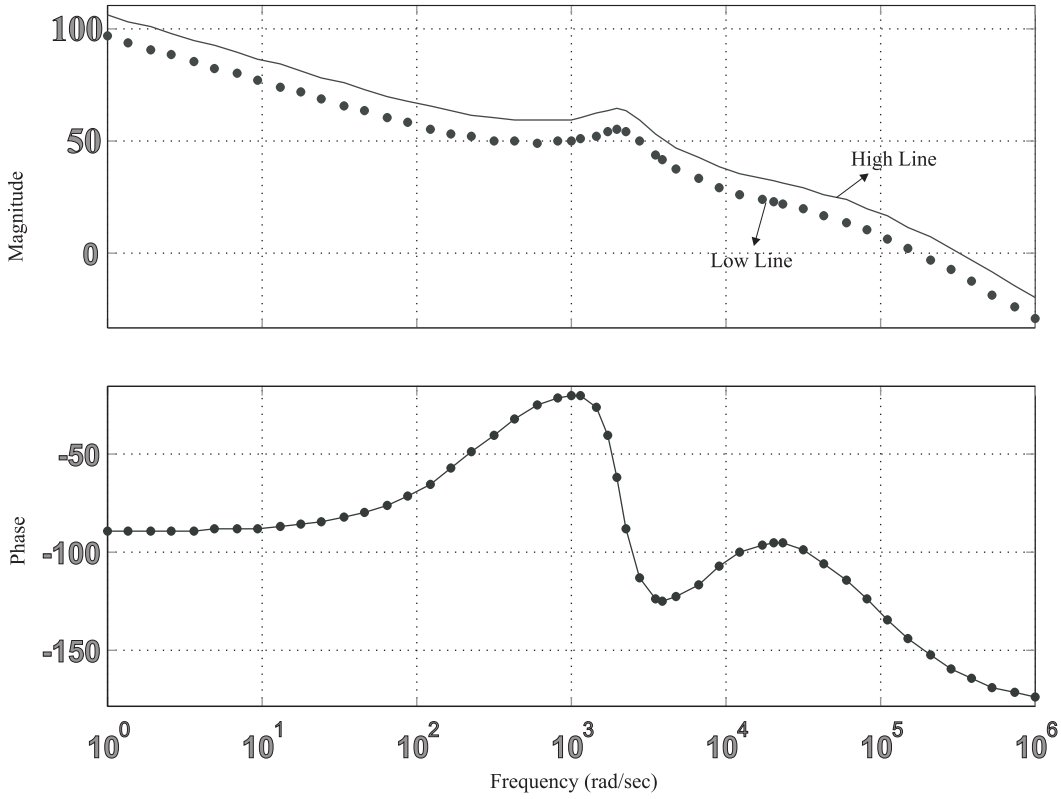

Figure 2.4: Frequency-response analysis of the closed-loop buck converter. It shows a stable system.

which cannot be predicted with the state-space averaged model. Moreover, prediction of the period-one slow-scale instability with the linearized averaged model is conservative as compared to that obtained with the nonlinear averaged model.

It follows from Figure 2.5 that the period-one orbits are stable for all values of the input voltage v_{in} below 53.8 volts. All of the Floquet multipliers are within the unit circle. As v_{in} increases past 53.8 volts, one of the Floquet multipliers exits the unit circle through -1, as shown in Figure 2.6, indicating a period-doubling or flip bifurcation. To study the stability of the created period-doubled orbits, we calculated the Floquet multipliers based on the second-order map for v_{in} =53.8 volts. The result is [0.1288, 0.8302+0.0389i, 0.8302-0.0389i,

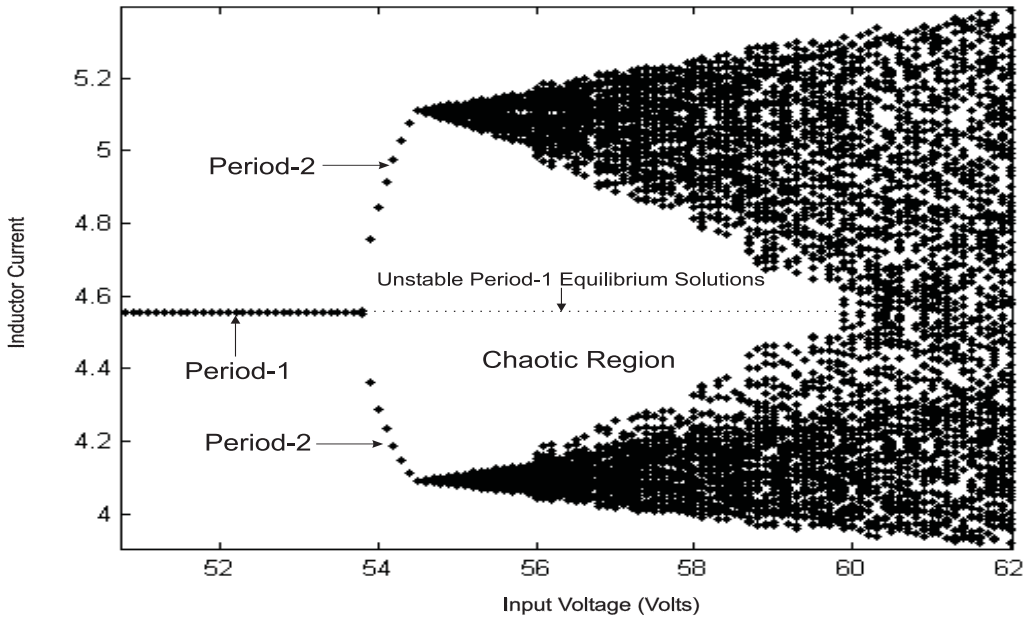

Figure 2.5: A theoretical bifurcation diagram of the closed-loop buck converter. It shows a fast-scale instability.

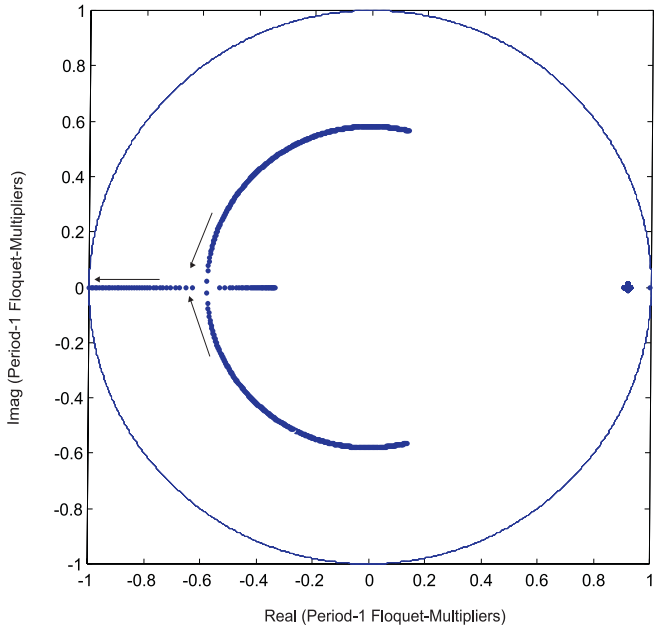

Figure 2.6: One of the period-one Floquet multipliers exits the unit circle through -1, indicating a period-doubling bifurcation.

0.9039, 0.9911]. Because all of these multipliers are inside the unit circle, the created period-two orbits are stable, and hence the period-doubling bifurcation is supercritical. Indeed, we were able to use long-time simulation to calculate period-two orbits beyond $v_{in} = 53.8$ volts, as shown in the bifurcation diagram in Figure 2.5.

Figure 2.7a shows that the duty ratio undergoes a period-doubling bifurcation as v_{in} increases beyond 53.8 volts. Immediately after the period-doubling bifurcation, all of the Floquet multipliers of the second-order map are within the unit circle: three of them are well within the unit circle and two are real and near 1+0i, as shown in Figure 2.7b. In Figure 2.7c, we show the movement of the latter multipliers as v_{in} increases. They approach each other, collide, and move away from the real axis. It follows from Figure 2.7a that as v_{in} approaches $v_{in} = v_{in_c} \approx 54.48$ volts, one of the duty ratios approaches zero and at $v_{in} = v_{in_c}$ the error signal v_e hits the ramp at the bottom, as shown in Figure 2.7d. As such, the system saturates, which we have confirmed experimentally. This saturation or pulse dropping initiates chaos, which is called border collision bifurcation by Nusse et al (1992) and Bannerjee et al (1997, 1999). Researchers in other fields have also reported similar non-smooth bifurcations, such as C-bifurcations in Filippov systems (Feigin, 1974; Feigin, 1995) and grazing bifurcation in impacting systems (Ivanov, 1993; Nordmark, 1997; Brogliato, 1999). In the saturated region, the second-order map used to derive (2.29) and (2.30) becomes invalid. As such, we are unable to plot the movement of the Floquet multipliers any more. For further increases in the input voltage, the response of the system becomes chaotic, which is shown in Figure 2.5.

Once chaos is initiated, we resort to time-domain simulation using the switching model. Bernardo and Vasca (1998) proposed the concept of impact map. However, for the chaotic region, where the switching instant is unknown, the difference in the computation time between the simulation and the approach based on the impact map is negligible. It follows from the bifurcation diagram in Figure 2.5 that initially chaos is confined to two small bands. As v_{in} is increased, the two chaotic bands increase in size until they collide with the unstable period-one response, resulting in a single large chaotic attractor in a so-called

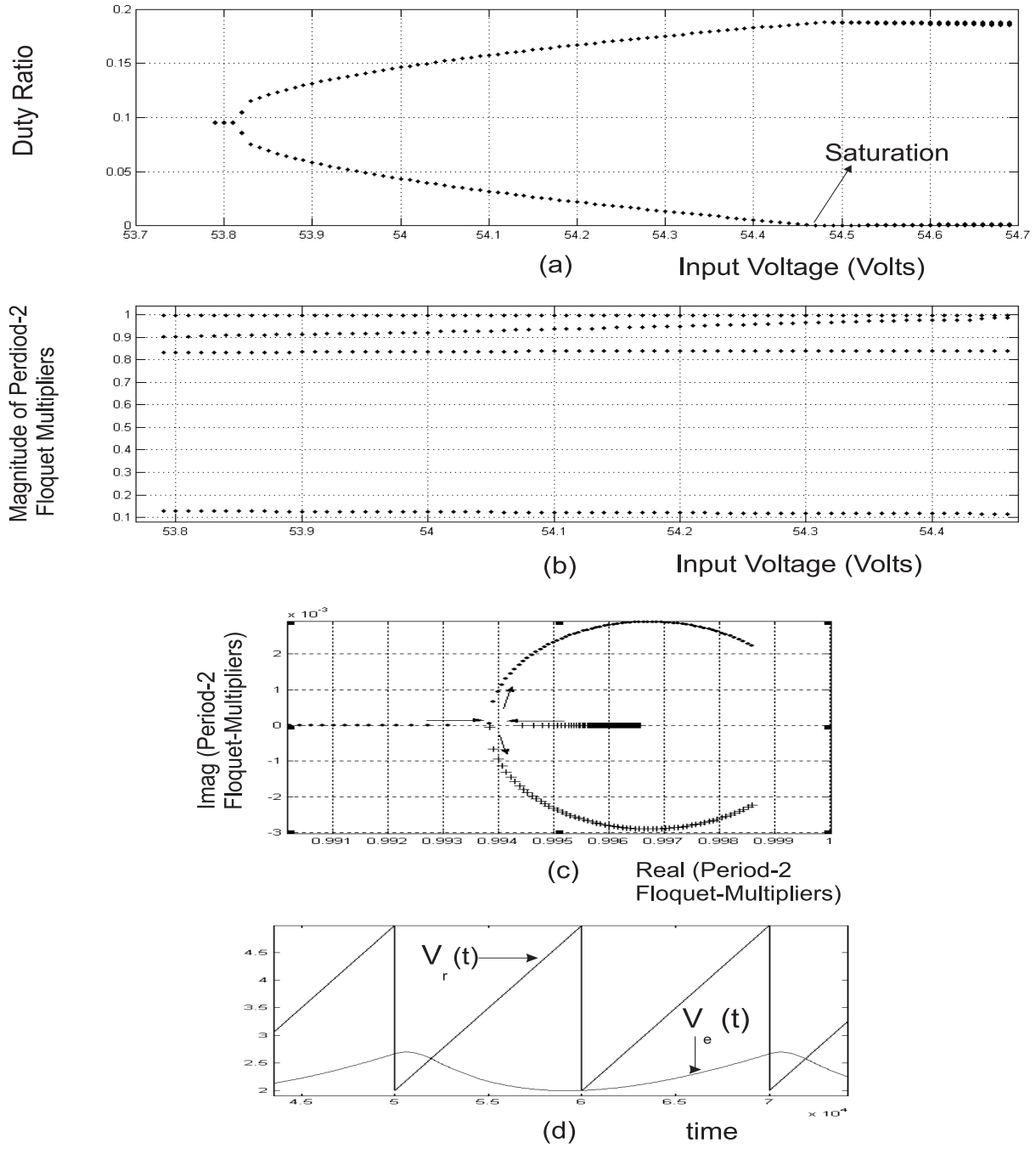

Figure 2.7: Variation of the duty ratio (a) and the magnitudes of the Floquet multipliers (b) with the input voltage in the period-two region. (c) Two of the Floquet multipliers in (b) first collide with each other and then move towards the imaginary axis. (d) The error signal hits the ramp at the lowest point (at the beginning of the switching cycle) and the closed-loop system saturates.

attractor merging crisis (Nayfeh and Balachandran, 1995).

We now explain qualitatively the transition in the response of the closed-loop converter from a period-two orbit to a chaotic attractor in the vicinity of $v_{in} = v_{in_c}$ by using Filippov's theory (Filippov, 1988). However, to proceed further, we use (2.12), (2.13) and Figure 2.1, to describe the dynamics of the states of the closed-loop buck converter as a differential equation with discontinuous right-hand side; that is,

$$\begin{aligned} &\tfrac{d\Psi(t)}{dt} = A\Psi(t) + Bv_{in}u + B_r v_{ref} \\ &u = \tfrac{1+\text{sign}(v_e(t)-v_r(t))}{2} = \tfrac{1+\text{sign}\left(v_e(t)-v_l-v_{ramp}\text{mod}(\frac{t}{T})f\right)}{2} \end{aligned} \tag{2.39}$$

where $f = \frac{1}{T}$, $A = A_1 = A_2$, $B = B_1$, and $B_r = B_{r1} = B_{r2}$. Equation (2.39) shows that when $v_e(t) = v_r(t)$, then $\frac{d\Psi}{dt}$ is undefined. However, as long as $v_l < v_e(t) < v_l + v_{ramp}$ at the point of impact with the ramp, the latching action of our controller ensures only a single turn-on and a single turn-off of the power switch in a switching cycle. As such, one can describe the dynamics of the system using a nonlinear discrete map, thereby eliminating the discontinuity. One such map is used to obtain (2.29) and (2.30). The general form of this map is

$$\begin{aligned} \Psi_{k+2} &= \Big(\Phi_4\Phi_3\Phi_2\Phi_1\Big)\Psi_k + \Big(\Phi_4\Phi_3\Phi_2\Lambda_1 + \Phi_4\Phi_3\Lambda_2 + \Phi_4\Lambda_3 + \Lambda_4\Big)v_{in} + \\ &\quad \Big(\Phi_4\Phi_3\Phi_2\Upsilon_1 + \Phi_4\Phi_3\Upsilon_2 + \Phi_4\Upsilon_3 + \Upsilon_4\Big)v_{ref} \\ v_{dc_{k+2}} &= P_1\Psi_{k+2} \\ 0 &= \sigma_1(\Psi_k, d_{1k}, v_{in}) \\ 0 &= \sigma_2(\Psi_k, d_{1k}, d_{2k}, v_{in}) \end{aligned} \tag{2.40}$$

where Φ_s, Λ_s, Υ_s, and P_1 are matrices, and the last two scalar equations describe the switching conditions. When $v_e(t) = v_l$ (or $v_l + v_{ramp}$) at the point of impact with the ramp, (e.g., Figure 2.7d), the system saturates and hence (2.40) fails. Using Figure 2.7d, we therefore construct another map as

$$\Psi_{k+2} = \Big(\underline{\Phi}_3\Phi_2\Phi_1\Big)\Psi_k + \Big(\underline{\Phi}_3\Phi_2\Lambda_1 + \underline{\Phi}_3\Lambda_2 + \underline{\Lambda}_3\Big)v_{in} + \Big(\underline{\Phi}_3\Phi_2\Upsilon_1 + \underline{\Phi}_3\Upsilon_2 + \underline{\Upsilon}_3\Big)V_{dcref}$$

$$\begin{aligned} v_{dc_{k+2}} &= P_2 \Psi_{k+2} \\ 0 &= \sigma_1(\Psi_k, d_{1k}, v_{in}) \end{aligned} \tag{2.41}$$

where $\underline{\Phi}$s, $\underline{\Lambda}$, and $\underline{\Upsilon}$ are matrices. The nonlinear map (2.41) is valid at the point given by $v_e(t) = v_l$ and in the vicinity of the fixed point. It is obvious that, in the vicinity of saturation, the two maps (given by (2.40) and (2.41)) that describe the same system have different forms. Let J^- and J^+ be the Jacobian matrices that are obtained by linearizing (2.40) and (2.41) in the vicinity of the saturation point. Depending on the values of J^- and J^+ in the neighborhood of the saturation point, we can have two different sets of Floquet multipliers (FM^- and FM^+). In a smooth system, the transition from FM^- to FM^+ is always gradual. However, this is not the case in a nonsmooth system; it has many other other bifurcations than a smooth system (Nayfeh and Balachandran, 1995). The bifurcation diagram in Figure 2.5 shows one such case, where chaos occurs due to saturation immediately after a period-doubling bifurcation. Although the Floquet multipliers are defined before and after the saturation point, they are not defined at this point. The Floquet multipliers at this point are obtained from the set-valued Jacobian matrix J=[J^-, J^+]. The viable solutions of this set are obtained by using the concept of convexity (Filippov, 1988; Mazumder et al., 2001c).

In Figure 2.8, we show the experimental results we obtained for the converter in the stable and unstable regions with the input voltage as the bifurcation parameter. In Figure 2.8a, we show a stable period-one response. As v_{in} is increased to 52.6 volts, the response becomes chaotic, as shown in Figure 2.8b, without undergoing a period-doubling bifurcation, as predicted by the theory. To explain this discrepancy, which is illustrated in Table 2.1, we used the high-frequency model, shown in Figure 2.2, to account for the impact of the very high-frequency dynamics due to parasitics and device nonlinearities. The high-frequency model is developed using actual device models and parasitic parameters obtained using the actual PCB layout. The parasitic parameters are obtained from the PCB using the finite-analysis pacakage INCA. The values of the parameters of the high-frequency model are

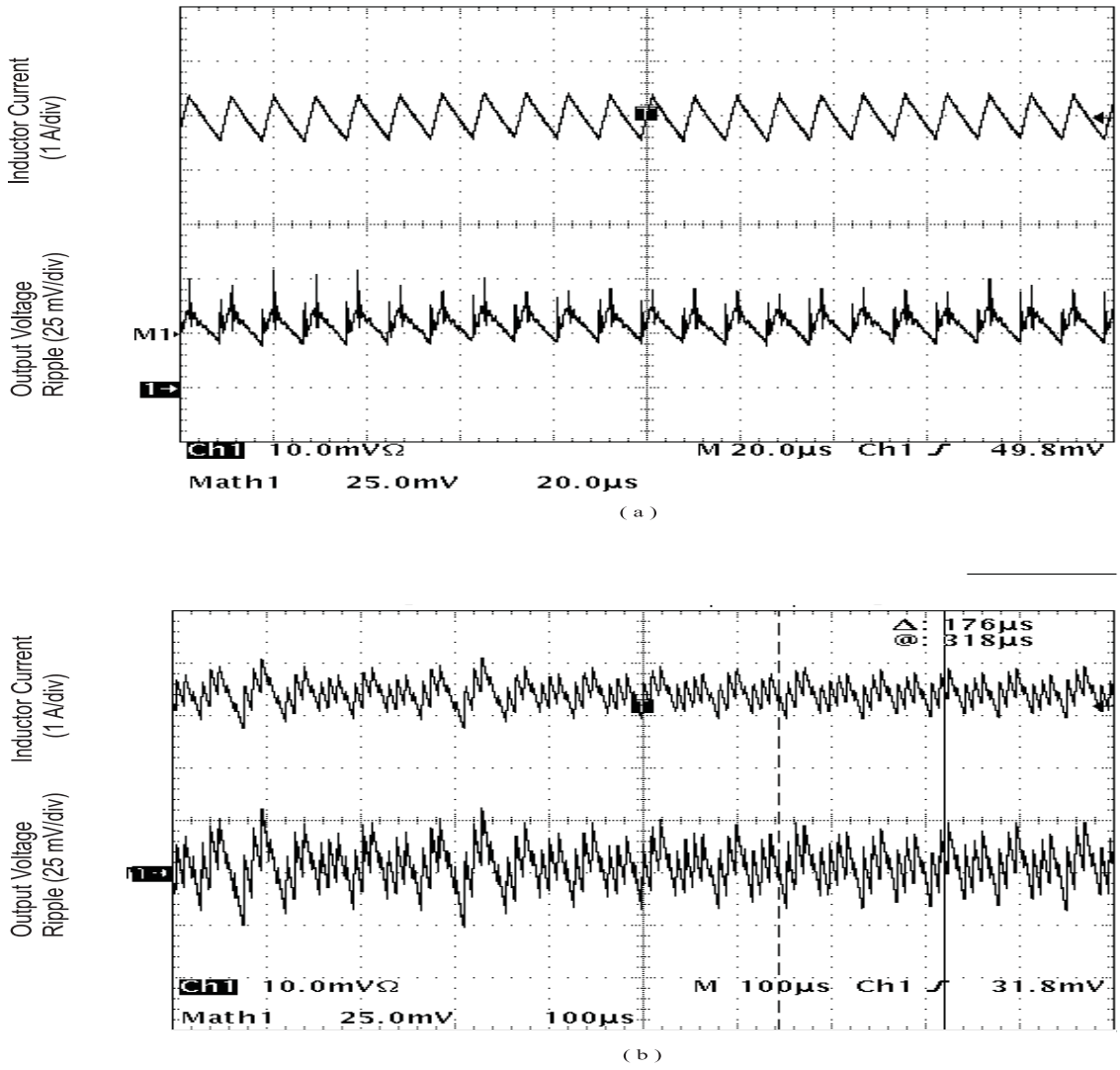

Figure 2.8: Experimental waveforms for (a) period-one and (b) chaotic responses.

$r_L = 0.021\ \Omega$, $v_{ref} = 2.0$ V, $R = 1\ \Omega$ - $5\ \Omega$, $C_1 = 30\ p$F, $C_2 = 100\ n$F, $C_3 = 100\ n$F, $C_4 = 2200\ \mu$F, $C_5 = 2200\ \mu$F, $L = 50\ \mu$H, $L_1 = 30\ n$H, $L_2 = 25\ n$H, $L_3 = 5\ n$H, $L_4 = 5\ n$H, $L_5 = 15\ n$H, $L_6 = 15\ n$H, $L_7 = 27\ n$H, $L_8 = 29\ n$H, $R_1 = 0.16\ \Omega$, $R_2 = 0.15\ \Omega$, $R_3 = 0.025\ \Omega$, $R_4 = 0.025\ \Omega$, $R_5 = 0.05\ \Omega$, $R_6 = 0.05\ \Omega$, $R_7 = 0.15\ \Omega$, $R_8 = 0.15\ \Omega$, $v_l = 1.8$ V, $v_{ramp} = 3.0$ V, and $f = \frac{1}{T} = 100\ k$Hz.

Table 2.1: Comparison of the results obtained using the nonlinear map and the averaged model of the buck converter with those obtained experimentally.

v_{in} (V)	Averaged model	Nonlinear map	Experiment
20 ↓ 52.5	stable equilibrium	stable period-one orbit	stable period-one orbit
52.6 ↓ 53.7	stable equilibrium	stable period-one orbit	chaos
53.8 ↓ 54.47	stable equilibrium	unstable period-one orbit stable period-two orbit	chaos
54.48 ↓ 62.0	stable equilibrium	chaos	chaos

In Figure 2.9, we present the Fourier spectra of the bus voltage for two separate cases: one based on the high-frequency model and the other based on the nominal model, as shown in Figure 2.1. These simulation results clearly indicate that the unmodeled uncertainties due the very high-frequency dynamics cause the earlier onset of chaos.

Interestingly, the chaotic response is stable, and the ripple in the output voltage caused by chaos is tolerable, as seen from the experimental waveforms. We also performed a dynamic-load test when the converter is in the chaotic region, and the result is shown in Figure 2.10. The load resistance was changed by 150% periodically every 1 ms. The test results show that chaos is stable. Within the chaotic region, we found narrow windows of periodic responses. Two such periodic waveforms are shown in Figures 2.11a and 2.11b.

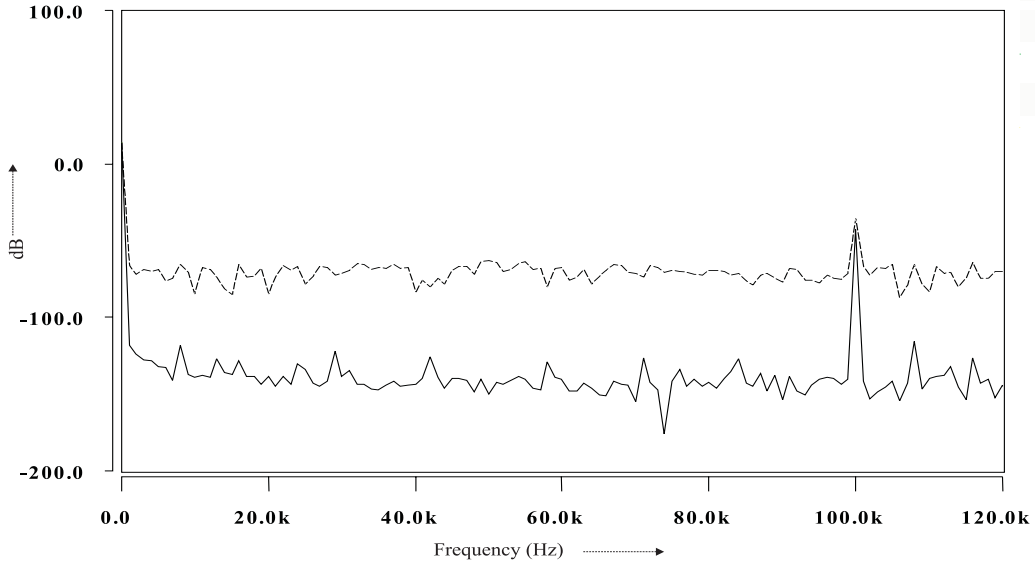

Figure 2.9: Impact of parasitics on the onset of chaos. Fourier spectra of the output voltage based on the nominal model (bottom trace) and on the high-frequency model (top trace). The latter predicts an earlier onset of chaos.

Using the nonlinear map of the nominal model, we then investigate the impact of load resistance (R) on the stability of the closed-loop converter. Figure 2.5 shows that, at $u = u^* = 53.8$, the period-one orbit becomes unstable. Therefore, we fix the input voltage (= 53 V) in the vicinity of u^*. All of the other power stage and controller parameters the same used to obtain Figure 2.5. Figure 2.12, shows a bifurcation diagram, which is obtained by increasing the value of R from 1 Ω to 9 Ω. Initially, the period-one orbit of the closed-loop system is stable. When $R = 1.7$ Ω, the period-one orbit becomes unstable and a stable period-two orbit emerges. As before, the period-doubling bifurcation was ascertained by computing the Floquet multiplers of the map. When $R = 6$ Ω, the period-two orbit becomes unstable and a chaotic attractor emerges. The onset of chaos occurs due to border collision/saturation.

The bifurcation diagram in Figure 2.13, shows the effect of variation of the output in-

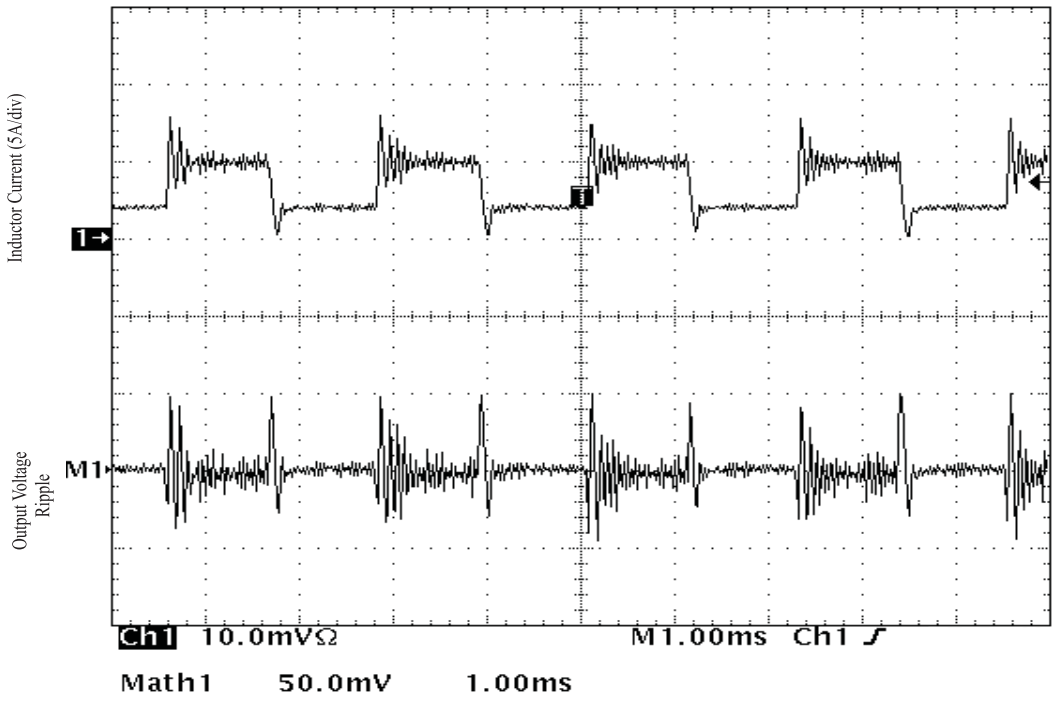

Figure 2.10: Experimental result shows the influence of a transient-load change on the chaotic attractor.

ductance (L), from 60 μH to 20 μH, on the stability of the closed-loop system. The input voltage and the load resistance are fixed at 53 V and 1 Ω, respectively. All other parameters remain the same. We find that, as long as L is larger than 49 μH, the period-one orbit is stable. When $L = 49\mu$H, the period-one orbit becomes unstable and a stable period-two orbit emerges. Furthermore, when L is reduced below 48 μH, the closed-loop system becomes chaotic. The onset of chaos occurs due to border collision/saturation.

Finally, we demonstrate the slow-scale instability in the buck converter. The controller for the closed-loop systems has the form $G_c(s) = \frac{\omega_I}{s}\frac{(s+\omega_{z1})}{(s+\omega_{p1})}$. The frequency-response function for this case is shown in Figure 2.14a for input voltages ranging from 20 to 62 volts. The load resistance was kept constant at five ohm. For the nonlinear model, given the same system parameters, we found that two of the Floquet multipliers [0.3119, 1.00001 + 0.0899i, 1.00001

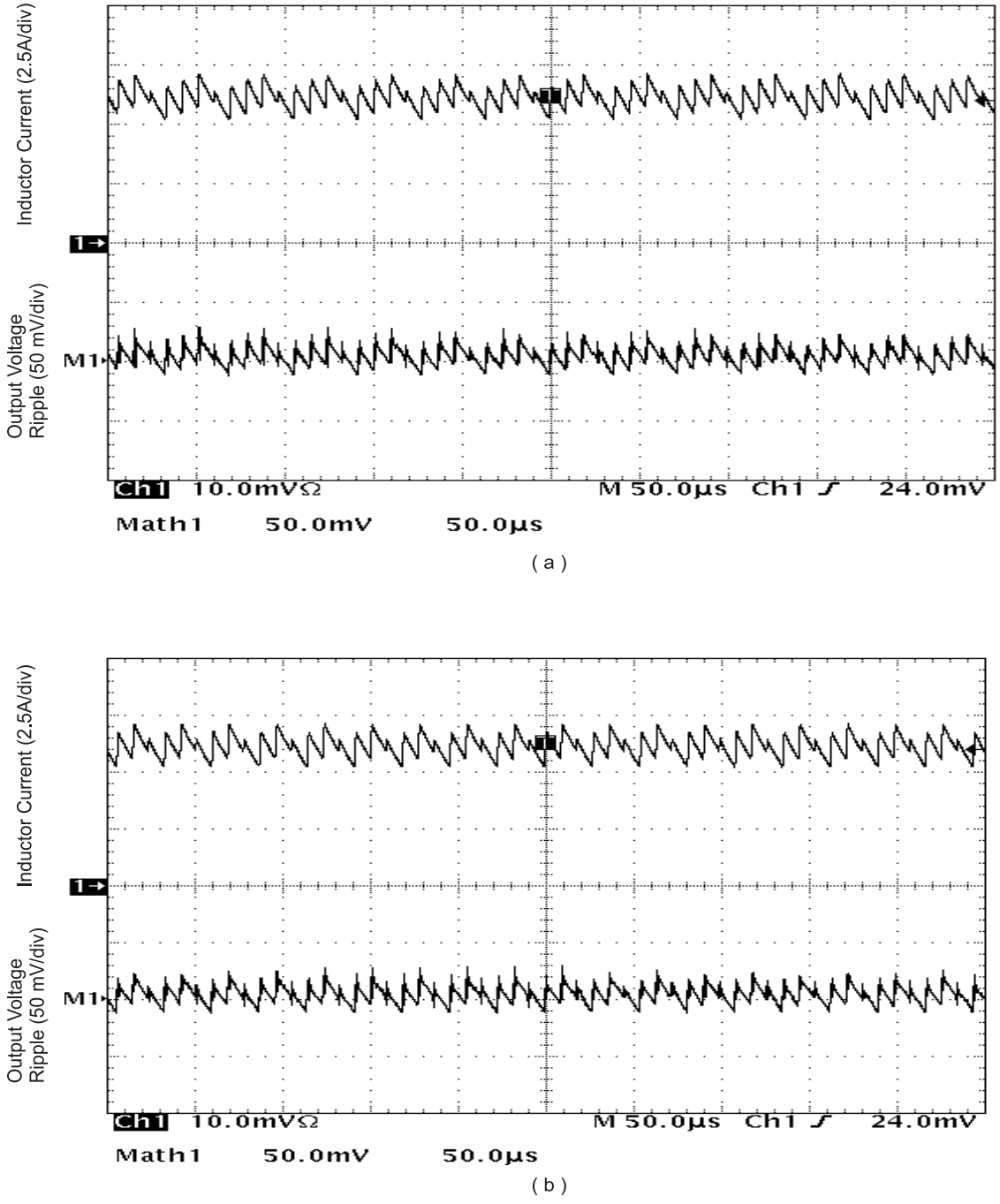

Figure 2.11: Experimental result shows (a) a period-4 and (b) a period-3 waveform within the chaotic region.

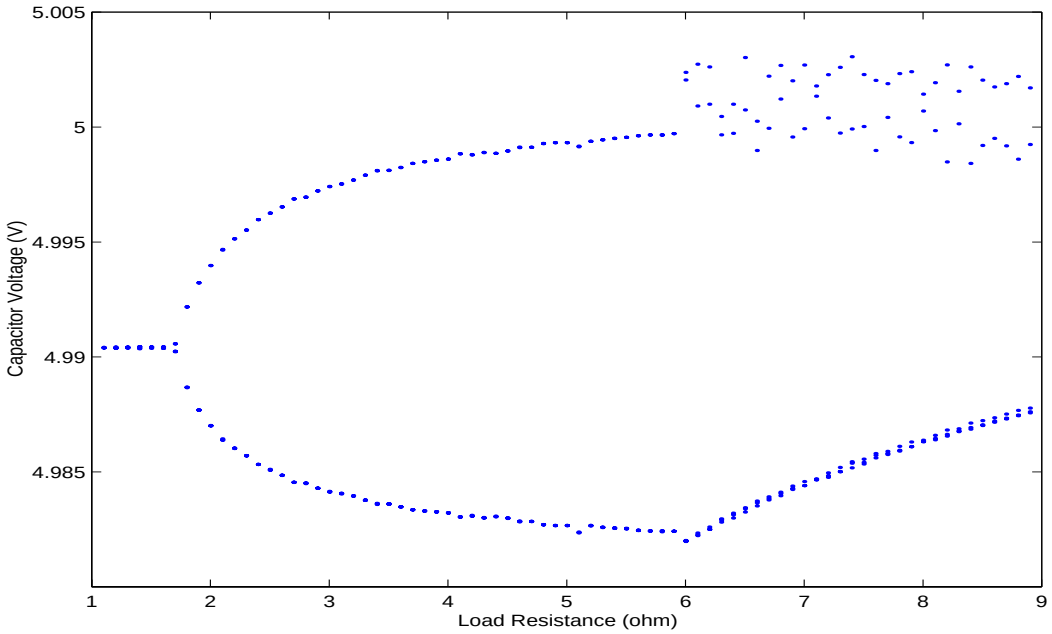

Figure 2.12: A bifurcation diagram, shows the response of the capacitor voltage with increasing value of load resistance (R). A period-doubling bifurcation occurs when $R = 1.7\ \Omega$ and the onset of chaos occurs at $R = 6\ \Omega$.

- 0.0899i, 0.9533] exit the unit circle as complex conjugates at an input voltage of 31 volts. Hence, both of the averaged and discrete models predict the slow-scale instability.

The experimental result in Figure 2.14d shows that the response of the system suddenly bursts into an oscillation as the input voltage s gradually reduced below the point of instability. Beyond the point of instability, the current is not always in the CCM, as seen from the theoretical and experimental results shown in Figures 2.14b and 2.14c. To analyze the dynamics beyond this point of instability, we had to switch between the CCM and DCM models. The CCM model was augmented with one more additional topology in which both the switch S_1 and diode D_1 are off. In other words, the system of equations (2.6) is modified as

$$\begin{aligned} X_{k+1} &= \Phi_3(t_3)\,\Phi_2(t_2)\,\Phi_1(t_1)\,X_k + \\ &\left[\Phi_3(t_3)\,\Phi_2(t_2)\int_0^{t_{11}}\Phi_1(\tau)\,B_1 d\tau + \Phi_3(t_3)\int_{t_{11}}^{t_{12}}\Phi_2(\tau)\,B_2 d\tau + \int_{t_{12}}^{T}\Phi_3(\tau)\,B_3 d\tau\right] v_{in} \end{aligned}$$

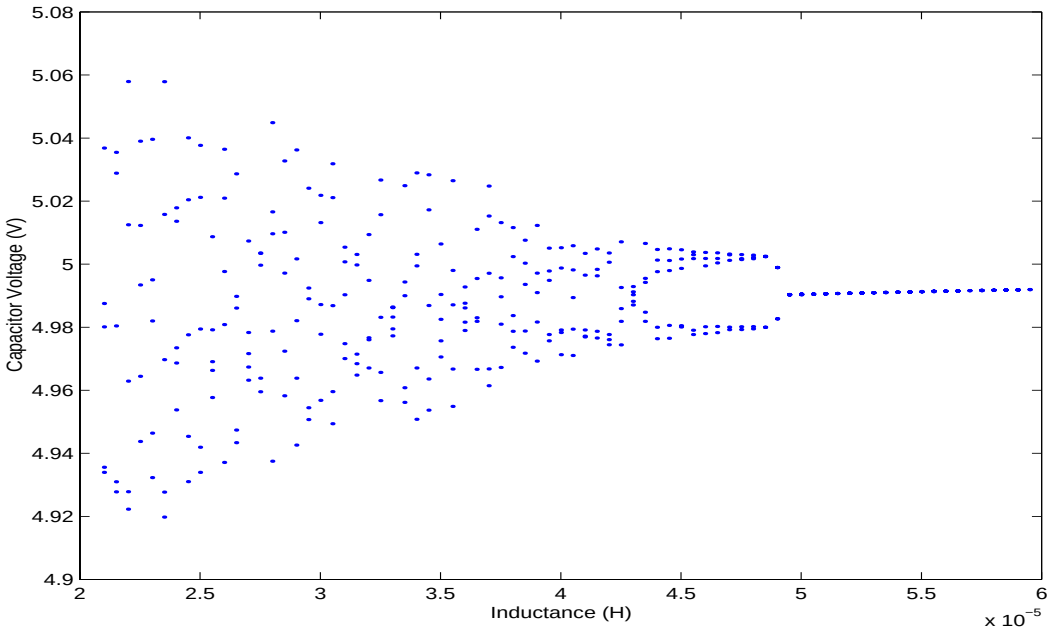

Figure 2.13: A bifurcation diagram, shows the response of the capacitor voltage with increasing value of inductance (L). A period-doubling bifurcation occurs when $L = 48.9$ μH and the onset of chaos occurs at $L = 48$ μH.

$$v_{dc_{k+1}} = C_3^o X_{k+1} \tag{2.42}$$

where $\Phi_k(\tau) = e^{A_k^o \tau}$ $[k = 1, 3]$ and $t_1 = t_{11} = d_k T$, $t_2 = t_{12} - t_{11}$, $t_3 = T - t_{12}$. The additional state-space matrices A_3^o, B_3^o, C_3^o, A_3, B_3, B_{r3}, C_3, and H_3 required for the DCM model are given by

$$\begin{aligned} A_3^o &= \begin{bmatrix} 0 & 0 \\ 0 & -\frac{1}{(R+r_C)C} \end{bmatrix}, \quad B_3^o = \begin{bmatrix} 0 \\ 0 \end{bmatrix}, \quad C_3^o = \begin{bmatrix} \frac{r_C R}{R+r_C} & \frac{R}{R+r_C} \end{bmatrix} \\ A_3 &= \begin{bmatrix} A_3^o & 0 \\ SC_3^o & A_c \end{bmatrix}, B_3 = \begin{bmatrix} B_3^o \\ 0 \end{bmatrix}, B_{r3} = \begin{bmatrix} 0 \\ B_{rc} \end{bmatrix}, C_3 = \begin{bmatrix} C_3^o & 0 \end{bmatrix}, H_3 = \begin{bmatrix} H_c & 0 \end{bmatrix}. \end{aligned} \tag{2.43}$$

In (2.42) the duty ratio is calculated as before. The additional timing information needed is the instant at which the inductor goes to zero in the discharging mode.

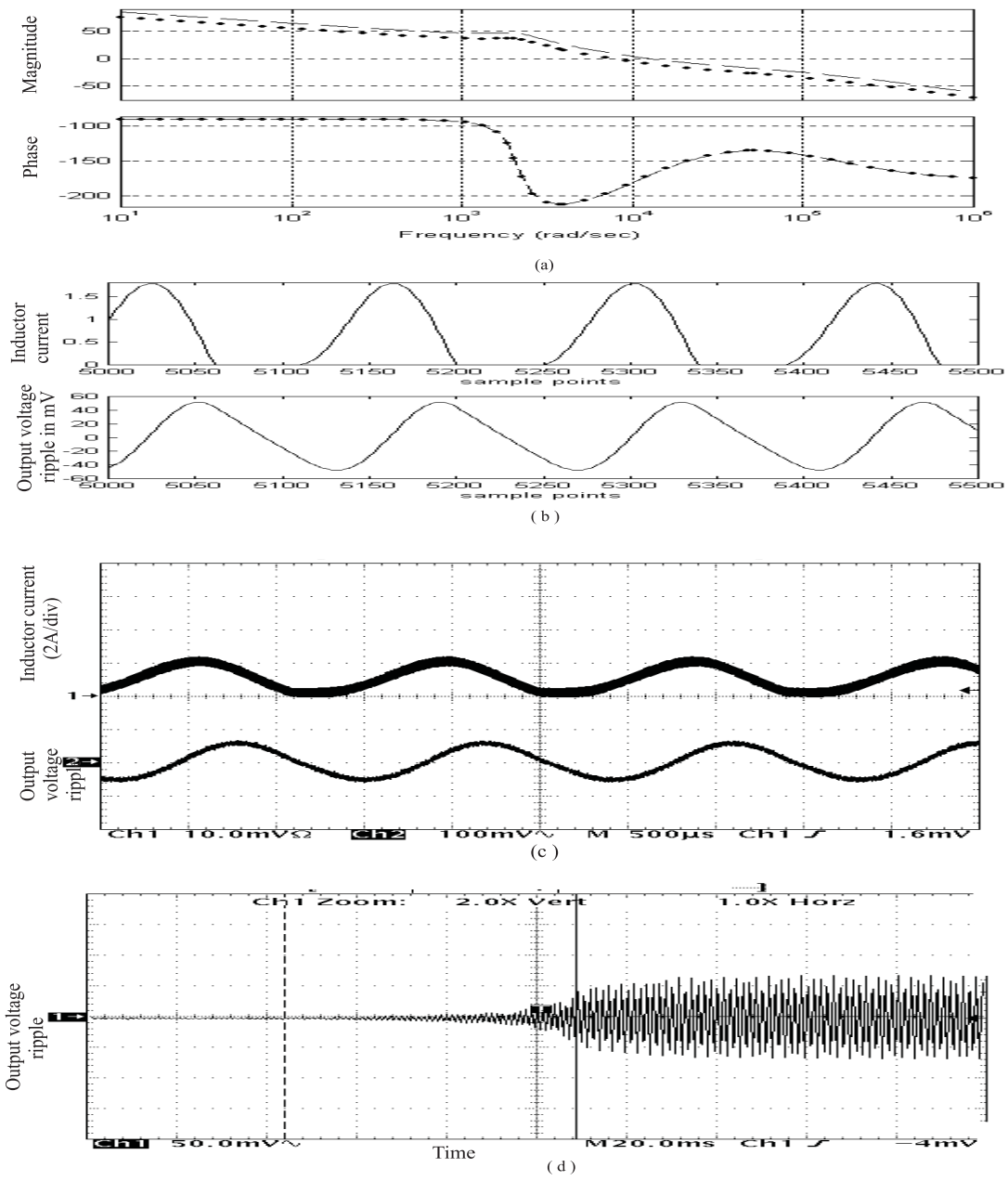

Figure 2.14: Slow-scale instability of the closed-loop buck converter. (a) and (b) Linear and nonlinear analyses, which show an unstable response. (c) An experimental result that verifies the result in (b). (d) An experimental result that shows the onset of a sudden slow-scale instability as the input voltage (bifurcation parameter) is changed.

2.7 Summary

Using an exact formulation based on nonlinear maps, we investigated the fast-scale and slow-scale instabilities of a closed-loop dc-dc converter and predicted the boundaries of these instabilities. For the standalone converter, the fast-scale instability results in a supercritical period-doubling bifurcation followed by a border collision bifurcation (due to saturation), which leads to chaos. The averaged model does not predict the boundary of the period-one instability correctly. Moreover, it can not account for post-instability dynamics.

The impact of parasitics on the onset of chaos is studied using a high-frequency model. The model is developed based on an actual PCB layout and power-device models. We found that the onset of chaos on the fast scale occurs earlier due to parasitics. However, it has negligible impact on the slow-scale instability. This was confirmed experimentally. The boundedness of the response in the chaotic region under transient-load conditions was confirmed experimentally.

Chapter 3

Modeling and Stability Analyses. II. Extension to Complex Standalone PWM Converters

We demonstrate how to extend the methodologies, developed in Chapter 2, to more complex standalone systems, which may have more than one switch. We begin, by analyzing the stability of an integrated system, which comprises a filter followed by a dc-dc converter. We investigate two such integrated systems: one is stable as per Middlebrook's criterion (Middlebrook, 1976) and the other is unstable. We find that this criterion fails to predict the fast-scale instability for the first design. For the second design, which is unstable on the slow scale due to a subcritical Hopf bifurcation, this criterion (which is based on linear analysis) does not give the domain of attraction of the period-one orbits near the bifurcation point. We find that the domain of attraction of the period-one orbits reduces considerably even before the Hopf bifurcation point due to the simultaneous presence of two stable and one unstable solutions. This reduces the disturbance rejection capability of the closed-loop system in this region. Conventional methods based on small-signal averaged-model techniques do not show this reduction in the domain of attraction.

Next, we show how to analyze a multilevel dc-dc PWM converter, which is an area of growing prominence (Pinheiro and Barbi, 1995; Canales et al., 2000), using nonlinear maps. We show that the analysis of such multi-switch systems is the same as explained in Chapter 1, except that the switching condition is a vector equation rather than a scalar one.

We then analyze the stability of a single-phase boost PFC circuit, which are widely used in power electronics. However, very few have even attempted to properly analyze the stability of this system. The system of equations for the boost PFC circuit involves discontinuity in control and non-differentiability in state and time. These qualities, in addition to the time-varying nature of the converter, make the analysis of the boost PFC circuit difficult. In this chapter, we begin the analysis of boost PFC by developing a state-space model for the boost PFC circuit, which is designed to operate in the continuous-conduction mode (CCM). Although the converter operates in CCM, when the input voltage is low, the inductor current becomes zero during a small interval. The converter operates in the discontinuous-conduction mode (DCM) in that interval. With the proper choice of the circuit parameters, this duration can be minimized, but for a feasible converter it can not be made zero. Consequently, we show that global existence of a smooth hypersurface is not possible. Using the developed model, we analyze the stability and dynamics of the converter in the saturated and unsaturated regions using Lyapunov's method and a bifurcation analysis. Our analysis predicts not only the instabilities, but also the mechanism of these instabilities. Our general stability analysis does not require the forcing function (or the input voltage) to be harmonic (e.g., $\cos \omega t$), which has been a common feature in previous analyses. However, we show that, if we make such an assumption, then we can compute the exact solution of the time-varying system.

Finally, we extend the ideas developed for boost PFC circuits to bidirectional CCM single-phase boost converters. Although the number of switches for this converter is more, we find that the analysis of this converter is realatively easier because of two reasons: the forcing function in the model is not nonsmooth and the phase current is continuous. Using a nonlinear map, we determine that the mechanism of instability in this case is similar to that of the boost PFC.

3.1 Integrated Filter-Converter System

An input filter is often required between a switching converter and its power source. An ideal source has no impedance and remains unperturbed regardless of the input current waveform of the converter. However, in reality, input sources are non-ideal. To prevent the input current waveform of the switching regulator from interfering with the source and to preserve the integrity of the source for other equipment, which may be operating from a common source, the converter must have an electromagnetic interference (EMI) filter. The input filter is also required to isolate the source voltage transients so as not to degrade the performance of the switching regulator.

3.1.1 Modeling

In Figure 3.1, we show a circuit model for a dc-dc regulator with a second-order input EMI filter. The filter consists of an inductance L_f and a capacitance C_f with resistances of R_{f1} and R_{f2}, respectively. The transfer function of the output impedance of the second-order filter is

$$Z_{of}(s) = \frac{s^2\left(L_f C_f R_{f2}\right)+s\left(C_f R_{f1} R_{f2}+L_f\right)+R_{f1}}{s^2\left(L_f C_f\right)+sC_f\left(R_{f1}+R_{f2}\right)+1}. \tag{3.1}$$

The nominal values of the parameters for the filter ($L_f = 200$ μH, $R_{f1} = 0.1$ Ω, $R_{f2} = 0.021$ Ω, and $C_f = 440$ μF) are chosen such that the filter adequately attenuates the interference due to the signals at the switching frequency and its higher harmonics. Using the methods used in Chapter 2, one can realize the state-space averaged model

$$\begin{aligned} \frac{d\overline{\Psi_a(t)}}{dt} &= \left[A_{1a}d + A_{2a}\overline{d}\right]\overline{\Psi_a(t)} + \left[B_{1a}d + B_{2a}\overline{d}\right]\overline{v_{in}} + \left[B_{r1a}d + B_{r2a}\overline{d}\right]v_{ref} \\ \overline{v}_{dc}(t) &= \left(C_{1a}d + C_{2a}\overline{d}\right)\overline{\Psi_a(t)} \end{aligned} \tag{3.2}$$

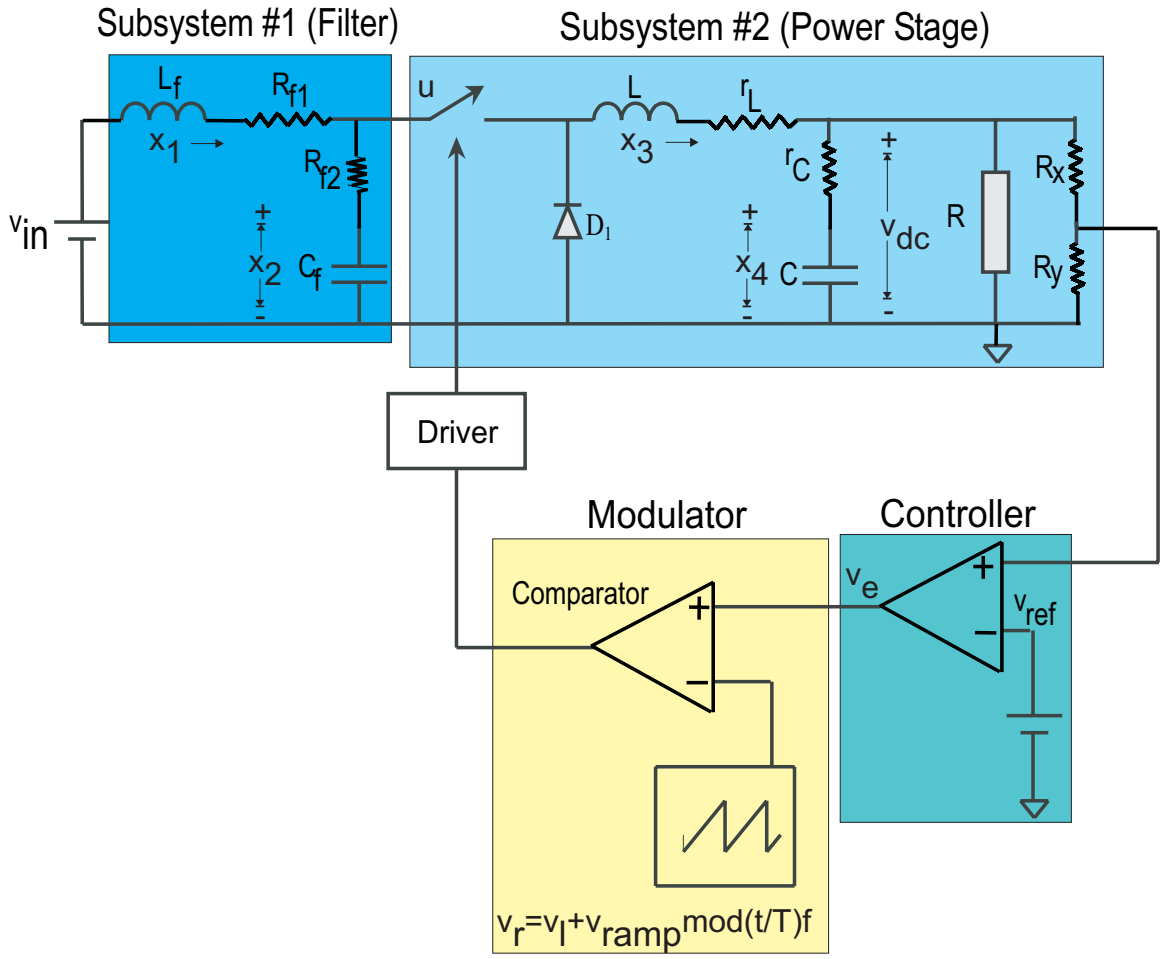

Figure 3.1: A closed-loop buck converter with a second-order filter at its front end.

and the nonlinear map

$$\begin{aligned}
\Psi_{a_{k+1}} &= f_1\left(\Psi_{a_k}, d_k, v_{in}\right) \\
&= e^{A_{2a}(1-d_k)T} e^{A_{1a}d_kT} \Psi_{a_k} \\
&\quad + \left[e^{A_{2a}(1-d_k)T}\left(e^{A_{1a}d_kT} - I\right)\left(A_{1a}\right)^{-1} B_{1a} + \left(e^{A_{2a}(1-d_k)T} - I\right)\left(A_{2a}\right)^{-1} B_{2a}\right] v_{in} \\
&\quad + \left[e^{A_{2a}(1-d_k)T}\left(e^{A_{1a}d_kT} - I\right)\left(A_{1a}\right)^{-1} B_{r1a} + \left(e^{A_{2a}(1-d_k)T} - I\right)\left(A_{2a}\right)^{-1} B_{r2a}\right] v_{ref} \\
v_{dc_{k+1}} &= f_2\left(\Psi_{a_k}, d_k, v_{in}\right) = C_{2a}\Psi_{a_{k+1}}.
\end{aligned} \tag{3.3}$$

for the filter-converter system shown in Figure 3.1. In (3.2) and (3.3), A_{1a}, A_{2a}, B_{1a}, B_{2a}, B_{r1a}, B_{r2a}, C_{1a}, and C_{2a} are matrices; $\Psi_a(t)$ represents the combined states of the controller, the power stage, and the filter; $\overline{\Psi_a(t)}$ represents the averaged states of the interconnected

system; and d is the duty ratio. The auxiliary equation for the switching condition of the closed-loop feedback system is

$$\sigma\left(\Psi_{a_k}, d_k, v_{in}\right) = \varphi \cdot \left[e^{A_{1a}d_kT}\Psi_{a_k} + \left(e^{A_{1a}d_kT} - I\right)\left(A_{1a}\right)^{-1}\left(B_{1a}v_{in} + B_{r1a}v_{ref}\right)\right] - v_{ramp}d_k = 0. \quad (3.4)$$

In (3.4), the term φ represents the feedback controller and v_{ramp} is the magnitude of the ramp shown in Figure 3.1.

3.1.2 Stability Analysis

To facilitate analytical evaluation of the effect of the input filter on the regulator operation, we use the previous design of the buck converter. The structure of the feedback controller is the same as (2.16). Furthermore, the method of analysis of stability of the interconnected system using the map (3.3) follows the same procedure used to analyze the map (2.14).

For the averaged model, we use the impedance criterion approach originally proposed by Middlebrook (1976). Stability, as per this criterion, demands that the input impedance (Z_{icl}) of the closed-loop converter be greater than the output impedance (Z_{of}) of the input filter. For the closed-loop converter, shown in Figure 3.1, Z_{icl} can be shown to be

$$Z_{icl}(s) = \frac{[1+T_v(s)]Z_{iol}(s)}{1+T_v(s)-G_i(s)G_v(s)H(s)(FM)(A)} \quad (3.5)$$

where $T_v(s)$ is given by (2.34), $Z_{iol}(s)$, $G_i(s)$, and $G_v(s)$ represent the transfer functions for the open-loop input impedance, the control to the inductor current, and the audio susceptibility, respectively. The expressions for the last three transfer functions are given by

$$Z_{iol}(s) = \left(\frac{r_L+R}{D^2}\right)\frac{s^2LC\left(\frac{R+r_C}{R+r_L}\right)+s\left(\frac{r_LR+r_Lr_C+r_CR}{R+r_L}+\frac{L}{r_L+R}\right)+1}{1+sr_CC} \quad (3.6)$$

$$G_v(s) = \frac{D(1+sr_CC)}{s^2LC+s\left(r_LC+r_C(1-D)C+\frac{L}{r_C}\right)+1} \quad (3.7)$$

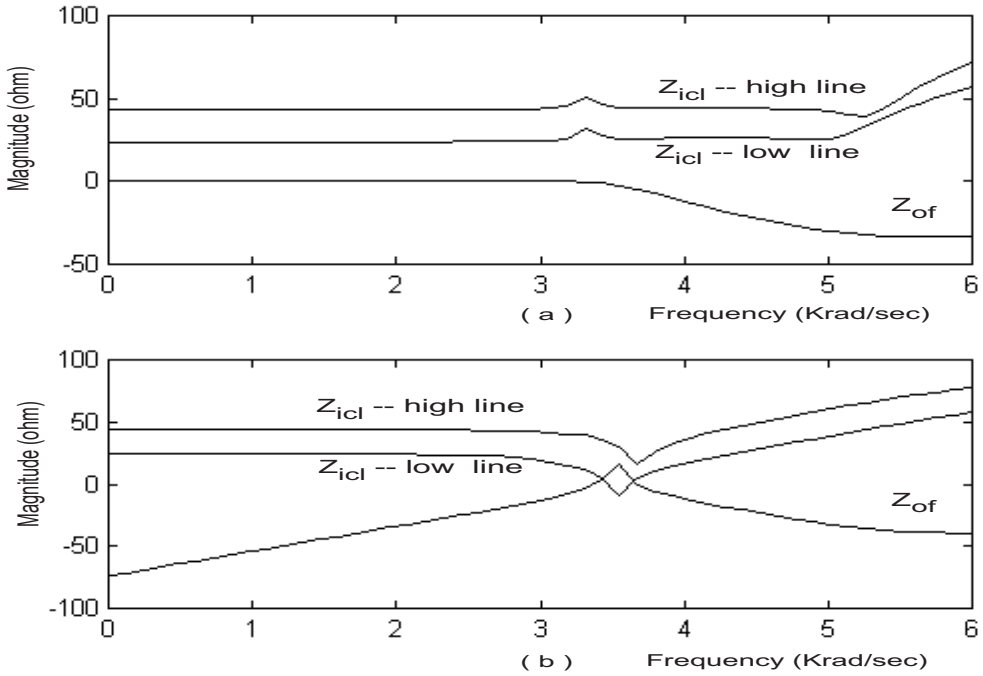

Figure 3.2: Results of an integrated filter-converter system based on small-signal analysis. A frequency-response analysis based on Middlebrook's criterion predicts a stable (a) and an unstable (b) system.

$$G_i(s) = \left(\frac{Du}{r_L+R}\right) + D\left[\left(\frac{u}{r_L+R}\right)\frac{1+s(r_C+R)C}{s^2LC\left(\frac{R+r_C}{R+r_L}\right)+s\left(\frac{r_LR+r_Lr_C+r_CR}{R+r_L}+\frac{L}{r_L+R}\right)+1}\right]. \tag{3.8}$$

For some designs, if the strictly conservative condition for stability of the integrated system is violated, then an extended analysis of the minor-loop gain T_m $(= Z_{of}/Z_{icl})$ using the Nyquist criterion needs to be done.

Next, we consider two separate cases for the filter-converter system shown in Figure 3.1. The first is a stable integrated system based on the stability criterion of Middlebrook. The other is a poorly designed filter. The frequency-response plots of Z_{icl} and Z_{of} for both cases are shown in Figure 3.2. For the second case, in line with the result obtained for the standalone converter in Chapter 2, we found that a slow-scale instability can be predicted by both the averaged and nonlinear models. Figure 3.3 shows that, when the input voltage

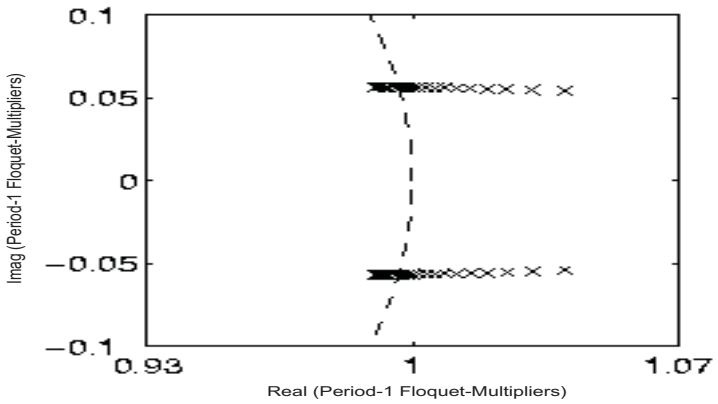

Figure 3.3: Nonlinear analysis shows a slow-scale instability for the second filter-converter system. Analysis using normal form in the vicinity of the bifurcation point indicates that the Hopf bifurcation is subcritical in nature.

is gradually reduced, the slow-scale instability occurs due to a Hopf bifurcation. Using the method of multiple scales, we simplify the large-signal model near the Hopf bifurcation into the two-dimensional system of equations called the normal form (Nayfeh and Balachandran, 1995)

$$\begin{aligned} \dot{r} &= \gamma_1(v_{in} - v_{in_{bp}})r + \gamma_2 r^3 \\ r\dot{\theta} &= \gamma_3(v_{in} - v_{in_{bp}})a + \gamma_4 r^4 \end{aligned} \tag{3.9}$$

where r is a measure of the amplitude of the created limit cycles and $v_{in_{bp}}$ is the value of the source voltage at the Hopf bifurcation point. The bifurcation is generic if γ_1 is different from zero; $\gamma_2 < 0$ indicates a subcritical bifurcation; and $\gamma_2 > 0$ indicates a supercritical bifurcation. Using the normal form of the large-signal averaged model in the vicinity of the bifurcation point, we find that the Hopf bifurcation is subcritical in nature. Using a nonlinear analysis (Alfayyoumi et al., 1999), we find that the domain of attraction of the period-one orbit is reduced due to the simultaneous presence of one unstable and two stable solutions as shown in Figure 3.4. This reduces the disturbance rejection capability of the closed-loop system in this region. Conventional methods based on small-signal averaged-

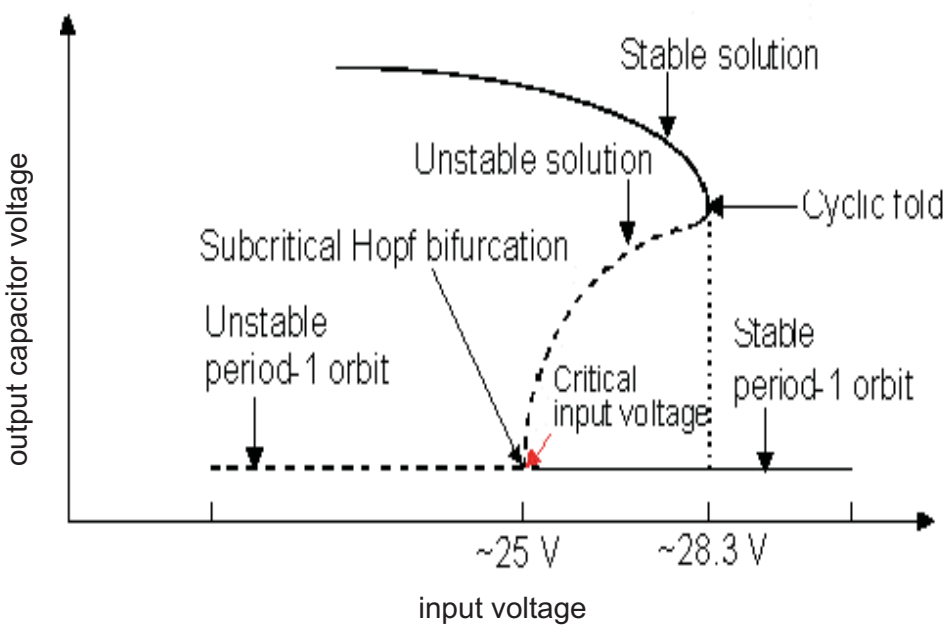

Figure 3.4: Nonlinear analysis, for the system whose small-signal response is shown in Figure 3.2b, shows that the domain of attraction of the period-one orbit is reduced due to the co-existence of one unstable and two stable solutions.

model techniques do not show this reduction in the domain of attraction.

Next, we investigate the first design of the filter-converter system, which according to the linear criterion (see Figure 3.2a) is a stable system. However, the result of a nonlinear analysis, as shown in Figure 3.5, clearly shows that the integrated system is unstable on a fast scale and an instability occurs due to a period-doubling bifurcation. An experimental validation of the fast-scale instability is shown in Figure 3.6.

3.2 Multilevel Converter: Procedure for Modeling and Stability Analysis

Figure 3.7 shows a three-level converter with an input voltage of v_{in} and a load resistance of r_{load}. It has a capacitor C_{i1} with an esr of r_{Ci1}. The output filter is a second-order filter,

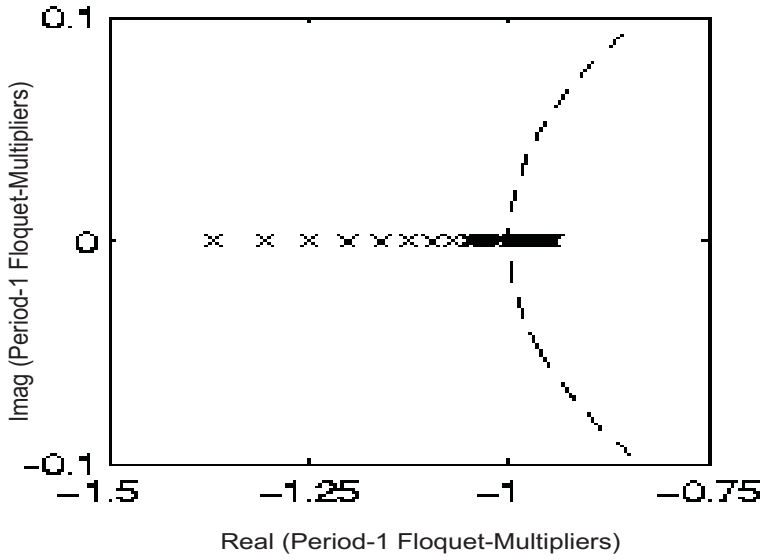

Figure 3.5: Nonlinear analysis shows that one of the Floquet multipliers exits through -1, thereby indicating a period-doubling bifurcation, which leads to a fast-scale instability.

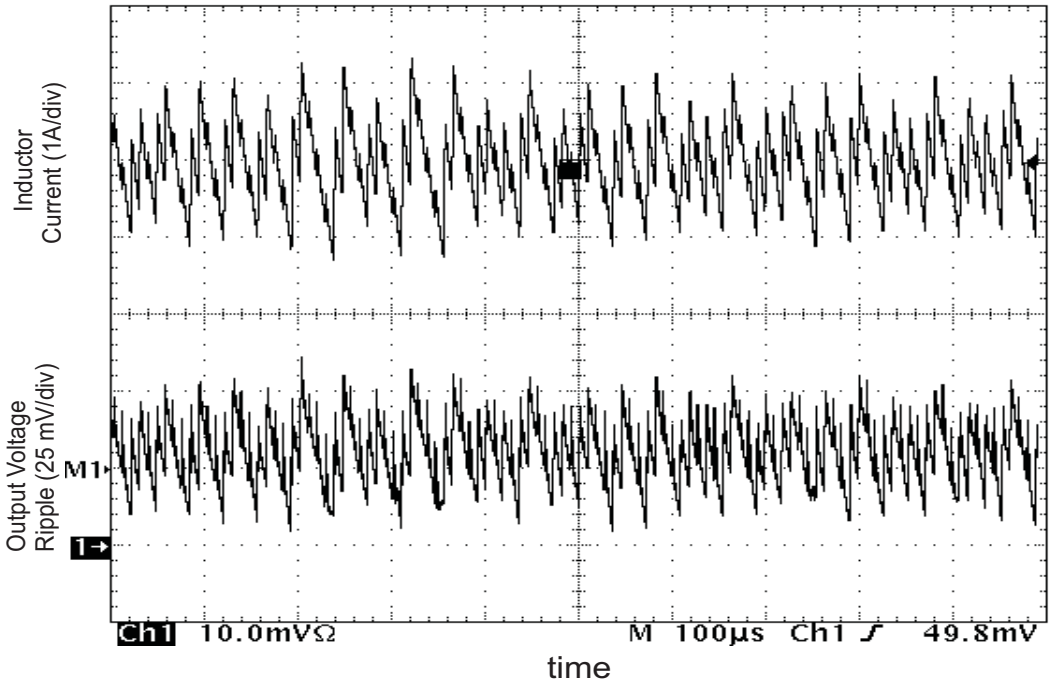

Figure 3.6: An experimental result, which shows a fast-scale instability for the first filter-converter system.

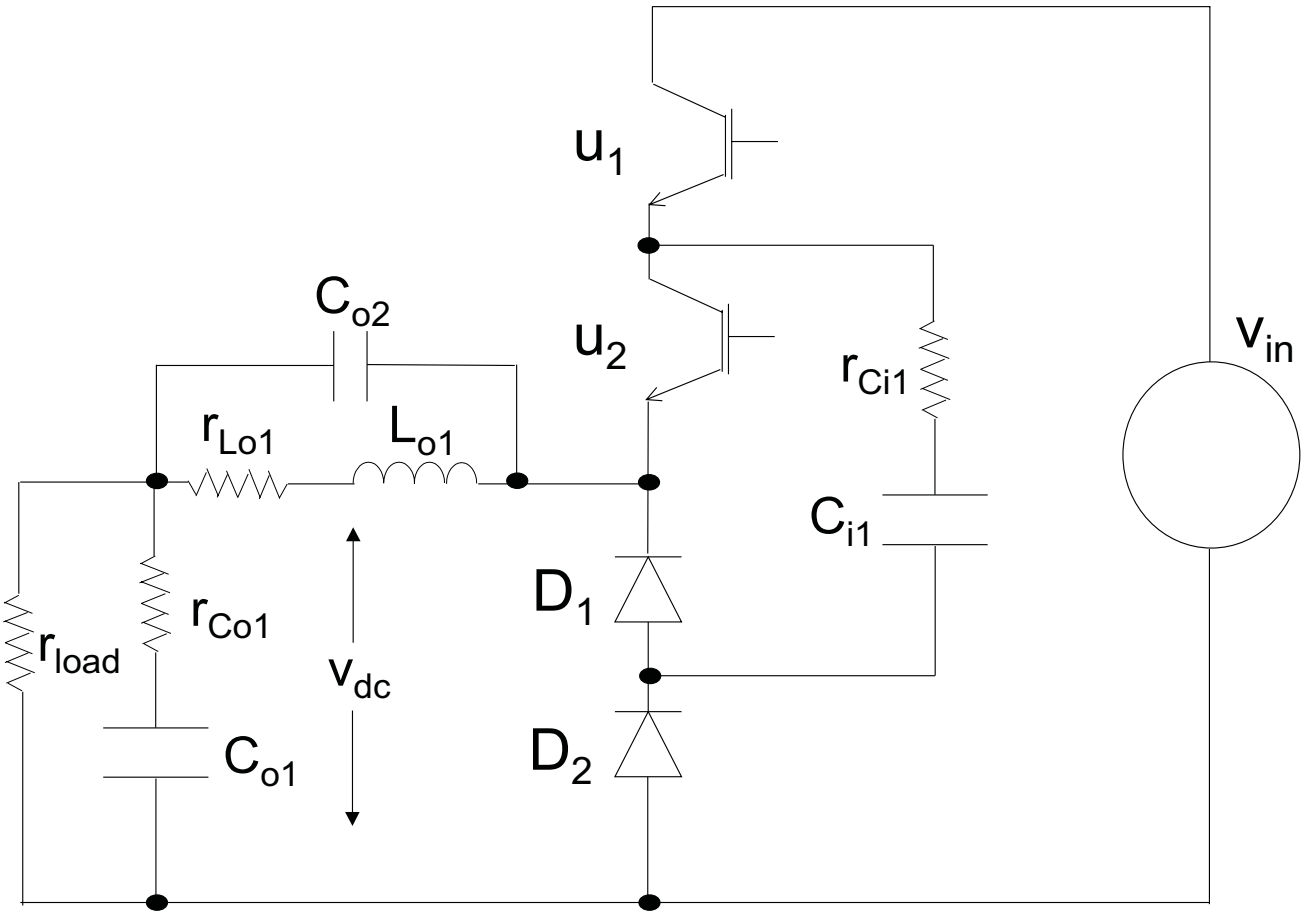

Figure 3.7: A multilevel converter.

which has a capacitance C_{o1} (with an esr of r_{Co1}) and an inductance L_{o1} (with an esl of r_{Lo1}). In addition, there is a parasitic capacitance C_{o2}. We represent the four states of the converter, corresponding to the capacitor voltages and inductor current, by $X(t)$. The converter is so designed such that the flow of current through L_{o1} is continuous.

The switching sequence of the multilevel converter is shown in Figure 3.8. In a given switching cycle (of duration T), the variable-structure network attains five topologies. The gate signals of the switches are phase shifted by 180^o, and the duty ratio d_k is greater than 0.5. Furthermore, the time shift between the two gating signals is assumed to be δ_k. The

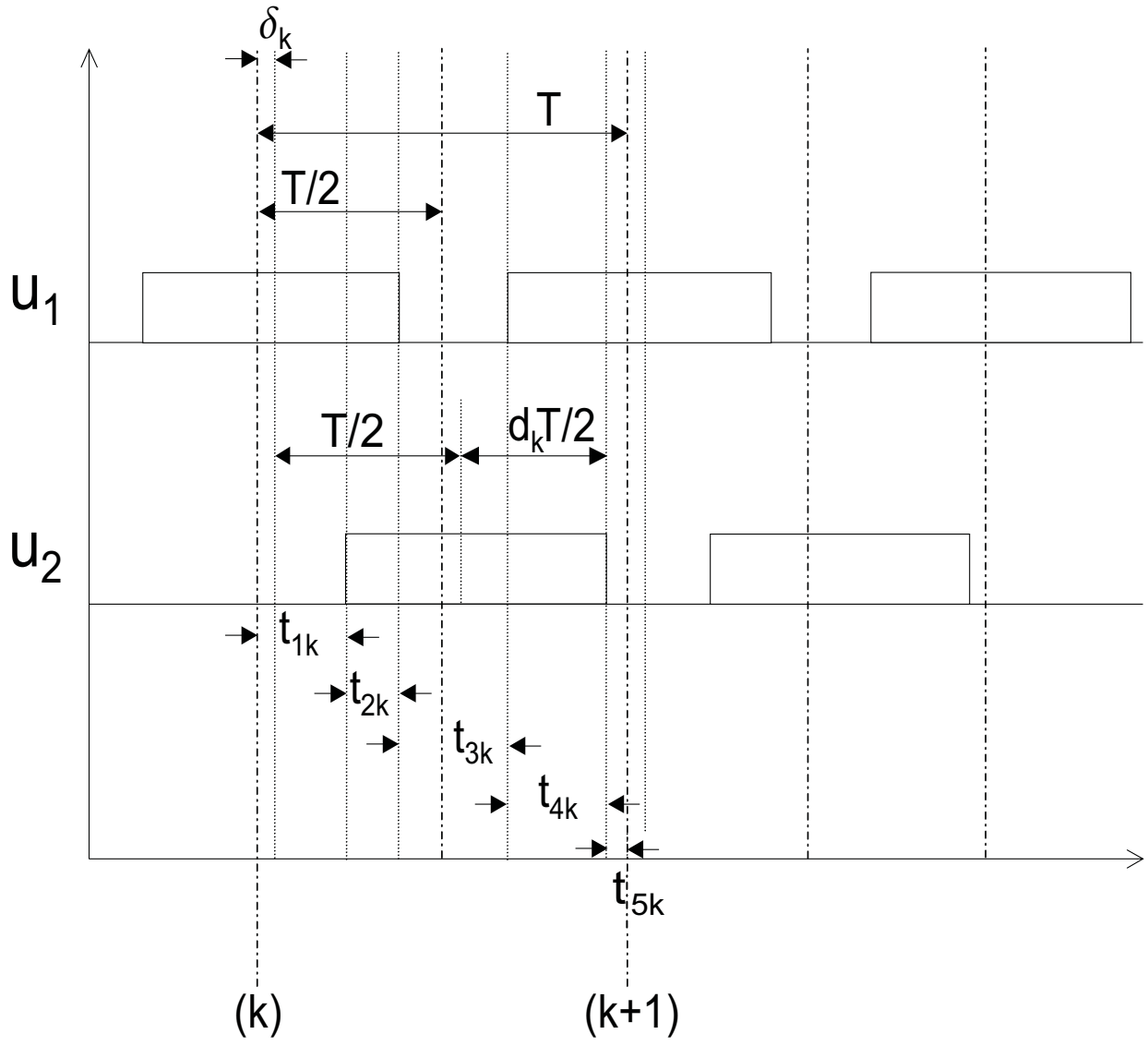

Figure 3.8: Switching sequence of the multilevel converter shown in Figure 1.

dynamics of the multilevel converter for the i^{th} topology is described by

$$\begin{aligned}\dot{X}(t) &= A_i X(t) + B_i \\ \overline{v}_{dc}(t) &= C_i X(t) + D_i\end{aligned} \tag{3.10}$$

for $i = 1, 2, \cdots, 5$, where A_i, B_i, C_i, and D_i are matrices. Depending on the five switching states of u_1 and u_2 (of duration t_{1k}, t_{2k}, t_{3k}, t_{4k}, and t_{5k}), these five matrices can be computed for each topology using the piecewise linear differential equations described by (3.10). The solution of (3.10) is given by

$$\begin{aligned}X(t) &= e^{A_i t} X(t_0) + \left(e^{A_i t} - I\right) {A_i}^{-1} B_i \\ \overline{v}_{dc}(t) &= C_i X(t) + D_i\end{aligned} \tag{3.11}$$

where I is the identity matrix and $X(t_0)$ is the initial condition of the states. Using (3.11) and cascading the solutions of all of the five switching states, we obtain a map of the following form:

$$\begin{aligned}X_{k+1} &= f(X_k, t_{1k}, t_{2k}, t_{3k}, t_{4k}, t_{5k}, \delta_k, d_k, v_{in}) \\ \overline{v}_{dc_{k+1}} &= C_i X_{k+1} + D_i\end{aligned} \tag{3.12}$$

where the switching constraints are

$$\begin{aligned}&\sigma_1(X_k, t_{1k}, \delta_k, d_k, v_{in}) = t_{1k} - \delta_k - \tfrac{1}{2}(1 - d_k)T = 0 \\ &\sigma_2(X_k, t_{1k}, t_{2k}, \delta_k, d_k, v_{in}) = t_{2k} + t_{1k} - \tfrac{1}{2} d_k T = 0 \\ &\sigma_3(X_k, t_{1k}, t_{2k}, t_{3k}, \delta_k, d_k, v_{in}) = t_{3k} - (1 - d_k)T = 0 \\ &\sigma_4(X_k, t_{1k}, t_{2k}, t_{3k}, t_{4k}, \delta_k, d_k, v_{in}) = t_{4k} + t_{3k} + t_{2k} + t_{1k} - \delta_k - \tfrac{1}{2}(1 + d_k)T = 0 \\ &\sigma_5(X_k, t_{1k}, t_{2k}, t_{3k}, t_{4k}, t_{5k}, \delta_k, d_k, v_{in}) = t_{5k} + t_{4k} + t_{3k} + t_{2k} + t_{1k} - T = 0.\end{aligned} \tag{3.13}$$

In (3.13), we have expressed the switching constraints in terms of states so that the present analysis can be extended to the case where the multilevel converter operates under closed-loop control.

The period-one operating point of (3.12) is obtained using the constraint $X_{k+1} = X_k$. We let the steady-state values of the variables of the period-one orbit be X_s, T_1, T_2, T_3, T_4, T_5, D, δ_s, v_{in}. To determine the stability, we perturb the nominal values as

$$\begin{aligned} &\hat{X} = X - X_s, \quad \hat{d} = d - D, \quad \hat{\delta} = \delta - \delta_s, \hat{v}_{in} = v_{in} - V_{in} \\ &\hat{t_1} = t_1 - T_1, \quad \hat{t_2} = t_2 - T_2, \quad \hat{t_3} = t_3 - T_3, \quad \hat{t_4} = t_4 - T_4, \quad \hat{t_5} = t_5 - T_5. \end{aligned} \tag{3.14}$$

Using (3.12)-(3.14), we obtain the following linearized map, which describes the dynamics of the multilevel converter in the vicinity of the operating point:

$$\hat{X}_{k+1} = \tfrac{\partial f}{\partial X}\hat{X}_k + \tfrac{\partial f}{\partial t_{1k}}\hat{t}_{1k} + \tfrac{\partial f}{\partial t_{2k}}\hat{t}_{2k} + \tfrac{\partial f}{\partial t_{3k}}\hat{t}_{3k} + \tfrac{\partial f}{\partial t_{4k}}\hat{t}_{4k} + \tfrac{\partial f}{\partial t_{5k}}\hat{t}_{5k} + \tfrac{\partial f}{\partial v_{in}}\hat{v}_{in} + \tfrac{\partial f}{\partial \delta}\hat{\delta}_k + \tfrac{\partial f}{\partial d}\hat{d}_k \tag{3.15}$$

To determine $\hat{t}_{1k}$, $\hat{t}_{2k}$, $\hat{t}_{3k}$, $\hat{t}_{4k}$, $\hat{t}_{5k}$, we linearize (3.13) and obtain

$$\begin{aligned} \hat{t}_{1k} &= -\Big(\tfrac{\partial \sigma_1}{\partial t_1}\Big)^{-1}\Big(\tfrac{\partial \sigma_1}{\partial X}\hat{X}_k + \tfrac{\partial \sigma_1}{\partial \delta}\hat{\delta}_k + \tfrac{\partial \sigma_1}{\partial d}\hat{d}_k + \tfrac{\partial \sigma_1}{\partial v_{in}}\hat{v}_{in}\Big) \\ \hat{t}_{2k} &= -\Big(\tfrac{\partial \sigma_2}{\partial t_2}\Big)^{-1}\Big(\tfrac{\partial \sigma_2}{\partial X}\hat{X}_k + \tfrac{\partial \sigma_2}{\partial t_1}\hat{t}_{1k} + \tfrac{\partial \sigma_2}{\partial \delta}\hat{\delta}_k + \tfrac{\partial \sigma_2}{\partial d}\hat{d}_k + \tfrac{\partial \sigma_2}{\partial v_{in}}\hat{v}_{in}\Big) \\ \hat{t}_{3k} &= -\Big(\tfrac{\partial \sigma_3}{\partial t_3}\Big)^{-1}\Big(\tfrac{\partial \sigma_3}{\partial X}\hat{X}_k + \tfrac{\partial \sigma_3}{\partial t_1}\hat{t}_{1k} + \tfrac{\partial \sigma_3}{\partial t_2}\hat{t}_{2k} + \tfrac{\partial \sigma_3}{\partial \delta}\hat{\delta}_k + \tfrac{\partial \sigma_3}{\partial d}\hat{d}_k + \tfrac{\partial \sigma_3}{\partial v_{in}}\hat{v}_{in}\Big) \\ \hat{t}_{4k} &= -\Big(\tfrac{\partial \sigma_4}{\partial t_4}\Big)^{-1}\Big(\tfrac{\partial \sigma_4}{\partial X}\hat{X}_k + \tfrac{\partial \sigma_4}{\partial t_1}\hat{t}_{1k} + \tfrac{\partial \sigma_4}{\partial t_2}\hat{t}_{2k} + \tfrac{\partial \sigma_4}{\partial t_3}\hat{t}_{3k} + \tfrac{\partial \sigma_4}{\partial \delta}\hat{\delta}_k + \tfrac{\partial \sigma_4}{\partial d}\hat{d}_k + \tfrac{\partial \sigma_4}{\partial v_{in}}\hat{v}_{in}\Big) \\ \hat{t}_{5k} &= -\Big(\tfrac{\partial \sigma_5}{\partial t_5}\Big)^{-1}\Big(\tfrac{\partial \sigma_5}{\partial X}\hat{X}_k + \tfrac{\partial \sigma_5}{\partial t_1}\hat{t}_{1k} + \tfrac{\partial \sigma_5}{\partial t_2}\hat{t}_{2k} + \tfrac{\partial \sigma_5}{\partial t_3}\hat{t}_{3k} + \tfrac{\partial \sigma_5}{\partial t_4}\hat{t}_{4k} + \tfrac{\partial \sigma_5}{\partial \delta}\hat{\delta}_k + \tfrac{\partial \sigma_5}{\partial d}\hat{d}_k + \tfrac{\partial \sigma_5}{\partial v_{in}}\hat{v}_{in}\Big). \end{aligned} \tag{3.16}$$

In (3.16), $\hat{t}_{1k}$ depends only on $\hat{X}_k$, $\hat{\delta}_k$, $\hat{d}_k$, and $\hat{v}_{in}$. We substitute for $\hat{t}_{1k}$ in the expression for $\hat{t}_{2k}$ and obtain

$$\begin{aligned} \hat{t}_{2k} \;=\; & \Big(\tfrac{\partial \sigma_2}{\partial t_2}\Big)^{-1}\left(\tfrac{\partial \sigma_2}{\partial t_1}\Big(\tfrac{\partial \sigma_1}{\partial t_1}\Big)^{-1}\tfrac{\partial \sigma_1}{\partial X} - \tfrac{\partial \sigma_2}{\partial X}\right)\hat{X}_k + \Big(\tfrac{\partial \sigma_2}{\partial t_2}\Big)^{-1}\left(\tfrac{\partial \sigma_2}{\partial t_1}\Big(\tfrac{\partial \sigma_1}{\partial t_1}\Big)^{-1}\tfrac{\partial \sigma_1}{\partial \delta} - \tfrac{\partial \sigma_2}{\partial \delta}\right)\hat{\delta}_k + \\ & \Big(\tfrac{\partial \sigma_2}{\partial t_2}\Big)^{-1}\left(\tfrac{\partial \sigma_2}{\partial t_1}\Big(\tfrac{\partial \sigma_1}{\partial t_1}\Big)^{-1}\tfrac{\partial \sigma_1}{\partial d} - \tfrac{\partial \sigma_2}{\partial d}\right)\hat{d}_k + \Big(\tfrac{\partial \sigma_2}{\partial t_2}\Big)^{-1}\left(\tfrac{\partial \sigma_2}{\partial t_1}\Big(\tfrac{\partial \sigma_1}{\partial t_1}\Big)^{-1}\tfrac{\partial \sigma_1}{\partial v_{in}} - \tfrac{\partial \sigma_2}{\partial v_{in}}\right)\hat{v}_{in}. \end{aligned} \tag{3.17}$$

Similarly, by substituting for $\hat{t}_{1k}$ and $\hat{t}_{2k}$ from (3.16) and (3.17), respectively, into the expression for $\hat{t}_{3k}$ in (3.16), we obtain an expression for $\hat{t}_{3k}$, which depends only on $\hat{X}_k$, $\hat{\delta}_k$, $\hat{d}_k$, and $\hat{v}_{in}$. By continuing this procedure, we obtain expressions for $\hat{t}_{4k}$ and $\hat{t}_{5k}$, which depend only on $\hat{X}_k$, $\hat{\delta}_k$, $\hat{d}_k$, and $\hat{v}_{in}$. We then, substitute for $\hat{t}_{1k}$, $\hat{t}_{2k}$, $\hat{t}_{3k}$, $\hat{t}_{4k}$, and $\hat{t}_{5k}$ in (3.15) and

obtain an expression for X_{k+1}. The result is

$$\hat{X}_{k+1} = H_1 X_k + H_2 \hat{\delta}_k + H_3 \hat{d}_k + H_4 \hat{v}_{in}. \tag{3.18}$$

where

$$\begin{aligned}
H_1 \;=\; & \tfrac{\partial f}{\partial X} - \\
& \tfrac{\partial f}{\partial t_1}\left(\tfrac{\partial \sigma_1}{\partial t_1}\right)^{-1}\tfrac{\partial \sigma_1}{\partial X} - \\
& \tfrac{\partial f}{\partial t_2}\left(\tfrac{\partial \sigma_2}{\partial t_2}\right)^{-1}\left(\tfrac{\partial \sigma_2}{\partial X} - \tfrac{\partial \sigma_2}{\partial t_1}\left(\tfrac{\partial \sigma_1}{\partial t_1}\right)^{-1}\tfrac{\partial \sigma_1}{\partial X}\right) - \\
& \tfrac{\partial f}{\partial t_3}\left(\tfrac{\partial \sigma_3}{\partial t_3}\right)^{-1}\left(\tfrac{\partial \sigma_3}{\partial X} - \tfrac{\partial \sigma_3}{\partial t_1}\left(\tfrac{\partial \sigma_1}{\partial t_1}\right)^{-1}\tfrac{\partial \sigma_1}{\partial X} - \tfrac{\partial \sigma_3}{\partial t_2}\left(\tfrac{\partial \sigma_2}{\partial t_2}\right)^{-1}\left(\tfrac{\partial \sigma_2}{\partial X} - \tfrac{\partial \sigma_2}{\partial t_1}\left(\tfrac{\partial \sigma_1}{\partial t_1}\right)^{-1}\tfrac{\partial \sigma_1}{\partial X}\right)\right) - \\
& \tfrac{\partial f}{\partial t_4}\left(\tfrac{\partial \sigma_4}{\partial t_4}\right)^{-1}\left(\tfrac{\partial \sigma_4}{\partial X} - \tfrac{\partial \sigma_4}{\partial t_1}\left(\tfrac{\partial \sigma_1}{\partial t_1}\right)^{-1}\tfrac{\partial \sigma_1}{\partial X} - \tfrac{\partial \sigma_4}{\partial t_2}\left(\tfrac{\partial \sigma_2}{\partial t_2}\right)^{-1}\left(\tfrac{\partial \sigma_2}{\partial X} - \tfrac{\partial \sigma_2}{\partial t_1}\left(\tfrac{\partial \sigma_1}{\partial t_1}\right)^{-1}\tfrac{\partial \sigma_1}{\partial X}\right) - \right. \\
& \qquad \tfrac{\partial \sigma_4}{\partial t_3}\left(\tfrac{\partial \sigma_3}{\partial t_3}\right)^{-1}\left(\tfrac{\partial \sigma_3}{\partial X} - \tfrac{\partial \sigma_3}{\partial t_1}\left(\tfrac{\partial \sigma_1}{\partial t_1}\right)^{-1}\tfrac{\partial \sigma_1}{\partial X} - \right. \\
& \qquad\qquad \left.\left. \tfrac{\partial \sigma_3}{\partial t_2}\left(\tfrac{\partial \sigma_2}{\partial t_2}\right)^{-1}\left(\tfrac{\partial \sigma_2}{\partial X} - \tfrac{\partial \sigma_2}{\partial t_1}\left(\tfrac{\partial \sigma_1}{\partial t_1}\right)^{-1}\tfrac{\partial \sigma_1}{\partial X}\right)\right)\right) - \\
& \tfrac{\partial f}{\partial t_5}\left(\tfrac{\partial \sigma_5}{\partial t_5}\right)^{-1}\left(\tfrac{\partial \sigma_5}{\partial X} - \tfrac{\partial \sigma_5}{\partial t_1}\left(\tfrac{\partial \sigma_1}{\partial t_1}\right)^{-1}\tfrac{\partial \sigma_1}{\partial X} - \tfrac{\partial \sigma_5}{\partial t_2}\left(\tfrac{\partial \sigma_2}{\partial t_2}\right)^{-1}\left(\tfrac{\partial \sigma_2}{\partial X} - \tfrac{\partial \sigma_2}{\partial t_1}\left(\tfrac{\partial \sigma_1}{\partial t_1}\right)^{-1}\tfrac{\partial \sigma_1}{\partial X}\right) - \right. \\
& \qquad \tfrac{\partial \sigma_5}{\partial t_3}\left(\tfrac{\partial \sigma_3}{\partial t_3}\right)^{-1}\left(\tfrac{\partial \sigma_3}{\partial X} - \tfrac{\partial \sigma_3}{\partial t_1}\left(\tfrac{\partial \sigma_1}{\partial t_1}\right)^{-1}\tfrac{\partial \sigma_1}{\partial X} - \right. \\
& \qquad\qquad \left. \tfrac{\partial \sigma_3}{\partial t_2}\left(\tfrac{\partial \sigma_2}{\partial t_2}\right)^{-1}\left(\tfrac{\partial \sigma_2}{\partial X} - \tfrac{\partial \sigma_2}{\partial t_1}\left(\tfrac{\partial \sigma_1}{\partial t_1}\right)^{-1}\tfrac{\partial \sigma_1}{\partial X}\right)\right) \\
& \qquad \tfrac{\partial \sigma_5}{\partial t_4}\left(\tfrac{\partial \sigma_4}{\partial t_4}\right)^{-1}\left(\tfrac{\partial \sigma_4}{\partial X} - \tfrac{\partial \sigma_4}{\partial t_1}\left(\tfrac{\partial \sigma_1}{\partial t_1}\right)^{-1}\tfrac{\partial \sigma_1}{\partial X} - \right. \\
& \qquad\qquad \tfrac{\partial \sigma_4}{\partial t_2}\left(\tfrac{\partial \sigma_2}{\partial t_2}\right)^{-1}\left(\tfrac{\partial \sigma_2}{\partial X} - \tfrac{\partial \sigma_2}{\partial t_1}\left(\tfrac{\partial \sigma_1}{\partial t_1}\right)^{-1}\tfrac{\partial \sigma_1}{\partial X}\right) \\
& \qquad\qquad \tfrac{\partial \sigma_4}{\partial t_3}\left(\tfrac{\partial \sigma_3}{\partial t_3}\right)^{-1}\left(\tfrac{\partial \sigma_3}{\partial X} - \tfrac{\partial \sigma_3}{\partial t_1}\left(\tfrac{\partial \sigma_1}{\partial t_1}\right)^{-1}\tfrac{\partial \sigma_1}{\partial X} - \right. \\
& \qquad\qquad\qquad \left.\left.\left. \tfrac{\partial \sigma_3}{\partial t_2}\left(\tfrac{\partial \sigma_2}{\partial t_2}\right)^{-1}\left(\tfrac{\partial \sigma_2}{\partial X} - \tfrac{\partial \sigma_2}{\partial t_1}\left(\tfrac{\partial \sigma_1}{\partial t_1}\right)^{-1}\tfrac{\partial \sigma_1}{\partial X}\right)\right)\right).
\end{aligned} \tag{3.19}$$

The stability of a period-one orbit is ascertained by the Floquet multipliers of H_1. For asymptotic stability, all of the Floquet multipliers of H_1 should be within the unit circle. As a control parameter is varied, if one of the Floquet multipliers exits the unit circle through +1 then, we have a static bifurcation. If one of the Floquet multipliers exit the unit circle through -1, we have a period-doubling bifurcation. A Hopf bifurcation occurs if two of the Floquet multipliers exit the unit circle as complex conjugates. One of the ways to determine

the post-instability dynamics for either of these cases is to use a discrete normal form, which is described in Chapter 4.

3.3 Single Phase Boost PFC Circuit

Power-factor-correction circuits are widely used in power electronics. One of the most common circuits used to achieve unity power factor is the time-varying boost PFC circuit, which is shown in Figure 3.9. We begin by modeling the boost PFC circuit and then analyze its stability.

3.3.1 Modeling

The boost PFC circuit shown in Figure 3.9 is designed to operate in CCM and switches among three structures. The jump between two of these structures is governed by the switching function $u(t)$. The system attains the third structure only when the inductor current is zero and $u(t)$ has no control over it. In general, $x_1(t) \to 0$ as $v_{in}(t) \to 0$. We note that the inductor current in a boost PFC circuit designed solely for DCM attains a value of zero in every switching cycle (of period $T = \frac{1}{f_s}$). We describe the dynamics of the open-loop states of the boost PFC circuit (operating in CCM) using the following hybrid equations:

$$\begin{aligned}\dot{x}_1(t) = \Bigg[&- \tfrac{1}{L}\Big(r_L + \tfrac{r_C R}{R+r_C}\big(1-u(t)\big)\Big)x_1(t) - \tfrac{1}{L}\tfrac{R}{R+r_C}\big(1-u(t)\big)x_2(t) + \\ &\tfrac{1}{L}|v_{in}(t)|\Bigg] g_1\left(x_1(t), u(t)\right) \\ \dot{x}_2(t) = &\tfrac{R}{(R+r_C)C}\big(1-u(t)\big)x_1(t) - \tfrac{1}{(R+r_C)C}x_2(t)\end{aligned} \tag{3.20}$$

where $x_1(t)$ is the inductor current, $x_2(t)$ is the voltage across the capacitor, and

$$g_1\left(x_1(t), u(t)\right) = \begin{cases} 1 & \text{if } x_1(t) > 0 \\ 1 & \text{if } x_1(t) = 0,\ u(t) = 1 \\ 0 & \text{if } x_1(t) = 0,\ u(t) = 0 \end{cases} . \tag{3.21}$$

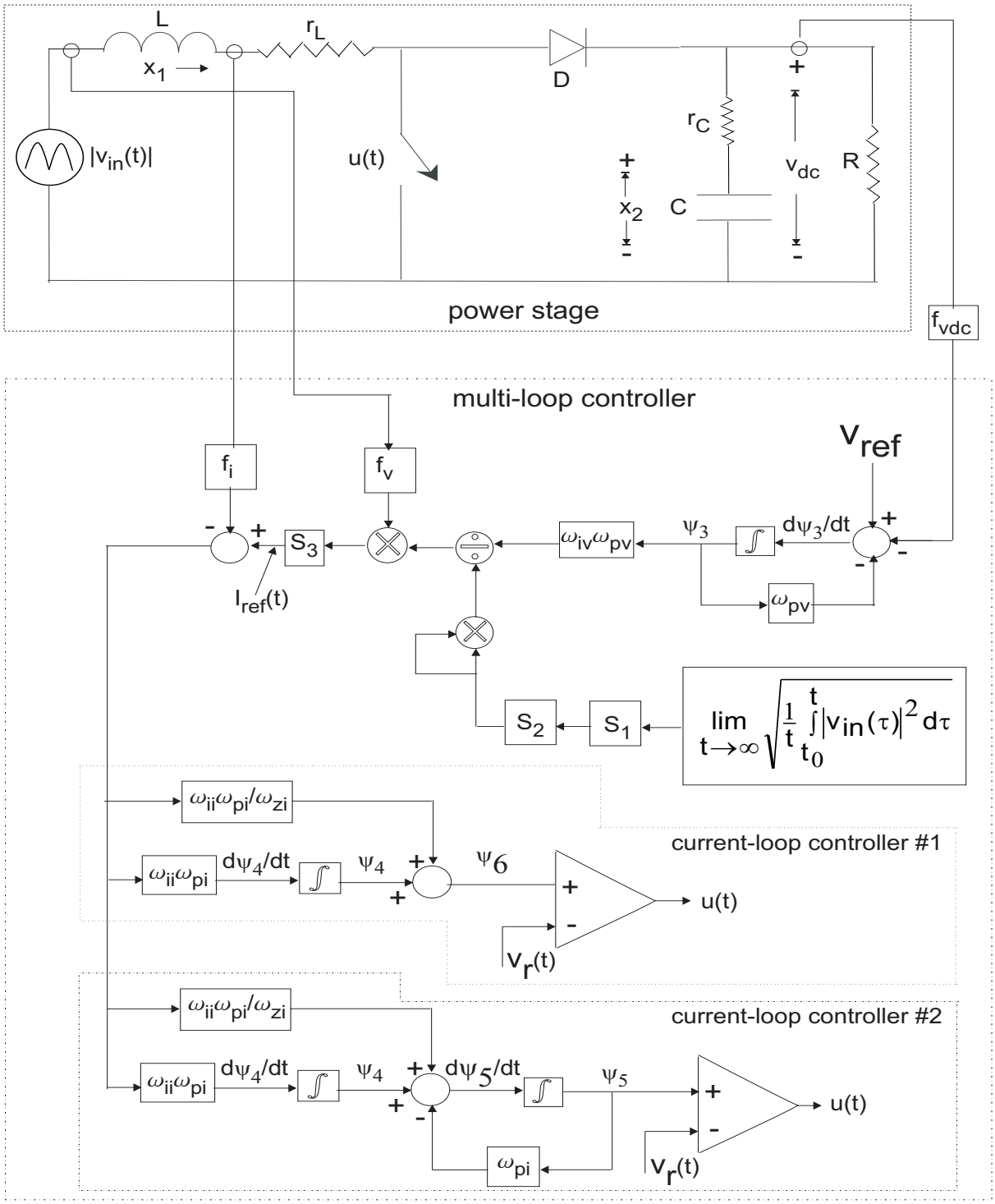

Figure 3.9: A closed-loop boost PFC circuit. We consider two different multi-loop controllers for the power stage.

For an open-loop converter, $u(t)$ is a predetermined pulse function. For a closed-loop converter, $u(t)$ is a function of the states of the power stage for a static-feedback controller and is a function of both the states of the controller and the power stage for a dynamic feedback controller. The objective of the closed-loop converter is to regulate the bus voltage and to draw line current from the utility in synchronicity with the input voltage.

There are numerous ways to design the feedback controller. Although, our analysis can be extended to any other controller, we select two multi-loop controllers, one of which (controller two) is already being used in a commercial product (Andreycak, 1997; Todd, 1999). The voltage-loop controller for both multi-loop controllers is the same. However, the current-loop controllers are slightly different.

As shown in Figure 3.9, the closed-loop system has an outer voltage loop and an inner current loop. The voltage loop provides the reference for the inner current loop. The mathematical model describing feedback controllers one and two is given by

$$\begin{aligned}
\dot{\psi}_3(t) &= -f_{vdc}v_{dc}(t) - \omega_{pv}\psi_3(t) + v_{ref} \\
\dot{\psi}_4(t) &= \lambda_1(t)\psi_3(t) - \lambda_2 x_1(t) \\
\dot{\psi}_5(t) &= -\lambda_3 x_1(t) + \lambda_4(t)\psi_3(t) + \psi_4(t) - \omega_{pi}\psi_5(t) \\
v_{dc}(t) &= \tfrac{R}{R+r_C}x_2(t) + \tfrac{Rr_C}{R+r_C}\Big(1-u(t)\Big)x_1(t).
\end{aligned} \tag{3.22}$$

In (3.22), the $\psi_i(t)$ represent the states of the dynamic-feedback controller, f_{vdc} is the sensor gain for the bus voltage, and v_{ref} is the reference for the bus voltage. The coefficients $\lambda_i(t)$ are positive, bounded, and given by

$$\lambda_1(t) = \omega_{ii}\omega_{pi}\frac{\omega_{iv}\omega_{pv}}{S_1^2 S_2^2\Big(\frac{1}{t}\int_{t_0}^{t}|v_{in}(\tau)|^2 d\tau\Big)}f_v|v_{in}(t)|S_3,\ \lambda_2 = \omega_{ii}\omega_{pi}f_i,\ \lambda_3 = \tfrac{\lambda_2}{\omega_{zi}},\ \text{and}\ \lambda_4(t) = \tfrac{\lambda_1(t)}{\omega_{zi}} \tag{3.23}$$

where f_v and f_i are the sensor gains for the line voltage and inductor currents and S_1, S_2, and S_3 are feedback gains for the voltage and current loops. For convenience, we represent $x(t)$, $\psi(t)$, and $u(t)$ as x, ψ, and u from now on.

The switching function for controllers one and two is defined as

$$u(t) = \begin{cases} 1 & \text{if } \sigma_1 > v_r(t) \\ 0 & \text{if } \sigma_1 < v_r(t) \end{cases} \tag{3.24}$$

where $\sigma_1 = \psi_6$ (for controller one), $\sigma_1 = \psi_5$ (for controller two), $v_r(t) = v_l + v_{ramp} \mathrm{mod}(t, T) f_s$, and v_l and v_{ramp} are the lower limit and height of the ramp. In (3.24), $v_r(t)$ represents the carrier waveform (ramp) and creates a time-varying boundary layer.

3.3.2 Concepts of Discontinuous Systems

The condition for the existence of the i^{th} discontinuity surface ($\sigma_i = 0$) of a differential equation

$$\dot{y} = f(y, t, u) \tag{3.25}$$

with discontinuous right-hand side in the neighborhood of $\sigma_i = 0$ is (Utkin, 1992)

$$\lim_{\sigma_i \to -0} \dot{\sigma}_i > 0 \quad \text{and} \quad \lim_{\sigma_i \to +0} \dot{\sigma}_i < 0 \qquad \text{or} \qquad \dot{\sigma}_i \sigma_i < 0. \tag{3.26}$$

If the hypersurface exists globally, then all of the solutions of (3.25) in the continuity region reach it and stay on it. The motion on the discontinuity surface is known as a sliding mode, and hence the discontinuity surface is also known as a sliding surface (or smooth hypersurface) (Utkin, 1992; Filippov, 1988). If the sliding surface does not exist globally, then the solutions may not reach it.

In Figure 3.10, using a single discontinuity surface given by $\sigma_1 = 0$, we show some possible trajectories when global existence fails. The trajectories marked T_1 reach the discontinuity surface from both sides. Hence they satisfy (3.26). The trajectories marked T_2 do not reach the discontinuity surface from both sides. Although these trajectories reach the discontinuity surface, they do not satisfy the existence condition. The trajectories marked T_3 approach

the sliding surface tangentially and hence do not satisfy (3.26) because the velocity vectors on both sides of the discontinuity surface have the same sign. Finally, T_4 represents the set of trajectories which do not reach the discontinuity surface at all.

When global existence of a sliding surface fails, it is still possible that the existence of $\sigma_1 = 0$ may be satisfied locally. If in addition, the saturated region does not have equilibrium solution(s) or stable orbit(s), then a solution that leaves the local sliding surface can not stabilize in the saturated region. For example, a piecewise linear boost dc-dc converter feeding a resistive load may have one equilibrium solution in the saturated region (Erickson, 1982; Mazumder et al., 2000 b, 2001a, e). Hence, the dynamics of an improperly designed boost converter may be attracted by this solution if subjected to a strong disturbance. If the resistive load is replaced with a constant-power load, then the saturated region may have more than one equilibrium solution.

Once we demonstrate that a sliding surface exists locally or globally, we analyze the stability of the system dynamics on the sliding surface. In the continuity region, the definition of a solution is clear (Filippov, 1988). However, the definition of a solution (almost everywhere) as an absolutely continuous function satisfying (3.25) is not always applicable for equations whose right-hand sides are discontinuous on an arbitrary smooth surface. Using the Lebesgue measure, one can apply the definition in the case in which the solutions approach the discontinuity surface on one side and leave it on the other side. When the solutions approach a discontinuity surface on both sides, the conventional definition is unsuitable because there is no indication of how a solution that reaches the discontinuity surface may continue.

Filippov (1988) defined a solution for the vector differential equation

$$\dot{y} = f(y, t, u(y)) = h(y, t) \tag{3.27}$$

where $h : \Re \times \Re^n \rightarrow \Re^n$ is measurable and essentially locally bounded. A vector function $y(t)$, defined on the interval (t_1, t_2), is a Filippov solution of (3.27) if it is absolutely continuous

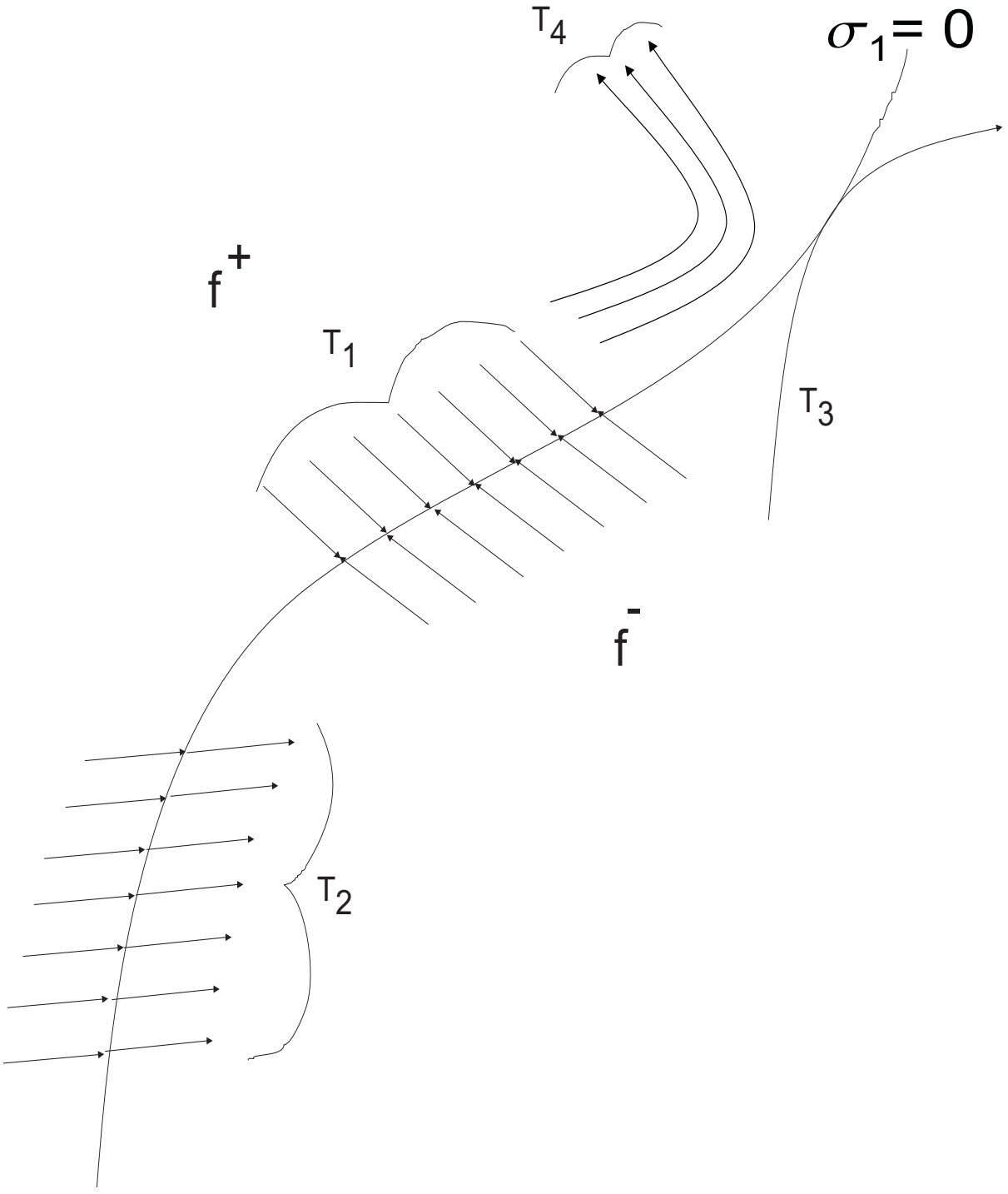

Figure 3.10: Some possible trajectories for the variable-structure system described by (3.25). Only T_1 satisfies the existence condition, T_4 stays in the saturated/continuity region.

and, for almost all $t \in (t_1, t_2)$ and for arbitrary $\delta > 0$, the vector $dy(t)/dt$ belongs to the smallest convex closed set of an n-dimensional space containing all of the values of the vector function $h(t, y')$; where y' ranges over the entire δ neighborhood of the point $y(t)$ in the space y (with t fixed) except for a set of measure $\mu N = 0$; that is,

$$\frac{dy(t)}{dt} \in K[h](y,t) \tag{3.28}$$

where $K[h](.)$ is called the Filippov's differential inclusion and is defined as

$$K[h](t,y) \equiv \bigcap_{\delta>0} \bigcap_{\mu N>0} \overline{co}\, h\left(B(y,\delta) - N\right). \tag{3.29}$$

In the differential inclusion (3.29), $\overline{co}$ denotes the convex hull of a set, N represents a set of zero Lebesgue measure μN, and B is a ball of radius δ centered at y. The content of Filippov's solution is that the tangent vector to a solution at a time t, where it exists, must lie in the convex closure of the limiting values of the vector field in progressively smaller neighborhoods around the solution evaluated at time t.

Let us consider a single switching surface H (shown in Figure 3.11), which is a smooth surface (manifold) separating the space into regions H^+ and H^-. Suppose that H is regular so that it can be divided by a smooth real-valued function $\sigma(y)$ (i.e., $H = \{y : \sigma(y) = 0\}$ and suppose that $h(t, y)$ is bounded and, for any fixed t, its limiting values $h^+(y,t)$ and $h^-(y,t)$ exist when H is approached from H^+ and H^-. Let $h_0^+(t,y)$ and $h_0^-(y,t)$ be the projections of $h^+(y,t)$ and $h^-(y,t)$ on the normal $\bigtriangledown\sigma$ to the surface H directed towards H^+ and H^-. Then, for an absolutely continuous $y \in H$ satisfying $h_0^+(y,t) \leq 0$, $h_0^-(y,t) \geq 0$, and $h_0^-(y,t) - h_0^+(y,t) > 0$, the trajectories pointing towards H are solutions of (3.27) according to the differential inclusion (3.28) if and only if

$$\frac{dy}{dt} = \beta(t)h^+(y,t) + (1-\beta(t))h^-(y,t) \tag{3.30}$$

where

$$\beta(t) = \frac{h_0^-(y,t)}{h_0^-(y,t) - h_0^+(y,t)} \tag{3.31}$$

We note that the right-hand side of (3.30) is orthogonal to $\bigtriangledown\sigma$ and hence the solution remains on the surface H.

The sliding mode in a real-life system actually occurs not on its discontinuity surface, but within some boundary layer on which the control components may take up values different from u_i^+ and u_i^- (Utkin, 1992). The vector $f(y,t,u)$ in (3.25) may, therefore, take up values which differ from those obtained with $u_i = u_i^+$ and $u_i = u_i^-$. This results in a wider convex set in the Filippov continuation method and, consequently, in a richer set of motions on the sliding mode. In order to handle the regularization problem and find feasible solutions to (3.25), Utkin (1992) proposed an equivalent control method.

Assume that a sliding mode exits on the manifold

$$\sigma(y) = 0, \qquad \sigma^T(y) = [\sigma_1(y), \cdots, \sigma_m(y)] \tag{3.32}$$

which lies at the intersection of m discontinuity surfaces. Then, we can find a continuous control such that, under the initial position of the state vector on this manifold, the time derivative of the vector $\sigma(y)$ along the trajectories of the system of equations (3.25) is identically equal to zero; that is,

$$\dot{\sigma} = \bigtriangledown\sigma_y.f(y,t,u_1^{eq}(y,t), \cdots, u_m^{eq}(y,t)) = 0 \tag{3.33}$$

In (3.33), $u^{eq}(y) = [u_1^{eq}, \cdots, u_m^{eq}]$ is referred to as the equivalent control for the vector equation (3.25) on the sliding surface $\sigma(y) = 0$. Therefore, the dynamics of (3.25) on the sliding surface are governed by

$$\dot{y} = f[y,t,u^{eq}(y,t)]. \tag{3.34}$$

Thus a solution is an absolutely continuous vector-valued function, which outside the surfaces σ_i satisfies (3.25) and on these surfaces and on their intersections satisfies (3.34) for almost all t.

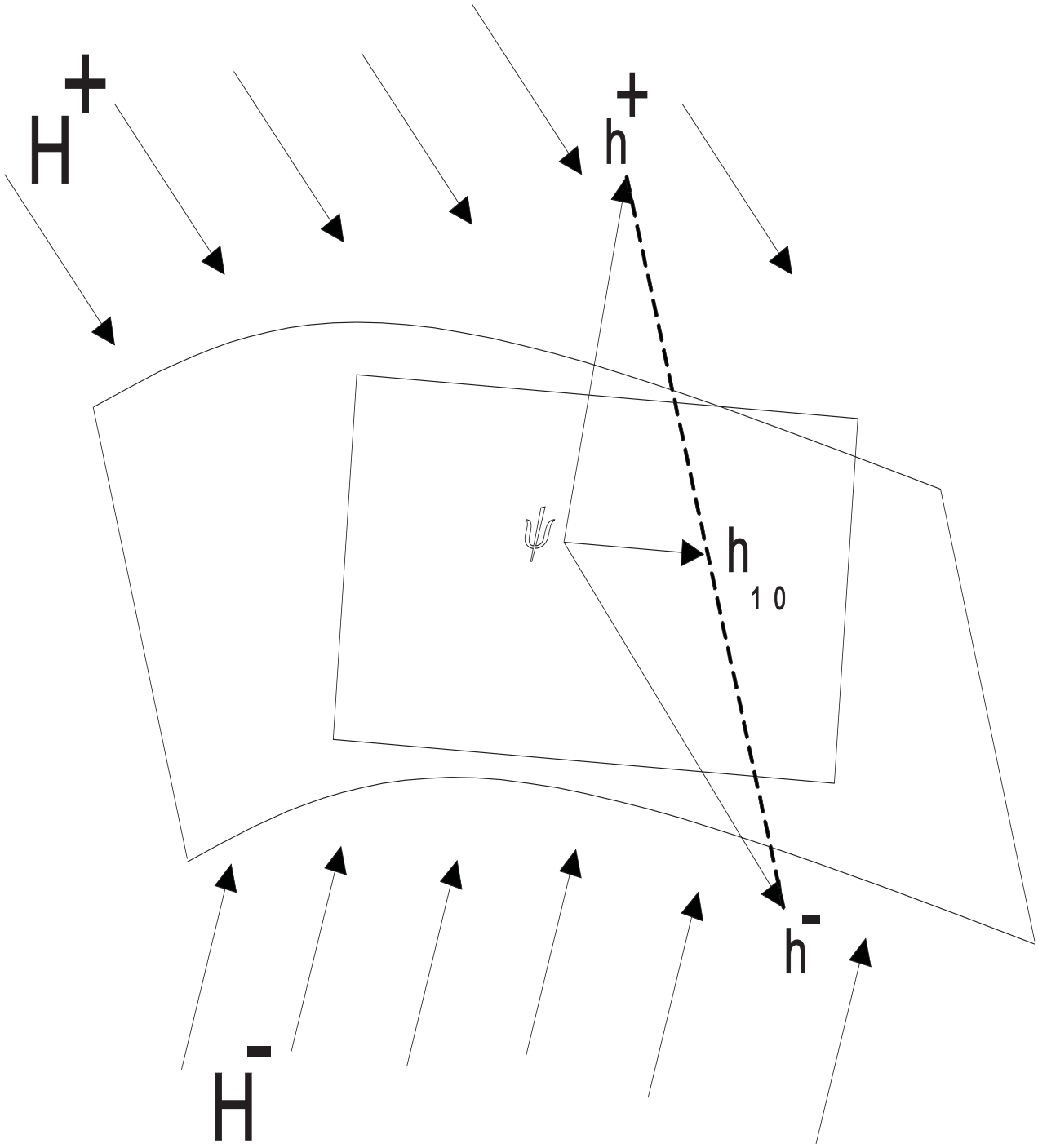

Figure 3.11: A description of Filippov's solution (often called sliding motion) on the discontinuity surface σ.

For a system which is linear with respect to control, when the width of the boundary layer is zero, the solutions obtained using the equivalent control method and Filippov's method are the same. The stability of the solutions of either (3.30) or (3.34) is determined using linear techniques if the sliding manifold is linear. If, however, the sliding manifold is nonlinear, then Lyapunov's method (II, I) and bifurcation analyses are suitable approaches (Hahn, 1963; Wiggins, 1990; Nayfeh and Balachandran, 1995; Khalil, 1996; Kuznetsov, 1998; Sastry, 1999).

3.3.3 Analysis of the Discontinuous Converter when the Switching Frequency Approaches Infinity

We use the concepts of discontinuous systems to analyze the boost PFC circuit, the dynamics of which are described by (3.20)-(3.24). First, let us consider the closed-loop system operating with controller one. In this case, $\sigma_1 = \psi_6$ because $v_r(t) = 0$ for an infinite frequency. A sliding mode exists if the trajectories converge on $\psi_6 = 0$ (Utkin, 1992). Let us define a Lyapunov function

$$V(\psi_6) = \tfrac{1}{2}{\psi_6}^2. \tag{3.35}$$

so that the existence condition for the sliding surface is

$$\dot{V}(\psi_6) = \psi_6\dot{\psi}_6 \leq 0. \tag{3.36}$$

where

$$\dot{\sigma}_1 = \dot{\psi}_6 = \dot{\psi}_4 - \lambda_3\dot{x}_1 + \dot{\lambda}_4(t)\psi_3 + \lambda_4(t)\dot{\psi}_3 \tag{3.37}$$

$$\dot{\lambda}_4(t) = c_1 f_v S_3\Big[\dot{v}_{in}(t)\text{sign}(v_{in}(t))\frac{1}{\frac{1}{t}\int_{t_0}^{t}|v_{in}(\tau)|^2 d\tau} - |v_{in}(t)| \left(\frac{1}{t}\int_{t_0}^{t}|v_{in}(\tau)|^2 d\tau\right)^{-2}\left(-\frac{1}{t^2}\int_{t_0}^{t}|v_{in}(\tau)|^2 d\tau + \frac{|v_{in}(t)|^2}{t}\right)\Big]. \tag{3.38}$$

and $c_1 = \left(\frac{\omega_{ii}\omega_{pi}\omega_{iv}\omega_{pv}}{\omega_{zi}S_1^2S_2^2}\right)$. The derivative of $\lambda_4(t)$ is bounded even though $\dot{\lambda}_4(t)$ is not defined at $v_{in}(t) = 0$. Substituting for $\dot{x}_1, \dot{\psi}_3$, and $\dot{\psi}_4$ from (3.20) and (3.22) into (3.37) yields

$$\begin{aligned}\dot{\sigma}_1 = \dot{\psi}_6 = \lambda_4(t)v_{ref} - \tfrac{\lambda_3 g_1}{L}|v_{in}| + \left(\lambda_1 + \lambda_4(t) - \dot{\lambda}_4(t)\omega_{pv}\right)\psi_3 \\ - \left(\lambda_2 - \tfrac{\lambda_3 r_L g_1}{L}\right)x_1 - \tfrac{\lambda_4(t) f_{vdc} R}{R+r_c}x_2 + \tfrac{R}{L(R+r_c)}\Big[\lambda_3\left(r_c x_1 + x_2\right)g_1 \\ - f_{vdc}Lr_c\lambda_4(t)x_1\Big](1-u)\end{aligned} \tag{3.39}$$

Let us assume that the sliding surface exists globally. Then

$$u = u_{eq} + u_n \tag{3.40}$$

where u_{eq} is the equivalent control and u_n is the nonlinear switching control, which satisfies

$$u^- - u_{eq} \le u_n \le u^+ - u_{eq} \tag{3.41}$$

The equivalent control u_{eq} is obtained by setting $\dot{\psi}_6 = 0$ in (3.39). The result is

$$u_{eq} = \frac{g_2}{f_{vdc}r_C L x_1 \lambda_4(t) - \lambda_3 g_1(x_1, u)\left(r_C x_1 + x_2\right)} \tag{3.42}$$

where

$$\begin{aligned}g_2 = \tfrac{L(R+r_c)}{R}\Bigg[\lambda_4(t)v_{ref} - \tfrac{\lambda_3 g_1}{L}|v_{in}| + \left(\lambda_1 + \lambda_4(t) - \lambda_4(t)\omega_{pv}\right)\psi_3 \\ - \left(\lambda_2 - \tfrac{\lambda_3 r_L g_1}{L}\right)x_1 - \tfrac{f_{vdc}R\lambda_2}{R+r_c}x_2\Bigg]\end{aligned} \tag{3.43}$$

The functional g_2 is always defined and bounded for all x, ψ, and t. We know that for the sliding mode to exist

$$u^- < u_{eq} < u^+ \qquad (u^- = 0,\ u^+ = 1). \tag{3.44}$$

It follows from (3.42) that, when $x_1 = 0$ and hence $g_1(x_1, u) = 0$, u_{eq} does not satisfy (3.44). Therefore, our assumption, that the sliding mode for the boost PFC circuit exists globally, is incorrect.

Having shown that global existence is not possible, we focus on local existence of the sliding surface when $g_1(x_1, u) = 1$ (or $x_1 > 0$). We substitute (3.40) into (3.39), use (3.42), and obtain

$$\dot{\psi}_6 = ku_n \tag{3.45}$$

where

$$k = \frac{R}{L(R+r_c)} \left[\left(f_{vdc} L \lambda_4 - \lambda_3 \right) r_c x_1 - \lambda_3 x_2 \right] \tag{3.46}$$

In (3.46), the term $f_{vdc} L \lambda_4(t)$ is negligible compared to $-\lambda_3(r_C x_1 + x_2)$ and hence $k < 0$ for all practical purposes. Then, it follows from (3.36) that for local existence

$$\dot{V}(\psi_6) = \psi_6 \dot{\psi}_6 = \psi_6 (ku_n) \leq 0 \tag{3.47}$$

Inequlity (3.47) is satisfied if

$$u_n > 0 \, (u^+ > u_{eq}) \quad \text{when} \quad \psi_6 > 0 \quad \text{and} \quad u_n < 0 \, (u^- < u_{eq}) \quad \text{when} \quad \psi_6 < 0. \tag{3.48}$$

Next we consider the boost PFC circuit operating with the second controller. First, we consider the existence of the sliding surface. It follows from (3.24) and Figure 3.9 that when the width of the boundary layer is zero, u changes state when ψ_5 is less than or greater than zero. Apparently $\psi_5 = 0$ is a sliding surface. Because $\dot{\psi}_5$ is a continuous function of time, the existence condition given by (3.26) is not satisfied. Thus, the sliding mode in the conventional sense (i.e., the trajectories being oriented towards the switching surface) does not exist. The existence condition may be derived from

$$\dot{\sigma}_1 = \ddot{\psi}_5 = -\lambda_3 \dot{x}_1 + \dot{\lambda}_4(t)\psi_3 + \lambda_4(t)\dot{\psi}_3 + \dot{\psi}_4 - \omega_{pi}\dot{\psi}_5 \tag{3.49}$$

where $\dot{\lambda}_4(t)$ is given by (3.38). Substituting for $\dot{x}_1, \dot{\psi}_3$, and $\dot{\psi}_5$ from (3.20) and (3.22) into (3.49), we have

$$\begin{aligned}\dot{\sigma}_1 = \ddot{\psi}_5 = \lambda_4 v_{ref} - \tfrac{\lambda_3 g_1}{L}|v_{in}| + \left(\tfrac{\lambda_3 r_L g_1}{L} - \lambda_2 + \lambda_3\omega_{pi}\right) x_1 - \tfrac{f_{vdc}\lambda_4 R}{R+r_c} x_2 \\ + \left(\lambda_1 + \dot{\lambda}_4 - \lambda_4\omega_{pi}\right)\psi_3 - \omega_{pi}\psi_4 + \omega_{pi}^2\psi_5 \\ + \tfrac{R}{L(R+r_c)}\left[\lambda_3 g_1 x_2 + \lambda_3 r_c g_1 x_1 - f_{vdc}\lambda_4 r_c L x_1\right](1-u)\end{aligned} \tag{3.50}$$

A sliding mode exists if the trajectories converge on the origin in the plane $\left(\psi_5, \dot{\psi}_5\right)$ (Chang, 1990; Elmali and Olgac, 1992). We see from Figure 3.12a that, for this high-order sliding mode, all possible velocities lie in the space tangent to the manifold and, even when a switching error is present, the state trajectory is tangent to the manifold at the time of leaving, in contrast to the behavior of the closed-loop system operating with controller one. In the latter case, when a switching error is present, the trajectory leaves the manifold ($\dot{\psi}_6 = 0$) at a certain angle.

Let us now assume that the sliding mode exists globally on the plane $\left(\psi_5, \dot{\psi}_5\right)$ for $g_1(x_1, u) = 0$. The equivalent control u_{eq} is obtained by solving $\ddot{\psi}_5 = 0$. The result is

$$u_{eq} = \frac{g_2}{\lambda_3(x_2 + r_c x_1)g_1 + f_{vdc}\lambda_4 r_c L x_1} \tag{3.51}$$

where

$$\begin{aligned}g_2 = \tfrac{L(R+r_c)}{R}\Bigg[\lambda_4 v_{ref} - \tfrac{\lambda_3 g_1}{L}|v_{in}| + \left(\tfrac{\lambda_3 r_L g_1}{L} + \lambda_3\omega_{pi} - \lambda_2\right) x_1 - \tfrac{f_{vdc}\lambda_4 R}{R+r_c} x_2 \\ + \left(\lambda_1 + \dot{\lambda}_4 - \lambda_4\omega_{pi}\right)\psi_3 - \omega_{pi}\psi_4 + \omega_{pi}^2\psi_5\Bigg]\end{aligned} \tag{3.52}$$

For the nominal values of the states and the parameters in Tables 3.1 and 3.2, we find from (3.51) and (3.52) that

$$u_{eq} \approx 1 - \tfrac{|v_{in}|}{x_2} - \tfrac{\omega_{pi}}{g_1(x_2/L)\lambda_3}\left(\lambda_4\psi_3 - \lambda_3 x_1\right) \tag{3.53}$$

It is obvious that u_{eq} obtained from (3.53) does not satisfy (3.44) when $x_1 = 0$. Therefore, global existence is not possible. We focus on local existence of the sliding surface when

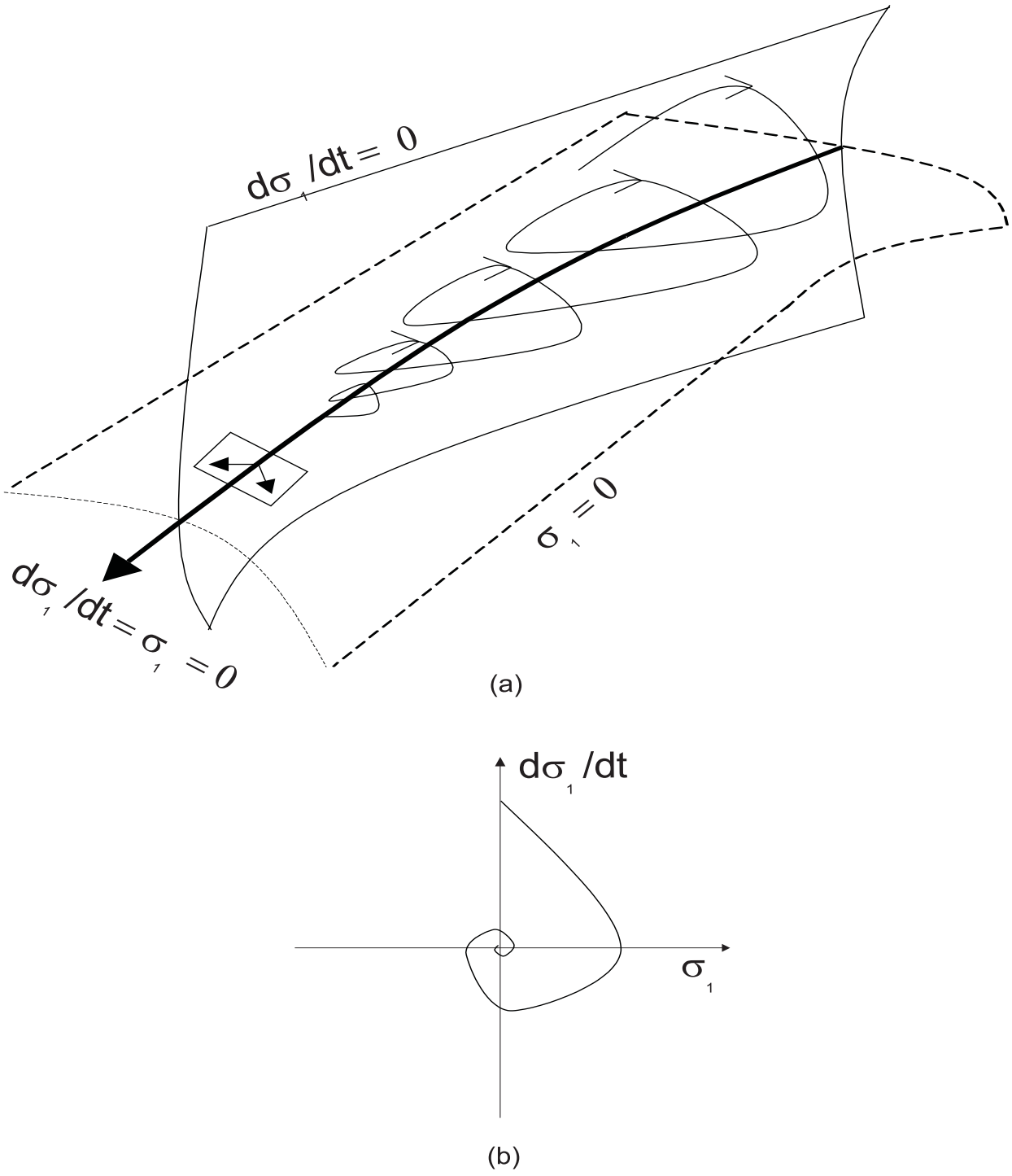

Figure 3.12: (a) A sliding-mode trajectory for the boost PFC circuit operating with current-loop controller number two. (b) A projection of the second-order sliding-mode trajectory on the plane $(\sigma_1, \dot{\sigma}_1)$.

$g_1(x_1, u) = 1$ (or $x_1 > 0$) and on the dynamics of the solutions once they leave the sliding surface. We choose the following positive definite Lyapunov function to find out whether the solutions converge on the origin in the plane $(\psi_5, \dot{\psi}_5)$:

$$V\left(\psi_5, \dot{\psi}_5\right) = \tfrac{1}{2}\left(\psi_5 \ \dot{\psi}_5\right) P \left(\psi_5 \ \dot{\psi}_5\right)^T \tag{3.54}$$

where $P = \begin{pmatrix} 1 & 0 \\ 0 & 1 \end{pmatrix}$. Substituting (3.40) into (3.50) and using (3.51) and (3.52), we find that $\dot{\psi}_5 = ku_n$, where k is defined in (3.46). Then, the local existence condition for the boost PFC circuit operating with the second controller can be expressed as

$$\dot{V}\left(\psi_5, \dot{\psi}_5\right) = \dot{\psi}_5\left(\psi_5 + \ddot{\psi}_5\right) = \dot{\psi}_5\left(\psi_5 + ku_n\right) \leq 0. \tag{3.55}$$

We now analyze the existence condition (3.55) by considering the following two cases:
Case 1 $\left[\psi_5 > 0\,(\psi_5 < 0) \Rightarrow u_n > 0(u_n < 0), |ku_n| > |\psi_5|\right]$: For the boost PFC circuit, this is the operating condition for most of the time since k has a very large negative value. Hence,

$$\dot{V}(\psi_5, \dot{\psi}_5) = \dot{\psi}_5\left(\psi_5 + ku_n\right)\left(\approx ku_n\dot{\psi}_5\right) \leq 0 \qquad \text{if} \qquad \dot{\psi}_5 \geq 0\left(\dot{\psi}_5 \leq 0\right). \tag{3.56}$$

Case 2 $\left[\psi_5 > 0, -ku_n < \psi_5 \text{ or } \psi_5 < 0, -ku_n > \psi_5\right]$: The condition for local existence in this case is

$$\dot{V}(\psi_5, \dot{\psi}_5) = \dot{\psi}_5\left(\psi_5 + ku_n\right)\left(\approx \psi_5\dot{\psi}_5\right) \leq 0 \qquad \text{if} \qquad \dot{\psi}_5 \leq 0\left(\dot{\psi}_5 \geq 0\right). \tag{3.56}$$

Initially, if the closed-loop system satisfies $\ddot{\psi}_5 = \dot{\psi}_5 = \psi_5 = 0$ and if the switching frequency is infinite, then the closed-loop system is invariant in nature. However, if the frequency is not infinite and if the system is subjected to a perturbation, then because ψ_5 and $\dot{\psi}_5$ are continuous and $\psi_5 = \int\int \ddot{\psi}_5 d\tau d\beta$, $\dot{\psi}_5 = \int \ddot{\psi}_5 d\tau$, the solutions do not converge immediately to $\ddot{\psi}_5 = \dot{\psi}_5 = \psi_5 = 0$. In fact it is not possible to satisfy either (3.56a) or (3.56b) all the time if not at all. It is obvious from (3.53) and (3.56b) that the system is most vulnerable to instability when the conditions in Case 2 are achieved.

When the existence condition fails, then the solutions leave the sliding surface. If there exists a stable orbit in the saturated region, then there is a possibility that the solutions may not return to the sliding surface. Under ideal operating conditions, one can show that, in the boost PFC circuit (operating with a finite load resistance), the solutions, which fail to satisfy the local existence condition but satisfy

$$\psi_5 \frac{d}{dt}\left(\overline{\lambda_1}(t)\psi_3 - \overline{\lambda_2}x_1\right) \leq 0 \quad \left(\overline{\lambda_1}(t) = \frac{\lambda_1(t)}{\omega_{ii}\omega_{pi}},\ \ \overline{\lambda_2} = \frac{\lambda_2}{\omega_{ii}\omega_{pi}}\right) \tag{3.57}$$

can not stay in the saturated region. Qualitatively, inequality (3.57) shows that, for the boost PFC circuit, if the dynamic response (or bandwidth in a linearized sense) of the voltage loop is much slower than that of the current loop, then the steady-state solution in the saturated region is virtual. If inequality (3.57) is satisfied, then one can show that, even though the local existence condition is not always satisfied, a spiraling motion (as shown in Figure 3.12b) may be achieved.

3.3.4 Extension of the Analysis to the Regularized Problem

We rewrite the dynamic equations of the closed-loop boost PFC circuit described by (3.20) through (3.23) as a vector equation in the form

$$\dot{\xi} = l_1(\xi, t) + l_2(\xi, t)u \qquad \left(g_1(x_1, u) \neq 0\right) \tag{3.58}$$

where $\xi = \left[x_i\ \psi_j\right]^T$ and dim(ξ)=4×1 (or 5×1). For the closed-loop system operating with controller one, using (3.20), (3.22), and (3.39), we obtain u (in a general form) as

$$u = [q_2(\xi, t)]^{-1}\left(\dot{\sigma}_1 - q_1(\xi, t)\right) \tag{3.59}$$

by replacing ψ and x with ξ. Substituting equation (3.59) into (3.58), we obtain

$$\dot{\xi} = l_1(\xi, t) + l_2(\xi, t)\Big([q_2(\xi)]^{-1}\left(\dot{\sigma}_1 - q_1(\xi, t)\right)\Big). \tag{3.60}$$

The integral equation equivalent to (3.60) is

$$\xi(t) = \xi(t_0) + \int_{t_0}^{t} \Big[l_1(\xi,\tau) - l_2(\xi)[q_2(\xi,\tau)]^{-1} q_1(\xi,\tau)\Big] d\tau + \int_{t_0}^{t} l_2(\xi)[q_2(\xi,\tau)]^{-1}\dot{\sigma}_1 d\tau \quad (3.61)$$

If $\dot{\sigma}_1$=0 then (3.61) reduces to

$$\xi^*(t) = \xi^*(t_0) + \int_{t_0}^{t} \Big[l_1(\xi^*,\tau) - l_2(\xi^*)[q_2(\xi^*,\tau)]^{-1} q_1(\xi^*,\tau)\Big] d\tau \quad (3.62)$$

which describes the dynamics of the system on the sliding surface. We subtract (3.62) from (3.61), use the property of the norm, and obtain the following relation for the norm of the difference:

$$\begin{aligned} \|\xi - \xi^*\| \leq\ & \|\xi(t_0) - \xi^*(t_0)\| + \| \int_{t_0}^{t} \Big[l_1(\xi,\tau) - l_2(\xi)[q_2(\xi,\tau)]^{-1} q_1(\xi,\tau)\Big] d\tau - \\ & \int_{t_0}^{t} \Big[l_1(\xi^*,\tau) - l_2(\xi^*)[q_2(\xi^*,\tau)]^{-1} q_1(\xi^*,\tau)\Big] d\tau \| + \\ & \| \int_{t_0}^{t} l_2(\xi)[q_2(\xi,\tau)]^{-1}\dot{\sigma}_1 d\tau \|. \end{aligned} \quad (3.63)$$

If we chose $\|\xi(t_0) - \xi^*(t_0)\| = R_1 \triangle$ (where $\triangle$ is the width of the boundary layer, which is assumed to be fixed just for the following expression), then we reduce (3.63) using a theorem by Utkin (1992) to

$$\|\xi - \xi^*\| \leq R_1 \triangle + \int_{t_0}^{t} L \|\xi(\tau) - \xi^*(\tau)\| d\tau \qquad (R_1 > 0) \quad (3.64)$$

provided that a Lipschitz constant L exists for $l_1(\xi^*,t) - l_2(\xi^*)[q_2(\xi^*,\tau)]^{-1} q_1(\xi^*,t)$ and $\|l_1(\xi,t) + l_2(\xi)u\| \leq W_1 + W_2\|\xi\|$ $(W_1 > 0, W_2 > 0)$. Using the Bellman-Gronwall lemma (Khalil, 1996), we can further reduce (3.64) to

$$\|\xi - \xi^*\| \leq R_2 \triangle \qquad (R_2 > 0) \quad (3.65)$$

It follows from inequality (3.65) that as $\triangle \to 0$ then $\xi \to \xi^*$. Hence, if the initial conditions of the differential equations describing the real and ideal sliding motions are sufficiently close, then their solutions are also close. We can extend the same procedure for the closed-loop system operating with controller two.

Inequality (3.65), however, does not give any idea about the dynamics of the nonlinear system if the two initial conditions are not sufficiently close. In other words, (3.65) does not give any information regarding the mechanism of instability if there is one. We, therefore, extend the analysis in Section 3.3.3 to the operation of the boost PFC circuit with a finite frequency f_s. The solution of this regularized problem is defined everywhere (in a limiting sense) except at the point defined by $\psi_5 = v_r(t)$. At this point, the derivative of the solution is not defined. Such discontinuities do not occur more than once in each switching cycle. However, the states match at this point. Therefore, using the concept of Lebesgue measure, we can obtain a numerical solution (almost everywhere) to this system.

Let us consider the closed-loop boost PFC circuit operating with controller two. For a given switching structure (i.e., for a given $g_1(x_1, u), u$), the closed-loop in (3.20) through (3.24) can be rewritten as

$$\dot{\xi} = A(t)\xi + B_1|v_{in}(t)| + B_2 v_{ref} \tag{3.66}$$

where A is a square matrix, B_1 and B_2 are column matrices, $\xi = \begin{bmatrix} x_i & \psi_j \end{bmatrix}^T$, and $\dim(\xi)=5\times 1$. The solution of (3.66) can be expressed as

$$\xi = \begin{cases} e^{\int_{t_0}^{t} A(\tau)d\tau}\xi(t_0) + \int_{t_0}^{t} e^{\int_{\tau}^{t_0} A(\gamma)d\gamma} B_1 v_{in}(\tau)d\tau + \int_{t_0}^{t} e^{\int_{\tau}^{t_0} A(\gamma)d\gamma} B_2 v_{ref} d\tau & \text{if } v_{in}(t) > 0 \\ e^{\int_{t_0}^{t} A(\tau)d\tau}\xi(t_0) - \int_{t_0}^{t} e^{\int_{\tau}^{t_0} A(\gamma)d\gamma} B_1 v_{in}(\tau)d\tau + \int_{t_0}^{t} e^{\int_{\tau}^{t_0} A(\gamma)d\gamma} B_2 v_{ref} d\tau & \text{if } v_{in}(t) < 0 \end{cases} . \tag{3.67}$$

Obviously, the integrals in (3.67) cannot be computed in closed-form. We can use the method of successive approximations to obtain an approximate state-transition matrix using

$$\begin{aligned} e^{\int_{t_0}^{t} A(\tau)d\tau} = I_5 + \int_{t_0}^{t} A(\tau_0)d\tau_0 + \int_{t_0}^{t} A(\tau_0)\int_{t_0}^{\tau_0} A(\tau_1)d\tau_1 d\tau_0 + \\ \int_{t_0}^{t} A(\tau_0)\int_{t_0}^{\tau_0} A(\tau_1)\int_{t_0}^{\tau_1} A(\tau_2)d\tau_2 d\tau_1 d\tau_0 + \cdots \end{aligned} \tag{3.68}$$

where I_5 is the identity matrix of dimension 5×5. If we make one further assumption that $v_{in}(t)$ does not vary appreciably in a small interval, then, using (3.67) and (3.68), we obtain

a closed-form expression for $\xi(t)$. Alternately, if we assume that both $A(t)$ and $v_{in}(t)$ do not vary appreciably in this small interval, then (3.67) reduces to

$$\xi = \begin{cases} e^{At}\xi(t_0) + \Big(e^{At} - I\Big)A^{-1}B_1 v_{in}(t_0) + \Big(e^{At} - I\Big)A^{-1}B_2 v_{ref} & \text{if } \; v_{in}(t_0) > 0 \\ e^{At}\xi(t_0) - \Big(e^{At} - I\Big)A^{-1}B_1 v_{in}(t_0) + \Big(e^{At} - I\Big)A^{-1}B_2 v_{ref} & \text{if } \; v_{in}(t_0) < 0 \end{cases} . \quad (3.69)$$

Thus, using either (3.67) or (3.69) and (3.21) and (3.24), we find an approximate solution to the dynamical equations of the closed-loop boost PFC circuit in a small interval of time.

On the other hand, if we assume that $v_{in}(t)$ is a harmonic function (e.g., $v_m \cos(\omega t)$, where ω and v_m are the frequency and amplitude of the line voltage), then we obtain a closed-form solution of (3.66) spanned over one switching cycle. Since $v_{in}(t)$ is periodic,

$$\tfrac{1}{t}\int_0^t |v_{in}(\tau)|^2 d\tau = \tfrac{v_m^2}{\pi}\int_0^\pi |\cos(\omega\tau)|^2 d\tau = \text{constant}. \quad (3.70)$$

Hence the coefficients $\lambda_1(t)$ and $\lambda_4(t)$ are constants. Let us define two additional fictitious states ξ_6 and ξ_7 as

$$\begin{aligned} &\xi_6 = v_m \cos(\omega t), \\ &\xi_7 = \dot{\xi}_6 = -\omega v_m \sin(\omega t) \\ &\Rightarrow \dot{\xi}_7 = -\omega^2 \xi_6. \end{aligned} \quad (3.71)$$

Then (3.71) changes (3.66) to the form

$$\dot{\xi}' = A'\Big(\xi_6\Big)\xi' + B_2' v_{ref} \quad (3.72)$$

where $\xi' = \begin{bmatrix} \xi & \xi_6 & \xi_7 \end{bmatrix}^T$. If $v_{in}(t)$ is periodic having harmonics besides the fundamental frequency ω, then the procedure in (3.69) can be extended with additional fictitious states representing the additional harmonic terms in $v_{in}(t)$.

In (3.72), the equations governing $\dot{\xi}_1, \dot{\xi}_2, \dot{\xi}_3, \dot{\xi}_6$, and $\dot{\xi}_7$, represented by $\dot{\xi}''$, do not possess cross couplings of the states. Because the equation governing $\dot{\xi}''$ is time invariant, its solution

can be expressed as

$$\xi'' = e^{A''t}\,\xi''(t_0) + \left(e^{A''t} - I_5\right)\left(A''\right)^{-1} B_2'' v_{ref} \tag{3.73}$$

Once we obtain ξ'', we use it to obtain ξ_4 and ξ_5. The solution of $\xi_4 (= \psi_4)$ is

$$\xi_4 = \xi_4(t_0) + \int_{t_0}^{t} g(\tau) d\tau \tag{3.74}$$

where

$$g(\tau) \;\; = \;\; P_1 M \underline{\xi}'' + P_6 M \underline{\xi}'' P_3 M \underline{\xi}'' \tag{3.75}$$

In (3.75), P_1 and P_6 are suitable row vectors and M is a matrix whose columns are the eigenvectors of A'' such that

$$\underline{\xi}'' = M^{-1}\xi'' = e^{J\tau} M^{-1}\xi(t_0) + \left(e^{J\tau} M^{-1} - M^{-1}\right)\left(A''\right)^{-1} B_2' v_{ref} \tag{3.76}$$

where J is the Jordan form of A''. The advantage of using the Jordan form in (3.76) is that it simplifies the analysis. Substituting (3.76) into (3.75) and with little simplification, one can reduce the number of terms in (3.75) to six. Five of these terms, when integrated using (3.74), give a closed-form solution. The sixth is integrated term by term. We did this integration easily using MATHEMATICA. Thus, using a little mathematical manipulation, we solved for ξ_4 exactly. Once ξ_4 and ξ'' are known, we solve for $\xi_5 (= \psi_5)$ exactly using a procedure similar to that used for solving ξ_4. The solution of ξ obtained using the above procedure is exact. This could be particularly helpful in the analysis when the switching and the line frequencies are not wide apart. It can also be used to find the accuracy of numerical solutions of (3.66). Using (3.74) and the expressions for ξ_4 and ξ_5, we obtain a discrete form of the solution of ξ for a given switching topology as

$$\xi_{n+1} = \Phi_n \xi_n + \Gamma_n v_{ref} \tag{3.77}$$

The closed-loop converter has two fundamental frequencies: the forcing frequency and the switching frequency. Hence, the dynamics of the discontinuous system evolve over a torus. Using a first-order Poincare map, we obtain a reduced-order system that has no discontinuity due to control. The first-order Poincare map is obtained by generating a map, which relates the values of the states ξ at the end of a switching cycle to those at the beginning of the next cycle (Alfayyoumi et al., 1999; Mazumder et al., 2000a). To obtain this map, we stacked the solution in (3.77) for two consecutive switching topologies (if the converter is in CCM) or for three consecutive switching topologies (if the converter is in DCM). The switching instant in any switching cycle is obtained by solving a transcendental equation of the form

$$\rho\Big(\xi_n, t\Big) - v_m = 0. \tag{3.78}$$

The validity of the results obtained with the first-order Poincare map is upto half the switching frequency. The stability of the closed-loop boost PFC circuit is verified by determining the orbital stability of the first-order map. Alternatively, one can determine the stability using a second-order Poincare map, which is generated by taking a transversal section of the first-order map. The advantage of the second-order map is that the problem of determining the stability of an orbit is reduced to determining the stability of a point. However, the stability analysis is valid only for the reduced-order problem.

3.3.5 Results

The parameters of the power stage and the multi-loop controller of the experimental boost PFC converter, as shown in Figure 3.13, are listed in Tables 3.1 and 3.2. Due to lack of space and to avoid repetition, all the results in this section (except for the one shown in Figure 3.19) are obtained using the second current-loop controller, which is being commercially used. We begin with Figure 3.14, which shows that, even when the width of the boundary layer approaches zero, the existence condition fails at $x_1 = 0$. This is evident from the jumps in the values of ψ_5 and $(\psi_5\dot{\psi}_5)$ at that point. Hence, global existence of a

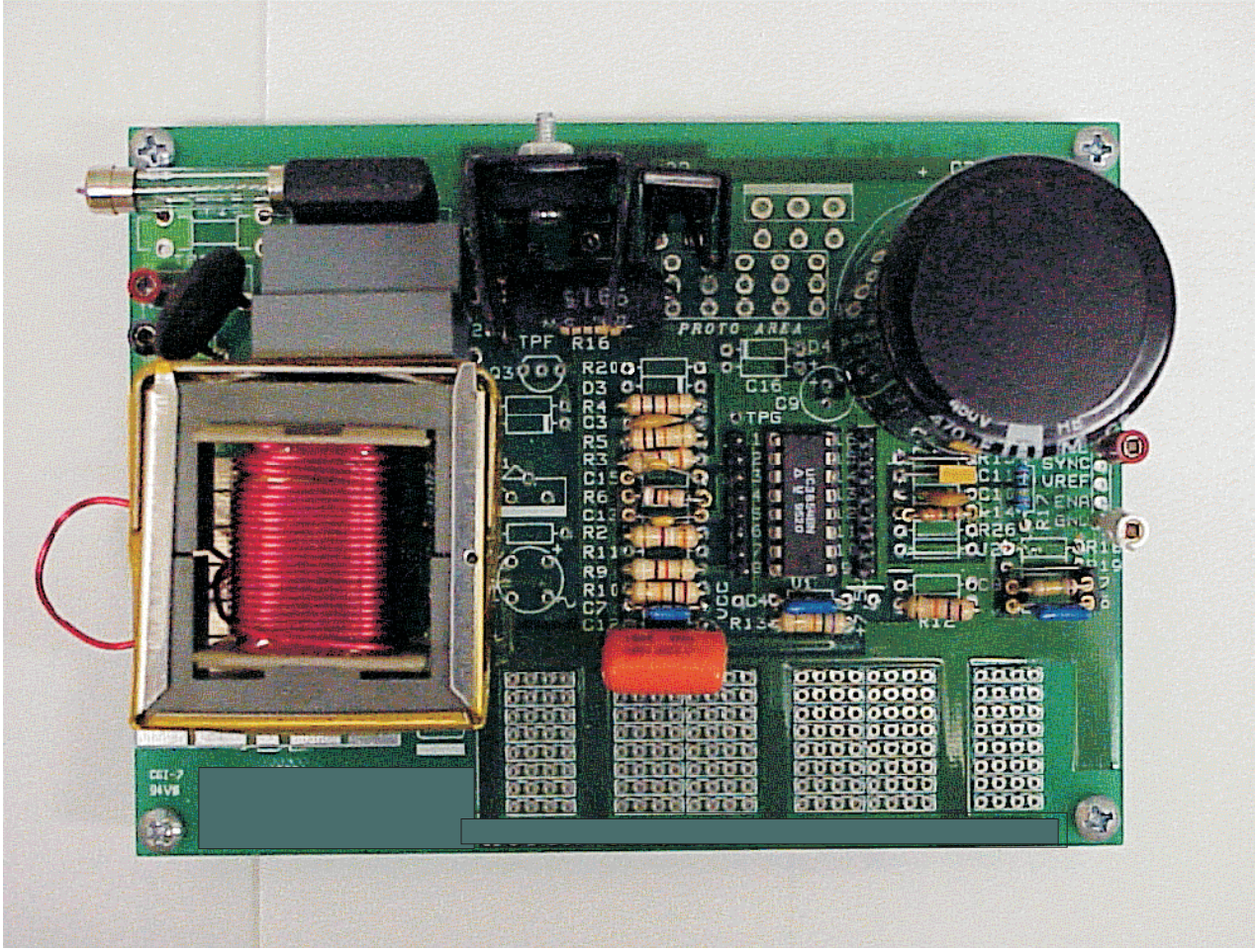

Figure 3.13: Experimental closed-loop boost PFC circuit.

smooth hypersurface in a boost PFC circuit is not possible.

When the existence condition fails, then the solutions leave the sliding surface. If these solutions do not satisfy (3.57), then they stay in the saturated region permanently. To demonstrate this, we designed a closed-loop system with a fast voltage loop so that (3.57) is violated. Figure 3.15 shows that ψ_5 continues to increase, and hence, u stays permanently at a value of one. As a result the capacitor voltage continues to decay until it stabilizes at a zero, which is the equilibrium state for the capacitor voltage in this saturated region. We should note that, in a real boost PFC circuit, the fault-handling systems will shut down the converter prior to this outcome. The boost PFC circuit is used as a universal power

Table 3.1: Power-stage parameters for the boost PFC circuit.

Parameter	Nominal Value
r_L	0.5 Ω
r_C	0.5 Ω
R	1000Ω
L	1 mH
C	440 μF
f_s	90kHz
ω	60Hz
v_m	5.8 V
V_l	0.8 V

supply. In other words, it should be stable even if the root-mean-square (rms) value of the input voltage varies between 90 volts (low line) to 265 volts (high line). In Figure 3.16, we show that, for a finite frequency of operation (90 kHz), a fast-scale instability (in the vicinity of $x_1 = 0$) occurs earlier for low line voltage. Under normal operating conditions, the third term in (3.53) is quite small. Consequently, as $|v_{in}(t)| \to 0$, $u_{eq} \to 1$. Hence, it follows from (3.40) that, for low line, $u_n \to 0$ faster as the input voltage decreases and hence the (local) existence condition for a sliding manifold may be violated earlier, which results in an earlier onset of instability. On the other hand, using (3.44) and (3.53), we can also show that when $|v_{in}(t)|_{max} \to x_2$, $u_{eq} \to 0$ and (3.44) will be violated. Hence the system is vulnerable to instability because the local existence condition may fail. This instability will occur earlier for high line. In Figure 3.17, we show that a boost PFC circuit (whose controller gains have not been optimized) loses stability on a fast scale as the input voltage is increased from low line to high line. In Figure 3.18, we show that, when $|v_{in}(t)|_{max} \to x_2$ and the current-loop controller gain ($\propto k$) is high, a fast-scale instability occurs not only at the peak of the current but also when it approaches zero. This result can be explained, as before, using (3.44) and

Table 3.2: Controller parameters for the boost PFC circuit.

Parameter	Nominal Value
v_{ref}	3 V
f_i	0.25/A
f_{Vdc}	$7.83807917*10^{-3}$/V
f_V	$6.67081869*10^{-7}\mu$A/V
S_1	0.9
S_2	0.326797385
S_3	3900/μA
ω_{iv}	30.61974
ω_{pv}	14.1 Hz
ω_{ii}	$3.5993418*10^5$
ω_{zi}	$9.7521411*10^3$ Hz
ω_{pi}	$1.0727355*10^5$ Hz

(3.53).

In Figure 3.19 we show that, if the switching of the boost PFC circuit is based on $\psi_6 = 0$ rather than on $\psi_5 = 0$, then the stability of the system improves provided that the signal to noise ratio of x_1 is high. For these two cases, the results agree with the explanation given in Section 3.3.3 using the local existence conditions (3.47) and (3.55). Finally, using a first-order Poincare map, we explore the mechanism of the fast-scale instability when the converter is operated with a finite frequency of 90kHz and the current-loop controller gain ω_{ii} (see Figure 3.9) is gradually increased. We show in Figure 3.20 that, as ω_{ii} is increased, a fast-scale instability occurs in the vicinity of the point $x_1 = 0$. The fast-scale instability doubles the switching period, which ultimately leads to chaos. In Figure 3.21, we show experimental results confirming the existence of the fast-scale instability. The figure shows doubling of

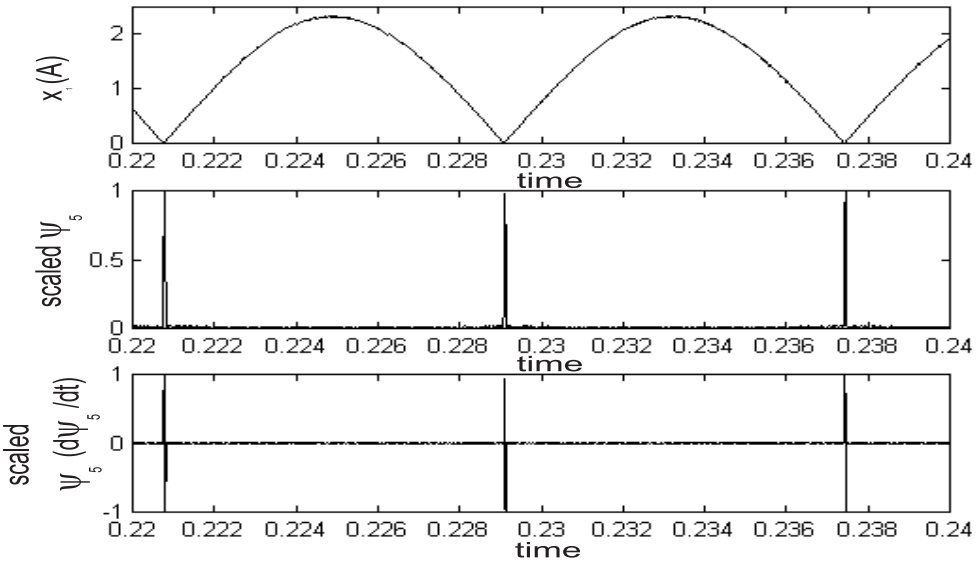

Figure 3.14: Existence condition fails at $x_1 = 0$. Hence only local existence is possible for the boost PFC circuit.

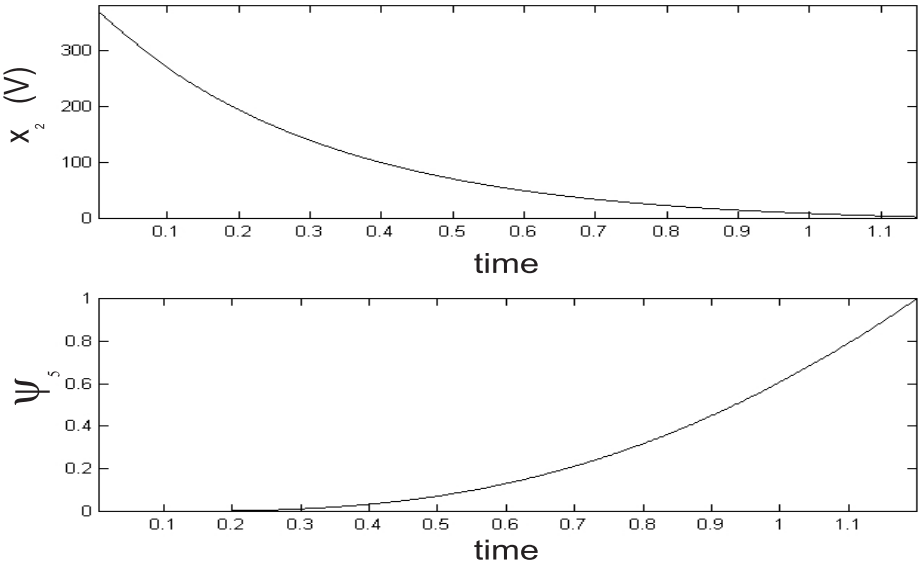

Figure 3.15: Condition (3.57) is violated and hence the solution leaves the local sliding surface.

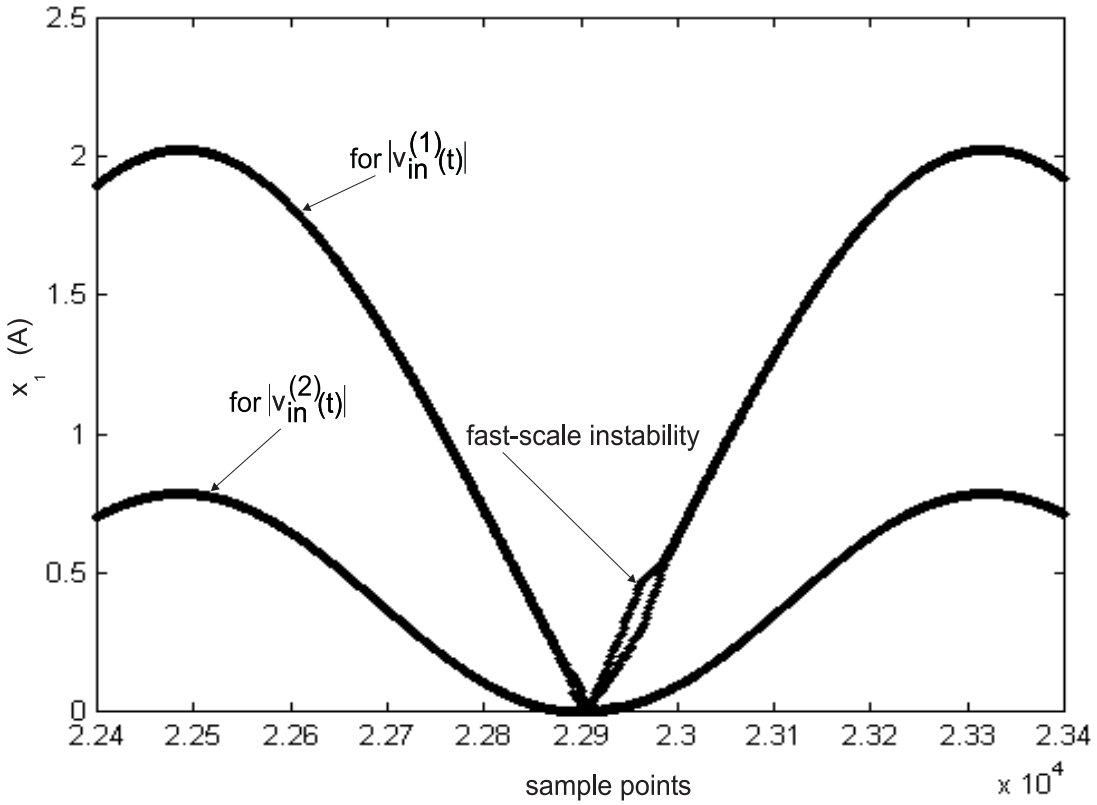

Figure 3.16: Using a first-order Poincare map we show that a fast-scale instability occurs for a lower input voltage ($|v_{in}^{(1)}(t)|_{max} < |v_{in}^{(2)}(t)|_{max}$) when all of thge other parameters are kept the same.

the switching period. We note that, when the switching frequency of the converter is finite, then the dynamics of the closed-loop system evolve on a torus. Hence the instabilities, in Figure 3.20, actually show projections of the torus breakdown.

We note that, unlike dc-dc converters, the boost PFC circuit exhibits period-two, period-four, higher-order periods, and chaotic dynamics in one line cycle due to the time variation in $|v_{in}(t)|$. Interestingly, when we analyzed the closed-loop system using Floquet theory (based on a second-order Poincare map), we found all of the four cases in Figure 3.20 to be stable. Clearly this is not the case. The reason behind this fallacy is that, using a second-order Poincare map, one can predict orbital instability only on the slow scale (Kaas-Peterson,

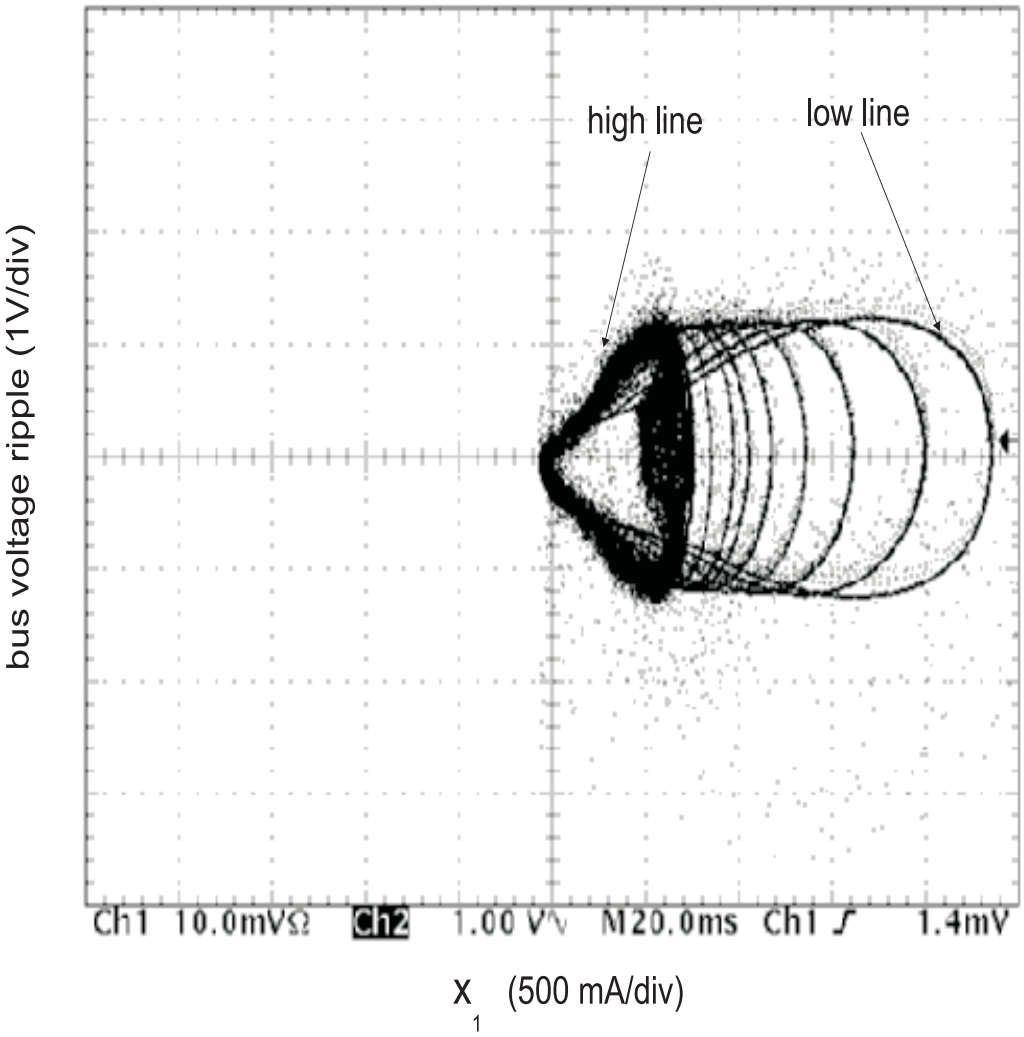

Figure 3.17: An experimental result, which shows that, if the controller gains are not properly optimized, the onset of a fast-scale instability occurs when $|v_{in}(t)|_{max} \rightarrow x_2$.

1986; Wang, 1997).

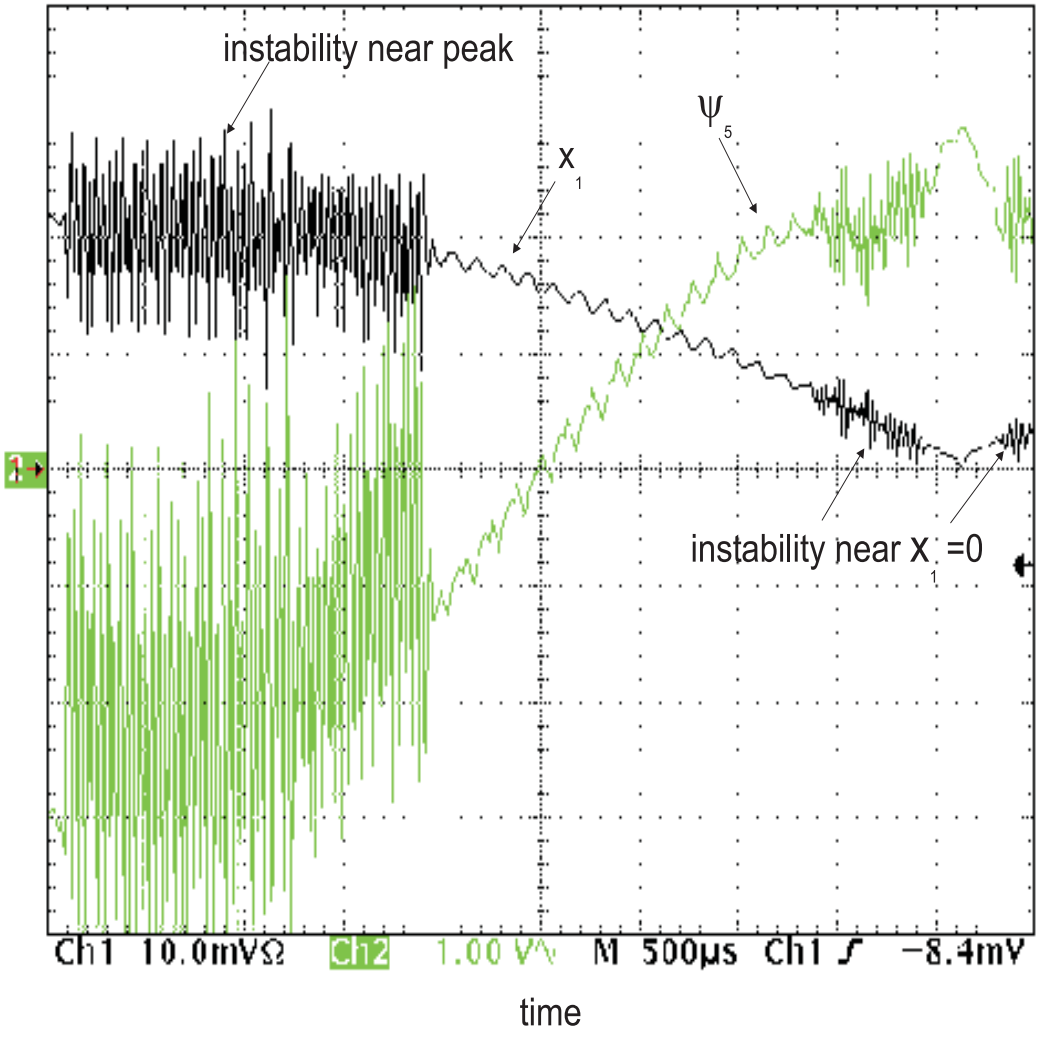

Figure 3.18: An experimental result, which shows that, if the controller gains are not properly optimized, the boost PFC circuit becomes unstable on a fast scale not only when $x_1 \rightarrow 0$ but also when $|v_{in}(t)|_{max} \rightarrow x_2$.

3.4 Single Phase Bidirectional Converter

Figure 3.22 shows a single phase bidirectional converter (SPBC), has applications ranging from traction drives to telecommunications. Unlike the boost PFC circuit shown in

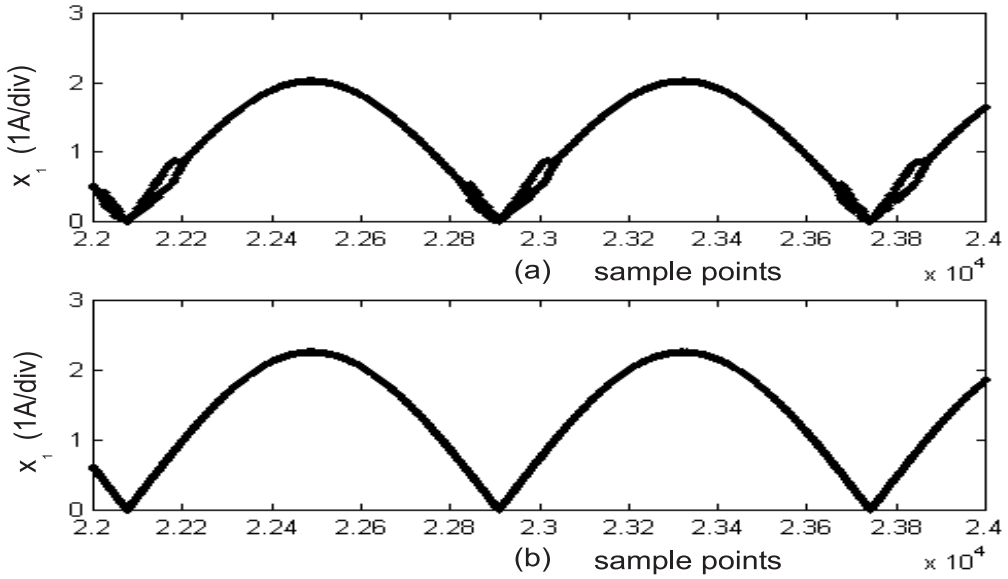

Figure 3.19: Performance of the boost PFC circuit on the fast scale: (a) switching based on $\psi_5 = 0$ and (b) switching based on $\psi_6 = 0$.

Figure 3.9, the bidirectional converter has the capability to draw sinusoidal line currents at unity power factor, thereby significantly minimizing the total harmonic distortion of the line current.

We assume that all of the switches of the SPBC are ideal and that it operates as a boost converter. The analysis of the SPBC for other modes of operation remains same. The status of the four switches at any instant defines a switching state. For the bidirectional converter, 16 switching states are possible. However, only four of these are feasible for the SPBC. Two of these states are zero states (ZS); the other two are the active states (AS). As shown in Figure 3.22, the four switching states of the SPBC are generated by comparing the error signals $v_{e1}(t)$ and $-v_{e1}(t)$ with a triangular carrier waveform $v_r(t)$ of frequency f_s ($= \omega_s/2\pi = \frac{1}{T_s}$). The present methodology also holds for case in which the carrier waveform is different from the one shown in Figure 3.23.

The dynamical equation of the converter in the i^{th} sub-interval (of duration δ_i) of the k^{th}

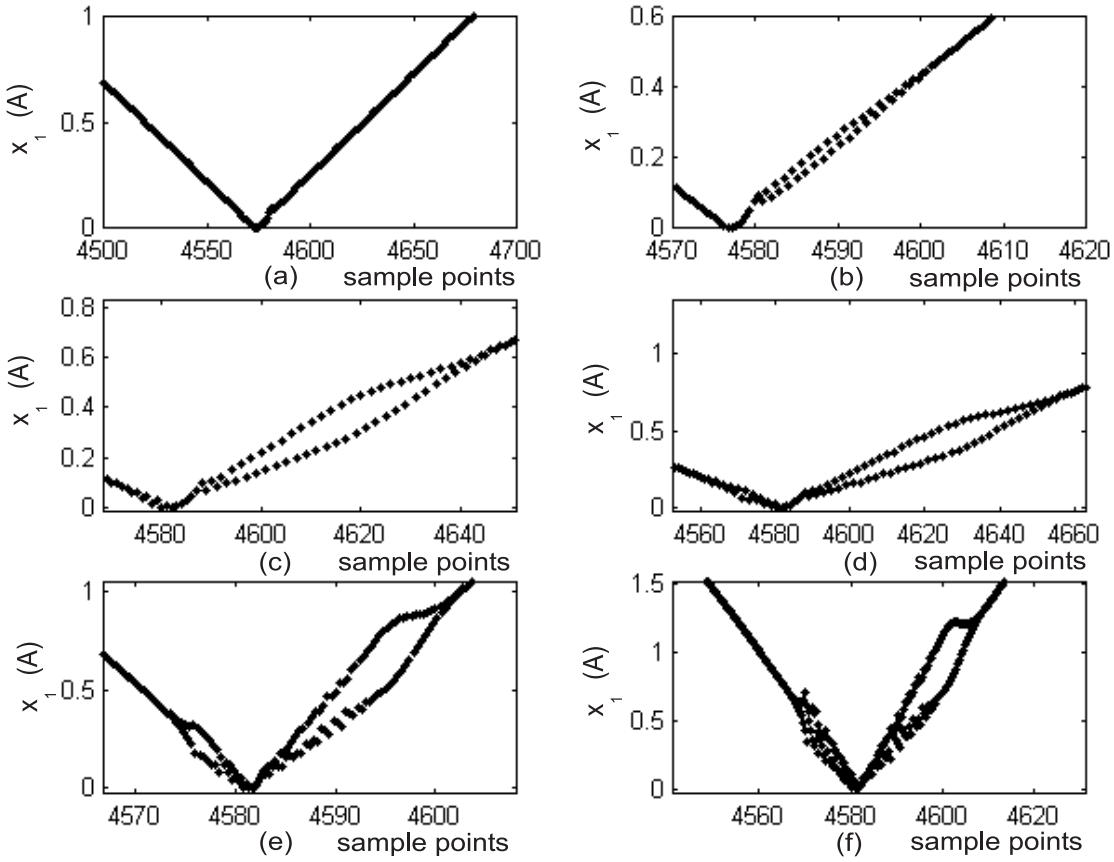

Figure 3.20: Results based on a first-order Poincare map, which show the onset and progress of a fast-scale instability as ω_{ii} is increased. The fast-scale instability occurs via period doubling of the switching period, which ultimately leads to chaos.

switching cycle is described by

$$\dot{X}(t) = A_i X(t) + B_i v_{in}(t) \tag{3.79}$$

where the A_i and B_i are matrices, $X(t) = [i_L(t)\ v_C(t)]^T$ represents the states of the converter, and $v_{in}(t)$ is a time-varying input voltage. The solution of (3.79) is given by

$$X(t) = e^{\int_{t_0}^{t} A_i d\tau} X(t_0) + \int_{t_0}^{t} e^{\int_{\tau}^{t} A_i d\xi} B_i v_{in}(\tau) d\tau \tag{3.80}$$

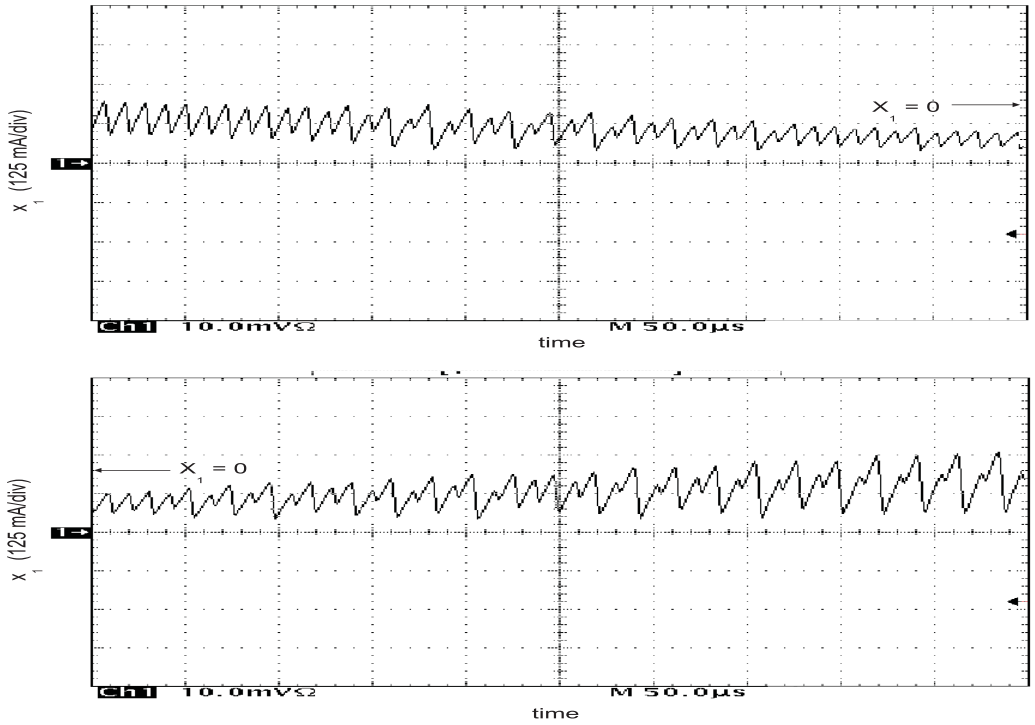

Figure 3.21: An experimental result, which confirms the fast-scale instability near $x_1 = 0$. The fast-scale instability results in a period doubling of the ripple of the inductor current x_1 in these cases.

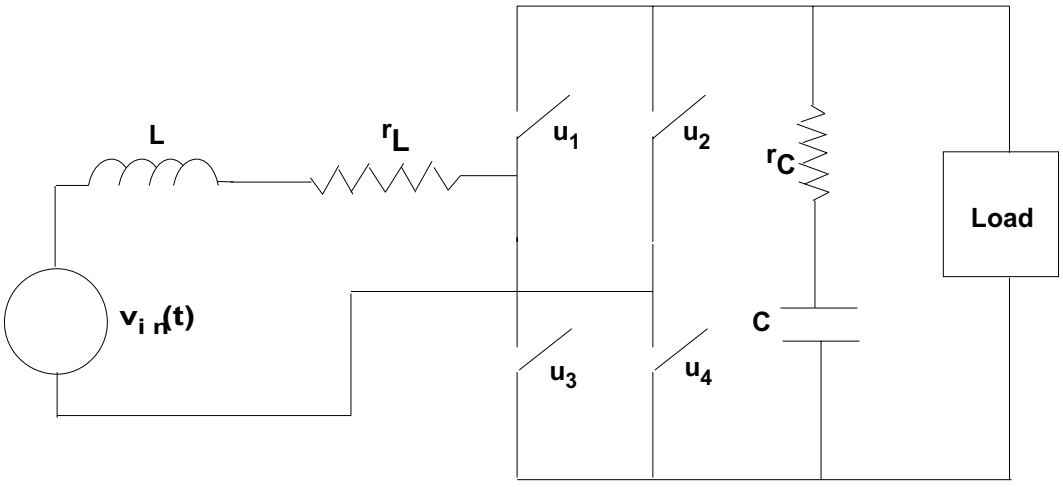

Figure 3.22: A single-phase-bidirectional converter.

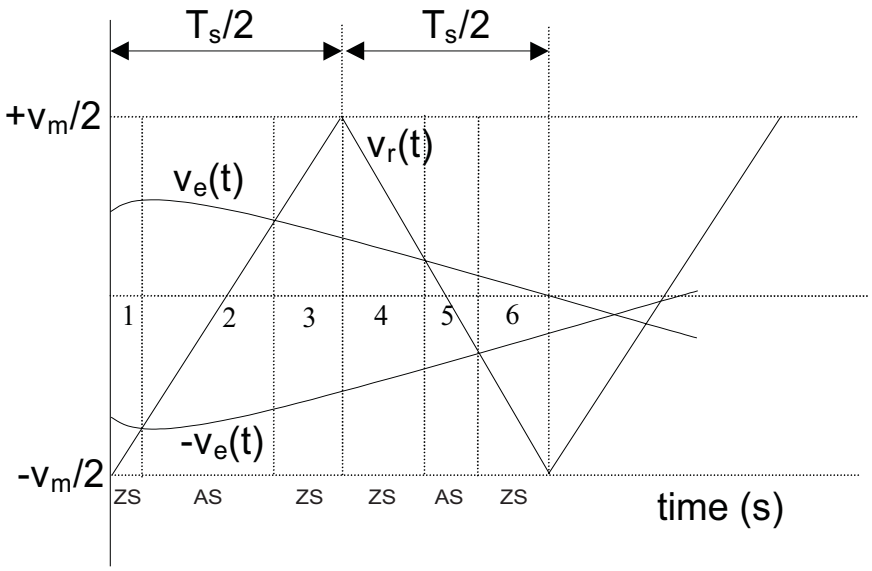

Figure 3.23: Modulation scheme of the single-phase-bidirectional converter shown in Figure 3.22.

where t_0 is the initial time. By cascading the solutions of (3.80) over all of the subintervals of the k^{th}-switching cycle, we obtain a first-order Poincare map for the SPBC. Next, we assume that the forcing function is given by

$$v_{in}(t) = v_m \cos(\omega_l t) \tag{3.81}$$

where v_m and ω_l are the amplitude and frequency of $v_{in}(t)$. Such an assumption is quite close to reality for most of the practical cases and has been used in many earlier papers (see Chapter 1). Using (3.80) and (3.81) and some simple algebra, one can show that the map, which describes the dynamics of the SPBC, in the i^{th} sub-switching cycle (of duration δ_i) of the k^{th} switching cycle is given by

$$\begin{aligned} X(k+i+1) &= e^{A_i\delta_i}X(k+i) + \frac{e^{j\omega_l\delta_i}}{2}v_m M_i\left(e^{(J_i-j\omega_l I)\delta_i} - I\right)\left(J_i - j\omega_l I\delta_i\right)^{-1} {M_i}^{-1}B_i + \\ &\quad \frac{e^{-j\omega_l\delta_i}}{2}v_m M_i\left(e^{(J_i+j\omega_l I)\delta_i} + I\right)\left(J_i + j\omega_l I\delta_i\right)^{-1} {M_i}^{-1}B_i \end{aligned} \tag{3.82}$$

where J_i and M_i are the Jordan and modal matrices of A_i, I is the identity matrix, and j is a

complex operator. Although (3.82) looks like a map in complex space, a simple manipulation would show that it is actually real.

Special case ($\omega_l = 0$): When $\omega_l = 0$, then (3.82) reduces to

$$X(k+i+1) = e^{A_i\delta_i}X(k+i) + \left(e^{A_i\delta_i} - I\right){A_i}^{-1}B_i v_m \tag{3.83}$$

which is the expression we obtained for a dc-dc converter in a sub-switching cycle (see Chapter 2). This confirms that (3.82) is a general map, which can be used for ac-dc as well as dc-dc converters.

Using (3.82), we obtain the solutions in all of the sub-intervals of the k^{th} switching cycle, and by cascading all of these solutions, one can obtain a map that relates X_{k+1} to X_k. Such a map has the following form:

$$X(k+1) = f(X(k), t_1(k), t_2(k), \cdots, t_6(k)). \tag{3.84}$$

and is referred to throughout the paper as the first-order Poincare map of the SPBC.

If $v_{in}(t)$ has finite (N) higher-order harmonics and is described by

$$v_{in}(t) = \Sigma_{p=1}^{N} v_{\alpha_p}\cos(p\omega_l t + \phi_{\alpha_p}) + \Sigma_{p=1}^{N} v_{\beta_p}\sin(p\omega_l t + \phi_{\beta_p}) \tag{3.85}$$

where v_{α_p} and v_{β_p} and are the amplitudes and ϕ_{α_p} and ϕ_{β_p} are the phases of the corresponding harmonics, then the procedure to obtain the solution of (3.80) is the same as that used to obtain (3.82), but it becomes more involved.

Another approach to obtain the solution of (3.79) when v_{in} has higher-order harmonics is as follows. Let

$$\begin{aligned} x_{\alpha_1}(t) &= \cos(\omega_l t + \phi_{\alpha_1}) \\ x_{\alpha_2}(t) &= \cos(2\omega_l t + \phi_{\alpha_2}) \\ &\vdots \\ x_{\alpha_N}(t) &= \cos(N\omega_l t + \phi_{\alpha_N}) \end{aligned} \tag{3.86}$$

and

$$\begin{aligned} x_{\beta_1}(t) &= \sin(\omega_l t + \phi_{\beta_1}) \\ x_{\beta_2}(t) &= \sin(2\omega_l t + \phi_{\beta_2}) \\ &\vdots \\ x_{\beta_N}(t) &= \sin(N\omega_l t + \phi_{\beta_N}) \end{aligned} \tag{3.87}$$

then using (3.86) and (3.87), one can rewrite $v_{in}(t)$ as

$$v_{in}(t) = v_{\alpha_1}x_{\alpha_1}(t) + v_{\alpha_2}x_{\alpha_2}(t) + \cdots + v_{\alpha_N}x_{\alpha_N}(t) + v_{\beta_1}x_{\beta_1}(t) + v_{\beta_2}x_{\beta_2}(t) + \cdots + v_{\beta_N}x_{\beta_N}(t) \tag{3.88}$$

where

$$\begin{aligned} \dot{x}_{\alpha_1}(t) &= x_{\alpha_{1a}}(t) = -\omega_l \sin(\omega_l t + \phi_{\alpha_1}) \\ \dot{x}_{\alpha_{1a}}(t) &= -\omega_l^2 \cos(\omega_l t + \phi_{\alpha_1}) = -\omega_l^2 x_{\alpha_1}(t) \\ \dot{x}_{\alpha_2}(t) &= x_{\alpha_{2a}}(t) = -2\omega_l \sin(2\omega_l t + \phi_{\alpha_2}) \\ \dot{x}_{\alpha_{2a}}(t) &= -4\omega_l^2 \cos(2\omega_l t + \phi_{\alpha_2}) = -4\omega_l^2 x_{\alpha_2}(t) \\ &\vdots \\ \dot{x}_{\alpha_N}(t) &= x_{\alpha_{Na}}(t) = -N\omega_l \sin(N\omega_l t + \phi_{\alpha_N}) \\ \dot{x}_{\alpha_{Na}}(t) &= -N^2\omega_l^2 \cos(N\omega_l t + \phi_{\alpha_N}) = -N^2\omega_l^2 x_{\alpha_N}(t) \end{aligned} \tag{3.89}$$

and

$$\begin{aligned} \dot{x}_{\beta_1}(t) &= x_{\beta_{1a}}(t) = \omega_l \cos(\omega_l t + \phi_{\beta_1}) \\ \dot{x}_{\beta_{1a}}(t) &= -\omega_l^2 \sin(\omega_l t + \phi_{\beta_1}) = -\omega_l^2 x_{\beta_1}(t) \\ \dot{x}_{\beta_2}(t) &= x_{\beta_{2a}}(t) = 2\omega_l \cos(2\omega_l t + \phi_{\beta_2}) \\ \dot{x}_{\beta_{2a}}(t) &= -4\omega_l^2 \sin(2\omega_l t + \phi_{\beta_2}) = -4\omega_l^2 x_{\beta_2}(t) \\ &\vdots \\ \dot{x}_{\beta_N}(t) &= x_{\beta_{Na}} = -N\omega_l \cos(N\omega_l t + \phi_{\beta_N}) \\ \dot{x}_{\beta_{Na}}(t) &= -N^2\omega_l^2 \sin(N\omega_l t + \phi_{\beta_N}) = -N^2\omega_l^2 x_{\beta_N}(t). \end{aligned} \tag{3.90}$$

Thus, by using (3.86-3.90) instead of (3.81), we obtain a first-order Poincare map. Overall, the procedures for obtaining (3.82) and (3.84) if $v_{in}(t)$ is described by (3.81) or (3.85) are similar.

Once a fist-order map is obtained, we use it to obtain a second-order Poincare map. Unlike a dc-dc converter, a second-order Poincare map may be necessary for the stability analysis of a SPBC. This is because, even under steady-state conditions, the output of the first-order Poincare map of a SPBC, as described by (3.84), is time varying. A second-order Poincare map converts the problem from one of analyzing the stability of an orbit to that of analyzing the stability of a fixed point. Depending on the ratio of ω_l and ω_s, the second-order Poincare map is obtained as follows:

- $\frac{\omega_s}{\omega_l}$ is an integer: In this case, the map is obtained by cascading $\frac{\omega_s}{\omega_l}$ solutions of (3.84).
- ω_s and ω_l have a least common multiple (LCM): In this case, the map is obtained by cascading $\frac{\omega_s}{LCM(\omega_s,\omega_l)}$ solutions of (3.84).
- ω_s and ω_l have no common multiple: In this case, the map is obtained by interpolation (Kaas-Petersen, 1986).

3.5 Analytical Map of a Closed-Loop Single-Phase-Bidirectional Converter

Having modeled the open-loop converter, we extend the idea to model a closed-loop converter. We select a control such that the converter operates with unity power factor. There are many possible control laws; we select the simple one shown in Figure 3.24 to demonstrate the modeling methodology. Using (3.81), the idea described in (3.86-3.90), and Figure 3.24, we obtain the following state-space model, which describes the dynamics of the converter for

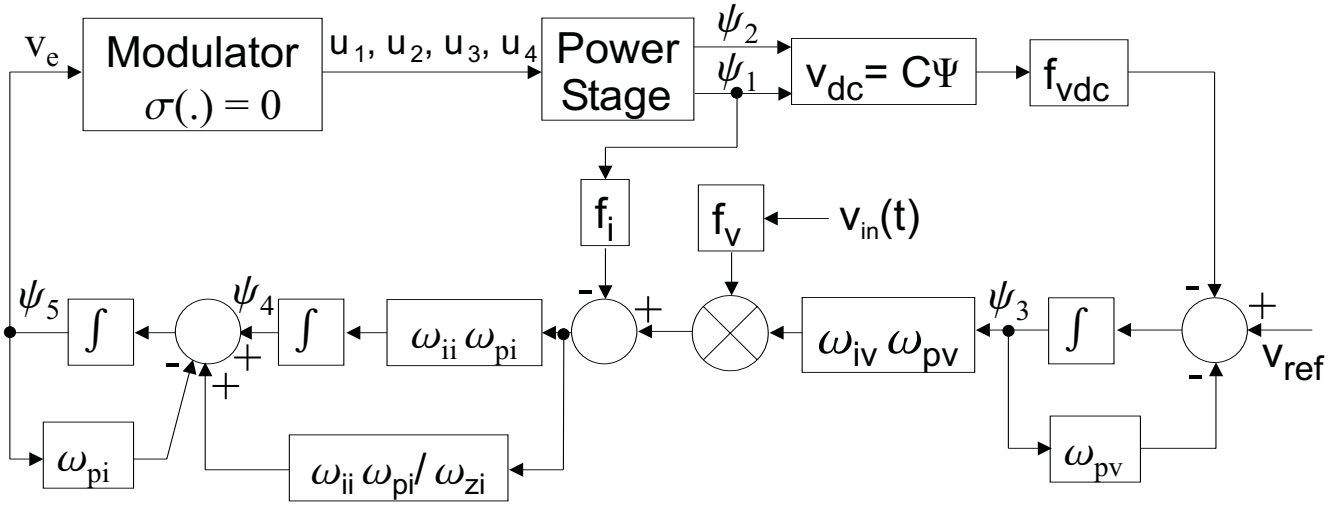

Figure 3.24: A simple closed-loop controller for the single-phase bidirectional converter to achieve unity power-factor operation where C is a row matrix.

the i^{th} switching state:

$$\dot{\Psi}(t) = \begin{pmatrix} \dot{\psi}_1(t) \\ \dot{\psi}_2(t) \\ \dot{\psi}_3(t) \\ \dot{\psi}_4(t) \\ \dot{\psi}_5(t) \\ \dot{\psi}_6(t) \\ \dot{\psi}_7(t) \end{pmatrix} = \begin{pmatrix} c_{i_{11}} & c_{i_{12}} & 0 & 0 & 0 & c_{i_{16}} & c_{i_{17}} \\ c_{i_{21}} & c_{i_{22}} & 0 & 0 & 0 & 0 & 0 \\ c_{i_{31}} & c_{i_{32}} & c_{i_{33}} & 0 & 0 & 0 & 0 \\ c_{i_{41}} & 0 & c_{i_{43}}\psi_6(t) & 0 & 0 & 0 & 0 \\ c_{i_{51}} & 0 & c_{i_{53}}\psi_6(t) & c_{i_{54}} & c_{i_{55}} & 0 & 0 \\ 0 & 0 & 0 & 0 & 0 & 0 & 1 \\ 0 & 0 & 0 & 0 & 0 & c_{i_{76}} & 0 \end{pmatrix} \begin{pmatrix} \psi_1(t) \\ \psi_2(t) \\ \psi_3(t) \\ \psi_4(t) \\ \psi_5(t) \\ \psi_6(t) \\ \psi_7(t) \end{pmatrix} + \begin{pmatrix} 0 \\ 0 \\ 1 \\ 0 \\ 0 \\ 0 \\ 0 \end{pmatrix} v_{ref} \quad (3.91)$$

In (3.91), $X(t) = \begin{pmatrix} \psi_1(t) & \psi_2(t) \end{pmatrix}^T$ and the $c_{i_{jk}}$ are coefficients, which can be easily obtained from the dynamical equations of the i^{th} topology. We note that, if instead of (3.81), we use the v_{in} described by (3.85), then, as shown in Section 3.4, the overall analysis for the closed-loop system remains the same but becomes more involved.

The solutions of $\psi_1(t)$, $\psi_2(t)$, $\psi_3(t)$, $\psi_6(t)$, and $\psi_7(t)$ in matrix form are

$$\begin{aligned}\Psi_a(t) &= \Big(\psi_1(t)\ \psi_2(t)\ \psi_3(t)\ \psi_6(t)\ \psi_7(t)\Big)^T \\ &= e^{A_{a_i}t}\Psi_a(t_0) + \Big(e^{A_{a_i}t} - I\Big)A_{a_i}^{-1}B_{a_i}v_{ref} \\ &= M_{a_i}e^{J_{a_i}t}{M_{a_i}}^{-1}\Psi_a(t_0) + \Big(M_{a_i}e^{J_{a_i}t}{M_{a_i}}^{-1} - I\Big)A_{a_i}^{-1}B_{a_i}v_{ref}.\end{aligned} \tag{3.92}$$

In (3.92), $\Psi_a(t) = \Big(\psi_1(t)\ \psi_2(t)\ \psi_3(t)\ \psi_6(t)\ \psi_7(t)\Big)^T$ and J_{a_i} and M_{a_i} are the Jordan and modal matrices of A_{a_i}. We assume in (3.92) that Jordan decomposition of A_{a_i} is possible. This is based on following values of the power-stage parameters: $L = 5$ mH, $r_L = 0.75\ \Omega$, $r_C = 0.5\ \Omega$, $C = 1000\ \mu$F, $f_{vdc} = 0.01$, $f_i = 0.1$, $v_m = 110\sqrt{2}$ V, $\omega_s = 2\pi 10000$ rad/s, and $\omega_l = 2\pi 60$ rad/s. In almost all of the practical cases, this assumption is true. Even if this assumption fails, the remaining procedure is the same but is more involved.

Letting

$$\underline{\Psi}_a(t) = {M_{a_i}}^{-1}\Psi_a(t) \tag{3.93}$$

and then substituting (3.93) into (3.92), we obtain

$$\begin{aligned}\underline{\Psi}_a(t) &= e^{J_{a_i}t}\underline{\Psi}_a(t_0) + \Big(e^{J_{a_i}t}{M_{a_i}}^{-1} - {M_{a_i}}^{-1}I\Big)A_{a_i}^{-1}B_{a_i}v_{ref} \\ &= e^{J_{a_i}t}\xi_0 + L_0\end{aligned} \tag{3.94}$$

where

$$\begin{aligned}\xi_0 &= \Big(\xi_{10}\ \xi_{20}\ \xi_{30}\ \xi_{60}\ \xi_{70}\Big)^T = \underline{\Psi_a}(t_0) + {M_{a_i}}^{-1}{A_{a_i}}^{-1}B_{a_i}v_{ref} \\ L_0 &= \Big(L_{10}\ L_{20}\ L_{30}\ L_{60}\ L_{70}\Big)^T = -{M_{a_i}}^{-1}I{A_{a_i}}^{-1}B_{a_i}v_{ref}.\end{aligned} \tag{3.95}$$

Using (3.91-3.93), we rewrite $\dot{\psi}_4(t)$ as

$$\dot{\psi}_4(t) = P_{1a_i}M_{a_i}\underline{\Psi}_a(t) + P_{6a_i}M_{a_i}\underline{\Psi}_a(t)P_{3a_i}M_{a_i}\underline{\Psi}_a(t) \tag{3.96}$$

where $P_{1a_i} = \Big(1\,0\,0\,0\,0\,0\Big)$, $P_{3a_i} = \Big(0\,0\,1\,0\,0\,0\Big)$, and $P_{6a_i} = \Big(0\,0\,0\,0\,0\,1\Big)$. Solving (3.96) yields

$$\psi_4(t) = \psi_4(t_0) + \int_{t_0}^{t} g(\tau)d\tau. \tag{3.97}$$

where

$$g(\tau) = P_{1a_i} M_{a_i} \underline{\Psi}_a(\tau) + P_{6a_i} M_{a_i} \underline{\Psi}_a(\tau) P_{3a_i} M_{a_i} \underline{\Psi}_a(\tau). \tag{3.98}$$

Using (3.94) and (3.98), one can show that all of the integral terms in (3.97) except for one term can be determined exactly in matrix form. The exact solution of the latter is found by integrating its individual elements. Once $\psi_4(t)$ is obtained, the solution of $\psi_5(t)$ is obtained in a similar manner. Thus, we have an analytical solution for $\Psi(t)$ in the i^{th} switching cycle. The procedure to obtain the first- and second-order Poincare map using the solution of the closed-loop states $\Psi(t)$ is the same as that described in Section 3.4.

3.6 Results

Figure 3.25 shows the behavior of the open-loop SPBC during startup obtained using the first-order Poincare map described by (3.84). The error signal v_e, which determines the duration of the zero and active states, is predetermined such that at steady state the average of the bus voltage is 245 V. It takes about 4000 iterations to achieve the steady state. Using the analytical map, the entire simulation is completed in about 2 minutes. Using ideal switches, a standard simulator, like Saber, running on the same machine took significantly longer to complete the same simulation.

Next, we investigate the dynamics of the closed-loop SPBC, which operates as a power-factor correction circuit. Using the shooting method, we trace the Floquet multipliers of the second-order map of the SPBC as the voltage-loop controller gain (ω_{iv}) is gradually increased from its nominal value. For stability, all of the Floquet multipliers should be within the unit circle. Figure 3.26 shows the impact of variations in ω_{iv} on the stability of the SPBC. It shows that as ω_{iv} is gradually increased, two of the Floquet multipliers exit the unit circle away from real axis, indicating a Hopf bifurcation. This results in a slow scale instability, which can be predicted using an averaged model of the SPBC (Chandrasekaran, 2000).

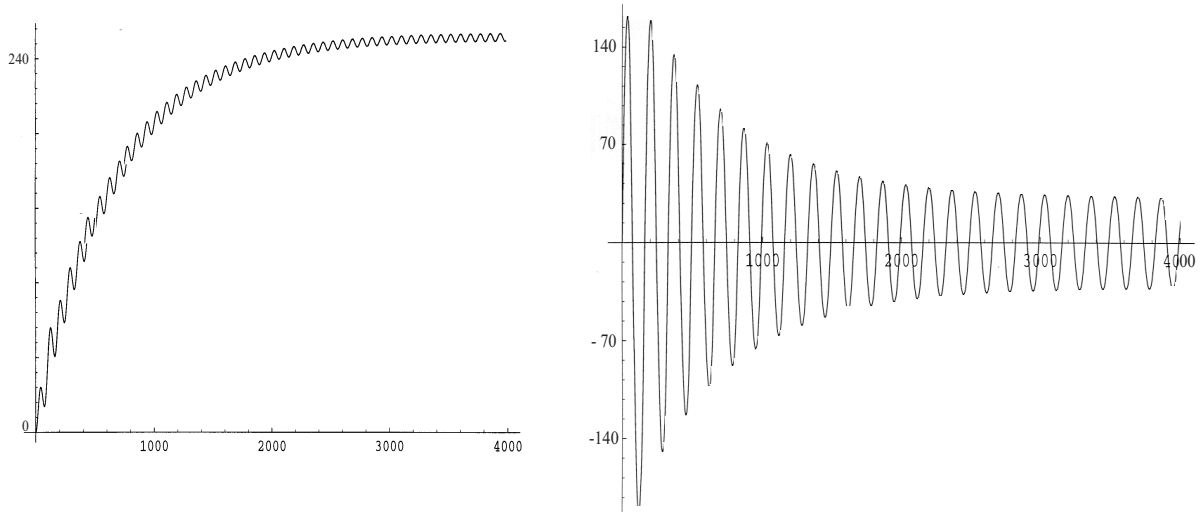

Figure 3.25: Open-loop response of the SPBC: (top) capacitor voltage in volts; (bottom) inductor current in amperes. The horizontal axes for both plots represent the number of switching cycles.

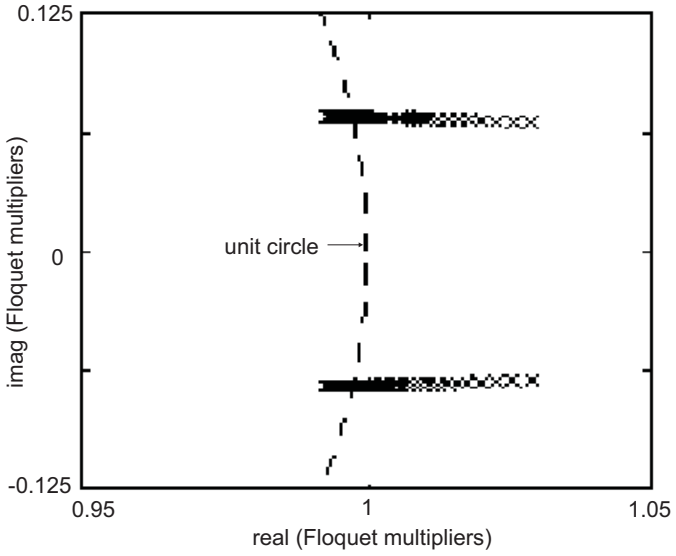

Figure 3.26: As the current-loop controller gain ω_{iv} is gradually increased, two of the Floquet multipliers exit the unit circle as complex conjugates, which indicates a Hopf bifurcation. This leads to an instability on the slow scale.

Figure 3.27a shows the impact of variations in ω_{ii} (dc gain) on the stability of the SPBC. As the controller gain is gradually increased, one of the Floquet multipliers exits the unit circle via -1 indicating a period-doubling bifurcation. The Poincare maps in Figure 3.28 show that as the gain is increased, the system which is initially stable (Figure 3.28a) undergoes a torus breakdown via period-doubling bifurcation (Figure 3.28b), which ultimately leads to chaos (Figure 7d). This type of instability, which occurs on the fast scale can not be predicted by an averaged model of the SPBC. Figure 3.27b confirms this prediction. It shows that, for the same variation in ω_{ii} used to obtain Figure 3.27a, all of the eigenvalues of the linearized averaged model of the SPBC are in the left-half plane; it indicates a stable system (Nayfeh and Balachandran, 1995).

3.7 Summary

We extend the methodology for modeling and stability analysis of a standalone dc-dc converter to an integrated system consisting of a second-order filter and a dc-dc converter. We investigate two such integrated systems: one is stable as per Middlebrook's criterion (Middlebrook, 1976) and the other is unstable. We find that this criterion fails to predict the fast-scale instability for the first design. For the second design, which is unstable on the slow scale, this criterion (which is based on linear analysis) does not give the domain of attraction of the period-one orbits near the bifurcation point. Using a nonlinear analysis (Alfayyoumi et al., 1999), we find that the domain of attraction of the period-one orbits reduces considerably even before the Hopf bifurcation point due to the simultaneous presence of two stable and one unstable solutions.

Next, we investigate the stability of a discontinuous, time-varying boost PFC circuit operating with a multi-loop controller. We treat two separate cases: one for which the switching frequency is infinite and the other for which the switching frequency is finite but large. We show that, even when the frequency is approaching infinity, the existence condition

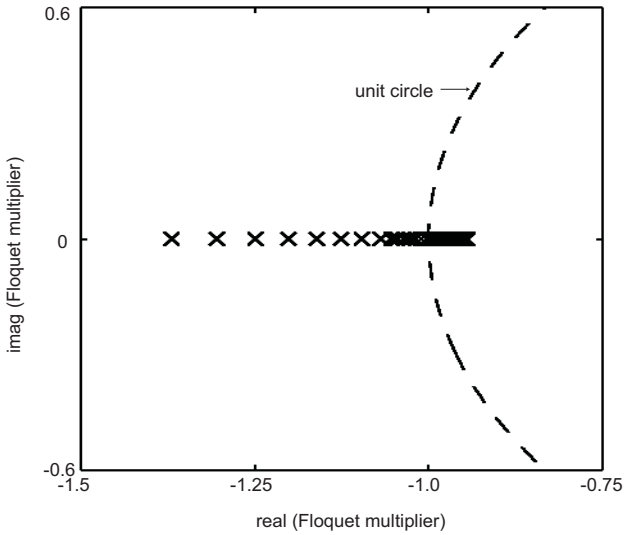

(a)

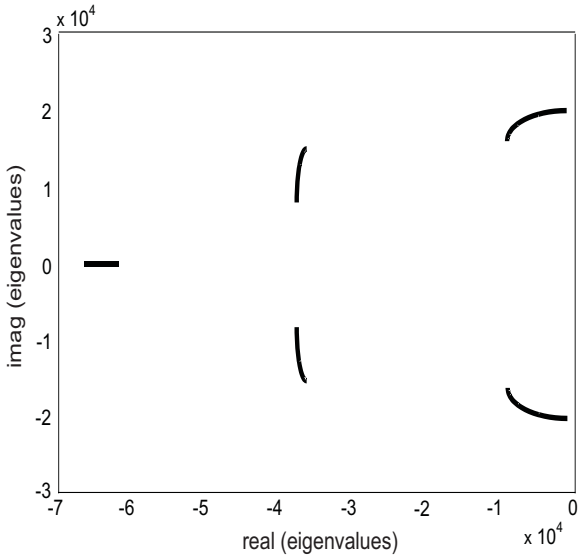

(b)

Figure 3.27: (a) As the current-loop controller gain ω_{ii} is gradually increased, one of the Floquet multipliers of the map exits the unit circle via -1, which indicates a period-doubling bifurcation. This leads to an instability on the fast scale. (b) The eigenvalues of the averaged model show a stable system because the averaged model can not account for the switching-frequency dynamics.

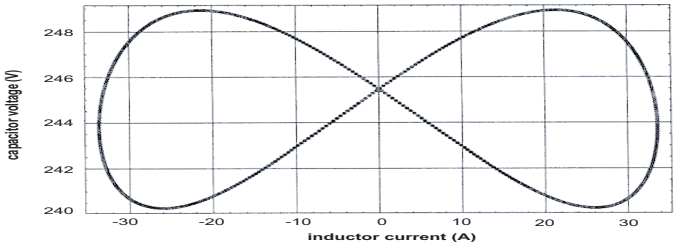

(a)

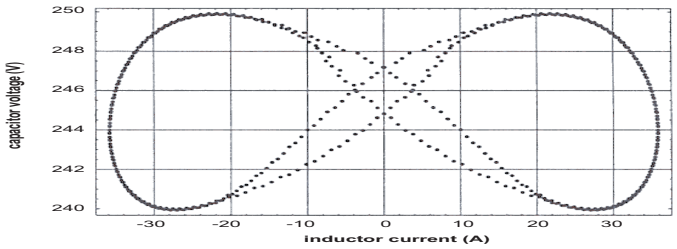

(b)

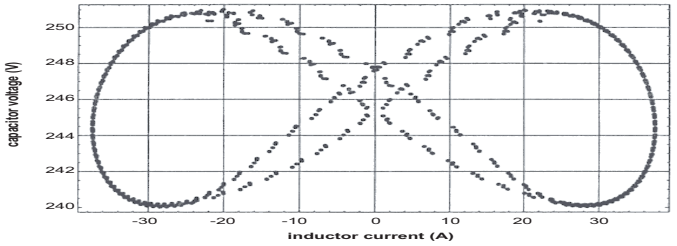

(c)

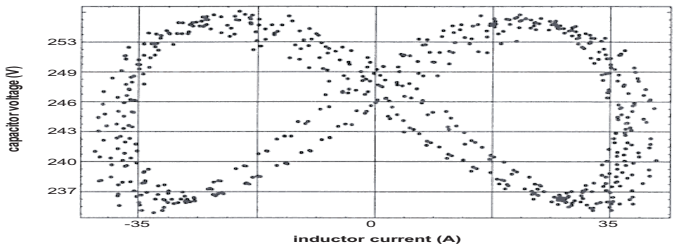

(d)

Figure 3.28: The impact of variations in ω_{ii} on the stability of the bidirectional converter: (a) stable system, (b) a period-doubling bifurcation results in a fast-scale instability, and (c) and (d) increasing value of the bifurcation parameter (ω_{ii}) ultimately leads to chaos.

is violated when $x_1 = 0$.

Having shown that global existence is not possible, we develop conditions for local existence using Lyapunov functions. We show that, for the closed-loop system operating with controller one, the local existence condition (3.47) is satisfied as long as the nonlinear control u_n satisfies (3.48). However, for the boost PFC circuit operating with the second controller, the existence condition (3.55) is difficult to satisfy. The reason behind this difficulty is that, while the desired sliding motion ($\ddot{\psi}_5 = 0$) is second order in nature, the control is based on ψ_5, which along with $\dot{\psi}_5$ are both continuous functions. Although the control effort for this case is lower than that in the previous case, the closed-loop system is more susceptible to fast-scale instabilities when the frequency is not infinite.

For the closed-loop system operating with the second controller, using the local existence conditions and the concept of equivalent control, we show why fast-scale instabilities near the point $x_1 = 0$ may occur earlier for a lower line voltage. We also show that, if the controllers are not properly optimized, then the boost PFC circuit loses stability on a fast scale when $x_1 \to 0$ and also when $|v_{in}(t)|_{max} \to x_2$. When a trajectory leaves a sliding surface, it may or may not stay in the saturated region permanently. We show in (3.57) a condition that ensures the nonexistence of a real equilibrium trajectory in the saturated region under ideal conditions. The design implication of this is that, for the given closed-loop system, the dynamic response (or the bandwidth in a linearized sense) of the voltage loop must be slower than that of the current loop.

For a converter operating with a finite switching frequency, there is a boundary layer around the region of discontinuity. Therefore, we do not have to deal with generalized solutions. Using the second controller (as an example), we show two different approaches for obtaining a solution for the closed-loop system. We find that, within the boundary layer, the dynamics of the nonlinear system evolve on a torus. The toroidal dynamics have two fundamental frequencies: the frequency of $v_{in}(t)$ and the switching frequency. Using a first-order Poincare map, we show how the closed-loop system loses stability on a fast scale in the

neighborhood of $x_1 = 0$ as the controller gain for the current loop increases. Using the slope of x_1, we show that the fast-scale instability results in a doubling of the switching period. The existing averaged models of the boost PFC circuit, most of which are designed to predict the slow-scale dynamics, do not predict these fast-scale instabilities until the subharmonics (in a linearized sense) of the switching frequency affect the slow scale as well.

Apart from the detailed investigation of the filter-converter system and the boost PFC circuit, we also outlined the techniques to extend the nonlinear analysis to multilevel dc-dc and single-phase bidirectional converters. For the multilevel converter, we showed that the procedure to obtain the map, which describes the dynamics of the converter remain similar to that of the standalone dc-dc converter. However, the switching condition for the multilevel converter is a vector and not a scalar equation. Using the map, we formulate an analytic stability condition for the multilevel converter. For the single-phase bidirectional converter, we outlined the procedure to obtain a first-order Poincare map for an open- and closed-loop converter. Using such a map, we showed how the closed-loop converter loses stability when a bifurcation parameter is varied. The result shows how a stable system undergoes torus breakdown and ultimately enters a chaotic state. This kind of instability, which occurs on t he fast scale, can not be predicted by existing averaged models.

Chapter 4

Investigation of the Stability and Dynamics of Parallel DC-DC PWM Converters

Parallel dc-dc converters are widely used in telecommunication power supplies. They operate under closed-loop feedback control to regulate the bus voltage and enable load sharing. These closed-loop converters are inherently nonlinear systems. The major sources of nonlinearities are the switching nonlinearity and converter interaction. So far, however, analyses in this area of power electronics are based primarily on linearized (small-signal) averaged models. When a nonlinear converter has solutions other than the nominal one, small-signal analyses cannot predict the basin of attraction of the nominal solution and the dynamics of the system after the nominal solution loses stability. The dependence of the converter dynamics on the initial conditions is also ignored in small-signal analyses. In addition, averaged models cannot predict the dynamics of a switching converter in a saturated region.

To analyze the stability of these switching systems, one has to deal first with their discontinuity. The concept of stability of the equilibrium solutions of a continuous, smooth system is well-defined (Nayfeh and Balachandran, 1995; Khalil, 1996). However, for discon-

tinuous systems, the definition of solution is itself not straightforward (Aubin and Cellina, 1984; Filippov, 1988; Utkin, 1992). To analyze the stability of an n-dimensional discontinuous system with m switching planes, one has to first define a region of operation, which in general lies at the intersection of these m hyperplanes. The global stability of this region is defined as follows (Filippov, 1988). One has to show first that all of the trajectories approach this region (reaching condition) and that, once on this hypersurface, they cannot leave it (existence condition). If these two conditions are satisfied, then the discontinuous system has a solution surface or a sliding mode. The dynamics of the system on this hypersurface is described by a set of equations, which are smooth and continuous. Finally, one has to show that all of the solutions on this surface tend to a single equilibrium point as $t \rightarrow \infty$.

Analysis of a variable-structure system using an averaged model assumes two things. First, a solution surface exists. In other words, the reaching and existence conditions are satisfied. Second, the control has no delay or the switching frequency is infinite. In reality, the switching frequency is finite, and for many converters, global existence of a solution surface for any controller is not possible.

If the frequency is finite, then we do not have a solution surface but a boundary layer around it (Utkin, 1992). Thus stability in the sense of Filippov (1988) can be applied only if the width of the boundary layer is zero. Under this condition, the dynamics of the system on the solution surface are described accurately by the averaged model. However, when the width of the boundary layer is not zero, we convert the periodic system to a map. Thus, within the boundary layer, we redefine the stability problem from one of analyzing the stability of a periodic orbit to that of analyzing the stability of a fixed point.

In this chapter, we use these basic concepts to investigate the local and global stabilities of nonlinear, nonautonomous parallel dc-dc converters in the unsaturated and saturated regions. Within the unsaturated region, we develop techniques to predict the fast-scale and slow-scale stability boundaries and to determine the type of instability of the nominal orbit. Using these ideas, we investigate the instabilities of two closed-loop buck converters operating

in synchronicity with interleaving. For these two cases, we compare the results obtained using a nonlinear map with those obtained using the averaged model and demonstrate the shortcomings of the latter. We also demonstrate the impact of parametric variations of the parallel converter on its fast-scale and slow-scale instabilities. Finally, we investigate the impact of a strong feedforward disturbance on the stability of two buck converters when they have the same parameters and when they have parametric variation. Using concepts developed in this chapter, we predict the dynamics of the converter in the saturated and unsaturated regions under steady-state and transient conditions.

4.1 Modeling of the Power Stage

We assume that the nonlinearities due to the power devices and parasitics are negligible and that the converter, operating in CCM, is clocked at a rate equal to the switching frequency. Moreover, the controller is designed in such a way that, once a change of state is latched, it can be reset only by the next clock. This effectively eliminates the possibility of multiple pulses within a switching cycle. In Figure 4.1, we show a schematic of a generic basic parallel dc-dc converter with one switch per converter. The total number of converters connected in parallel is N. Each individual module within these multi-topological systems is in the on-state when the switch is closed and in the off-state when it is open. We represent these switching functions by a switching vector $U(t)$. We assume that the phase shift between the carrier waveforms of two successive converters is equal to $\delta = \frac{T}{N}$, which is constant (where T is the switching cycle time). We note that, when $\delta = 0$, the converters are switching in synchronicity. If we represent the states of the open-loop converter (i.e., the inductor currents $i_{L_i}(t)$ and the capacitor voltages $v_{C_i}(t)$) by $X(t)$, then the equations governing a either parallel-boost or a parallel-buck converter can be expressed as

$$\dot{X}(t) = \Phi_1^o\left(X(t), v_{in}(t), U(t)\right), \tag{4.1a}$$

$$v_{dc}(t) = \Phi_2^o\left(X(t), v_{in}(t), U(t)\right), \tag{1b}$$

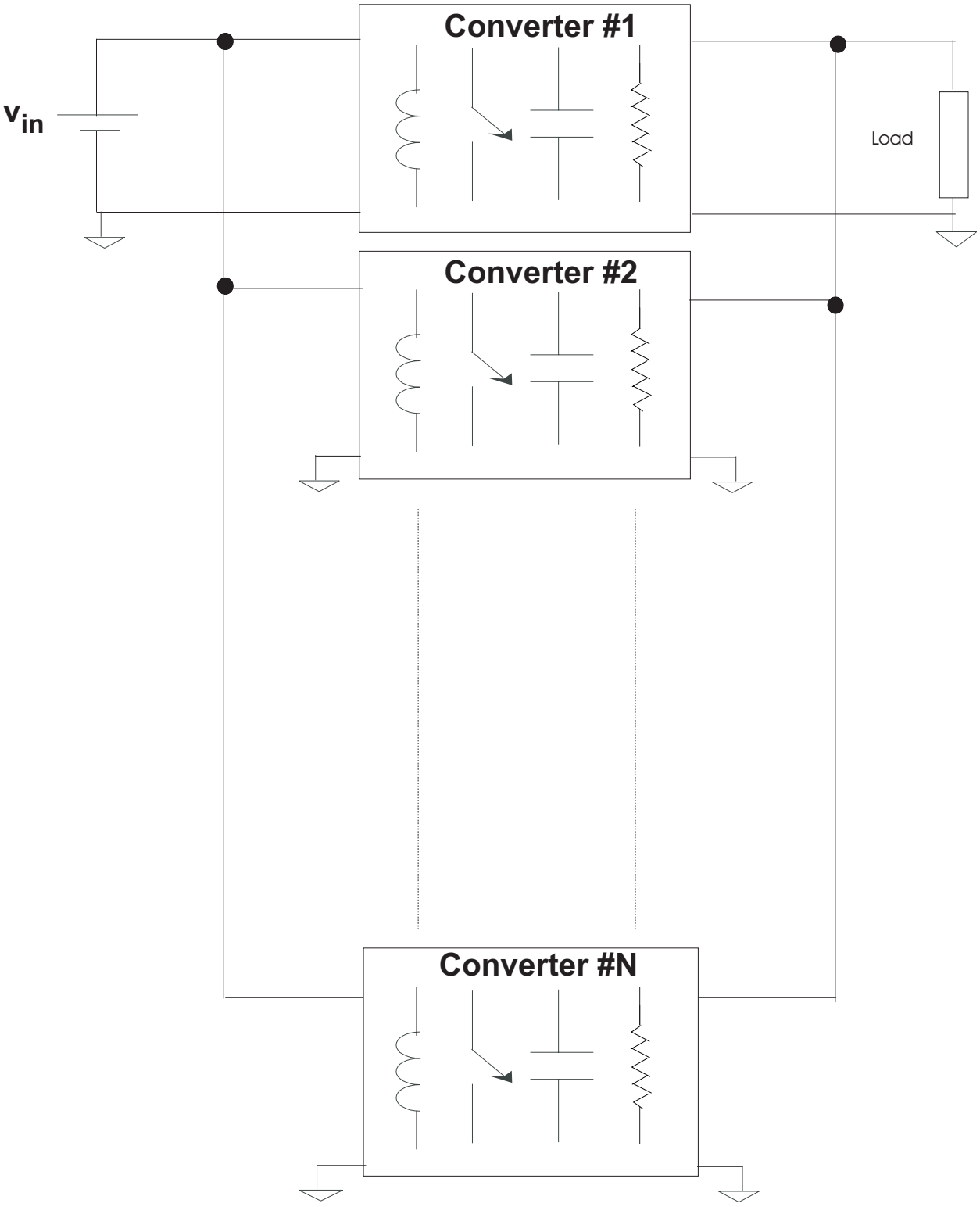

Figure 4.1: Generic configuration of N parallel dc-dc converters operating with a single voltage source and load.

where $v_{in}(t)$ is the forcing input. Equations (4.1) represent a discontinuous and nonautonomous system. The discontinuity is due to $U(t)$. For convenience, we drop the notation of time from now on and rewrite (4.1) as

$$\dot{X} = F^o(X, v_{in}) + G^o(X, v_{in})\,U + W_1^o(X, U)\,, \tag{4.2a}$$

$$v_{dc} = H^o(X) + W_2^o(X, U)\,, \tag{4.2b}$$

where F^o, G^o, and H^o are continuous functions. For some systems (e.g., the parallel-buck converter), W_1^o and W_2^o are continuous because terms containing the esr are not coupled with the switching function. Hence, W_1^o and W_2^o can be lumped with the other terms in equations (4.2a) and (4.2b). However, for other systems like the parallel-boost converter, they are discontinuous. If we neglect the esr, then (4.2) simplifies to

$$\dot{X} = F^o(X, v_{in}) + G^o(X, v_{in})\,U, \tag{4.3a}$$

$$v_{dc} = H^o(X)\,. \tag{4.3b}$$

Equations (4.2) and (4.3) represent generic switching models of parallel-buck and parallel-boost converters when the effect of esr is incorporated and when it is not.

An alternate way to model the variable-structure system represented by (4.2) is to use a map (Deane and Hamill, 1990; Tse, 1994; Alfayyoumi et al., 1999; Mazumder et al., 2000a). Because there are N converters, which are operating in parallel with a phase shift of δ, there are N switchings that occur in each switching cycle (of duration T) of the nominal steady-state system. The state-space equations for the i^{th} sub-switching cycle of duration t_i (as shown in Figure 4.2) are written as

$$\dot{X} = A_i^o X + B_i^o v_{in}, \tag{4.4a}$$

$$v_{dc} = C_i^o X, \tag{4.4b}$$

where

$$\sum_{i=1}^{N} t_i = T, \tag{4.5}$$

and A_i^o, B_i^o, and C_i^o are matrices that describe the open-loop system in the time interval t_i. In each switching subcycle, these matrices can be obtained from (4.2) by substituting an appropriate vector consisting of binary numbers for the switching vector U.

Next we derive an exact solution of the open-loop system by stacking the consecutive solutions of (4.4) over a switching period. The resulting discrete-time difference equation can be written in state-space form as

$$X_{k+1} = f_1^o\left(X_k, t_1, t_2, \cdots, t_{2N}, v_{ink}\right) = \Phi^o\left(t_1, t_2, \cdots, t_{2N}\right) X_k + \Gamma^o\left(t_1, t_2, \cdots, t_{2N}\right) v_{ink}, \tag{4.6a}$$

$$v_{dc_{k+T}} = f_2^o\left(X_k, t_1, t_2, \cdots, t_{2N}, v_{ink}\right) = C_{2N}^o X_{k+T}, \tag{4.6b}$$

where

$$\Phi^o\left(t_1, t_2, \cdots, t_{2N}\right) = \prod_{i=1}^{2N} \Phi_{2N-i+1}^o\left(t_i\right) \text{ and } \Phi_{2N-i+1}^o\left(\tau\right) = e^{A_{2N-i+1}^o \tau}, \tag{4.7a}$$

$$\begin{aligned}\Gamma^o\left(t_1, t_2, \cdots, t_{2N}\right) &= \left(\prod_{i\neq 1}^{2N} \Phi_{2N-i+1}^o\right) \int_0^{t_1} \Phi_1^o\left(\tau\right) B_1^o d\tau + \left(\prod_{i\neq 1,2}^{2N} \Phi_{2N-i+1}^o\right) \int_0^{t_2} \Phi_2^o\left(\tau\right) B_2^o d\tau \\ &\quad + \cdots + \int_0^{t_{2N}} \Phi_{2N}^o\left(\tau\right) B_{2N}^o d\tau,\end{aligned} \tag{4.7b}$$

$$t_j = \delta - t_{j-1} \qquad [\forall j = 2, 4, \cdots, 2N], \quad \text{and} \quad \sum_{i=1}^{N} t_i = T. \tag{4.7c}$$

Using

$$\int_0^t e^{A_i^o \tau} B_i^o d\tau = \left[e^{A_i^o t} - I\right] \left(A_i^o\right)^{-1} B_i^o \tag{4.8}$$

and (4.7), we simplify the expression for X_{k+1} in (4.6) to

$$\begin{aligned} X_{k+1} &= f_1^o\left(X_k, t_1, t_2, \cdots, t_{2N}, v_{ink}\right) \\ &= \prod_{i=1}^{2N} e^{A_i^o t_{2N-i+1}} X_k + \left[\left(\prod_{i\neq 1}^{2N} e^{A_{2N-i+1}^o t_i}\right)\left(e^{A_1^o t_1} - I\right)\left(A_1^o\right)^{-1} B_1^o + \right. \\ &\quad \left(\prod_{i\neq 1,2}^{2N} e^{A_{2N-i+1}^o t_i}\right)\left(e^{A_2^o t_2} - I\right)\left(A_2^o\right)^{-1} B_2^o + \cdots + \\ &\quad \left.\left(e^{A_{2N}^o t_{2N}} - I\right)\left(A_{2N}^o\right)^{-1} B_{2N}^o\right] v_{ink}. \end{aligned} \tag{4.9}$$

Equations (4.6b) and (4.9) describe a map for dc-dc parallel-buck and parallel-boost converter. If we compare the map with the switching model described in (4.2), we see that the map does not have discontinuities due to the switching vector U. This helps in studying the dynamics because the concept of solution for smooth systems is well-defined. Besides, simulations based on this map are much faster because they correlate the states in one switching cycle (of duration T) with those in the next switching cycle. Because the map does not depend on time any more, it describes a reduced-order system. Hence it cannot predict the dynamics of a parallel converter beyond half the switching frequency. However, it can predict the subharmonics accurately.

Another approach to modeling parallel converters is based on state-space averaging (Middlebrook and Cuḱ, 1977; Lee, 1990). In this case, we convert the discontinuous differential system of equations described by (4.2) to a continuous system by replacing the vector representing the switching functions with a smooth and continuous duty-ratio vector. In Section 4.7, we illustrate the derivation of an averaged model with two examples based on a parallel-buck converter operating with two different switching schemes. The general expression for the averaged model is

$$\dot{\overline{X}} = F^o\left(\overline{X}, \overline{v_{in}}\right) + G^o\left(\overline{X}, \overline{v_{in}}\right)\overline{d} + W_{1_{av}}^o\left(\overline{X}, \overline{d}\right), \tag{4.10a}$$

$$\overline{v}_{dc} = H^o\left(\overline{X}\right) + W_{2_{av}}^o\left(\overline{X}, \overline{d}\right), \tag{4.10b}$$

where $W^o_{1_{av}}$ and $W^o_{2_{av}}$ are continuous functions and $\overline{X}$ represents the averaged value of the open-loop states. The symbol $\overline{d}$ is a vector, which denotes the duty ratios of a parallel converter. For some converters (e.g., parallel buck), $W^o_{1_{av}}$ and $W^o_{2_{av}}$ are independent of $\overline{d}$. Hence, they can be lumped with F_0 and H_0. However, for others, like parallel boost converters, they depend on $\overline{d}$. Equation (4.10) describes a system of ordinary-differential equations, which can be used for investigating only slow-scale dynamics.

4.2 Modeling of the Controller

There are more than one scheme for paralleling dc-dc converters, including the master-slave method (Rajagopalan et al., 1996) and the active-current sharing method (Kohama et al., 1994; Thottuvelil and Verghese, 1996). The objectives of all of these schemes, in general, are to regulate the bus voltage and share the load power equally among the converters. The stability techniques we develop in this chapter are generic. However, due to lack of space, we present simulation results for the performance of parallel converters operating with an active-current sharing scheme.

In Figure 4.2, we show a schematic for an active-current sharing control. The symbol I_{av} represents the average of all load currents. To share the load equally among the converters, the error between I_{av} and the load current supplied by each converter is added to the reference voltage v_{ref}. The updated voltage reference is then compared with the bus voltage for each converter. The output of the voltage loop is compared with the inductor current, which is the controller error signal. The controller can be simplified depending on the need and application. If we consider a static-feedback controller, then the expression of the error signal for each converter can be expressed as

$$v_{e_i} = P_{s_i} X + v_{ref}, \tag{4.11}$$

where P_{s_i} is a matrix. If, however, we consider a dynamic-feedback controller, then we obtain

$$v_{e_i} = P_{d_i} X_c, \tag{4.12}$$

where P_{d_i} is a matrix. In (4.12), X_c represents the additional states of the dynamic-feedback controller and is given by

$$\dot{X}_c = A_c X_{aug} + B_c v_{in} + B_r v_{ref}, \tag{4.13}$$

where $X_{aug} = [X\ X_c]^T$, A_c is a matrix, and B_c and B_r are column vectors. Equations (4.11)-(4.13) give the expressions for a multiloop static/dynamic feedback controller. If the multiloop system does not use an inner inductor-current loop then the matrices in equations (4.11)-(4.13) have to be modified.

4.3 Modeling of the Closed-Loop System

For a static-feedback controller, the order of the closed-loop system is the same as the open-loop system. The closed-loop switching model for the parallel converter is given by

$$\dot{\Psi} = F(\Psi, v_{in}, v_{ref}) + G(\Psi, v_{in})\, U + W_1(\Psi, U), \tag{4.14a}$$

$$v_{dc} = H(\Psi) + W_2(\Psi, U), \tag{4.14b}$$

where F, G, and H are continuous functions and v_{ref} is the reference voltage for the bus. The functions W_1 and W_2 are continuous for the parallel-buck converter and discontinuous for the parallel-boost converter. For a static-feedback controller, $\Psi = X$. But for a dynamic-feedback controller $\Psi = X_{aug}$. The individual components of the switching vector U are given by

$$u_i = \Omega_i\left(v_{e_i} - v_{ramp_i}(t, \delta)\right), \tag{4.15}$$

where

$$v_{ramp_i}(t,\delta) = v_{m_i} * \bmod (t + (i-1)\delta, T) * f \qquad [\forall i = 1, \ldots, N, \quad f = \tfrac{1}{T}]. \tag{4.16}$$

Equation (4.16) describes the equations for carrier waveforms with amplitudes v_{m_i}. Each of these ramp waveforms has a period of T. Between the two carrier waveforms, there is a phase shift δ. It follows from (4.15) that the u_i are functions of the states of the closed-loop converter. Hence the closed-loop switching model in (4.14) represents a nonlinear nonautonomous discontinuous system.

Next, we derive a nonlinear map based on (4.14). The state-space equation for the i^{th} sub-switching cycle (of duration t_i) is written as

$$\dot{\Psi} = A_i \Psi + B_i v_{in} + B_{r_i} v_{ref}, \tag{4.17a}$$

$$v_{dc} = C_i \Psi, \tag{4.17b}$$

where

$$\sum_{i=1}^{N} t_i = T, \tag{4.18}$$

and A_i, B_i, B_{r_i}, and C_i are matrices that describe the closed-loop system in each subcycle. In each switching subcycle, these matrices can be obtained from (4.14) by substituting an appropriate vector consisting of binary numbers for the switching vector U. Next, we derive an exact solution of the closed-loop system by stacking the consecutive solutions of (4.17) over a switching period. The resulting discrete-time difference equation can be written in state-space form as

$$\begin{aligned}
\Psi_{k+1} &= f_1\left(\Psi_k, t_1, t_2, \cdots, t_{2N}, v_{in_k}\right) \\
&= \prod_{i=1}^{2N} e^{A_i t_{2N-i+1}} \Psi_k + \left[\left(\prod_{i \neq 1}^{2N} e^{A_{2N-i+1} t_i} \right) \left(e^{A_1 t_1} - I \right) A_1^{-1} B_1 + \right.
\end{aligned}$$

$$\left(\prod_{i\neq 1,2}^{2N} e^{A_{2N-i+1}t_i}\right)\left(e^{A_2t_2}-I\right)A_2^{-1}B_2+\cdots+\left(e^{A_{2N}t_{2N}}-I\right)A_{2N}^{-1}B_{2N}\Bigg]v_{ink}+$$
$$\Bigg[\left(\prod_{i\neq 1}^{2N} e^{A_{2N-i+1}t_i}\right)\left(e^{A_1t_1}-I\right)A_1^{-1}B_{r_1}+$$
$$\left(\prod_{i\neq 1,2}^{2N} e^{A_{2N-i+1}t_i}\right)\left(e^{A_2t_2}-I\right)A_2^{-1}B_{r_2}+\cdots+$$
$$\left(e^{A_{2N}t_{2N}}-I\right)A_{2N}^{-1}B_{r_{2N}}\Bigg]v_{ref}, \tag{4.19a}$$

$$v_{dc_{k+1}}=f_2\left(\Psi_k,t_1,t_2,\cdots,t_{2N},v_{ink},v_{ref}\right)=C_{2N}\Psi_{k+T}, \tag{4.19b}$$

$$\sigma\left(\Psi_k,t_1,t_2,\cdots,t_{2N},v_{ink},v_{ref}\right)=0,\quad \text{and} \tag{4.19c}$$

$$t_j=\delta-t_{j-1}\qquad[\forall j=2,4,\cdots,2N]. \tag{4.19d}$$

In (4.19c), σ is a vector of dimension $N\times 1$, which represents the auxiliary switching conditions for all of the converters. For example, the switching condition for the converter that switches first is given by

$$\sigma_1\left(\Psi_k,t_1,v_{ink},v_{ref}\right)=\varphi\left[e^{A_1t_1}\Psi_k+\left(e^{A_1t_1}-I\right)A_1^{-1}\left(B_1v_{ink}+B_{r1}v_{ref}\right)\right]-v_{ramp_1}t_1=0, \tag{4.20}$$

where the vector φ^T represents the controller. Using (4.19d), we reduce the dimension of σ to N.

Finally, we obtain an averaged model for the closed-loop system. Using the same methodology used to develop the averaged model for the open-loop converter, we find that the closed-loop averaged model for the parallel converter is given by the following expressions:

$$\dot{\overline{\Psi}}=F\left(\overline{\Psi},\overline{v_{in}},v_{ref}\right)+G\left(\overline{\Psi},\overline{v_{in}}\right)\overline{d}+W_{1_{av}}\left(\overline{\Psi},\overline{d}\right), \tag{4.21a}$$

$$\overline{v}_{dc}=H\left(\overline{\Psi}\right)+W_{2_{av}}\left(\overline{\Psi},\overline{d}\right), \tag{4.21b}$$

$$\overline{d_i} = \frac{1}{v_{ramp_i}} \overline{v_{e_i}} = P_i \overline{\Psi}, \tag{4.21c}$$

where $W_{1_{av}}$ and $W_{2_{av}}$ are continuous functions, P_i represents a matrix, $\overline{\Psi}$ represents the averaged value of the closed-loop states, and $\overline{d}$ is a vector representing the duty ratios of the converters operating in parallel. The individual components of this vector $\overline{d}$ are given by (4.21c). Equation (4.21a) represents a nonlinear averaged model. It can be used for studying the slow-scale instability. If the esrs of the output capacitors is neglected, the averaged model cannot distinguish between the dynamics of interleaved and synchronized converters. Moreover, the averaged model cannot be used to study the impact of saturation.

4.4 Analysis

In this section, we show how to analyze the local and global stability of the dynamics of a parallel dc-dc converter operating in the unsaturated and saturated regions. The parallel converters, shown in Figure 4.1, operate with a finite switching frequency. The dynamics of these discontinuous nonlinear nonautonomous systems evolve on fast and slow scales. The stability analysis of these discontinuous systems is difficult because the definition of a solution is not clearly defined.

Filippov (1988) and Aubin and Cellina (1984) proposed differential inclusion to find solutions of such discontinuous systems with a multivalued right-hand side. The resulting solution of this set-valued map describes a solution of the slow dynamics (Aubin and Cellina, 1984). The averaged model in equations (4.21) approximately describes the slow dynamics for two reasons. First, the switching frequencies of the systems are finite. Hence, they do not have a discontinuous surface but a boundary layer around the discontinuity. The averaged model in equations (4.21) is based on the assumption of an infinite frequency and hence the width of the boundary layer is zero. Second, because switching of the converters in Figures 3.1 and 3.2 is based on a comparison of an error signal with a ramp rather than a hysteresis, the equivalent control approach proposed by Filippov (which forms the basis for

equations (4.21)) is not always directly applicable (Utkin, 1992). However, an analysis using an averaged model is straightforward because it is continuous and smooth. We deal with the stability based on an averaged model later in this section.

An alternate way to analyze the stability of these variable-structure systems is to use the nonlinear map in equations (4.19). We describe the evolution of the discontinuous system as a sequence. Besides, we eliminate the discontinuity due to switching by predicting the states at the beginning of the next switching cycle based on the information available at the end of the current switching cycle. Using these maps, we convert the problem of finding the stability of a nominal orbit (period-one orbit) to that of finding the stability of a fixed point.

Another way to investigate the stability of the nominal solution of equations (4.14) is numerical computation. We transform equations (4.14) to the following form:

$$\Psi_{k+1} = M_1 \left(\Psi_k, \underline{t}_k, \underline{t}_{k+1}, v_{ink}, v_{ref} \right). \tag{4.22}$$

By choosing a relatively small time step $(\underline{t}_{k+1} - \underline{t}_k)$, one can obtain a fairly accurate solution. In (4.22), the scalar $\underline{t}$ represents the actual time and not the instant of switching. How small the time step has to be depends on how fast the open-loop and closed-loop states evolve. The degree of accuracy depends not only on the time step but also on the type of numerical algorithm (Parker and Chua, 1989). We found that use of a combination of implicit and explicit numerical techniques gives the best results. The rationale behind obtaining the solution of a discontinuous system using numerical integration is provided by the Lebesgue measure theory (Royden, 1988). There are two primary reasons why it is applicable here. First, the total number of switchings in one switching cycle is finite because multiple pulsing cannot occur. Second, at each of these switching instants, the right- and left-hand limits of each of the states of the converters are equal. This is because we are considering hard-switched converters. Thus, at the points of discontinuity, we do not have any jump in the states. Based on these two pieces of information and on whether the sampling time for numerical integration is much smaller than the evolution time of the dynamics of the

system, the Lebesgue theory tells us that we can consider the points of discontinuities (due to switchings) to have zero measure (Royden, 1988; Filippov, 1988). In other words, though the system is undefined at the points of switching, we can carry out the integration and the resulting solution is valid almost everywhere.

4.4.1 Stability Analysis Using the Switching Model

We use a combination of a shooting technique and a Newton-Raphson procedure to calculate the periodic orbits and determine their stability. To accomplish this, we convert the initial-value problem in (4.14) to a two-point boundary-value problem. Let the dimension of Ψ be $n \times 1$. We seek an initial condition $\gamma = \Psi(0)$ such that the minimal solution $\Psi(t, \gamma)$ of (4.14) satisfies the condition

$$\Psi(T, \gamma) = \gamma = \Psi(0). \tag{4.23}$$

In other words, the trajectory that runs from $\gamma = \Psi(0)$ to the same location over a time period of T represents the desired periodic solution.

We start with a guess γ_0 and seek a $\delta\gamma$ such that

$$\Psi\left(T, \gamma_0 + \delta\gamma\right) - \left(\gamma_0 + \delta\gamma\right) \approx 0. \tag{4.24}$$

Expanding (4.24) in a Taylor series and keeping only the linear terms in $\delta\gamma$, we obtain

$$\left[\partial\Psi_\gamma\left(T, \gamma_0\right) - I\right]\delta\gamma = \gamma_0 - \Psi\left(T, \gamma_0\right)). \tag{4.25}$$

In (4.25), $\partial\Psi_\gamma\left(T, \gamma_0\right)$ represents the derivatives of Ψ with respect to γ evaluated at (T, γ_0). The dimension of the matrix $\partial\Psi_\gamma\left(T_0, \gamma_0\right)$ is $n \times n$. The individual components of this matrix are given by

$$\partial\Psi_{\gamma_i}\left(T, \gamma_0\right) = \lim_{h \to 0} \frac{\Psi^i(T, \gamma_0 + h\gamma_{0_i}) - \Psi(T, \gamma_0)}{h}. \tag{4.26}$$

Once $\partial\Psi_\gamma\left(T,\gamma_0\right)$ is known, we solve the system of n linear algebraic equations (4.25) for $\delta\gamma$. Then, we use $\delta\gamma$ to update the initial guess γ_0 and repeat the process until $\delta\gamma$ is within a tolerance level. Finally, the stability of the calculated periodic solution is ascertained from the eigenvalues of the monodromy matrix $\partial\Psi_\gamma$ evaluated at (T,γ_0). For the periodic solution to be asymptotically stable, every eigenvalue but one must be inside the unit circle in the complex plane.

4.4.2 Stability Analysis Using the Discrete Model

Let us assume that the closed-loop system described by equations (4.19) is operating in steady state. The fixed points of Ψ_k in (4.19a) correspond to period-one orbits of the closed-loop converter. They are obtained using the constraint $\Psi_{k+1}=\Psi_k=\Psi_s$. Letting $V_{in}=v_{ink}, t_1=t_{1_s}, t_2=t_{2_s},\cdots,t_{2N}=t_{2N_s}$, we find that the fixed points of (4.19a) are given by

$$\begin{aligned}
\Psi_s \;=\; & \left(I-\prod_{i=1}^{2N}e^{A_{2N-i+1}t_{i_s}}\right)^{-1}\left[\left(\prod_{i\neq 1}^{2N}e^{A_{2N-i+1}t_{i_s}}\right)\left(e^{A_1t_{1_s}}-I\right)A_1^{-1}B_1+\right.\\
& \left(\prod_{i\neq 1,2}^{2N}e^{A_{2N-i+1}t_{i_s}}\right)\left(e^{A_2t_{2_s}}-I\right)A_2^{-1}B_2+\cdots+\left.\left(e^{A_{2N}t_{2N_s}}-I\right)A_{2N}^{-1}B_{2N}\right]V_{in}+\\
& \left(I-\prod_{i=1}^{2N}e^{A_{2N-i+1}t_{i_s}}\right)^{-1}\left[\left(\prod_{i\neq 1}^{2N}e^{A_{2N-i+1}t_{i_s}}\right)\left(e^{A_1t_{1_s}}-I\right)A_1^{-1}B_{r_1}+\right.\\
& \left(\prod_{i\neq 1,2}^{2N}e^{A_{2N-i+1}t_{i_s}}\right)\left(e^{A_2t_{2_s}}-I\right)A_2^{-1}B_{r_2}+\cdots+\\
& \left.\left(e^{A_{2N}t_{2N_s}}-I\right)A_{2N}^{-1}B_{r_{2N}}\right]v_{ref}. \qquad (4.27)
\end{aligned}$$

Substituting (4.27) into (4.19c), we obtain

$$\sigma\left(\Psi_s,t_{1_s},t_{2_s},\cdots,t_{2N_s},V_{in},v_{ref}\right)=0. \qquad (4.28)$$

We solve equations (4.27) and (4.28) for the N unknowns Ψ and the t_{i_s}. One way to solve for the unknowns is to substitute for Ψ_s from (4.27) into (4.28) and solve for the t_{i_s}. Once the t_{i_s} are calculated, we solve for Ψ_s. This is difficult for higher-order systems because most of the mathematical packages, such as Matlab and Mathematica, cannot symbolically compute exponents of very large matrices. Besides, the computation of $\left(I - \prod_{i=1}^{2N} e^{A_{2N-i+1}t_{i_s}}\right)$ in (4.27) using these packages is inaccurate. Alternately, we use a Newton-Raphson method. We start with an initial guess Ψ^g and t_i^g for the steady-state values of Ψ_s and t_{i_s}. This guess is obtained using either simulation or the method of steepest decent (Dennis and Schnabel, 1983). Keeping the v_{ink} constant, we rewrite equations (4.19a) and (4.19c) as

$$\Psi^g + \delta\Psi^g = f_1\left(\Psi^g + \delta\Psi^g, t_1^g + \delta t_1^g, t_2^g + \delta t_2^g, \cdots, t_{2N}^g + \delta t_{2N}^g\right) \tag{4.29}$$

$$0 = \sigma\left(\Psi^g + \delta\Psi^g, t_1^g + \delta t_1^g, t_2^g + \delta t_2^g, \cdots, t_{2N}^g + \delta t_{2N}^g\right). \tag{4.30}$$

Expanding equations (4.29) and (4.30) in Taylor series, we obtain

$$\Psi^g + \delta\Psi^g = f_1\left(\Psi^g, t^g\right) + \frac{\partial f_1}{\partial \Psi^g}\delta\Psi^g + \frac{\partial f_1}{\partial t^g}\delta t^g \tag{4.31}$$

$$0 = \sigma\left(\Psi^g, t^g\right) + \frac{\partial \sigma}{\partial \Psi^g}\delta\Psi^g + \frac{\partial \sigma}{\partial t^g}\delta t^g, \tag{4.32}$$

where t^g is a vector representing $t_1^g, t_2^g, \cdots, t_{2N}^g$. We rewrite equations (4.31) and (4.32) as

$$\begin{pmatrix} \frac{\partial f_1}{\partial \Psi^g} - I & \frac{\partial f_1}{\partial t^g} \\ \frac{\partial \sigma}{\partial \Psi^g} & \frac{\partial \sigma}{\partial t^g} \end{pmatrix} \begin{pmatrix} \delta\Psi^g \\ \delta t^g \end{pmatrix} = J \begin{pmatrix} \delta\Psi^g \\ \delta t^g \end{pmatrix} = \begin{pmatrix} \Psi^g - f_1 \\ -\sigma \end{pmatrix}. \tag{4.33}$$

Here, (4.33) represents a set of linear algebraic equations, which are solved for $\delta\Psi^g$ and δt^g by using the LU decomposition method (Salon, 1993). To this end, we express J as $\underline{L}\,\underline{U}$, where the matrices $\underline{L}$ and $\underline{U}$ represent the lower and upper triangular matrices of J. Then, we rewrite (4.33) as

$$J \begin{pmatrix} \delta\Psi^g \\ \delta t^g \end{pmatrix} = \underline{L}\,\underline{U} \begin{pmatrix} \delta\Psi^g \\ \delta t^g \end{pmatrix} = \begin{pmatrix} \Psi^g - f_1 \\ -\sigma \end{pmatrix}. \tag{4.34}$$

Multiplying (4.34) from the left with L^{-1}, we have

$$\underline{U}\begin{pmatrix} \delta\Psi^g \\ \delta t^g \end{pmatrix} = Z = \underline{L}^{-1}\begin{pmatrix} \Psi^g - f_1 \\ -\sigma \end{pmatrix}, \tag{4.35}$$

which can be solved for the new set of variables Z. Then $\begin{bmatrix}\delta\Psi^g & \delta t^g\end{bmatrix}^T$ are calculated without inverting the matrix $\underline{U}$.

We found that, unlike the matrix J^{-1}, the matrix $\underline{L}^{-1}$ can always be computed correctly by either Matlab or Mathematica. If, however, this is not the case, then one can use more advanced algorithms, such as the conjugate gradient method (Salon, 1993) and globally convergent homotopy algorithms (Watson, 1990). However, homotopy algorithms have the disadvantage of giving both the real-valued as well as the complex-valued solutions.

To ascertain the stability of a given fixed point, we perturb the nominal values as

$$\Psi = \Psi_s + \delta\Psi, \quad t_s = t_s + \delta t, \quad v_{in} = u_s + \delta v_{in} \quad v_{dc} = v_{dc_s} + \delta v_{dc}. \tag{4.36}$$

Substituting (4.36) into equations (4.19a) and (4.19c), expanding the results in Taylor series, and keeping first-order terms, we obtain

$$\delta\Psi_{k+1} = \frac{\partial f_1}{\partial\Psi}\delta\Psi + \frac{\partial f_1}{\partial t}\delta t + \frac{\partial f_1}{\partial v_{in}}\delta v_{in}, \tag{4.37a}$$

$$\frac{\delta\sigma}{\partial\Psi}\delta\Psi + \frac{\partial\sigma}{\partial t}\delta t + \frac{\partial\sigma}{\partial v_{in}}\delta v_{in} = 0. \tag{4.37b}$$

It follows from (4.37b) that

$$\delta t = -\left[\frac{\partial\sigma}{\partial t}\right]^{-1}\left[\frac{\partial\sigma}{\partial\Psi}\delta\Psi + \frac{\partial\sigma}{\partial v_{in}}\delta v_{in}\right]. \tag{4.38}$$

Substituting (4.38) into (4.37a) yields

$$\delta\Psi_{k+1} = H_1\delta\Psi + H_2\delta v_{in}, \tag{4.39}$$

where

$$H_1 = \frac{\partial f_1}{\partial \Psi} - \left[\frac{\partial \sigma}{\partial t}\right]^{-1} \frac{\partial \sigma}{\partial \Psi}, \tag{4.40a}$$

$$H_2 = \frac{\partial f_1}{\partial v_{in}} - \left[\frac{\partial \sigma}{\partial t}\right]^{-1} \frac{\partial \sigma}{\partial v_{in}}. \tag{4.40b}$$

The stability of a given fixed point can be ascertained by the eigenvalues (Floquet multipliers) of H_1 (Nayfeh and Balachandran, 1995). For asymptotic stability, all of the Floquet multipliers must be within the unit circle.

To determine the region of attraction of the nominal solution, we need to select a Lyapunov function $V(.)$ for the nonlinear system in (4.19a) and a class K function $\alpha(.)$. If there is a ball $B(\tilde{\Psi}^*)$ with radius r centered at $\tilde{\Psi}^*$ such that for all $\tilde{\Psi}_k \, \epsilon \, B(\tilde{\Psi}^*)$, then the stability of the nominal solution of (4.19a) is guaranteed if (Brogliato, 1996)

$$V(\tilde{\Psi}_k) \geq \alpha \left(\parallel \tilde{\Psi}_k - \tilde{\Psi}^* \parallel \right), \tag{4.40a}$$

$$V(\tilde{\Psi}_{k+1}) - V(\tilde{\Psi}_k) \leq 0, \quad \text{and} \tag{4.41b}$$

$$V(\tilde{\Psi}^*) = 0, \tag{4.41c}$$

where $\tilde{\Psi}_k = \Psi_k - \Psi_s$.

If one of the Floquet multipliers exits the unit circle through +1, then either a cyclic-fold, symmetry-breaking, or a transcritical bifurcation occurs. If a Floquet multiplier exists the unit circle through -1, a period-doubling or flip bifurcation occurs. If, however, two of the Floquet multipliers exit the unit circle as complex conjugates, a secondary Hopf bifurcation occurs. To find out whether the bifurcation is subcritical or supercritical in nature, we calculate the normal form of the nonlinear system in the neighborhood of the bifurcation. Alternately, we can use numerical simulation.

Next, we describe briefly the procedure to determine the normal form of the map near the bifurcation. For a given bifurcation parameter (e.g., input voltage), let the nonlinear map describing the dynamics of the closed-loop converter be

$$\Psi_{k+1} = f_1\left(\Psi_k, t_k\right) = f_1\left(\Psi_k, \Phi(\Psi_k)\right) \tag{4.42a}$$

$$0 = \sigma\left(\Psi_k, t_k\right) = \sigma\left(\Psi_k, \Phi(\Psi_k)\right), \tag{4.42b}$$

where t_k is a vector representing $t_{1_k}, t_{2_k}, ..., t_{2N_k}$. Equation (4.42b) is solved for $\Phi(U)$. Expanding (4.42a) about its nominal point using Taylor series and keeping terms up to third-order, we obtain

$$\begin{aligned}
\hat{\Psi}_{k+1} \;=\; & \left(\frac{\partial f_1}{\partial \Psi} + \frac{\partial f_1}{\partial \Phi}\frac{d\Phi}{d\Psi}\right)\hat{\Psi}_k + \\
& \frac{1}{2}\left(\frac{\partial^2 f_1}{\partial \Psi^2} + \frac{\partial^2 f_1}{\partial \Phi \partial \Psi}\frac{d\Phi}{d\Psi} + \frac{\partial^2 f_1}{\partial \Psi \partial \Phi}\frac{d\Phi}{d\Psi} + \frac{\partial^2 f_1}{\partial \Phi^2}\left(\frac{d\Phi}{d\Psi}\right)^2 + \frac{\partial f_1}{\partial \Phi}\frac{d^2\Phi}{d\Psi^2}\right)\hat{\Psi}_k^2 + \\
& \frac{1}{6}\left(\frac{\partial^3 f_1}{\partial \Psi^3} + \frac{\partial^3 f_1}{\partial \Phi \partial \Psi^2}\frac{d\Phi}{d\Psi}\right)\hat{\Psi}_k^3 + \frac{1}{6}\left(\frac{\partial^2 f_1}{\partial \Phi \partial \Psi} + \frac{\partial^2 f_1}{\partial \Psi \partial \Phi}\right)\left(\frac{d^2\Phi}{d\Psi^2}\right)\hat{\Psi}_k^3 \\
& \frac{1}{6}\left(\frac{\partial^3 f_1}{\partial \Psi \partial \Phi \partial \Psi} + \frac{\partial^3 f_1}{\partial \Phi^2 \partial \Psi}\frac{d\Phi}{d\Psi} + \frac{\partial^3 f_1}{\partial \Psi^2 \partial \Phi} + \frac{\partial^3 f_1}{\partial \Phi \partial \Psi \partial \Phi}\frac{d\Phi}{d\Psi}\right)\left(\frac{d\Phi}{d\Psi}\right)\hat{\Psi}_k^3 \\
& \frac{1}{6}\left(\frac{\partial^3 f_1}{\partial \Psi \partial \Phi^2}\left(\frac{d\Phi}{d\Psi}\right)^2 + \frac{\partial^3 f_1}{\partial \Phi^3}\left(\frac{d\Phi}{d\Psi}\right)^3 + 2\frac{\partial^2 f_1}{\partial \Phi^2}\left(\frac{d\Phi}{d\Psi}\right)\left(\frac{d^2\Phi}{d\Psi^2}\right)\right)\hat{\Psi}_k^3 \\
& \frac{1}{6}\left(\frac{\partial^2 f_1}{\partial \Psi \partial \Phi}\frac{d^2\Phi}{d\Psi^2} + \frac{\partial^2 f_1}{\partial \Phi^2}\frac{d\Phi}{d\Psi}\frac{d^2\Phi}{d\Psi^2} + \frac{\partial f_1}{\partial \Phi}\frac{d^3\Phi}{d\Psi^3}\right)\hat{\Psi}_k^3,
\end{aligned} \tag{4.43}$$

where Φ and its derivatives are calculated from (4.42b). Next, we let $\Psi = W\xi$ (where W is a matrix whose column vectors are the eigenvectors of the linear term on the right-hand side of (4.43)) in (4.43) and obtain

$$\xi_{k+1} = J\xi_k + F_2(\xi_k) + F_3(\xi_k) + O(|\xi_k|^4), \tag{4.44}$$

where $F_2(\xi_k)$ and $F_3(\xi_k)$ represent the second-order and third-order nonlinear terms in ξ_k.

To determine the normal form of the map near a bifurcation resulting from a Floquet multiplier existing the unit circle either through +1 or -1, we arrange the eigenvectors in W so that the eigenvector corresponding to this multiplier is the first. Hence, (4.44) can be rewritten as

$$\xi_{k+1}^{1} = \alpha\xi_{k}^{1} + F_{2}^{1}\left(\xi_{k}\right) + F_{3}^{1}\left(\xi_{k}\right) \tag{4.45}$$

$$\hat{\xi}_{k+1} = \hat{J}\hat{\xi}_{k} + \hat{F}_{2}\left(\xi_{k}\right) + \hat{F}_{3}\left(\xi_{k}\right), \tag{4.46}$$

where $\alpha = \pm 1$ and the vectors with the hat exclude the first elements. To calculate the center manifold, we let $\hat{\xi} = h\left(\xi^{1}\right)$, where h is a quadratic function vector of ξ_{k}^{1} in (4.46) and obtain

$$h\left(\xi_{k+1}^{1}\right) = \hat{J}h\left(\xi_{k}^{1}\right) + \hat{F}_{2}\left(\xi_{k}^{1}, h\left(\xi_{k}^{1}\right)\right) + \hat{F}_{3}\left(\xi_{k}^{1}, h\left(\xi_{k}^{1}\right)\right). \tag{4.47}$$

Substituting (4.45) into (4.47) yields the functional

$$h\left(\alpha\xi_{k}^{1}\right) = \hat{J}h\left(\xi_{k}^{1}\right) + \hat{F}_{2}\left(\xi_{k}^{2}\right) + \cdots \tag{4.48}$$

which can be solved for $h\left(\xi^{1}\right)$. Substituting for $h\left(\xi^{1}\right)$ in (4.45) yields the normal form

$$\xi_{k+1}^{1} = \alpha\xi_{k}^{1} + F_{2}^{1}\left(\xi_{k}^{1}, h\left(\xi_{k}^{1}\right)\right) + F_{3}^{1}\left(\xi_{k}^{1}\right). \tag{4.49}$$

A similar procedure can be used to calculate the normal form in case two complex conjugate multipliers exist the unit circle.

4.4.3 Stability Analysis using the Averaged Model

The averaged model represents a continuous differential system, which is derived under the assumption of an infinite switching frequency. The closed-loop parallel converter described in (4.21a) may have more than one stable equilibrium solution. Therefore, in step

one of our analysis, we determine the equilibrium solutions of (4.21a) by setting $\dot{\bar{\Psi}} = 0$. The result is

$$F\left(\overline{\Psi}, \overline{v_{in}}, v_{ref}\right) + G\left(\overline{\Psi}, \overline{v_{in}}\right)\overline{d} + W_{1_{av}}\left(\overline{\Psi}, \overline{d}\right) = 0. \tag{4.50}$$

Substituting for the $\overline{d}_i$ from (4.21c) into (4.50) yields a nonlinear system of algebraic equations for the $\bar{\Psi}$. If there is only one equilibrium solution, which equals the nominal solution of the converter, then, based on the averaged model, we have a globally stable solution (in the unsaturated region). If there are more than one equilibrium solution, then we need to determine the stability of the nominal solution. This is achieved by first linearizing the nonlinear system in the neighborhood of an equilibrium solution and then computing the eigenvalues of the Jacobian matrix. For stability, none of the eigenvalues of the Jacobian matrix should have a positive real part.

It follows from equations (4.11)-(4.13) that, if the feedback controller is static, the dimension of the closed-loop system, described by (4.21c), is the same as that of the open-loop system, which is given by (4.10a). However, in the case of a dynamic-feedback controller, the dimension of (4.21c) could be much higher than that of (4.10a). In this case, we can compute the equilibrium solutions in an easier way. For example, let us assume that we have a multiloop feedback system with an outer load-current loop and an inner-voltage loop. Depending on the type of converter and the performance requirements, we can also choose an inner inductor-current loop, which receives its reference from the voltage loop. Let the vectors $\overline{X}_{c_I}$, $\overline{X}_{c_v}$, and $\overline{X}_{c_i}$ represent the states corresponding to the load-current loop, the inner-voltage loop, and the inner inductor-current loop, respectively. Rewriting (4.13), we obtain

$$\begin{pmatrix} \dot{\overline{X}}_{c_I} \\ \dot{\overline{X}}_{c_v} \\ \dot{\overline{X}}_{c_i} \end{pmatrix} = \begin{pmatrix} A_{I_P} & A_{I_I} & 0 & 0 \\ A_{v_P} & A_{v_I} & A_{v_v} & 0 \\ A_{i_P} & A_{i_I} & A_{i_v} & A_{i_i} \end{pmatrix} \begin{pmatrix} \overline{X} \\ \overline{X}_{c_I} \\ \overline{X}_{c_v} \\ \overline{X}_{c_i} \end{pmatrix} + \begin{pmatrix} B_I \\ B_v \\ B_i \end{pmatrix} \overline{v_{in}} + \begin{pmatrix} B_{r_I} \\ B_{r_v} \\ B_{r_i} \end{pmatrix} v_{ref}. \tag{4.51}$$

Setting the right-hand side of (4.51) equal to zero and solving the resulting equations, we obtain

$$\overline{X}_{c_i} = \Omega\left(\overline{X}\right). \tag{4.52}$$

Using (4.52), we rewrite (4.21c) as

$$\overline{d_j} = \frac{1}{v_{ramp_j}} H_{c_j} \overline{X}_{c_i} = \Omega'\left(\overline{X}\right) \quad \text{or} \quad \bar{d} = \Gamma \bar{X}. \tag{4.53}$$

Substituting (4.53) into (4.10a) and setting $\bar{X} = 0$, we obtain

$$F^o\left(\overline{X}, \overline{v_{in}}\right) + G^o\left(\overline{X}, v_{in}\right)\Gamma\left(\overline{X}\right) + W^o_{1_{av}}\left(\overline{X}, \Gamma\left(\overline{X}\right)\right) = 0. \tag{4.54}$$

Unlike (4.50), (4.54) depends only on $\overline{X}$ and hence is relatively easier to solve for the equilibrium solutions. Having obtained $\overline{X}$, we determine the equilibrium values of $\overline{X}_{c_I}$, $\overline{X}_{c_v}$, and $\overline{X}_{c_i}$ using (4.52), thereby obtaining the equilibrium solutions of $\overline{\Psi}$ $(= \overline{\Psi_s})$ for a given $\overline{v_{in}}(= U)$. Next we rewrite (4.21c) as

$$\overline{d} = P\left(\overline{\Psi}\right) \tag{4.55}$$

and rewrite (4.21a) as

$$\dot{\overline{\Psi}} = F\left(\overline{\Psi}, \overline{v_{in}}, v_{ref}\right) + G\left(\overline{\Psi}, \overline{v_{in}}\right) P\left(\overline{\Psi}\right) + W_{1_{av}}\left(\overline{\Psi}, P\left(\overline{\Psi}\right)\right). \tag{4.56}$$

The stability of a given equilibrium solution $\bar{\Psi}$ is ascertained by the eigenvalues of the Jacobian matrix of the right-hand side of (4.56) evaluated at $\bar{\Psi}_s$. To determine the post-bifurcation scenario, we compute the normal form of (4.56) in the vicinity of the bifurcation point (Nayfeh, 1993).

4.4.4 Stability Analysis Under Saturated Conditions

The unsaturated region for N parallel converters, operating with a finite but large frequency, is a boundary layer around the intersection of all of the N discontinuous hypersurfaces. The stability analysis (using bifurcation analyses and Lyapunov's method) performed so far assumes that the parallel converter is operating in this region. When one or more converters stop modulating for one or more switching cycles, then we have a saturated system. If all of the converters are not modulating, the system is fully saturated; otherwise, the system is partially saturated. In a parallel converter with N switches, there are 2^N ways by which a full saturation can occur. For the same system, there are $\sum_{i-1}^{N-1} \frac{N!}{(N-i)!\ i!}$ possibilities for partial saturation. Under full saturation, these piecewise-linear systems behave as autonomous systems because they are not switching. However, under partial saturation, the parallel converter still behaves as a nonlinear nonautonomous system because there is at least one converter, which is operating in the unsaturated region.

To analyze the stability of a saturated system, we need to address two issues. First, when a parallel converter operating in the unsaturated region saturates, does the solution remain inside the boundary layer or leave? Second, if the solution leaves the boundary layer, does the trajectory return back to it? The first issue deals with the question of existence; that is, under what conditions do all of the solution trajectories point toward the boundary layer. If all of the solution trajectories point toward the boundary layer for all values of the closed-loop states, then we have global existence of the boundary layer. The second issue, which deals with the reaching condition for the solution trajectories, becomes important in the absence of global existence of the boundary layer.

We deal with the issue of existence using Lyapunov's direct II method. The stability analysis using a positive definite smooth Lyapunov function $V(.)$ for a nonsmooth system with a discontinuous surface demands that the following three conditions be satisfied (Shevitz and Paden, 1994; Wu et al., 1998):

1. In the saturated/continuity region, $\dot{V}(.) < 0$.

2. As the solution approaches the discontinuity surface, $\dot{V}(.) \rightarrow 0$.

3. On the discontinuity surface, $\dot{V}(.) = 0$.

If these three conditions are satisfied, then the solution exists on the surfaces of discontinuity. The converters that we deal with have finite but large frequencies and hence have boundary layers around the discontinuity surfaces. If the widths of the boundary layer are zero (when the switching frequency is infinite), the above conditions apply directly. These conditions do not, however, carry over to a finite-frequency converter, and at best give an upper estimate of stability. The reason is that, within the boundary layer, the nominal solution for the parallel converter is a periodic trajectory and not an equilibrium point, for which Lyapunov's method does not apply. For the stability analysis in this region, one needs to reduce the order of the system and then use Lyapunov's method or bifurcation analyses. We have shown this in the preceding sections.

Outside the boundary layer, however, the converters are not switching. Hence, the condition $\dot{V}(.) < 0$ for a converter operating with no boundary layer is directly applicable to a finite-frequency, fully saturated converter, as long as the solutions are in the saturated region. For partial saturation, at least one of the converters is switching. To determine the stability of the quasi-solution surface, we resort to the discretized version of the three (Lyapunov-based) above conditions (Brogliato, 1996). However, to accomplish this, we need to modify the nonlinear map for the unsaturated region.

To determine the reaching conditions for the trajectories that leave the boundary layer (if global existence can not be established), we find the equilibrium solutions for the saturated converter. Using (4.17a), we show that the dynamics of a fully saturated system are given by

$$\Psi_{k+1} = e^{A_{1_{sat}} t_{1_{sat}}} \Psi_k + \left(e^{A_{1_{sat}} t_{1_{sat}}} - I \right) A_{1_{sat}}^{-1} B_{1_{sat}} v_{ink} + \left(e^{A_{1_{sat}} t_{1_{sat}}} - I \right) A_{1_{sat}}^{-1} B_{r1_{sat}} v_{ref}. \quad (4.57)$$

The equilibrium solutions of (4.57) are determined using the constraint $\Psi_{k+T} = \Psi_k = \Psi_{sat}$. The result is

$$\Psi_{sat} = \left(e^{A_{1_{sat}} t_{1_{sat}}} - I\right)^{-1} \left(\left(e^{A_{1_{sat}} t_{1_{sat}}} - I\right) A_{1_{sat}}^{-1} B_{1_{sat}} v_{ink} + \left(e^{A_{1_{sat}} t_{1_{sat}}} - I\right) A_{1_{sat}}^{-1} B_{r1_{sat}} v_{ref}\right). \quad (4.58)$$

If an equilibrium solution is virtual, then the error trajectories will be inside the boundary layer eventually. If it is real, then it will influence the unsaturated solution, and under certain conditions the system may remain permanently saturated. For partially saturated systems, we can similarly determine the equilibrium solutions for the discretized system.

4.5 Results

In the previous sections, we developed the methodologies and criteria for the stability analysis of parallel dc-dc PWM converters using different models. We applied these criteria to analyze the stability of two parallel buck converters (shown in Figure 4.2) operating with active-current-sharing control. The states of the plant are i_{L_1}, i_{L_2}, v_{C_1}, and v_{C_2}. There are additional states corresponding to the load-current and voltage-loop controllers. Each of these converters has a multiloop control with an outer load-sharing current loop and an inner voltage loop. The objective of the closed-loop system is to share the load power equally and regulate the bus voltage. It is worth noting that we can alos apply any other parallel-control scheme, such as the master-slave control, as well.

We chose the controller based on the works of Thottuvelli and Verghese (1996). In Figure 4.3 we plot the eigenvalues of the linearized averaged model as the input voltage is varied from 25 to 50 volts. Since none of the eigenvalues in Figure 4.3 has a positive real part, we conclude that the nominal solution is locally stable for the input voltage range.

Next, we analyze the stability of the same system using a nonlinear map. We consider two cases: one for which the effect of the esrs of the output capacitors are considered and the other for which they are not. In Figures 4.4a (esr $\neq 0$)and 4.4b (esr $= 0$), we show the

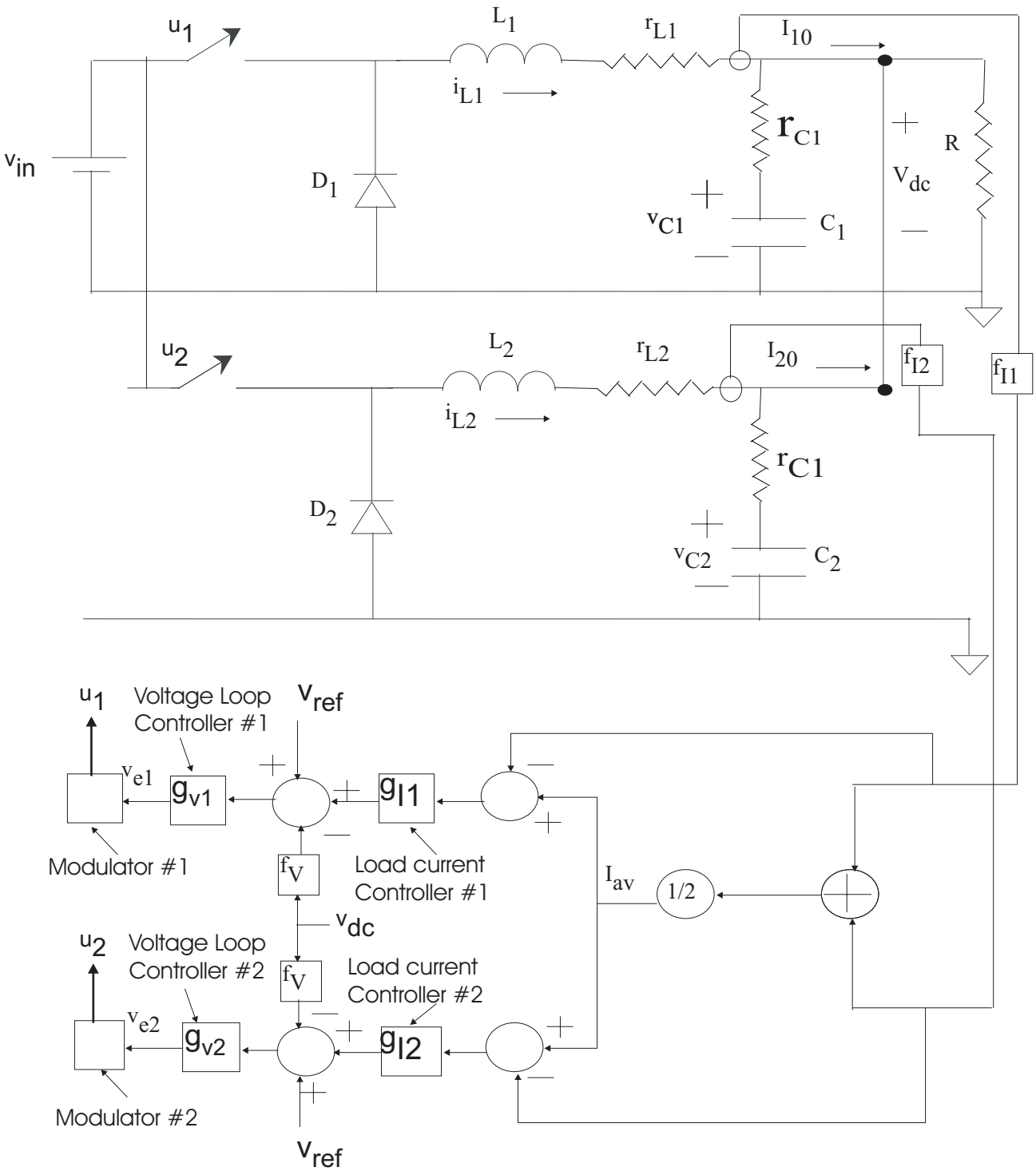

Figure 4.2: Two parallel buck converters operating with load-sharing control.

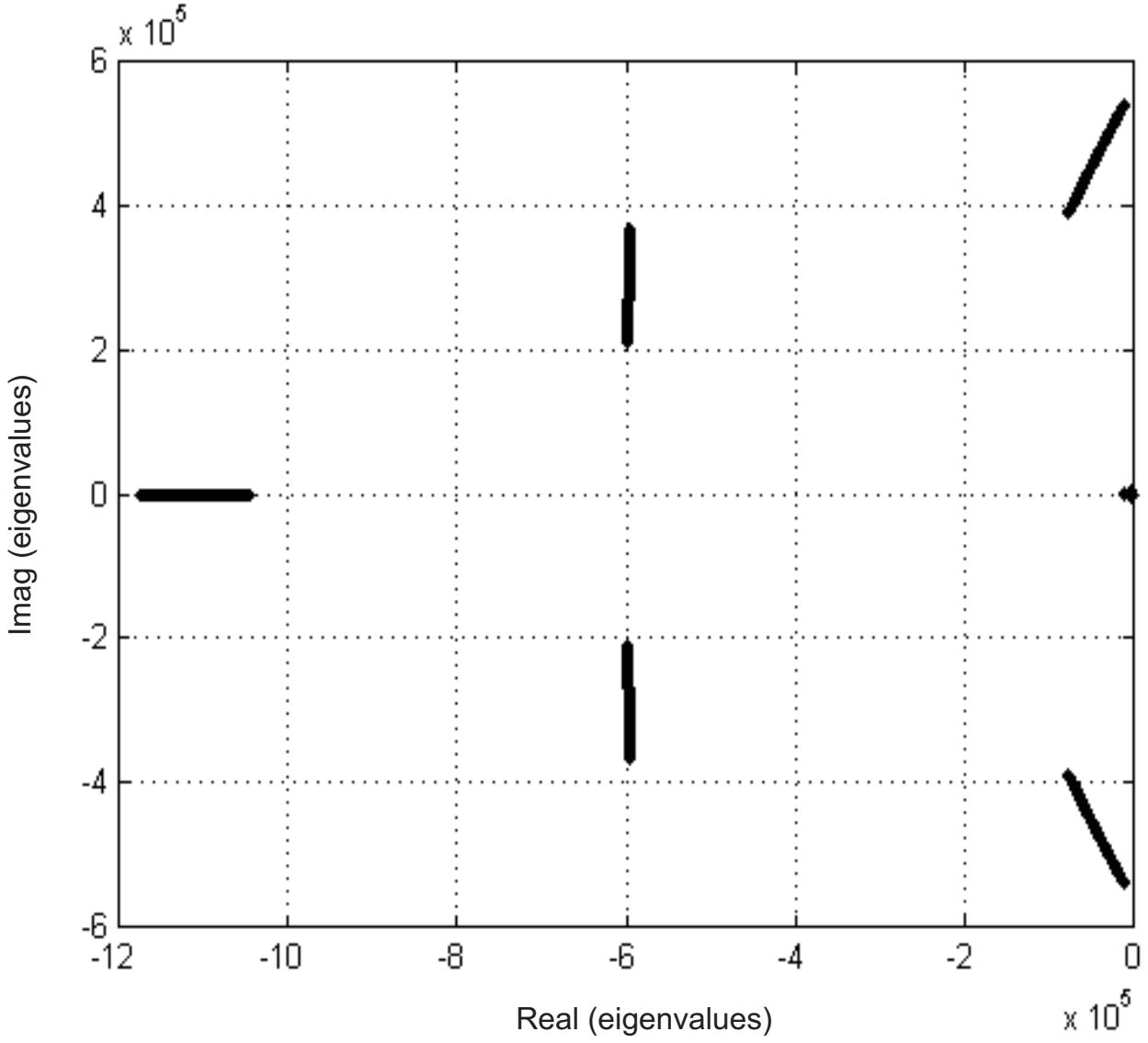

Figure 4.3: Eigenvalues of the averaged model for the parallel converter indicate a stable system.

Floquet multipliers of the linearized map for these two cases. For both cases, we see that, as the bifurcation parameter (input voltage) is increased, two complex conjugate Floquet multipliers exit the unit circle away from the real axis, indicating a Hopf bifurcation. This slow-scale instability is not observed in Figure 4.3. To find out the type of bifurcation, we compute the normal form of the nonlinear map in the neighborhood of the bifurcation point. The normal form indicates a subcritical Hopf bifurcation. Using a second-order Poincare map, we show that the post-bifurcation response is quasiperiodic. This is evident in Figure 4.5. Figure 4.6 shows the impact of variations in the output capacitance on the instability mechanism of the interleaved parallel-buck converters. Starting with the nominal values for C_1 and C_2, we reduce their magnitudes by a factor of two for each successive set of data, keeping all of the other parameters constant. For each set of capacitor values, we investigate the stability of the system for an input voltage varying from 25 to 50 volts. For values of the output capacitance close to the nominal value, a subcritical Hopf bifurcation occurs as the input voltage is increased. As the value of the output capacitor is reduced, no local instability occurs for the input-voltage variation. However, as the output capacitance is reduced even further, the parallel converter loses stability as the input voltage is increased. We find that the instability occurs due to a supercritical Hopf bifurcation and not due to a subcritical Hopf bifurcation.

Next, we consider the impact of variations in the input voltage on the operation of two parallel-buck converters operating in synchronicity rather than with a phase shift of 180^o. We find that, for the same nominal parameters (as considered above), the synchronized converters are stable for the entire input voltage range. However, for a higher gain of the voltage-loop controller, we observe the onset of a fast-scale instability with a increasing input voltage. The fast-scale instability occurs in the form of a period-doubling bifurcation, as shown in the bifurcation diagram in Figure 4.7, which ultimately leads to chaos as the input voltage is increased beyond 50 volts. In Figure 4.8, we show the movement of the Floquet multipliers of the period-one orbit. As the input voltage is increased, one of the Floquet multipliers exits the unit circle through -1, indicating a period-doubling bifurcation.

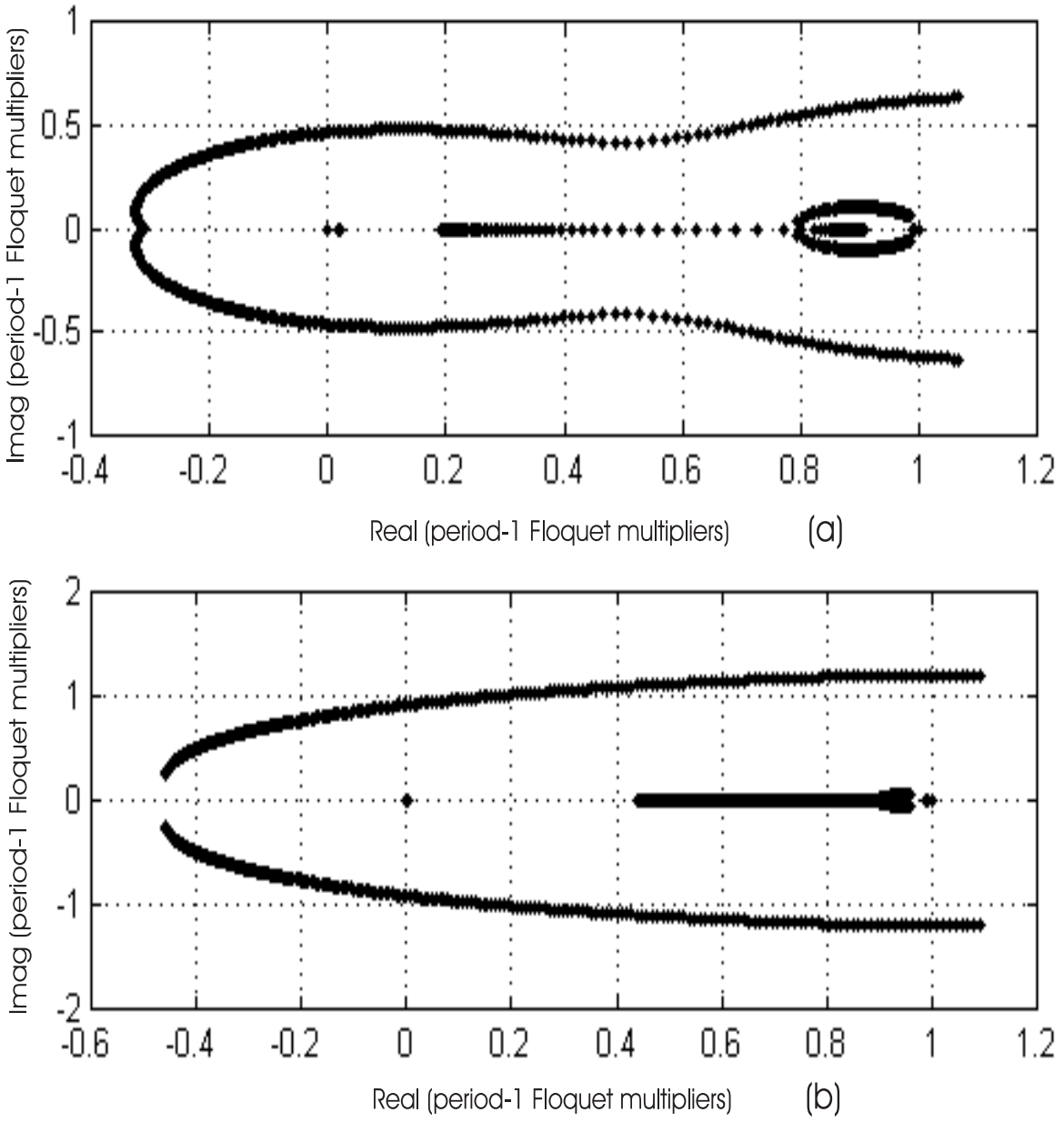

Figure 4.4: Onset of instability in the interleaved parallel buck converters: two Floquet multipliers of the period-one orbit exit the unit circle away from the real axis, indicating a Hopf bifurcation: (a) with esr and (b) without esr.

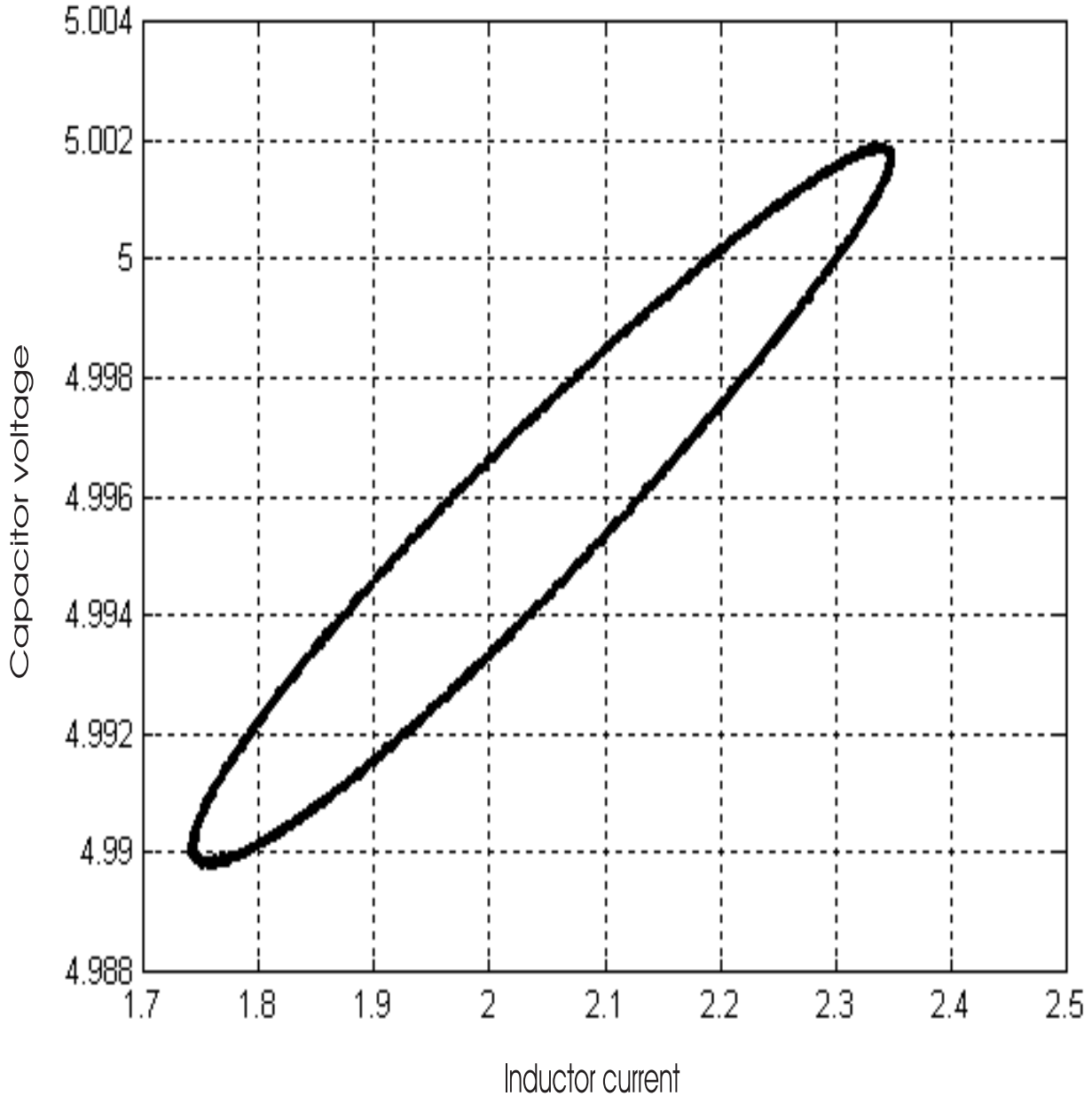

Figure 4.5: Post-Hopf bifurcation scenario of the interleaved parallel buck converters: a second-order Poincare map clearly shows a quasiperiodic response.

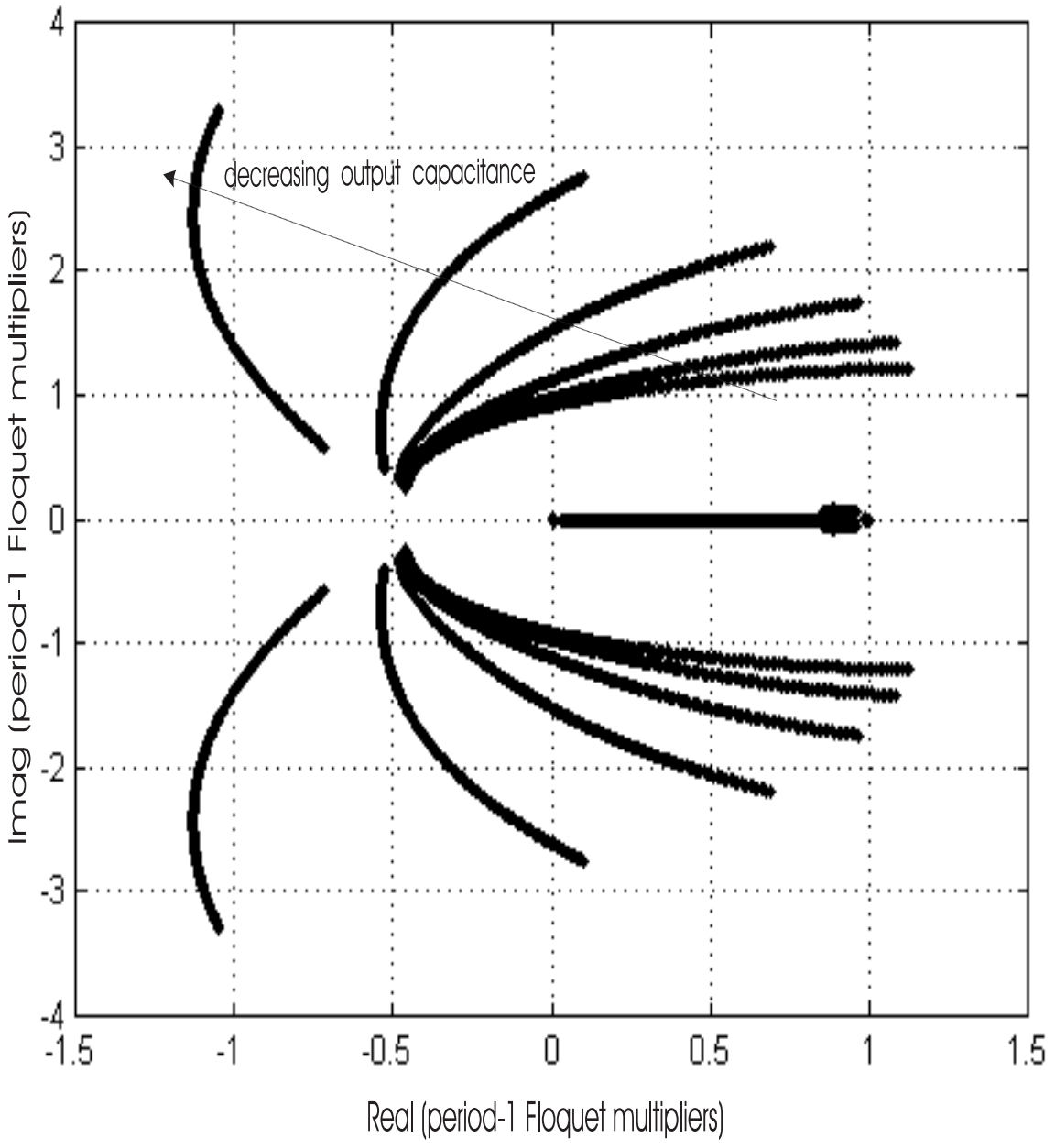

Figure 4.6: Impact of variations in the output capacitance on the mechanism of instability of the interleaved parallel converters.

A second-order nonlinear map (Mazumder et al., 2000a) reveals that the period-doubling bifurcation is supercritical in nature.

Finally, we demonstrate the behavior of two parallel-buck converters operating with a multiloop static feedback controller under saturated conditions. We discuss in detail only the cases when both switches are turned off. We can extend the same technique for the other three cases of full saturation.

To demonstrate our point, we consider only the Hamiltonian part of the system. The presence of the parasitic resistors makes the system more passive (Sanders, 1989; Van-der Scahft, 1996). In addition, we change the control strategy from load-current equalization to line-current equalization. For the buck converter, this change does not alter the control objectives, which are to regulate the capacitor voltage and share the load power equally. However, with these two simple changes, we prove our point more easily.

For the closed-loop parallel converter operating with static-feedback controllers, the switches u_1 and u_2 are turned off if the error signals of the controller are less than zero. In this continuity region, the error signals are given by

$$\sigma_k = g_{v_k}\left[v_{ref} - f_v X_3 + g_{I_k} f_I \left(\frac{1}{2}\sum_{j=1}^{2}(X_1 + X_2) - X_k\right)\right],\ k = 1, 2. \tag{4.59}$$

In (4.59), X_1 and X_2 are the inductor currents of the two modules, X_3 is the capacitor voltage, f_v is the feedback-sensor gain for the output voltage, and f_I is the current-sensor gain. We assume that the gains of the current sensor are the same for simplicity. We choose the following Lyapunov function in the continuity region:

$$V(\sigma_1, \sigma_2) = \frac{1}{2}\sigma^T D\sigma = \frac{1}{2}\begin{pmatrix} \sigma_1 & \sigma_2 \end{pmatrix}\begin{pmatrix} 1 & 0 \\ 0 & 1 \end{pmatrix}\begin{pmatrix} \sigma_1 \\ \sigma_2 \end{pmatrix}. \tag{4.60}$$

Therefore,

$$\dot{V} = g_{v_1}\left[v_{ref} - f_v X_3 + g_{I_1} f_I \left(\frac{1}{2}\sum_{j=1}^{2}(X_1 + X_2) - X_1\right)\right]\left[\frac{g_{v_1} g_{I_1} f_I}{2}\left(\dot{X}_2 - \dot{X}_1\right) - g_{v_1} f_v \dot{X}_3\right] +$$

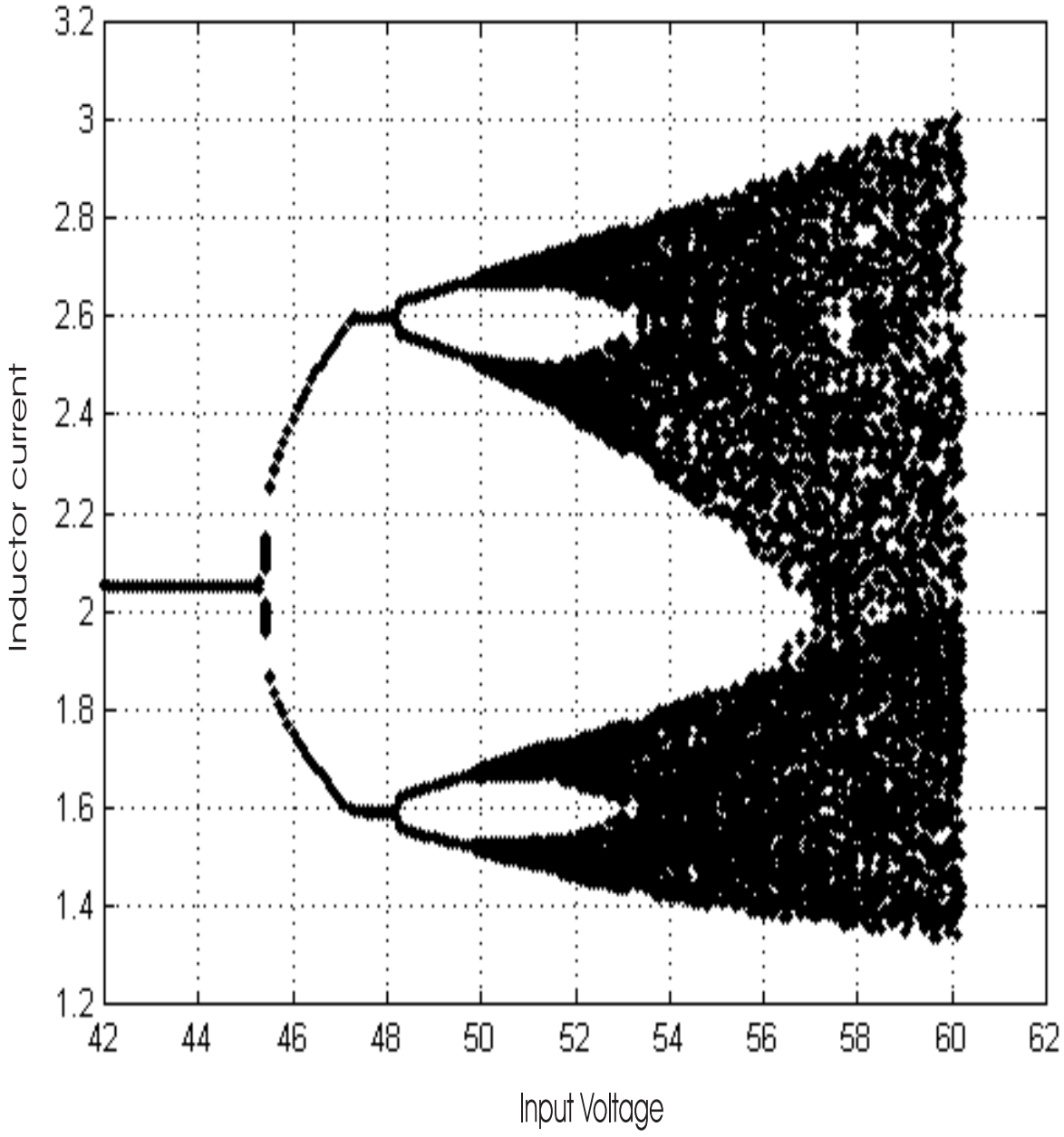

Figure 4.7: A bifurcation diagram of the closed-loop parallel buck converter operating in synchronicity. It shows a fast-scale instability.

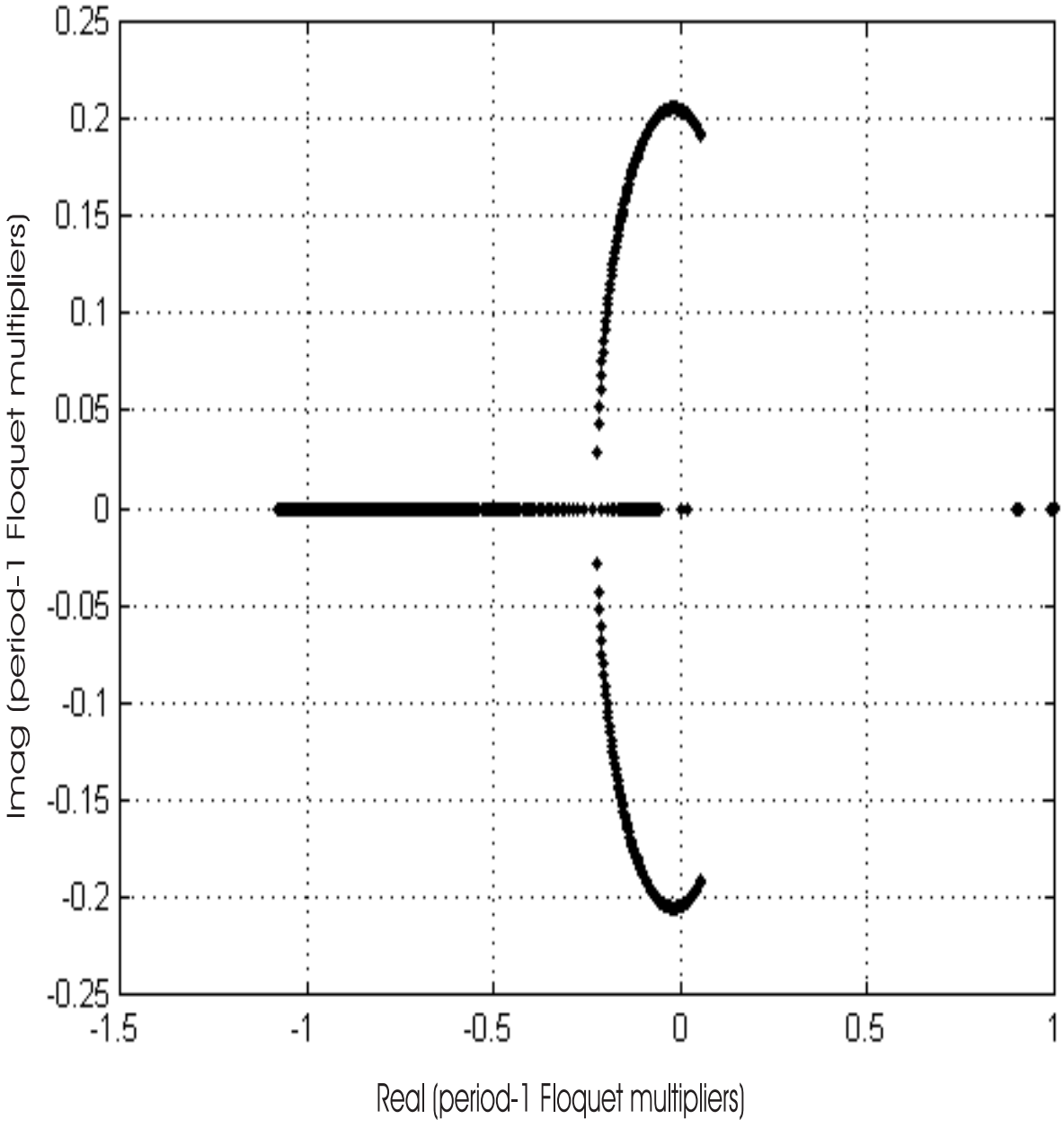

Figure 4.8: One of the Floquet multipliers of the period-one orbit exits the unit circle via -1, indicating a period-doubling bifurcation.

$$g_{v_2}\left[v_{ref}-f_vX_3+g_{I_2}f_I\left(\frac{1}{2}\sum_{j=1}^{2}(X_1+X_2)-X_2\right)\right]\left[\frac{g_{v_2}g_{I_2}f_I}{2}\left(\dot{X}_1-\dot{X}_2\right)-g_{v_2}f_v\dot{X}_3\right] \quad (4.61)$$

Using the equations for the Hamiltonian system

$$\dot{X}_k=-\frac{X_3}{L_k}+\frac{U_ku}{L_k} \qquad \forall(k=1,2) \quad (4.62a)$$

$$\dot{X}_3=\sum_{j=1}^{2}\frac{X_j}{C_1+C_2}-\frac{X_3}{(C_1+C_2)\,R}, \quad (4.62b)$$

and $u_1=u_2=0$, we obtain

$$\dot{V}_{(u_1=u_2=0)}=\frac{2g_v^2f_v}{C_1+C_2}\left(v_{ref}-f_vX_3\right)\left(\frac{X_3}{R}-X_1-X_2\right)+\frac{g_v^2g_I^2f_I^2}{2}\left(\frac{1}{L_1}-\frac{1}{L_2}\right)(X_2-X_1)\,X_3 \quad (4.63)$$

When the two modules have the same parameters, the second term in (4.63) vanishes. Using (4.63), we can show that, when the two converters have the same parameters, the error trajectories in the continuity region, given by $u_1=u_2=0$, move toward the boundary layer provided that $\frac{X_3}{R}>X_1+X_2$. Now, the closed-loop parallel converter (with the same parameters) operates in the saturated region given by $u_1=u_2=0$ only if $v_{ref}>f_vX_3$. However, the equilibrium solutions of (4.62) when $u_1=u_2=0$ are $X_1=0, X_2=0$, and $X_3=0$. Therefore, the equilibrium solution is virtual. In other words, the closed-loop converter can not remain in this saturated region permanently. Next, we consider two cases to demonstrate these two points.

First, we consider a parallel-buck converter with $C_1=C_2=4400\ \mu F$ and $L_1=L_2=50\ \mu H$. For the second case, we change only the value of the output capacitor to 100 μF. We find that the (unsaturated) nominal solution of the converter in case one is stable for an input voltage range of 70 volts, starting at 20 volts. The converter in the second case has a stable (unsaturated) nominal solution at 20 volts. However, the nominal solution is unstable at 90 volts. Let us assume that initially these converters are operating in steady state with an input voltage of 20 volts. We then subject them to a feedforward disturbance so that the

final input voltage is 90 volts. The disturbance is deliberately chosen to be strong enough so that the two switches turn off. In other words, $u_1 = 0$ and $u_2 = 0$.

Figure 4.9 shows the results for case one. We see that the converter is stable before and after the feedforward disturbance. We predic this based on the reaching condition and the stability of the (unsaturated) equilibrium solution. After the disturbance, when the system saturates, $\dot{V}$ becomes positive because $\frac{X_3}{R} > X_1 + X_2$. As a result, the error trajectories move away from the boundary layer. Because the equilibrium solution in the saturated region is virtual, the error trajectories approach the boundary layer when $\dot{V}$ is less than zero, and eventually modulation begins. The states of the system indicate a damped oscillatory behavior before settling down because the nominal solution is a stable focus.

Figure 4.10 shows the results for case two. It shows that, while the parallel converter is stable before the disturbance, the post-disturbance dynamics are unstable. We know that the error trajectories can not stay in the saturated region given by $u_1 = 0$ and $u_2 = 0$. However, inside the boundary layer, instead of a stable nominal solution, we have a chaotic attractor. Hence the dynamics of the converter after the disturbance are chaotic. The switching function in Figure 4.10b confirms this. We also see from Figure 4.10c that the derivative of the Lyapunov function correctly predicts the dynamics of the error trajectories.

We make two observations based on the results of cases one and two. First, for the same feedforward disturbance, the derivative of the Lyapunov function for case two spends much less time in the saturated region as compared to case one. This is because, for the second case, the voltage across the capacitor (for a given load), due to its smaller size, changes more rapidly with changes in the inductor current. We can verify this by neglecting the second term in (4.63). Second, although a reduction in the capacitance gives a better dynamic response, it results in an unstable nominal solution. In Figure 4.11, we show the steady-state and dynamic performances of the parallel converter with $L_1 = L_2 = 250\ \mu H$ and $C_1 = C_2 = 400\ \mu F$. This simple compromise, guided by $\dot{V}$ and the stability analysis of

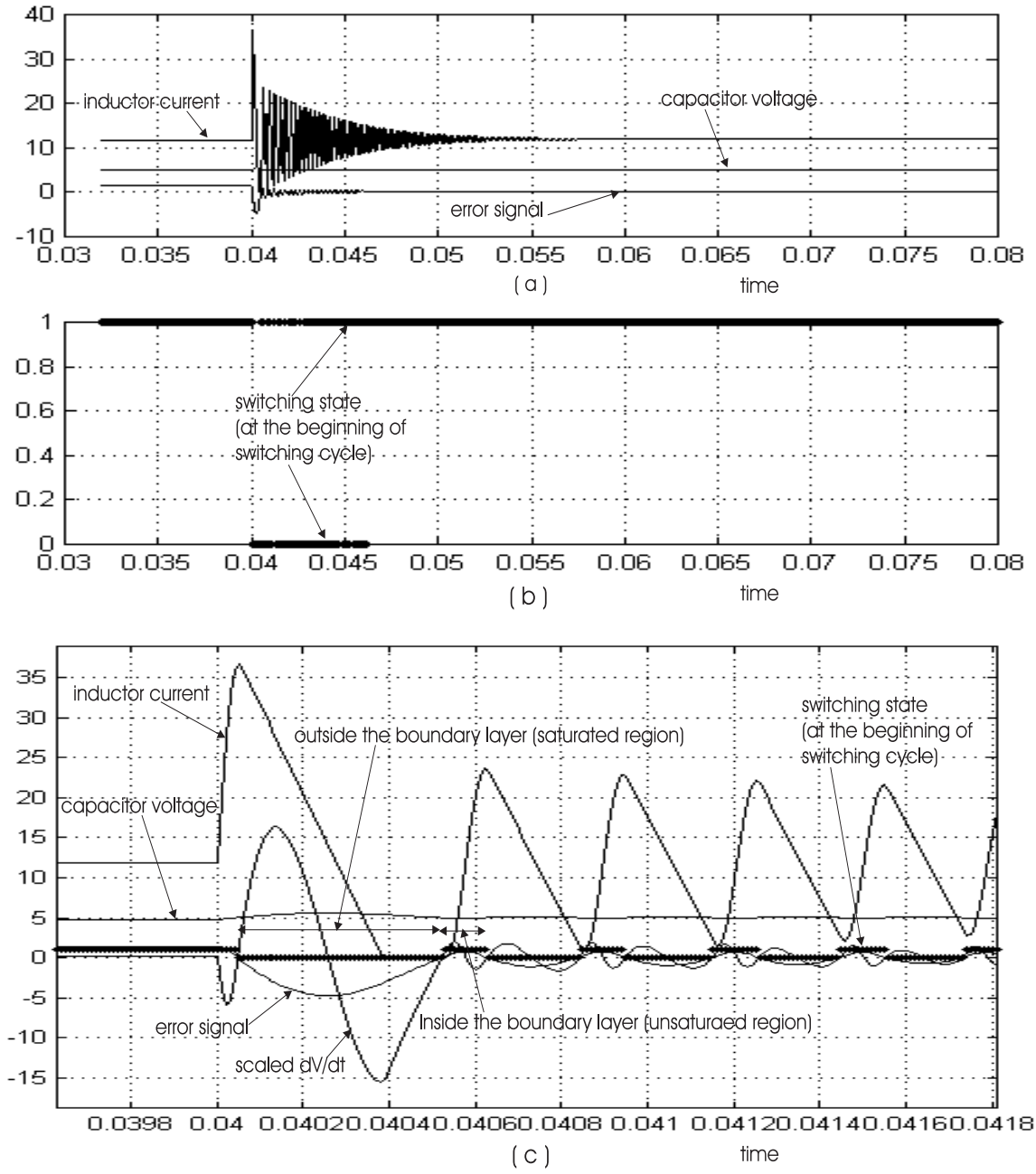

Figure 4.9: Stability analysis, based on the unsaturated model, predicts a stable equilibrium before and after the feedforward disturbance. However, during the transients, the system saturates. As a result, the existence condition is violated. Although the error trajectories return back to the sliding manifold (as predicted), the transient performance is unacceptable. Part (c) is an expansion of the transient region in (a) and (b).

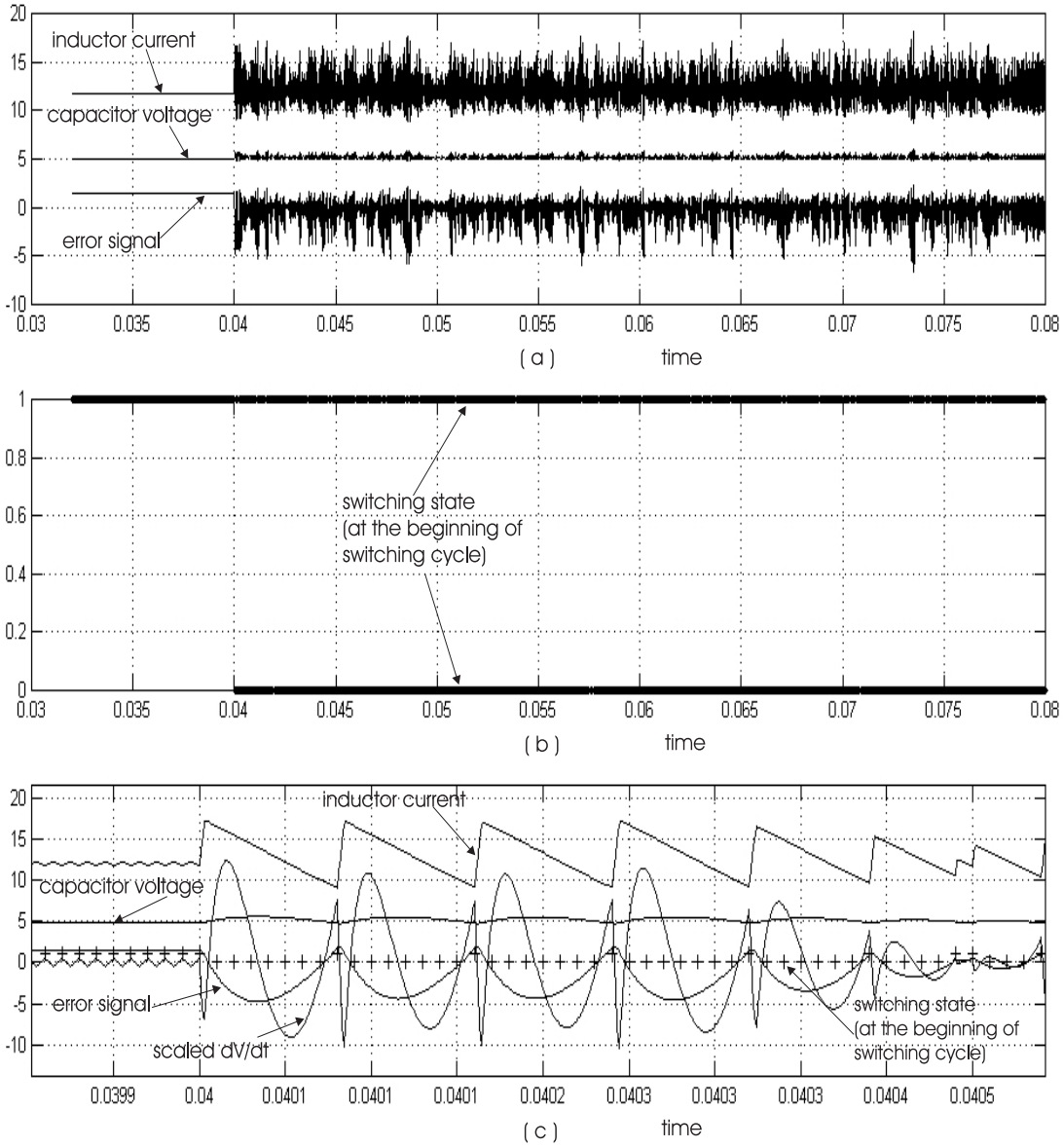

Figure 4.10: Stability analysis which predicts that, while the parallel converter is stable before the disturbance, the post-disturbance dynamics are unstable. Inside, there is chaotic attractor inside the boundary layer. Part (c) is an expansion of (a) and (b) in the region immediately after the disturbance.

the nominal solution, gives a better dynamic response.

So far we have considered identical converters. We now consider a case in which the two converters have about a 5% difference in the line inductance. Converter one has a line inductance of 250 μH, whereas converter two has a line inductance of 235 μH. The output capacitances of both converters are chosen to be 400 μF. We keep the values of the rest of the parameters, except g_I, the same as those in the other three cases. Because the inductors of the two converters are not identical, the term representing the difference in the two inductor currents in (4.63) is important. Equaton (4.63) shows that, unless these terms are bounded and small, the dynamics of these two parallel converters, even with a small variation in the parameter of one power stage, can be vastly different from the ideal system. In this case, one simple way to achieve load sharing would be to keep g_I small. However, too small a value of g_I would nullify load sharing.

In Figure 4.12, we show the steady-state and dynamic performances of the parallel converter with a suitable choice of g_I. The nominal solution of the system for the entire input voltage range is stable. Although the values of the inductors of the two modules are different, the performance of the system is similar to that of the ideal case. There is, however, a minor difference in the switching sequences. In the case of the ideal converter, both switching states are identical. Hence, the system switches between the unsaturated and saturated regions given by $u_1 = u_2 = 0$. However, now, due to the parametric difference of the converters, both of the error trajectories do not enter or exit the boundary layer at the same time. Hence, there is a time span during which the system is partially saturated before it operates in the unsaturated region. During this time, u_1 is turned off while u_2 modulates. We obtain the switching sequence $u_1 = u_2 = 0 \rightarrow u_1 = 0, u_2 \in (0,1) \rightarrow u_1 \in (0,1), u_2 \in (0,1)$ only because $\gamma\,(= X_1 - X_2)$ is constrained by a proper choice of g_I. For progressively larger values of g_I, we would obtain the switching sequences $u_1 = 0, u_2 = 1 \rightarrow u_1 \in (0,1), u_2 = 1$ or $u_1 = 0, u_2 = 1, u_1 = 1, u_2 = 1$ after the disturbance. This results in a deterioration of the steady-state and dynamic performances of the system.

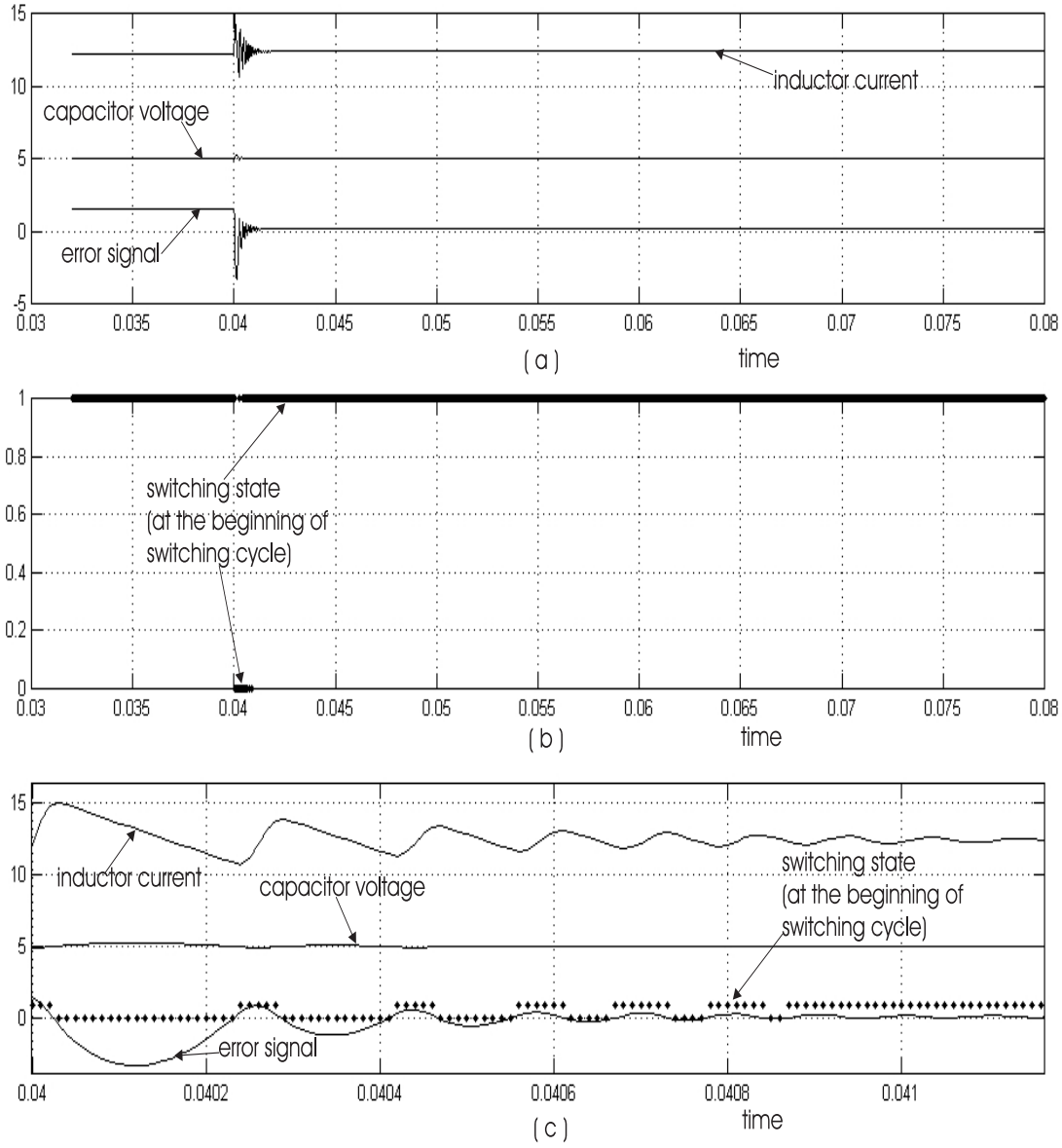

Figure 4.11: A properly designed parallel converter. It has excellent steady-state and transient performance.

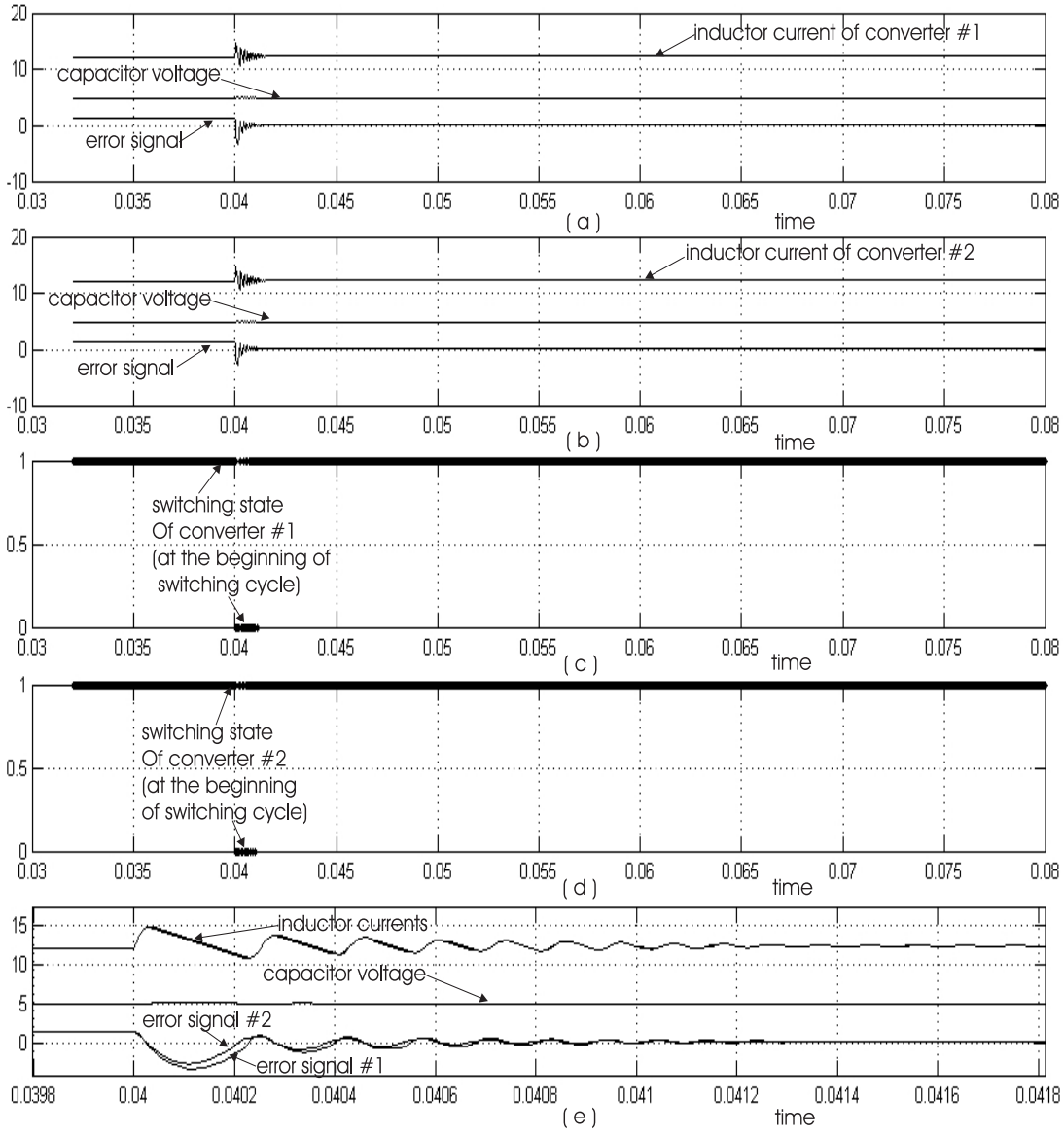

Figure 4.12: Performance of a parallel converter under parametric variation. Although the two error trajectories enter the unsaturated region at different times, a careful design consideration (based on Lyapunov function) results in a system with high performance. Part (c) is an expansion of the transient region in (a) and (b).

4.6 Summary

We investigate the local and global stability of parallel dc-dc converters in the unsaturated and saturated regions. Using a nonlinear map, we demonstrate the fast-scale and slow-scale instabilities in two parallel converters. The averaged model can not predict the fast-scale dynamics. Using a bifurcation analysis (with the input voltage as the bifurcation parameter) based on a nonlinear map, we show how the type of instability changes when the converters operate using interleaving instead of operate in synchronicity. The state-space averaged model can not distinguish between the converters operating in synchronicity from those operating using interleaving. For the interleaved converter, we show how the mechanism of instability changes from a subcritical Hopf bifurcation to a supercritical bifurcation as the values of the output capacitors are decreased. Using a second-order Poincare map, we find that the post-Hopf bifurcation dynamics are quasiperiodic.

To determine the post-bifurcation dynamics in the vicinity of the nominal solution, one can use either a higher-order map, numerical techniques, or the normal form of the system of equations. We used the first two methods for standalone converters (Mazumder et al., 2000a). Because the dimensionality of the closed-loop parallel converter is, in general, higher than that of standalone converters, the normal form may be a better alternative. In this chapter, we have outlined a technique to generate the normal form of a closed-loop system described by a nonlinear map.

We also outline ways to determine the stability of saturated regions, which we demonstrate using two synchronized parallel buck converters. Using a positive definite Lyapunov function, we show that, for a fully saturated parallel converter, the dynamics of the system in the saturated region are governed by the derivative of the Lyapunov function. When the derivative of the Lyapunov function is negative, the error trajectories approach the boundary layer. When the derivative is positive, the error trajectories leave the saturated region. In this case, we show that if the equilibrium solutions of the saturated regions are virtual, these trajectories will ultimately reach the boundary layer.

Finally, we apply these concepts of stability for the saturated and unsaturated regions to four cases. For the first three cases, we consider the parameters of the parallel converters to be the same. We show, using cases one and two, that the nominal solution (in the unsaturated region) is stable if and only if the dynamics of the system in the saturated and unsaturated regions are stable. That is why, while the post-disturbance steady-state dynamics of the closed-loop system in case one are stable, they are chaotic for the second case. However, we find that the transient dynamics for case one are much more oscillatory than those of case two. We explain this using the derivative of the Lyapunov function. Based on these two cases, we show in case three how easily one can improve the transient and steady-state performances of the system. For the fourth case, we consider two parallel buck converters with parametric variation. Using (4.63), we show how to tune the outer-loop current gain g_I so that the performance of the nonideal system is close to the ideal case. We also show how and why the switching sequence changes with increasing g_I.

4.7 Average Model for Two Parallel Buck Converters

Interleaved Converters

In each switching cycle (of duration T), there are four subintervals. The switching sequence in each switching cycle is $u_1 = 1, u_2 = 0 \rightarrow u_1 = 0, u_2 = 0 \rightarrow u_1 = 0, u_2 = 1 \rightarrow u_1 = 0, u_2 = 0$. Using (4a), we obtain the following state-space equations for these four subintervals:

$$\dot{X} = A_{10}^o X + B_{10}^o v_{in} \qquad t < t_1; \tag{4.64a}$$

$$\dot{X} = A_{00}^o X + B_{00} v_{in} \qquad t_1 < t < t_1 + t_2; \tag{4.64b}$$

$$\dot{X} = A_{01}^o X + B_{01} v_{in} \qquad t_1 + t_2 < t < t_1 + t_2 + t_3; \quad \text{and} \tag{4.64c}$$

$$\dot{X} = A_{00}^o X + B_{00} v_{in} \qquad t_1 + t_2 + t_3 < t < T. \tag{4.64d}$$

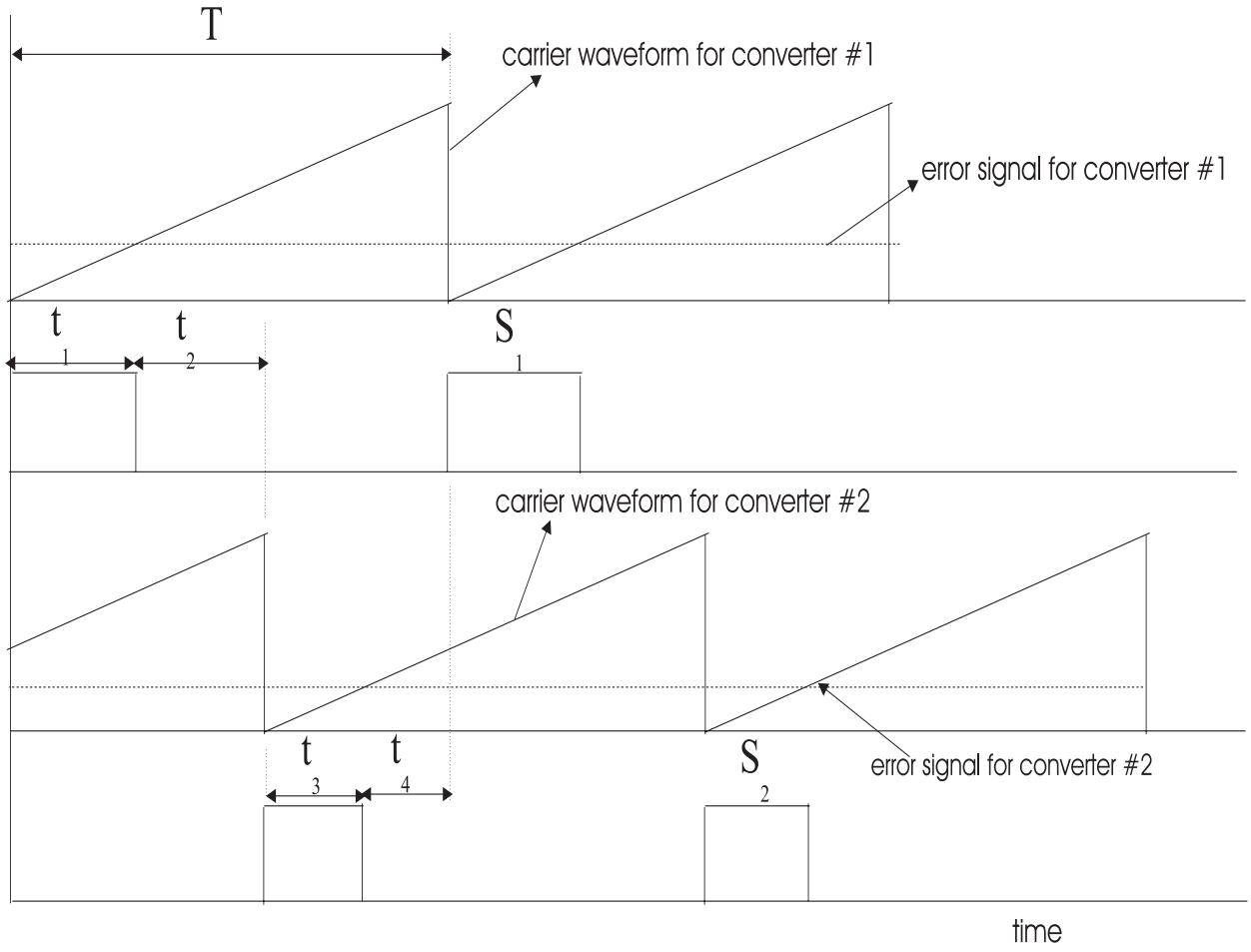

For the buck converter, $A^o_{10} = A^o_{01} = A^o_{00} = A$ and $B_{00} = 0$. Averaging the four equations (4.64) yields

$$\dot{X} = AX + \frac{t_1}{T} B_{10} v_{in} + \frac{t_3}{T} B_{01} v_{in}. \tag{4.65}$$

The duty ratio of converters one and two are $d_1 = \frac{t_1}{T}$ and $d_2 = \frac{t_3}{T}$, respectively. We rewrite (4.65) in terms of d_1 and d_2 and obtain the following averaged model:

$$\dot{X} = AX + (d_1 B_{10} + d_2 B_{01})\, v_{in}. \tag{4.66}$$

Synchronized Converters

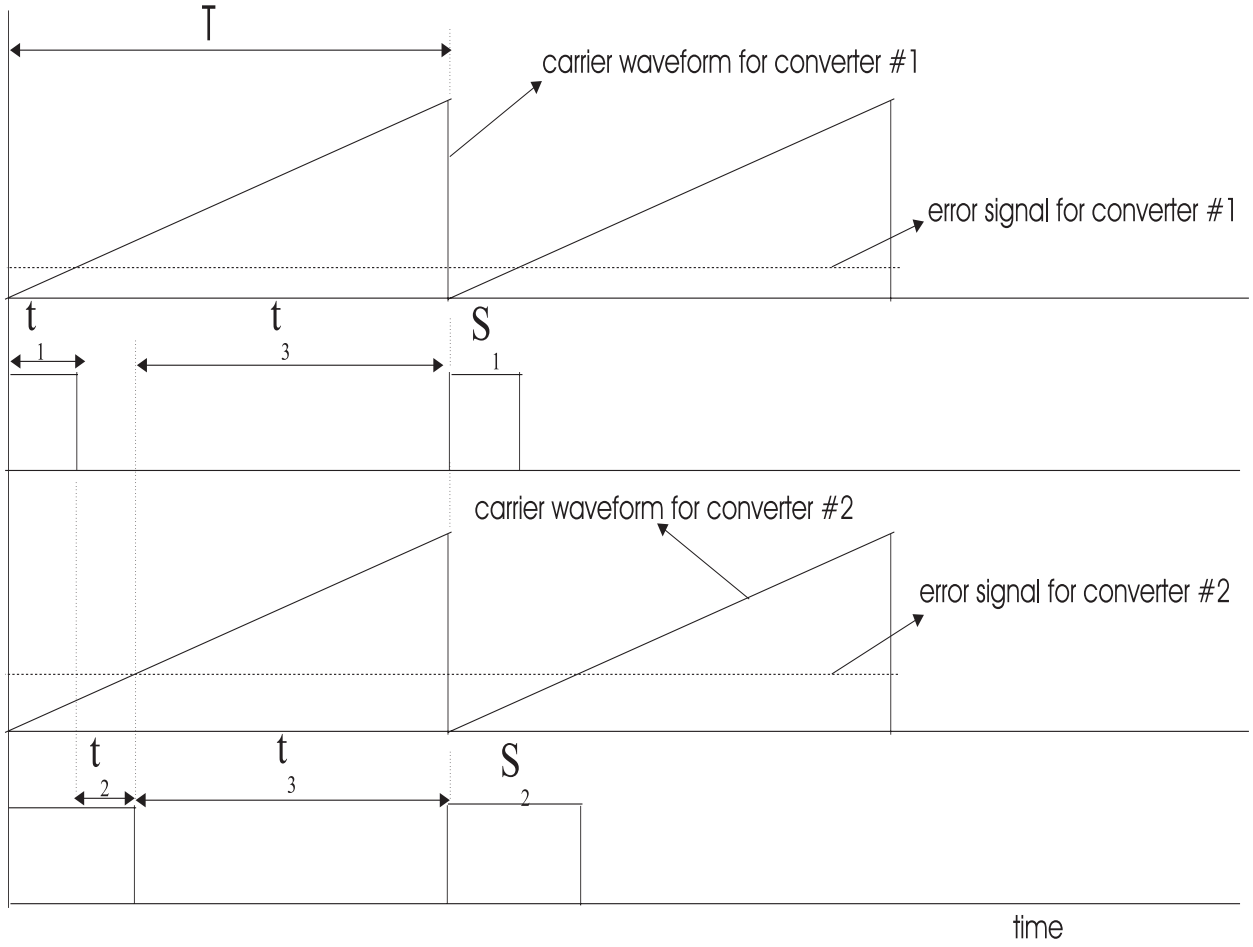

For the synchronized converter, there are three subintervals in each switching cycle (of duration T). The switching sequence in each switching cycle is $u_1 = 1, u_2 = 1 \rightarrow u_1 = 0, u_2 = 1 \rightarrow u_1 = 0, u_2 = 0$. The state-space equations for these three subintervals are

$$\dot{X} = A^o_{11}X + B^o_{11}v_{in} \qquad t < t_1, \tag{4.67a}$$

$$\dot{X} = A^o_{01}X + B_{01}v_{in} \qquad t_1 < t < t_1 + t_2, \quad \text{and} \tag{4.67b}$$

$$\dot{X} = A^o_{00}X + B_{00}v_{in} \qquad t_1 + t_2 < t < T. \tag{4.67c}$$

Averaging the four equations (4.67) yields

$$\dot{X} = AX + \frac{t_1}{T}B_{11}v_{in} + \frac{t_{1+t_2}}{T}B_{01}v_{in}. \tag{4.68}$$

The duty ratio of converters one and two are $d_1 = \frac{t_1}{T}$ and $d_2 = \frac{t_1+t_2}{T}$, respectively. We rewrite (4.68) in terms of d_1 and d_2 and obtain the following averaged model:

$$\dot{X} = AX + (d_1 B_{11} + d_2 B_{01})\, v_{in}. \tag{4.69}$$

Chapter 5

Robust Control of Parallel DC-DC PWM Converters Using the Concepts of Multiple-Sliding-Surface and Integral-Variable-Structure- Control

Parallel dc-dc converters are widely used in telecommunication power supplies. They operate under closed-loop feedback control to regulate the bus voltage and enable load sharing. These closed-loop converters are inherently nonlinear systems. The major sources of nonlinearities are the switching nonlinearity and the interaction among the converter modules. So far, however, analyses in this area of power electronics are based primarily on linearized averaged (small-signal) models. When a nonlinear converter has solutions other than the nominal one, small-signal analyses cannot predict the basin of attraction of the nominal solution and the dynamics of the system after the nominal solution loses stability. In addition, small-signal models cannot predict the dynamics of a switching converter in a saturated region. Obviously, linear controllers designed for such systems can not always give robust solutions and optimum performance.

One way to extract the best performance out of a parallel-converter system is to study its dynamics based on bifurcation analysis (Wiggins, 1990; Nayfeh and Balachandran, 1995; Kuznetsov, 1998; Sastry, 1999). In this approach, the stable and unstable dynamics of the system are studied as a parameter is varied. Since almost all of the converters are nonlinear and nonautonomous, we resort to nonlinear maps. Based on the movement of the Floquet multipliers associated with these maps, the bifurcations are categorized as static or dynamic. The advantage of this approach is that, if the dynamics of the systems beyond the linear region are known, one can optimize the performance of the converter. The implementation of this approach is discussed in Chapter 4.

Another approach, which is the topic of discussion here, is based on the design of a robust nonlinear controller that achieves global or semiglobal stability (Isidori, 1995; Marino and Tomei, 1995; Sastry, 1999) of the nominal orbit in the operating region of the parallel converter. Recently, there have been many studies of the nonlinear control of standalone dc-dc converters (Sanders and Verghese, 1990; Ueno et al., 1991; Mattavelli et al., 1995; Rios-Bolívar et al., 1995 and 1996; Scheffer et al., 1996; Sira-Ramirez, 1996; Angulo-Nunez and Sira-Ramirez, 1998; Stankovic et al., 1999; Kugi and Schlacher, 1999), which have focussed on variable-structure controllers (VSC) (Utkin, 1992; Utkin et al., 1999); Lyapunov-based controllers (Gutman, 1979; Kokotović, 1992; Miroslav et al., 1995; Freeman and Kokotović, 1996; Qu, 1998); feedback linearized and nonlinear H_∞ controllers (Ball and Helton, 1988; Isidori, 1995; Marino and Tomei, 1995; Van der Schaft, 1996; Sastry, 1999; William, 1999); and fuzzy logic controllers (Gupta and Yamakawa, 1988; Langholz and Kendel, 1993; Jamshidi et al., 1997). However, there are few studies on the nonlinear control of parallel dc-dc converters where, unlike standalone converters, there is a strong interaction among the converter modules apart from the feedforward and feedback disturbances.

Tomnescu and VanLandingham (1999) proposed a fuzzy-logic compensator for the master-slave control of a parallel dc-dc converter. The controller uses a proportional-integral-derivative (PID) expert to derive the fuzzy inference rules; it shows improved robustness as compared to linear controllers. However, the control design is purely heuristic and the

stability of the overall system has not been proven. López et al. (1998), proposed a VSC has been developed for a buck converter using interleaving. However, the interleaving scheme works only for three parallel modules. Besides, this paper does not give any details regarding the existence and stability of the sliding manifolds.

In this chapter, we develop integral-variable-structure control (IVSC) schemes for N parallel dc-dc buck converters. The choice of a VSC is logical for power converters because the control and plant are both discontinuous. All of the nonlinear controllers mentioned earlier (Ueno et al., 1991; Mattavelli et al., 1995; Rios-Bolívar et al., 1995; Scheffer et al., 1996; Stankovic et al., 1999; Kugi and Schlacher, 1999), which are not based on VSC, have completely relied on their averaged models. Therefore, the control is valid only on a reduced-order manifold.

The IVSC retains all of the properties of a VSC; that is, simplicity in design, good dynamic response, and robustness. In addition, the integral action of the IVSC eliminates the bus-voltage error and the error between the load currents of the converter modules under steady-state conditions, and it reduces the impact of very high-frequency dynamics due to parasitics on the closed-loop system. Finally, when the error trajectories are inside the boundary layer, by modifying the control using either the concept of multiple-sliding-surface control (MSSC) (Green and Hedrick, 1990; Swaroop et al., 1997) or the block-control principle (Drakunov et al., 1990a, b), we are able to reject mis-matched disturbances (Gutman, 1979; Corless and Leitmann, 1981; Barmish and Leitmann, 1982; Qu, 1998) and keep the steady-state switching frequency constant. We validate our theoretical results with some relevant simulation results. We demonstrate the performance of converter modules under steady-state and transient conditions when their parameters either match or do not match.

5.1 Models for Parallel DC-DC Buck and Boost Converters

Assuming ideal switches, one can express the dynamics of N buck converters (shown in Figure 5.1) operating in parallel by the following differential equations:

$$\begin{aligned} \frac{di_{L_k}}{dt} &= -\frac{1}{L_k}\left(r_{L_k} i_{L_k} + v_{C_k} - u_k v_{in}\right) \\ \frac{dv_{C_k}}{dt} &= \frac{1}{C_k}\left(i_{L_k} - I_{k_0}\right), \;\; k = 1, N \end{aligned} \tag{5.1}$$

where the u_k are the switching functions and v_{in} represents the input voltage. The constraints on the converter model are

$$\begin{aligned} & v_{C_1} = \cdots = v_{C_N} = v_C \\ & \tfrac{v_C}{v_{in}} < 1 \\ & \textstyle\sum_{k=1}^{N} I_{k_0} = I_0 \end{aligned} \tag{5.2}$$

where I_0 is the load current.

The dynamics of N boost converters (shown in Figure 5.2) operating in parallel are described by the following differential equations:

$$\begin{aligned} \frac{di_{L_k}}{dt} &= -\frac{1}{L_k}\left(r_{L_k} i_{L_k} + \overline{u_k} v_{C_k} - v_{in}\right) \\ \frac{dv_{C_k}}{dt} &= \frac{1}{C_k}\left(\overline{u_k} i_{L_k} - I_{k_0}\right), \quad \overline{u}_k = 1 - u_k. \end{aligned} \tag{5.3}$$

The constraints on the converter model are given by (5.2).

5.2 Concepts of Discontinuous Systems

The condition for the existence of the i^{th} discontinuity surface ($\sigma_i = 0$) of a differential equation

$$\dot{y} = f(y, t, u) \tag{5.4}$$

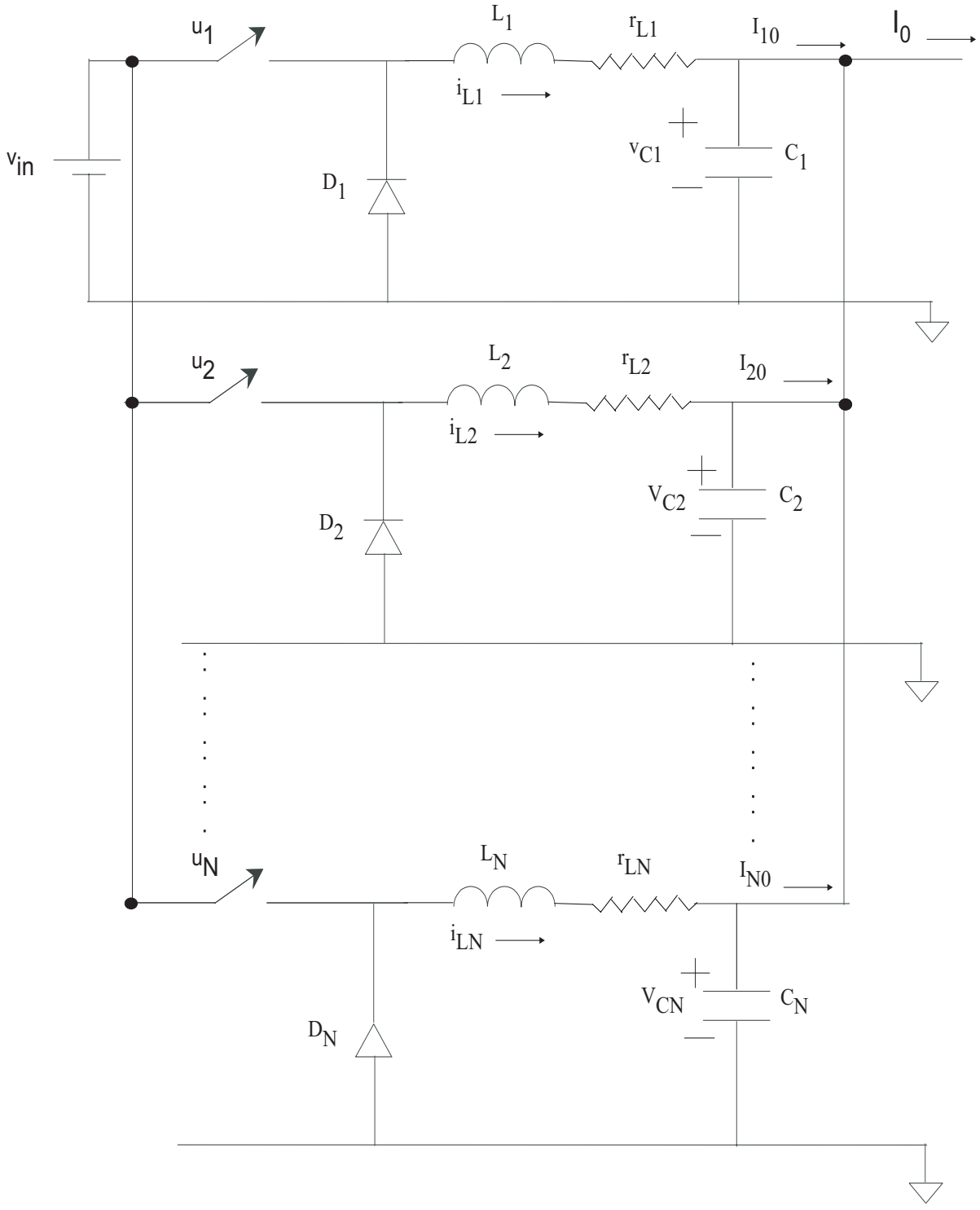

Figure 5.1: Parallel dc-dc buck converter.

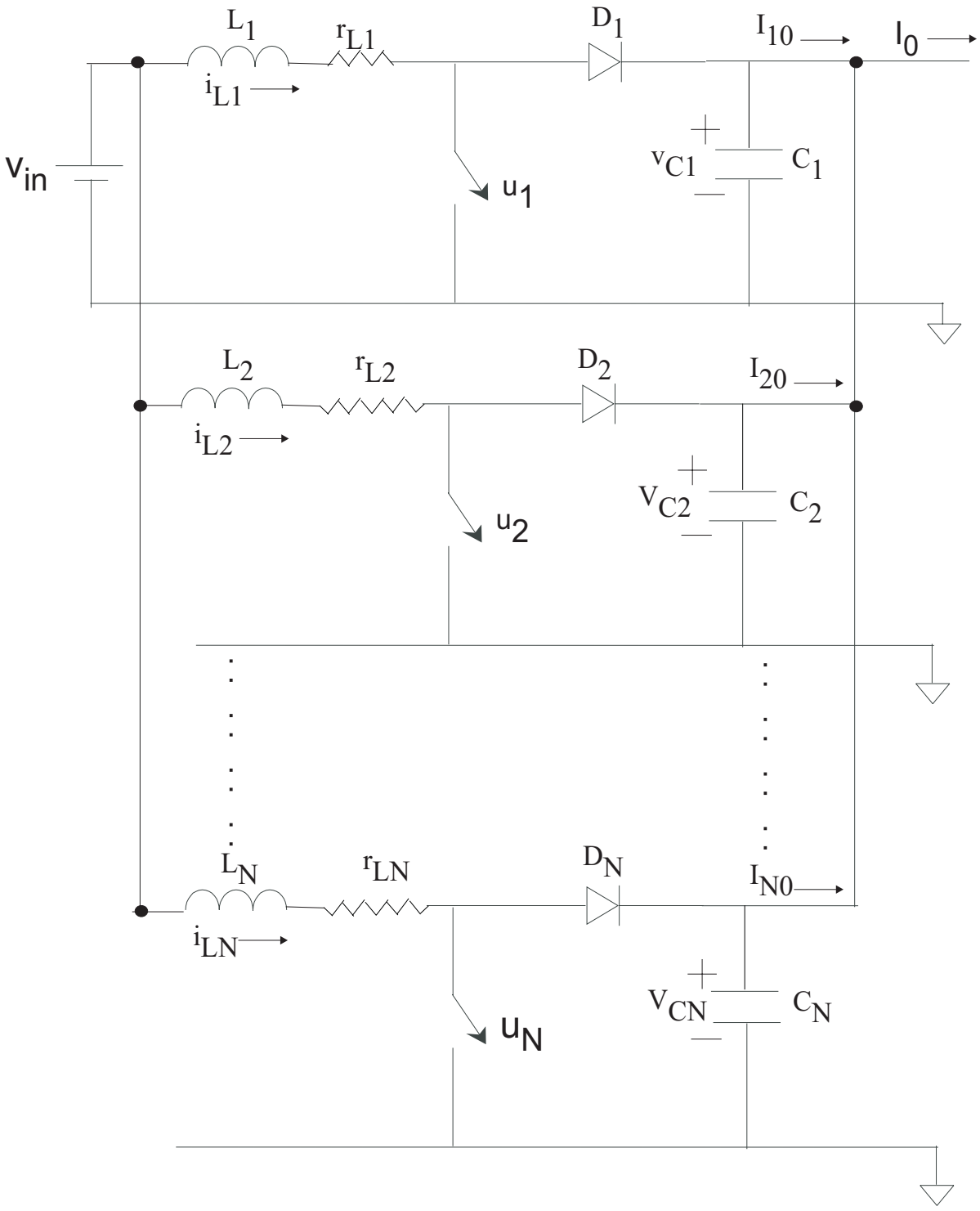

Figure 5.2: Parallel dc-dc boost converter.

with discontinuous right-hand side in the neighborhood of $\sigma_i = 0$ is (Filippov, 1988)

$$\lim_{\sigma_i \to -0} \dot{\sigma}_i > 0 \quad \text{and} \quad \lim_{\sigma_i \to +0} \dot{\sigma}_i < 0 \quad \text{or} \quad \dot{\sigma}_i \sigma_i < 0. \tag{5.5}$$

If the discontinuity surface exists globally, then all of the solutions of (5.4) in the continuity region reach it and stay on it. For the continuity region, the definition of solution is clear (Filippov, 1988). However, the definition of a solution (almost everywhere) as an absolutely continuous function satisfying (5.5) is not always applicable for equations whose right-hand sides are discontinuous on an arbitrary smooth surface. Using the Lebesgue measure, one can apply the definition to the case in which the solutions approach the discontinuity surface on one side and leave it on the other side. When the solutions approach a discontinuity surface on both sides, the conventional definition is unsuitable because there is no indication of how a solution that has reached the discontinuity surface may continue.

$$\dot{y} = f(t, y, u(y)) = h(t, y) \tag{5.6}$$

with discontinuous feedback $u = u(y)$, where $h : \Re \times \Re^n \to \Re^n$ is measurable and essentially locally bounded. A vector function $y(t)$, defined on the interval (t_1, t_2), is a Filippov solution of (5.6) if it is absolutely continuous and, for almost all $t \in (t_1, t_2)$ and for arbitrary $\delta > 0$, the vector $dy(t)/dt$ belongs to the smallest convex closed set of an n-dimensional space containing all of the values of the vector function $h(t, \hat{y})$; where $\hat{y}$ ranges over the entire δ neighborhood of the point $y(t)$ in the space y (with t fixed) except for a set of measure $\mu M = 0$; that is,

$$\frac{dy(t)}{dt} \in H(t, y) \tag{5.7}$$

where $H(.)$ is called Filippov's differential inclusion and is defined as

$$H(t, y) \equiv \bigcap_{\delta > 0} \bigcap_{\mu M > 0} \overline{co}\, h\left(B(y, \delta) - M\right). \tag{5.8}$$

In (5.8), $\overline{co}$ denotes the convex hull of a set, μ is the Lebesgue measure, and B is a ball of radius δ centered at y. The content of Filippov's solution is that the tangent vector to a solution at a time t, where it exists, must lie in the convex closure of the limiting values of the vector field in progressively smaller neighborhoods around the solution evaluated at time t. Let us consider a smooth surface u (shown in Figure 5.3), given by $\sigma(y) = 0$, on which the function $h(t, y)$ is discontinuous. The surface u separates its neighborhood in the y space into the domains P^- and P^+. Suppose that $h(t, y)$ is bounded and, for any fixed t, its limiting values $h^+(t, y)$ and $h^-(t, y)$ exist when u is approached from P^+ and P^-. Let $h_n^+(t, y)$ and $h_n^-(t, y)$ be the projections of $h^+(t, y)$ and $h^-(t, y)$ on the normal $\bigtriangledown\sigma$ to the surface u directed towards P^+ and P^-. Then, for an absolutely continuous $y \in u$ satisfying $h_n^+(t, y) \leq 0$, $h_n^-(t, y) \geq 0$, and $h_n^-(t, y) - h_n^+(t, y) > 0$, the trajectories pointing towards u are solutions of (5.6) according to the differential inclusion (5.7) if and only if

$$\frac{dy}{dt} = \beta(t)h^+(t, y) + (1 - \beta(t))h^-(t, y) = h_o(t, y) \tag{5.9}$$

where

$$\beta(t) = \frac{h_n^-(t, y)}{h_n^-(t, y) - h_n^+(t, y)} \tag{5.10}$$

We note that the right-hand side of (5.9) is orthogonal to $\bigtriangledown\sigma$ and hence the solution remains on the surface u. The sliding mode in a real-life system actually occurs not on its discontinuity surface, but within a boundary layer on which the control components may take up values different from u_i^+ and u_i^- (Utkin, 1992; Utkin et al., 1999). The vector $f(t, y, u)$ in (5.4) may, therefore, take up values which differ from those obtained with $u_i = u_i^+$ and $u_i = u_i^-$. This results in a wider convex set in the Filippov continuation method and, consequently, in a richer set of motions on the sliding mode. In order to handle the regularization problem and find feasible solutions to (5.4), Utkin (1992) proposed an equivalent control method.

Assume that a sliding mode exits on the manifold

$$\sigma(y) = 0, \quad \sigma^T(y) = [\sigma_1(y), \sigma_2(y), \cdots, \sigma_n(y)] \tag{5.11}$$

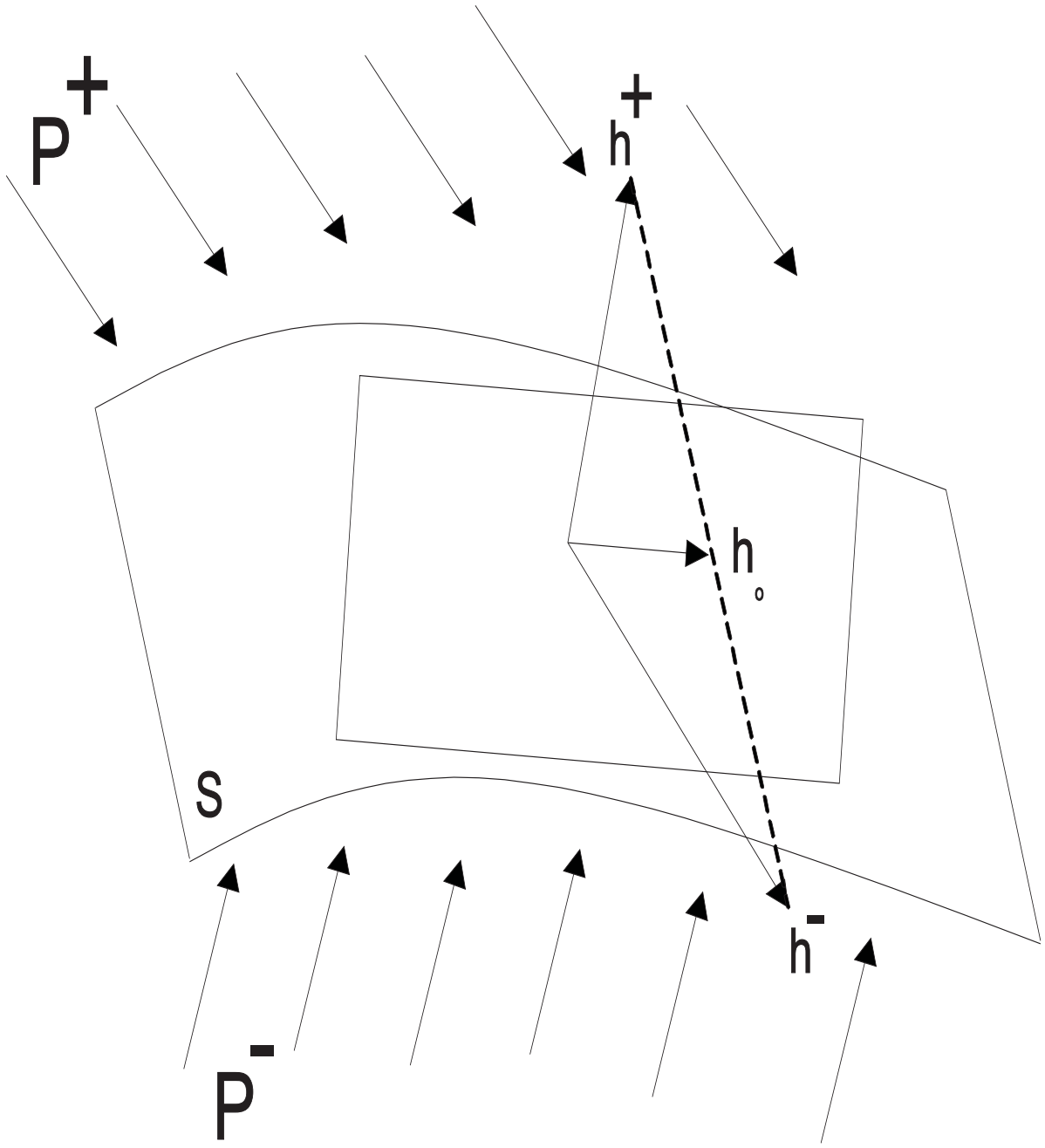

Figure 5.3: Description of Filippov's solution (often called sliding motion) on a discontinuity surface u.

which lies at the intersection of n discontinuity surfaces. Then, we can find a continuous control such that, under the initial position of the state vector on this manifold, the time derivative of the vector $\sigma(y)$ along the trajectories of system (5.4) is identically zero; that is,

$$\dot{\sigma} = \bigtriangledown\sigma_i(y).f(t, y, u_1^{eq}(t, y), \cdots, u_n^{eq}(t, y)) = 0, \quad i = 1, 2, \cdots, n. \tag{5.12}$$

In (5.12), $u^{eq}(t, y) = [u_1^{eq}(t, y), \cdots, u_n^{eq}(t, y)]$ is referred to as the equivalent control for the vector equation (5.4) on the sliding surface (5.11). Therefore, the dynamics of (5.4) on the sliding surface are governed by

$$\dot{y} = f[t, y, u^{eq}(t, y)]. \tag{5.13}$$

Thus a solution is an absolutely continuous vector-valued function, which outside the surfaces σ_i satisfies (5.4) and on these surfaces and on their intersections satisfies (5.13) for almost all t. For a system which is linear with respect to control, when the width of the boundary layer is zero, the solutions obtained using the equivalent control method and Filippov's method are the same. The stability of the solutions of either (5.9) or (5.13) is determined using linear techniques if the sliding manifold is linear. If, however, the sliding manifold is nonlinear, then Lyapunov's methods (II, I) (Hahn, 1963; Khalil, 1996; Sastry, 1999) and bifurcation analyses (Wiggins, 1990; Nayfeh and Balachandran, 1995; Kuznetsov, 1998; Sastry, 1999) are suitable approaches.

5.3 Control Scheme For Parallel DC-DC Buck Converter

The control scheme for the converter has two modes of operation: one when the error trajectories are outside the boundary layer and the other when they are inside the boundary layer. The boundary layer, which is time-varying, is formed by a ramp signal with a frequency

$f_s(=\frac{1}{T})$. The limits of this boundary layer correspond to the maximum and minimum values of the ramp. At the beginning of each switching cycle, we determine whether the error trajectories are within the limits of the time-varying ramp and, based on that, determine what is the mode of operation.

5.3.1 Control Outside the Boundary Layer

To achieve the control objectives, we use smooth hypersurfaces defined by

$$\sigma_k = g_{k_1}(v_{ref_k} - f_{v_k} v_{C_k}) + g_{k_2} \int (v_{ref_k} - f_{v_k} v_{C_k}) d\tau + g_{k_3} \int \Big(\frac{1}{N} \sum_{j=1}^{N} f_{i_j} i_{L_j} - f_{i_k} i_{L_k} \Big) d\tau - f_{i_k} i_{L_k} \tag{5.14}$$

where the g_{k_1}, g_{k_2}, and g_{k_3} are the controller gains, the f_{v_k} (≤ 1) and f_{i_k} (≤ 1) are the sensor gains for the output voltages, load currents, and inductor currents, and the v_{ref_k} are the reference voltages for the bus. The term $\frac{1}{N} \sum_{j=1}^{N} f_{i_j} i_{L_j}$ $(= i_{L_{av}})$ represents the average of all inductor currents. While the first two terms in (5.14) minimize the bus voltage error, the third term enables equal sharing of power among the converter modules. The last term enhances the dynamic response of the closed-loop system. Differentiating (5.14), we obtain

$$\dot{\sigma}_k = -g_{k_1} f_{v_k} \dot{v}_{C_k} + g_{k_2}(v_{ref_k} - f_{v_k} v_{C_k}) + g_{k_3} \Big(\frac{1}{N} \sum_{j=1}^{N} f_{i_j} i_{L_j} - f_{i_k} i_{L_k} \Big) - f_{i_k} \dot{i}_{L_k} \tag{5.15}$$

Using (5.1), we expand (5.15) as

$$\dot{\sigma}_k = -\frac{g_{k_1} f_{v_k}}{C_k} (i_{L_k} - I_{k_0}) + g_{k_2}(v_{ref_k} - f_{v_k} v_{C_k}) + g_{k_3} \Big(\frac{1}{N} \sum_{j=1}^{N} f_{i_j} i_{L_j} - f_{i_k} i_{L_k} \Big) + \frac{f_{i_k}}{L_k} \Big(r_{L_k} i_{L_k} + v_{C_k} - u_k v_{in} \Big). \tag{5.16}$$

Equation (5.16) shows that the sliding surfaces have independent control. The general form of $\dot{\sigma}_k$ is

$$\dot{\sigma}_k = a_k(\Psi_k) + b_k u_k + c_k I_{k_0} \tag{5.17}$$

where $\Psi_k = [i_{L_k}\ v_{C_k}]^T$ and

$$\begin{aligned} a_k &= -\tfrac{g_{k_1} f_{v_k}}{C_k} i_{L_k} + g_{k_2}(v_{ref_k} - f_{v_k} v_{C_k}) + g_{k_3}\Big(\tfrac{1}{N}\textstyle\sum_{j=1}^{N} f_{i_j} i_{L_j} - f_{i_k} i_{L_k}\Big) \\ &\quad + \tfrac{f_{i_k}}{L_k}\Big(r_{L_k} i_{L_k} + v_{C_k}\Big) \\ b_k &= -\tfrac{f_{i_k}}{L_k} v_{in} \\ c_k &= \tfrac{g_{k_1} f_{v_k}}{C_k}. \end{aligned} \tag{5.18}$$

We define

$$u_k = \frac{1}{2}\Big(1 + \text{sign}(\sigma_k)\Big) = u_{k_{eq}} + u_{k_n} \tag{5.19}$$

where $u_{k_{eq}}$ and u_{k_n} represent the equivalent control (Utkin, 1992) and the nonlinear switching control and

$$\text{sign}\,(\sigma_k) = \begin{cases} 1 & \text{if } \sigma_k > 0 \\ -1 & \text{if } \sigma_k < 0 \end{cases}. \tag{5.20}$$

These two controls must satisfy the following constraints:

$$\begin{aligned} &u_k^- < u_{k_{eq}} < u_k^+ \qquad (u_k^-{=}0 \text{ and } u_k^+{=}1) \\ &u_k^- - u_{k_{eq}} \le u_{k_n} \le u_k^+ - u_{k_{eq}}. \end{aligned} \tag{5.21}$$

Knowing that b_k^{-1} exists, we equate (5.17) to zero, solve for $u_{k_{eq}}$, and obtain

$$u_{k_{eq}} = -b_k^{-1}\left(a_k(\Psi_k) + c_k I_{k_0}\right). \tag{5.22}$$

Substituting $u_{k_{eq}}$ into (5.19) and using (5.17) and (5.5), we obtain the following existence condition:

$$\sigma_k b_k u_{k_n} < 0. \tag{5.23}$$

Because $b_k < 0$, (5.23) is satisfied provided that

$$u_{k_n} = \begin{cases} > 0 & \text{if } \sigma_k > 0 \\ < 0 & \text{if } \sigma_k < 0 \end{cases} \tag{5.24}$$

and $u_{k_{eq}}$ satisfies (5.21). For instance, substituting (5.18) into (5.22) yields

$$\begin{aligned} u_{k_{eq}} = & \tfrac{1}{v_{in}} \tfrac{L_k}{C_k} \tfrac{f_{v_k}}{f_{i_k}} g_{k_1} \left(I_{k_0} - i_{L_k}\right) + \tfrac{1}{v_{in}} \tfrac{L_k}{f_{i_k}} g_{k_2} (v_{ref_k} - f_{v_k} v_{C_k}) \\ & + \tfrac{1}{v_{in}} \tfrac{L_k}{f_{i_k}} g_{k_3} \left(\tfrac{1}{N} \textstyle\sum_{j=1}^{N} f_{i_j} i_{L_j} - f_{i_k} i_{L_k} \right) + \tfrac{1}{v_{in}} \left(r_{L_k} i_{L_k} + v_{C_k}\right) \end{aligned} \tag{5.25}$$

and knowing that $\frac{1}{v_{in}} < 1$, $\frac{f_{v_k}}{f_{i_k}}$ is small, $\frac{L_k}{C_k} < 1$ for proper design, and the fourth term in (5.25) is less than one (because $r_L \approx 0$), we can make $u_{k_{eq}}$ satisfy (5.21) by properly chosing g_{k_1}, g_{k_2}, and g_{k_3}.

The stability of the dynamics on the sliding manifold for the parallel buck converter is straightforward because the dynamical equations describing the closed-loop system are in regular form (Utkin, 1992) on this manifold. The dynamical equations on the reduced-order manifold $\bigcap \sigma_k = 0$ ($k = 1, N$) are given by

$$\begin{aligned} \dot{e}_{1_k} &= -f_{v_k} \dot{v}_{C_k} = -\tfrac{f_{v_k}}{C_k} \left(i_{L_k} - I_{k_0}\right) \\ \dot{e}_{2_k} &= e_{1_k} = v_{ref_k} - f_{v_k} v_{C_k} \\ \dot{e}_{3_k} &= \tfrac{1}{N} \textstyle\sum_{j=1}^{N} f_{i_j} i_{L_j} - f_{i_k} i_{L_k}. \end{aligned} \tag{5.26}$$

On the sliding surface $\sigma_k = 0$. Therefore, using (5.14) we obtain

$$f_{i_k} i_{L_k} = g_{k_1} e_{1_k} + g_{k_2} e_{2_k} + g_{k_3} e_{3_k}. \tag{5.27}$$

Substituting (5.27) into (5.26), we obtain a set of linear differential equations of the following form:

$$\begin{aligned} \dot{e}_{1_k} &= \phi_{1_k}(e_{1_k}, e_{2_k}, e_{3_k}) + \tfrac{f_{v_k}}{C_k} I_{k_0} \\ \dot{e}_{2_k} &= \phi_{2_k}(e_{1_k}) \\ \dot{e}_{3_k} &= \phi_{3_k}(e_{1_k}, e_{2_k}, e_{3_k}) + i_{L_{av}} \end{aligned} \tag{5.28}$$

where the ϕ_{1_k}, ϕ_{2_k}, and ϕ_{3_k} are linear functions. For a passive load, the stability of (5.28) can be determined by the eigenvalues of its Jacobian. For example, if the load is a resistor of R ohm, then $I_{k0} = \frac{v_{C_k}}{R}$. If I_{k0} has a time-varying perturbation in addition to its nominal value, then the stability of the solutions of (5.28) can be analyzed by using either Floquet theory or the Lyapunov's method or simply by analyzing the state-transition matrix of (5.28).

5.3.2 Control Inside the Boundary Layer

The derivation of the control laws in the preceding section assumes ideal sliding surfaces. In reality, the switching frequency is finite and hence, instead of the ideal sliding surfaces given by (5.15), we have boundary layers around them. For a boundary layer of finite width, the control laws drived in the preceding section only guarantee that the error trajectories will reach the boundary layer. Within the boundary layers/quasi-sliding surfaces, the dynamics of the system are infinite dimensional due to the delay. One way to describe the dynamics of the converter within the quasi-sliding surfaces is through a nonlinear map. Using one such map, Mazumder et al. (2001b), describe the design of a discrete controller for a parallel three-phase boost converter system. Another way to describe the dynamics within the quasi-sliding surfaces is through a state-space averaged model, which follows from Fillipov's concept of differential inclusion. We use the latter approach in this chapter.

The state-space averaged model for the parallel dc-dc buck converter is given by (Lee, 1990)

$$\begin{array}{l} \frac{d\bar{i}_{L_k}}{dt} = -\frac{1}{L_k}\left(r_{L_k}\bar{i}_{L_k} + \overline{v}_{C_k} - d_k v_{in}\right) \\ \frac{d\overline{v}_{C_k}}{dt} = \frac{1}{C_k}\left(\bar{i}_{L_k} - \overline{I}_{k0}\right), \ \ k = 1, N. \end{array} \tag{5.29}$$

where d_k is the duty ratio. We make an important observation at this point. The control based on the averaged model works only inside the boundary layer. Outside the boundary layer, the controller uses the switching model. Therefore, the controller can guarantee stability even under saturation. Conventional controllers based on small-signal models ignore

the impact of saturation and other nonlinearities. For instance, the averaged model of a parallel-boost converter is nonlinear.

Next, we define the following sliding surfaces:

$$\begin{aligned} \overline{\sigma}_{1_k} &= g_{k_1}\overline{e}_{1_k} + g_{k_2}\overline{e}_{2_k} + g_{k_3}\overline{e}_{3_k} \\ \overline{\sigma}_{2_k} &= \overline{i}_{L_{kd}} - \overline{i}_{L_k} \end{aligned} \tag{5.30}$$

where

$$\begin{aligned} \overline{e}_{1_k} &= v_{ref_k} - f_{v_k}\overline{v}_{C_k} \\ \overline{e}_{2_k} &= \int (v_{ref_k} - f_{v_k}\overline{v}_{C_k})d\tau \\ \overline{e}_{3_k} &= \int \left(\tfrac{1}{N}\textstyle\sum_{j=1}^{N} f_{i_j}\overline{i}_{L_j} - f_{i_k}\overline{i}_{L_k}\right)d\tau. \end{aligned} \tag{5.31}$$

Differentiating $\overline{\sigma}_{1_k}$, we obtain

$$\dot{\overline{\sigma}}_{1_k} = g_{k_1}\dot{\overline{e}}_{1_k} + g_{k_2}\dot{\overline{e}}_{2_k} + g_{k_3}\dot{\overline{e}}_{3_k}. \tag{5.32}$$

Substituting (5.29) into (5.32) yields

$$\dot{\overline{\sigma}}_{1_k} = -\tfrac{g_{k_1} f_{v_k}}{C_k}\left(\overline{i}_{L_k} - \overline{I}_{k_0}\right) + g_{k_2}\dot{\overline{e}}_{2_k} + g_{k_3}\dot{\overline{e}}_{3_k}. \tag{5.33}$$

Substituting for $\overline{i}_{L_k}$ from (5.30) into (5.33), we obtain

$$\dot{\overline{\sigma}}_{1_k} = \tfrac{g_{k_1} f_{v_k}}{C_k}\left(\overline{I}_{k_0} + \overline{\sigma}_{2_k} - \overline{i}_{L_{kd}}\right) + g_{k_2}\dot{\overline{e}}_{2_k} + g_{k_3}\dot{\overline{e}}_{3_k}. \tag{5.34}$$

We let

$$\overline{i}_{L_{kd}} = \beta_{1_k}\overline{\sigma}_{1_k} + \beta_{2_k}\text{sign}\left(\overline{\sigma}_{1_k}\right) + \beta_{3_k}\dot{\overline{e}}_{2_k} + \beta_{4_k}\dot{\overline{e}}_{3_k} \tag{5.35}$$

where β_{1_k}, β_{2_k}, β_{3_k}, and β_{4_k} are constants, in (5.34) and obtain

$$\begin{aligned} \dot{\overline{\sigma}}_{1_k} = &-\tfrac{g_{k_1} f_{v_k}}{C_k}\left(\beta_{1_k}\overline{\sigma}_{1_k} + \beta_{2_k}\text{sign}\left(\overline{\sigma}_{1_k}\right) - \overline{I}_{k_0} - \overline{\sigma}_{2_k}\right) - \left(\tfrac{g_{k_1} f_{v_k}\beta_{2_k}}{C_k} - g_{k_2}\right)\dot{\overline{e}}_{2_k} \\ &- \left(\tfrac{g_{k_1} f_{v_k}\beta_{3_k}}{C_k} - g_{k_3}\right)\dot{\overline{e}}_{3_k} \end{aligned} \tag{5.36}$$

Next we choose $\beta_{3_k} = \frac{C_k g_{k_2}}{f_{v_k} g_{k_1}}$ and $\beta_{4_k} = \frac{C_k g_{k_3}}{f_{v_k} g_{k_1}}$ and reduce (5.36) to

$$\dot{\overline{\sigma}}_{1_k} = -\frac{g_{k_1} f_{v_k}}{C_k} \left(\beta_{1_k} \overline{\sigma}_{1_k} + \beta_{2_k} \text{sign}\left(\overline{\sigma}_{1_k}\right) - \overline{I}_{k_0} - \overline{\sigma}_{2_k} \right) \tag{5.37}$$

Equation (5.37) shows that, when $\overline{\sigma}_{2_k} = 0$, the dynamics on $\overline{\sigma}_{1_k} = 0$ converge provided that $\beta_{2_k} > \overline{I}_{k_{0\,max}}$. We assume that $\overline{\sigma}_{2_k} = 0$ and design the control such that the rate of convergence of the dynamics on $\overline{\sigma}_{2_k} = 0$ are much faster than those on $\overline{\sigma}_{1_k} = 0$.

Next, we differentiate $\overline{\sigma}_{2_k}$ in (5.30) and assign it to $-\frac{\alpha_{1_k}}{L_k}\sigma_{2_k}$ (where α_{1_k} is a positive constant) to guarantee convergence of the dynamics on $\overline{\sigma}_{2_k} = 0$; the result is

$$\dot{\overline{\sigma}}_{2_k} \;=\; \dot{\overline{i}}_{L_{kd}} - \dot{\overline{i}}_{L_k} = \dot{\overline{i}}_{L_{kd}} + \frac{r_{L_k}}{L_k}\overline{i}_{L_k} + \frac{1}{L_k}\overline{v}_{C_k} - \frac{1}{L_k} d_k v_{in} = -\frac{\alpha_{1_k}}{L_k}\overline{\sigma}_{2_k} \tag{5.38}$$

Next, using the Lyapunov function

$$V\left(\overline{\sigma}_{1_k}, \overline{\sigma}_{2_k}\right) = \tfrac{1}{2}\left(\overline{\sigma}_{1_k}^2 + \overline{\sigma}_{2_k}^2\right) \tag{5.39}$$

and (5.37) and (5.38), we cfind that the time derivative of V is given by

$$\dot{V} = \overline{\sigma}_{1_k}\dot{\overline{\sigma}}_{1_k} + \overline{\sigma}_{2_k}\dot{\overline{\sigma}}_{2_k} \leq -\left(\frac{g_{k_1} f_{v_k}}{C_k}\beta_{1_k}\overline{\sigma}_{1_k}^2 + \frac{\alpha_{1_k}}{L_k}\overline{\sigma}_{2_k}^2\right) + \frac{g_{k_1} f_{v_k}}{C_k}\overline{\sigma}_{1_k}\overline{\sigma}_{2_k}. \tag{5.40}$$

is less than zero provided that $\frac{\alpha_{1_k} C_k \beta_{1_k}}{L_k g_{k_1} f_{v_k}} > \frac{1}{4}$.

From (5.38), we obtain

$$d_k = \frac{1}{v_{in}}\left(\alpha_{1_k}\sigma_{2_k} + L_k\dot{\overline{i}}_{L_{kd}} + r_{L_k}\overline{i}_{L_k} + \overline{v}_{C_k}\right). \tag{5.41}$$

Using this duty ratio and a ramp signal (with fixed frequency), we can operate N parallel converters in synchronicty or interleaving. The main difficulty in implementing (5.41) is calculating $\dot{\overline{i}}_{L_{kd}}$. Green and Hedrick (1990) solved this problem approximately by using the first principle of calculus and obtained

$$\dot{\overline{i}}_{L_{kd}} = \frac{\overline{i}_{L_{kd}}(n+1) - \overline{i}_{L_{kd}}(n)}{T}. \tag{5.42}$$

A better approach was proposed by Gerdes (1996) and Swaroop (1997) using the concept of a linear filter. With this approach, we make a minor change in our control derivation. First, we define an auxiliary variable $\underline{i}_{L_k}$ and then pass it through the linear filter

$$\tau_f \dot{\overline{i}}_{L_{kd}} + \overline{i}_{L_{kd}} = \underline{i}_{L_k}, \;\; \overline{i}_{L_{kd}}(0) = \underline{i}_{L_{kd}}(0) \tag{5.43}$$

to obtain $\dot{\overline{i}}_{L_{kd}}$. In (5.43), τ_f is a positive constant, which should be chosen large enough to reduce the high-frequency component of $\underline{i}_{L_k}$, but small enough so as not to alter the low-frequency component, which is, in fact, the equivalent control that we need (Stotsky et al). Finally, we substitute $\underline{i}_{L_k}$ for $\overline{i}_{L_k}$ in (5.35) and obtain

$$\underline{i}_{L_{kd}} = \beta_{1_k}\overline{\sigma}_{1_k} + \beta_{2_k}\text{sign}\,(\overline{\sigma}_{1_k}) + \beta_{3_k}\dot{\overline{e}}_{2_k} + \beta_{4_k}\dot{\overline{e}}_{3_k} \tag{5.44}$$

This solves the control problem inside the limits of the boundary layer.

The implementation of the overall control scheme described in this section and in Section 5.3.1 can be either analog or digital. At the beginning of each switching cycle, by determining whether the σ_k are outside or inside the limits of the boundary layer, we implement the control described in either Section 5.3.1 or in this section. To avoid the possibility of a border collision (Banerjee et al., 1997; Mazumder et al., 2001c), we use comparators with a small hysterisis.

5.4 Control Scheme for Parallel DC-DC Boost Converter

The derivation of the control laws for the parallel dc-dc boost converters is similar to that used in the case of parallel dc-dc buck converter. Hence, in the two subsequent sections, we focus only on the dissimilarities between the control laws of the two converters.

5.4.1 Control Outside the Boundary Layer

We select the sliding surfaces given by (5.14) and differentiate σ_k to obtain (5.15). Using (5.3), we expand $\dot{\sigma}_k$ as

$$\begin{aligned}\dot{\sigma}_k &= -\tfrac{g_{k_1} f_{v_k}}{C_k}\left(\overline{u}_k i_{L_k} - I_{k_0}\right) + g_{k_2}(v_{ref_k} - f_{v_k} v_{C_k}) + g_{k_3}\Big(\tfrac{1}{N}\textstyle\sum_{j=1}^{N} f_{i_j} i_{L_j} - f_{i_k} i_{L_k}\Big) \\ &\quad + \tfrac{f_{i_k}}{L_k}\Big(r_{L_k} i_{L_k} + \overline{u}_k v_{C_k} - v_{in}\Big).\end{aligned} \tag{5.45}$$

which can be written in the following form:

$$\dot{\sigma}_k = a_k(\Psi_k) + b_k(\Psi_k) u_k + c_k I_{k_0} \tag{5.46}$$

where $\Psi_k = [i_{L_k} \quad v_{C_k}]^T$. Using the same argument used to derive (5.23), we obtain the following existence condition for the parallel dc-dc boost converter:

$$\sigma_k b_k(\Psi_k) u_{k_n} < 0 \tag{5.47}$$

which is satisfied provided that

$$u_{k_n} = \begin{cases} > 0 & \text{if } \sigma_k b_k(\Psi_k) > 0 \\ < 0 & \text{if } \sigma_k b_k(\Psi_k) < 0 \end{cases} \tag{5.48}$$

and $u_{k_{eq}}$ satisfies (5.21). The choice of the controller and circuit parameters, such that $u_{k_{eq}}$ satisfies (5.21), is similar to that adopted for the parallel dc-dc buck converter.

5.4.2 Control Inside the Boundary Layer

The state-space averaged model for the parallel dc-dc boost converter is given by (Lee, 1990)

$$\begin{aligned}\tfrac{d\overline{i}_{L_k}}{dt} &= -\tfrac{1}{L_k}\left(r_{L_k}\overline{i}_{L_k} + \overline{d}_k \overline{v}_{C_k} - v_{in}\right) \\ \tfrac{d\overline{v}_{C_k}}{dt} &= \tfrac{1}{C_k}\left(\overline{d}_k \overline{i}_{L_k} - \overline{I}_{k_0}\right), \quad k = 1, N.\end{aligned} \tag{5.49}$$

where $\overline{d}_k = 1 - d_k$ and d_k is the duty ratio. We define the following sliding surfaces:

$$\begin{aligned} \overline{\sigma}_{1_k} &= g_{k_2} \int (v_{ref_k} - f_{v_k} \overline{v}_{C_k}) d\tau + g_{k_3} \int \left(\tfrac{1}{N} \textstyle\sum_{j=1}^{N} f_{i_j} \overline{i}_{L_j} - f_{i_k} \overline{i}_{L_k} \right) d\tau \\ \overline{\sigma}_{2_k} &= \overline{i}_{L_{kd}} - \overline{i}_{L_k}. \end{aligned} \tag{5.50}$$

Differentiating $\overline{\sigma}_{1_k}$, we obtain

$$\dot{\overline{\sigma}}_{1_k} = g_{k_2}(v_{ref_k} - f_{v_k} \overline{v}_{C_k}) + g_{k_3}(\tfrac{1}{N} \textstyle\sum_{j=1}^{N} f_{i_j} \overline{i}_{L_j} - f_{i_k} \overline{i}_{L_k} \Big). \tag{5.51}$$

Letting $i_{L_k} = \overline{i}_{L_{kd}} - \overline{\sigma}_{2_k}$ in (5.51) yields

$$\dot{\overline{\sigma}}_{1_k} = g_{k_2}(v_{ref_k} - f_{v_k} \overline{v}_{C_k}) + g_{k_3} f_{i_k} (\tfrac{1}{f_{i_k}} \tfrac{1}{N} \textstyle\sum_{j=1}^{N} f_{i_j} \overline{i}_{L_j} + \overline{\sigma}_{2_k} - \overline{i}_{L_{kd}} \Big). \tag{5.52}$$

We choose $\overline{i}_{L_{kd}}$ as

$$\overline{i}_{L_{kd}} = h_{1_k} \overline{\sigma}_{1_k} + h_{2_k} \text{sign}(\overline{\sigma}_{1_k}) + \tfrac{g_{k_2}}{g_{k_3} f_{i_k}} (V_{r_k} - f_{v_k} \overline{v}_{C_k}) + \tfrac{1}{f_{i_k}} \tfrac{1}{N} \textstyle\sum_{j=1}^{N} f_{i_j} \overline{i}_{L_j} \tag{5.53}$$

to guarantee convergence of the dynamics on the hypersurfaces $\overline{\sigma}_{1_k} = 0$.

Next, we differentiate σ_{2_k} and assign it to

$$\dot{\overline{\sigma}}_{2_k} = \dot{\overline{i}}_{L_{kd}} - \dot{\overline{i}}_{L_k} = -\tfrac{h_{4_k}}{L_k} \overline{\sigma}_{2_k} \tag{5.54}$$

to guarantee convergence of the dynamics on the hypersurfaces $\overline{\sigma}_{2_k} = 0$. By substituting (5.49) into (5.54) and using the same argument used to derive d_k for parallel dc-dc buck converter, we obtain

$$\overline{d}_k = 1 - d_k = 1 + \tfrac{1}{v_{C_k}} \left(L_k \dot{\overline{i}}_{L_{kd}} + r_{L_k} \overline{i}_{L_k} + h_{4_k} \overline{\sigma}_{2_k} - v_{in} \right) \tag{5.55}$$

which guarantees convergence on the hypersurface $\overline{\sigma}_{2_k} = 0$. The duty-ratio signal enables the PWM operation of the parallel dc-dc boost converter within the boundary layer. The procedure for solving the problem associated with $\dot{\overline{i}}_{L_{kd}}$ is the same as that described in Section 5.3.2.

5.5 Results

We performed several simulations on a parallel-buck converter that has two modules (M1 and M2). The nominal values of the parameters for M1 and M2 are shown in Table 5.1. The input voltage varies between 25-50 V. The output voltage is regulated at 5 volts. The objectives of the simulations are to find out the effectiveness of the sliding-mode control schemes in regulating the bus voltage and sharing the power delivered to a resistive load under steady-state and dynamic conditions. The controller parameters are tuned so that, for the worst case disturbance, the conditions of existence of the sliding modes are satisfied and the dynamics on the sliding manifold are stable. Because it is physically impossible to have identical converters and an infinite switching frequency, we demonstrate the transient and steady-state performance of the control to variations in the circuit parameters of the two modules under a finite switching frequency. To obtain a finite switching frequency inside the boundary layer, we compare the error signals of each module, obtained using d_k, with ramp signals having a switching frequency of 100 kHz. For operating the modules using interleaving, we phase shift the ramp signals of the two modules by half a switching-cycle period. Figure 5.4 shows the response of the closed-loop converter when it is subjected to a sudden change in the load resistance from 2.5 Ω to 0.625 Ω, which is the maximum variation in load allowed for the given converter. The input voltage is fixed at its minimum (i.e., 25 V), and hence M1 and M2 are subjected to the worst case of transients in the load. We consider two cases: one when M1 and M2 are identical and the other when they are different. The results for case one are shown in Figures 5.4a-5.4c. They show that the drop in the output voltage is less than 1% even though the load resistance is decreased four-fold. Besides, the sharing of the power delivered to the load is good under steady-state and transient conditions.

Although the responses of the converter for case one are good, in real life, due to manufacturing tolerances, it is not possible to have identical modules. Therefore, the second case considers a more practical scenario. We fix L_1, C_1, g_{1_1}, g_{1_2}, and g_{1_3} at their nominal

Table 5.1: Nominal parameters for modules M1 and M2 of the parallel dc-dc buck converter.

Parameter	Nominal Value
$r_{L_1} = r_{L_2} = r_{L_n}$	0.021 Ω
$L_1 = L_2 = L_n$	50 μH
$C_1 = C_2 = C_n$	4400 μF
$v_{ref_1} = v_{ref_2}$	2.0 V
$f_{i_1} = f_{i_2} = f_{i_n}$	1.0
$f_{v_1} = f_{v_2} = f_{v_n}$	0.4
$g_{1_1} = g_{2_1} = g_{n_1}$	$2*10^2$
$g_{1_2} = g_{2_2} = g_{n_2}$	$10*10^4$
$g_{1_3} = g_{2_3} = g_{n_3}$	$5*10^2$
Switching frequency	$100kHz$
DC offset of ramps	1.8 V
Height of ramps	3.0 V

values but change the parameters for M2 so that $L_2 = 0.75\ L_n$, $C_2 = 0.75\ C_n$, $g_{2_1} = 0.9\ g_{n_1}$, $g_{2_2} = 0.9\ g_{n_2}$, and $g_{2_3} = 0.9\ g_{n_3}$. These parametric variations are more than what one will typically encounter for such converters (McLyman, 1993). The results in Figures 5.4d-5.4f show that, inspite of the parametric variations, the transient and steady-state performances of the converter are close to those of the ideal case.

In the second case, we investigate whether M1 and M2 operate with interleaving. A closer examination of the inductor currents in Figures 5.5a-5.5b under steady-state and transient conditions show that indeed they operate with a phase shift of half the switching-cycle period. The ripple of the current i_{L_2} is larger than that of i_{L_1} because the magnitude of L_2 is smaller than that of L_1. The interleaved operation of the converter is possible because, inside the boundary layer, the controllers use the duty-ratio signals for pulse-width modulation. The latter ensures the operation of the converter with a constant switching frequency. We

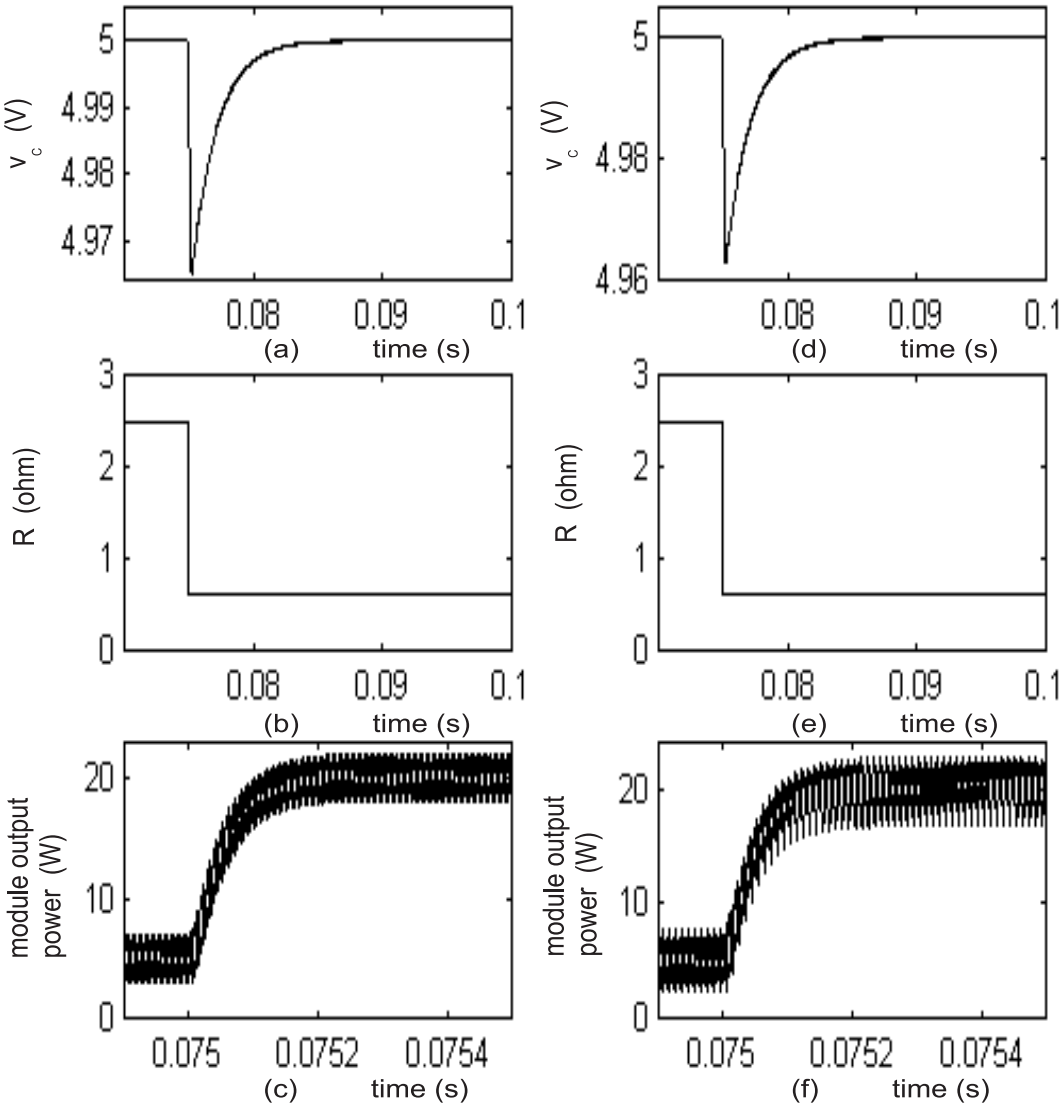

Figure 5.4: Dynamic and steady-state performances of a parallel-buck converter when the parameters of the two modules are the same (a-c) and when they are different (d-f). The converter is initially in steady state and then subjected to a sudden change in the load resistance.

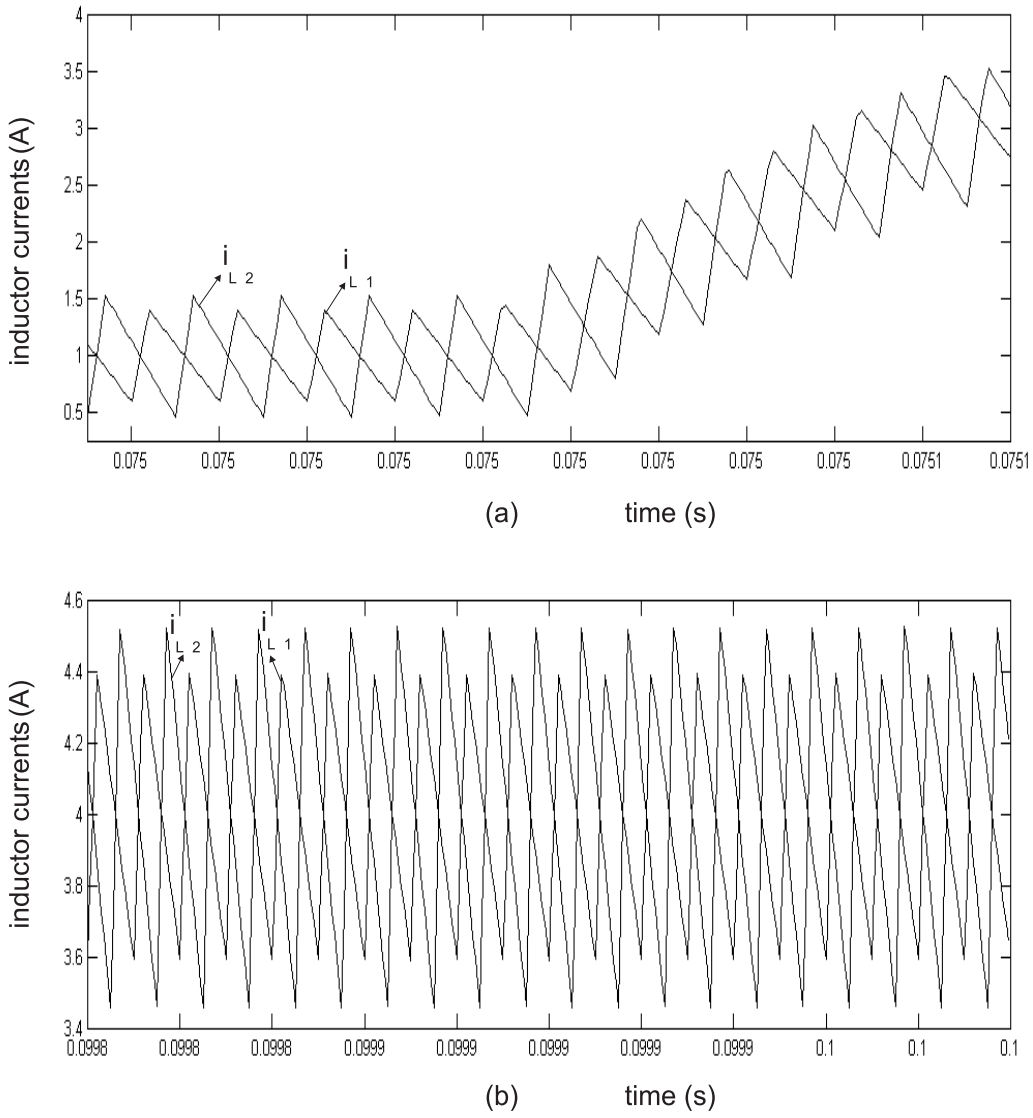

Figure 5.5: The waveforms of the inductor currents i_{L_1} and i_{L_2} are phase-shifted by half the switching-cycle period. Thus, the new variable-structure controller ensures interleaved/phase-shifted operation during (a) transient and (b) steady-state conditions and keeps the switching frequency constant.

note that, using a conventional sliding-mode control, interleaving and constant frequency of operation are not possible (Utkin et al., 1999).

The choice of the controller gains g_{1_1}, g_{2_1}, g_{1_2}, g_{2_2}, g_{1_3}, and g_{2_3} is critical to the steady-state and transient responses of the closed-loop converter. In Figures 5.6-5.8, we show the impact of variations in these controller gains on the performance of the converter for the second case. We fix the input voltage at 25 V and change the load resistance from 2.5 Ω to 0.625 Ω. We sample the inductor currents and the capacitor voltages at the switching frequency so that we can suppress the ripple from the waveforms and get a clearer comparison. The sampling is done at the beginning of each switching cycle of M1. At this instant and under steady-state conditions, i_{L_1} attains its lowest value. Because M2 operates with a phase shift of half a switching cycle as compared to M1, the sampled value of i_{L_2} will in general be larger than that of i_{L_1} at the sampling instant.

Figures 5.6a and 5.6b show the effect of variations in g_{1_1} and g_{2_1} on the output voltages and inductor currents. The plots marked $v_C(1)$, $i_{L_1}(1)$, and $i_{L_2}(1)$ are obtained using $g_{1_1} = g_{n_1}$ and $g_{2_1} = 0.9g_{n_1}$, with the remaining parameters being the same as in case two. The other sets of plots marked $v_C(2)$, $i_{L_1}(2)$, and $i_{L_2}(2)$, and $v_C(3)$, $i_{L_1}(3)$, and $i_{L_2}(3)$ are obtained by reducing only g_{1_1} and g_{2_1} by 50% and 75%, respectively. When g_{1_1} and g_{2_1} are reduced, the transient response of the system deteriorates. This is prominent in the plots marked $v_C(3)$, $i_{L_1}(3)$, and $i_{L_2}(3)$ in Figure 5.6; they show a strong undershoot and an overshoot.

Next, we show in Figures 5.7a and 5.7b the effect of variations in g_{1_2} and g_{2_2}. Initially, the values of all of the parameters of M1 and M2 are the same as in case two. The waveforms for this case are marked $v_C(1)$, $i_{L_1}(1)$, and $i_{L_2}(1)$. Then, we reduce g_{1_2} and g_{2_2} by 50% and 75%. The results for these three cases are denoted by $v_C(2)$, $i_{L_1}(2)$, and $i_{L_2}(2)$, and $v_C(3)$, $i_{L_1}(3)$, and $i_{L_2}(3)$, respectively. As g_{1_2} and g_{2_2} are reduced, the capacitor voltage takes much longer to attain steady state after a transient. On the other hand, increasing g_{1_2} and g_{2_2} too much results in overshoots of the inductor currents. The trade-off in the gains depends on the application of the power supply.

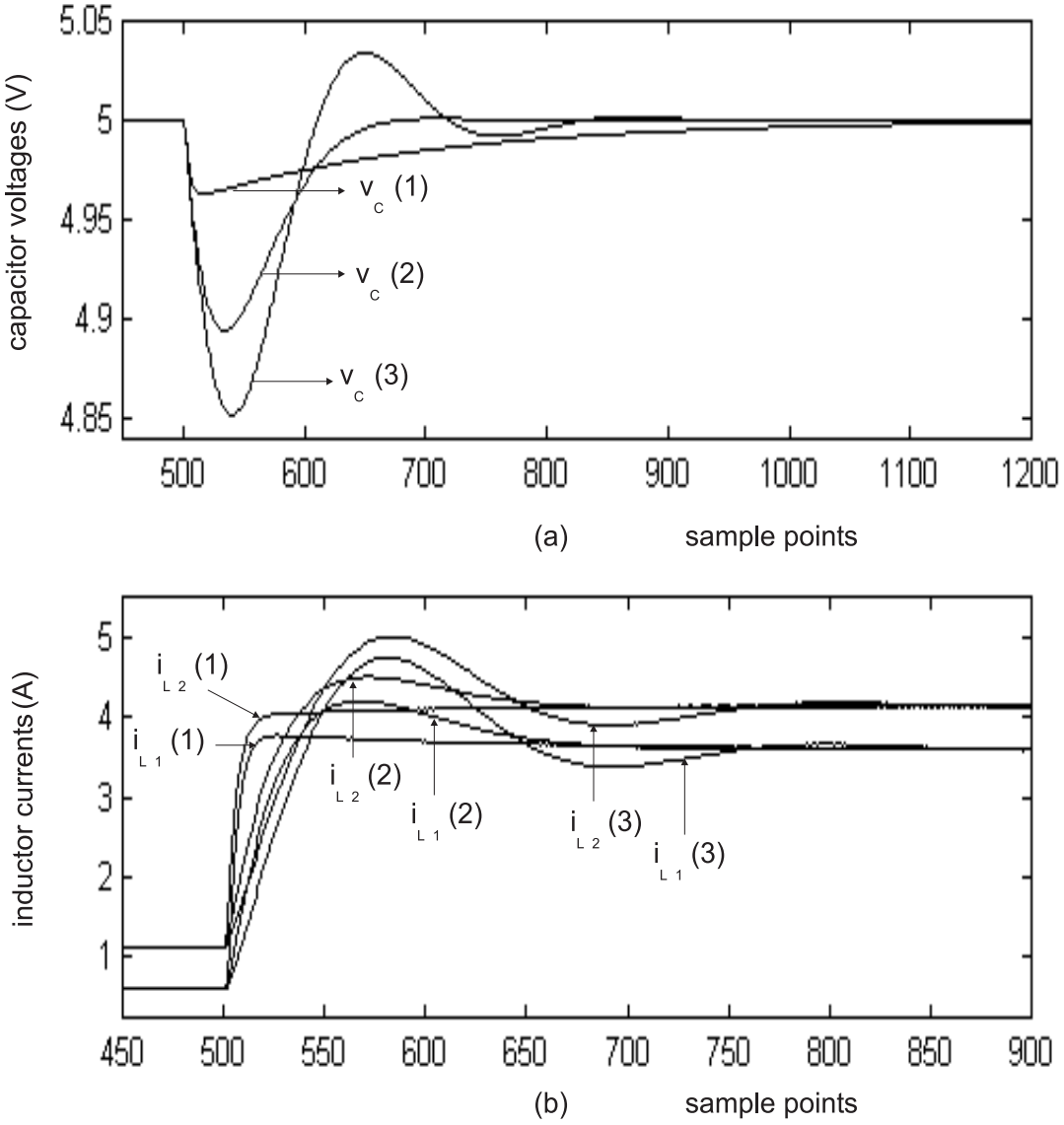

Figure 5.6: Impact of variations in the controller gains g_{1_1} and g_{2_1} on the (a) output voltages and (b) the inductor currents of M1 and M2.

Similarly, by swapping g_{1_3} for g_{1_2} and g_{2_3} for g_{2_2}, we obtain Figures 5.8a and 5.8b, which show the impact of these controller gains on the load sharing. The corresponding plots are

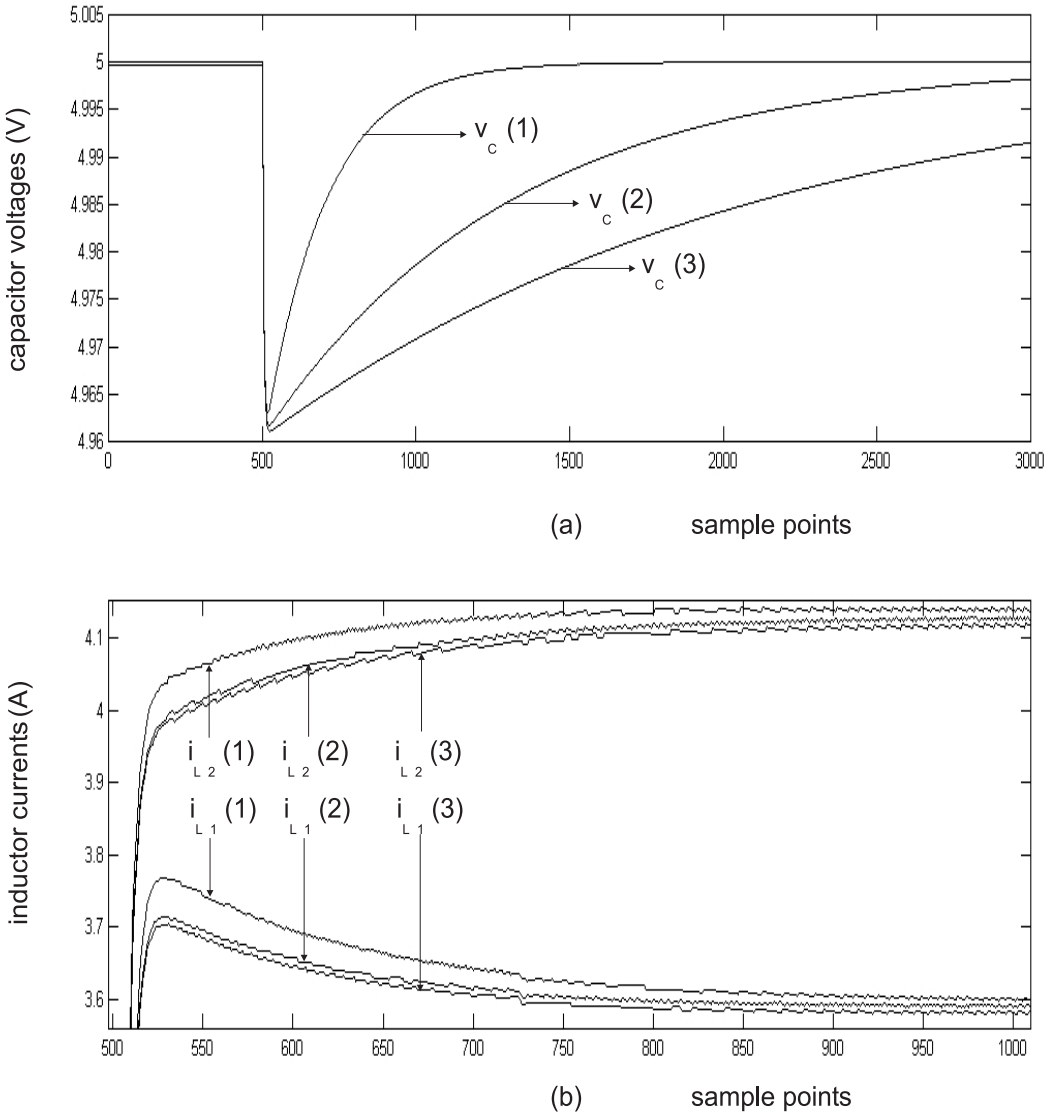

Figure 5.7: Effect of variations in the controller gains g_{1_2} and g_{2_2} on the (a) output voltages and (b) the inductor currents of the parallel converter.

marked $v_C(1)$, $i_{L_1}(1)$, and $i_{L_2}(1)$, $v_C(2)$, $i_{L_1}(2)$, and $i_{L_2}(2)$, and $v_C(3)$, $i_{L_1}(3)$, and $i_{L_2}(3)$, respectively. First, we observe that the effect of the variations in g_{1_3} and g_{2_3} on the output

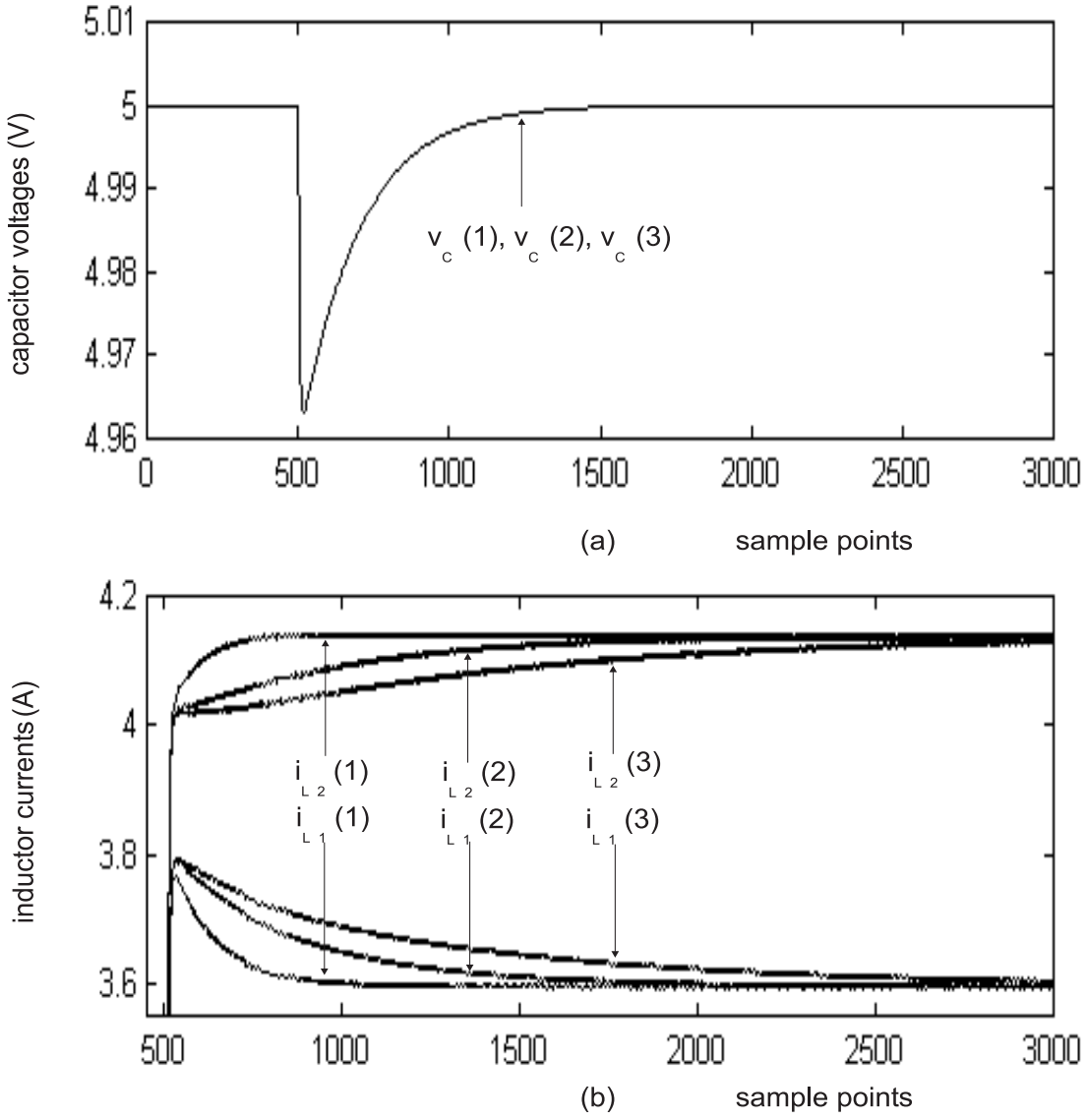

Figure 5.8: Impact of variations in the controller gains g_{1_3} and g_{2_3} on the (a) output voltages and (b) the inductor currents of the converter modules.

voltage is negligible. Second, with a reduction in the gains, the load sharing deteriorates immediately after the transient condition. Hence, g_{1_3} and g_{2_3} must be chosen carefully;

otherwise an uneven distribution of power among the converter modules occurs.

Next, we demonstrate the performance of the parallel converter when the input voltage changes from $50V$ to $25V$. This variation in the input voltage is the maximum allowed by the design specifications. The load resistance is fixed at its minimum (i.e., 0.625Ω), and hence M1 and M2 are subjected to the worst transient in the input voltage. We again consider the same two cases used to obtain Figures 5.4a-5.4f. Figures 5.9a-5.9c and 5.9d-5.9f show the results for cases one and two, respectively. They show that the drop in the output voltage is less than 1%. In addition, interleaving between the two converter modules, for the ideal and the realistic cases, is maintained under static and dynamic conditions. It is obvious, that even under a severe feedforward disturbance, the performance of the converter is good.

Finally, we show the results of the simulations performed on the parallel dc-dc boost converter having two modules. The nominal values for the circuit parameters are $r_{L_1} = r_{L_2} = 25$ mΩ, $L_1 = L_2 = 25\ \mu H$, and $C_1 = C_2 = 150\ \mu F$. The output voltage is regulated at 20 volts and the input voltage varies between 12-18 volts. In the vicinity of the boundary layer, the switching frequency is 100 kHz. In Figures 5.10-5.11, we compare the dynamic and steady-state performances of the parallel dc-dc boost converter for two cases: one when the modules have the same parameters, and the other when they have different parameters. The parametric variations between the two converter modules involve a 25% variation in the bus capacitance and line inductance and a 10% variation in the controller gains. Based on the negligible drop in the bus voltage and good load sharing, even when the converter is subjected to a maximum feedforward and feedback disturbance, we conclude that the dynamic response of the closed-loop system is good.

5.6 Summary and Conclusion

We describe a robust control scheme for parallel dc-dc buck and boost converters and determine the region of existence of the sliding surfaces and the stability of the reduced-

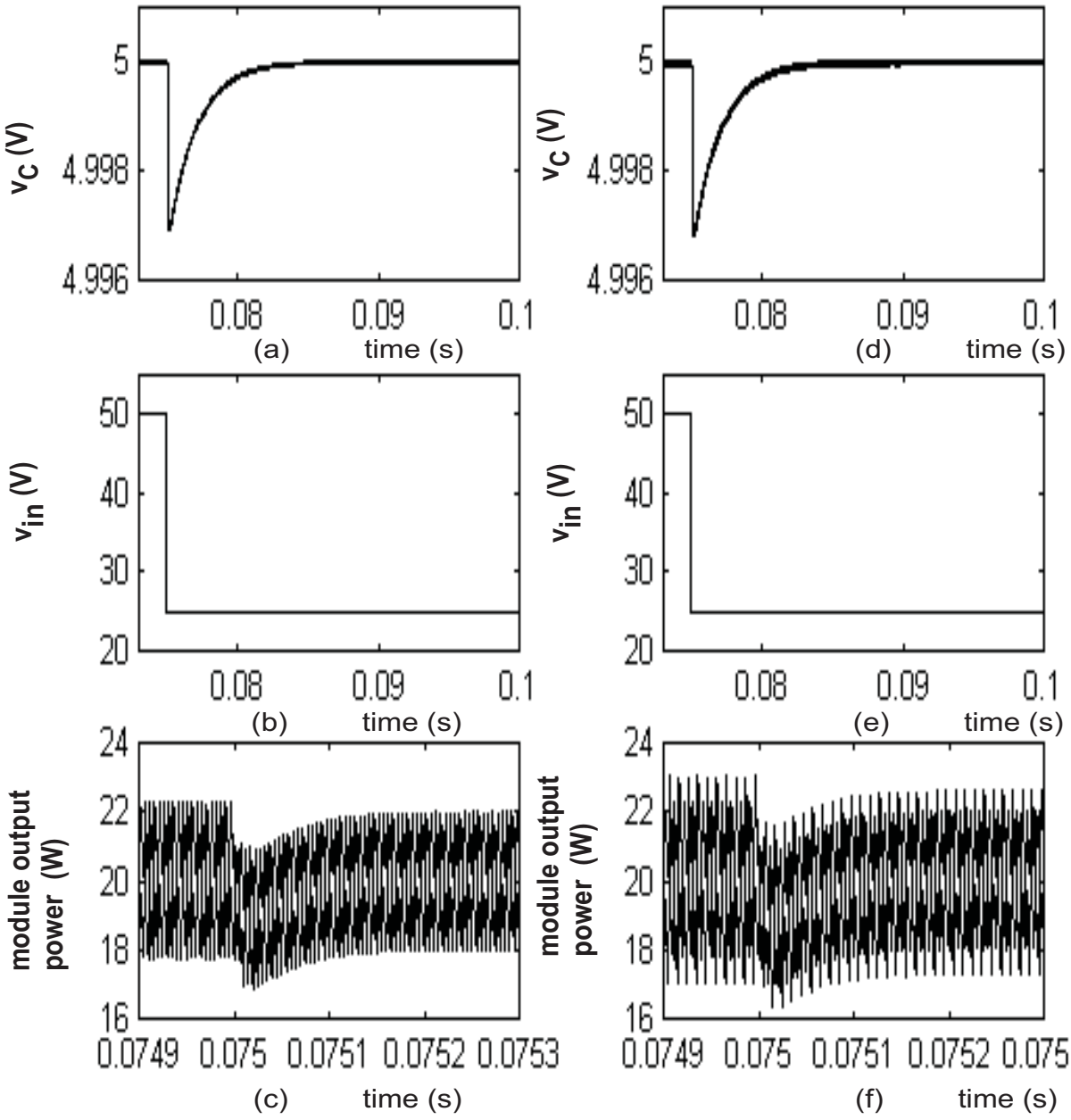

Figure 5.9: Transient and steady-state performances of a parallel-buck converter when the parameters of the two modules are the same (a-c) and when they are different (d-f). The converter is initially in steady state and then subjected to a sudden change in the input voltage.

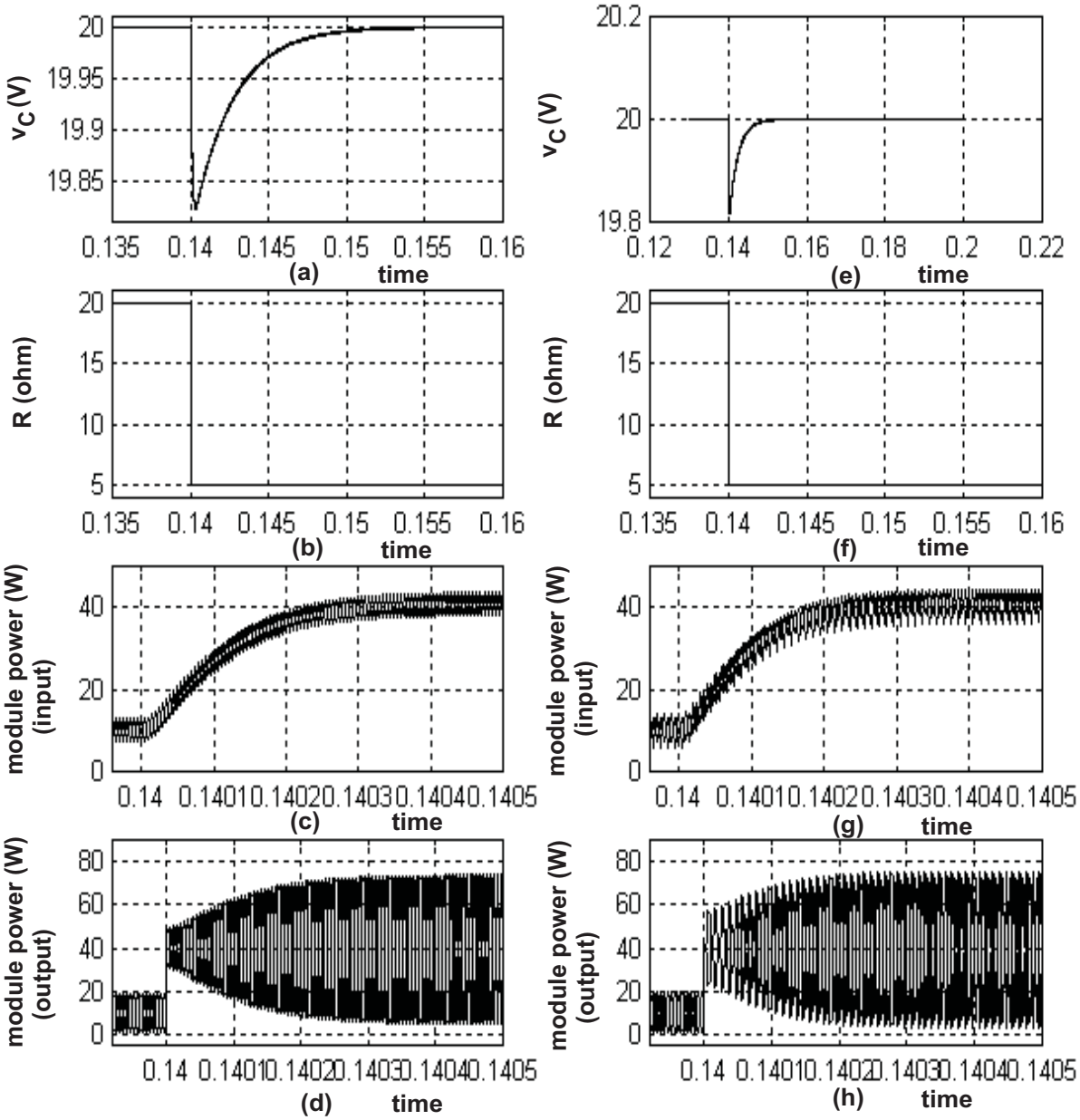

Figure 5.10: Performance of the parallel dc-dc boost converter when subjected to a change in the load resistance. The responses of the closed-loop system when the two modules have the same parameters are shown in (a-c). The performances of the parallel-boost converter when the parameters of the modules are different are shown in (d-f).

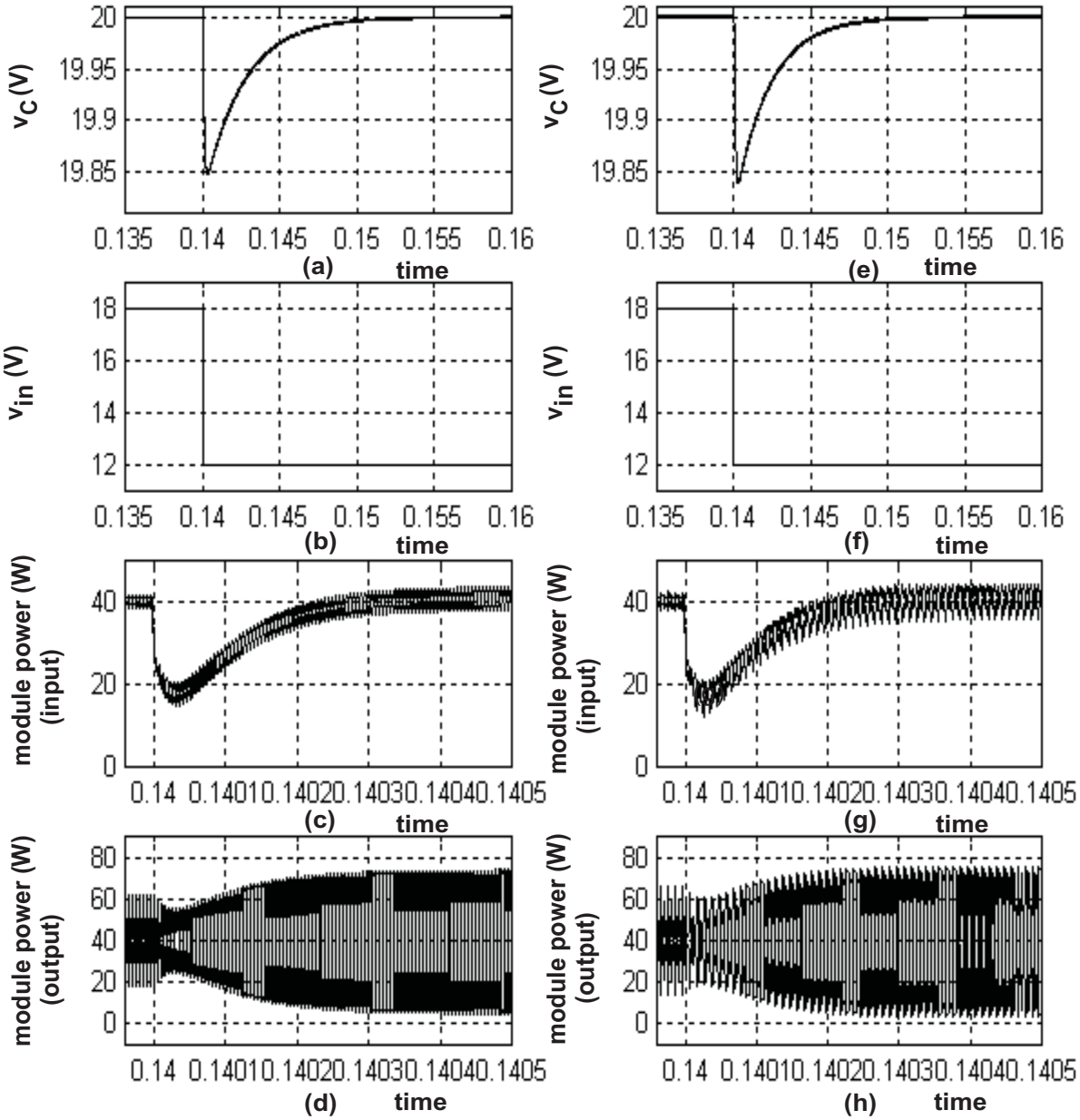

Figure 5.11: Dynamic and steady-state performances of the parallel dc-dc boost converter when the parameters of the two modules are the same (a-c) and when they are different (d-f). The converter is initially in steady state and then subjected to a sudden change in the input voltage.

order dynamical system on the sliding manifold. To keep the switching frequency constant, we adopt a hybrid control strategy within the boundary layer. In addition, the hybrid approach enables us to switch the converters using interleaved or synchronous modulation strategies. The proposed controller combines the concepts of intergral-variable-structure and multiple-sliding-surface controls. This enables the controller to achieve better steady-state and dynamic performance even in the presence of parametric variations and disturbances.

Chapter 6

Stabilization of Parallel Nonisolated Multi-Phase (and Multi-Stage) PWM Converters Using Nonlinear Variable-Structure Control

In this chapter, we develop nonlinear, variable-structure controllers to stabilize parallel multi-phase and multi-leg PWM converters. We begin by developing control schemes for a parallel converter, which has two three-phase PWM converter modules connected to a common output. This converter represents a nonlinear and nonminimum phase system, and hence the stability of the closed-loop system using the linear control schemes described in (Xing et al., 1998, 1999; Ye et al., 2000) may not be guaranteed except in the vicinity of a periodic orbit. By using a nonlinear controller, we intend to improve the stability and the dynamic performance of the closed-loop parallel converter under varying operating conditions. We propose three control schemes; two of which are developed in the continuous domain, and the third is developed in the discrete domain. The latter scheme combines SVM with a variable-structure controller. This is for the first time that such a control

scheme has been developed to control a parallel three-phase PWM converter. Using this scheme, we can keep the frequency of the power-converter modules constant under steady state and retain the superior dynamic performance of variable-structure controllers. For each of the controllers, the steady-state and dynamic performances of the closed-loop system are given. In addition, the two modules have different switching frequencies and they switch asynchronously. Hence, clock synchronization of the two modules is not necessary.

We then demonstrate how to extend the control scheme for stabilizing a multi-phase boost parallel converter having N (> 2) modules. Furthermore, we demonstrate how the same control scheme can be used to stabilize a parallel converter driving a constant-power, unbalanced, or dynamic load or operating under phase imbalance. We also demonstrate how the control schemes can be used to stabilize a multi-phase and four-leg inverter driving an unbalanced load.

6.1 Modeling and Analysis of the Parallel Three-Phase Boost Converter

In Figure 6.1, we show a schematic of a parallel three-phase boost converter (PTBC) with two power modules. For each individual module, we assume that the variation in the line inductance of each phase is negligible. However, the line inductances for two different modules are different. We also assume that the esr of the output capacitor is negligible and that the input voltages are balanced; that is, $V_a + V_b + V_c = 0$.

Based on Figure 6.1, we obtain the following differential equations (with discontinuous right-hand sides) that describe the dynamics of the PTBC:

$$\begin{aligned} \dot{v}_C(t) &= -\tfrac{1}{C} i_{load}(t) + \tfrac{1}{C} \textstyle\sum_{k=1}^{2} \Big(\sum_{j=1}^{3} i_{L_{kj}}(t) u_{kj}(t) \Big) \\ \dot{\vec{i}}^{abc}_{L_k}(t) &= \Big(P_{k1} + P_{k2} \Big) \vec{i}^{abc}_{L_k}(t) + P_{k3} \vec{V}^{abc}(t) + P_{k4} \vec{u}^{abc}_1(t) v_C(t) + P_{k5} \vec{u}^{abc}_2(t) v_C(t). \end{aligned} \tag{6.1}$$

In (6.1) and for the rest of the chapter, $k = 1$ and 2. The vectors representing the phase

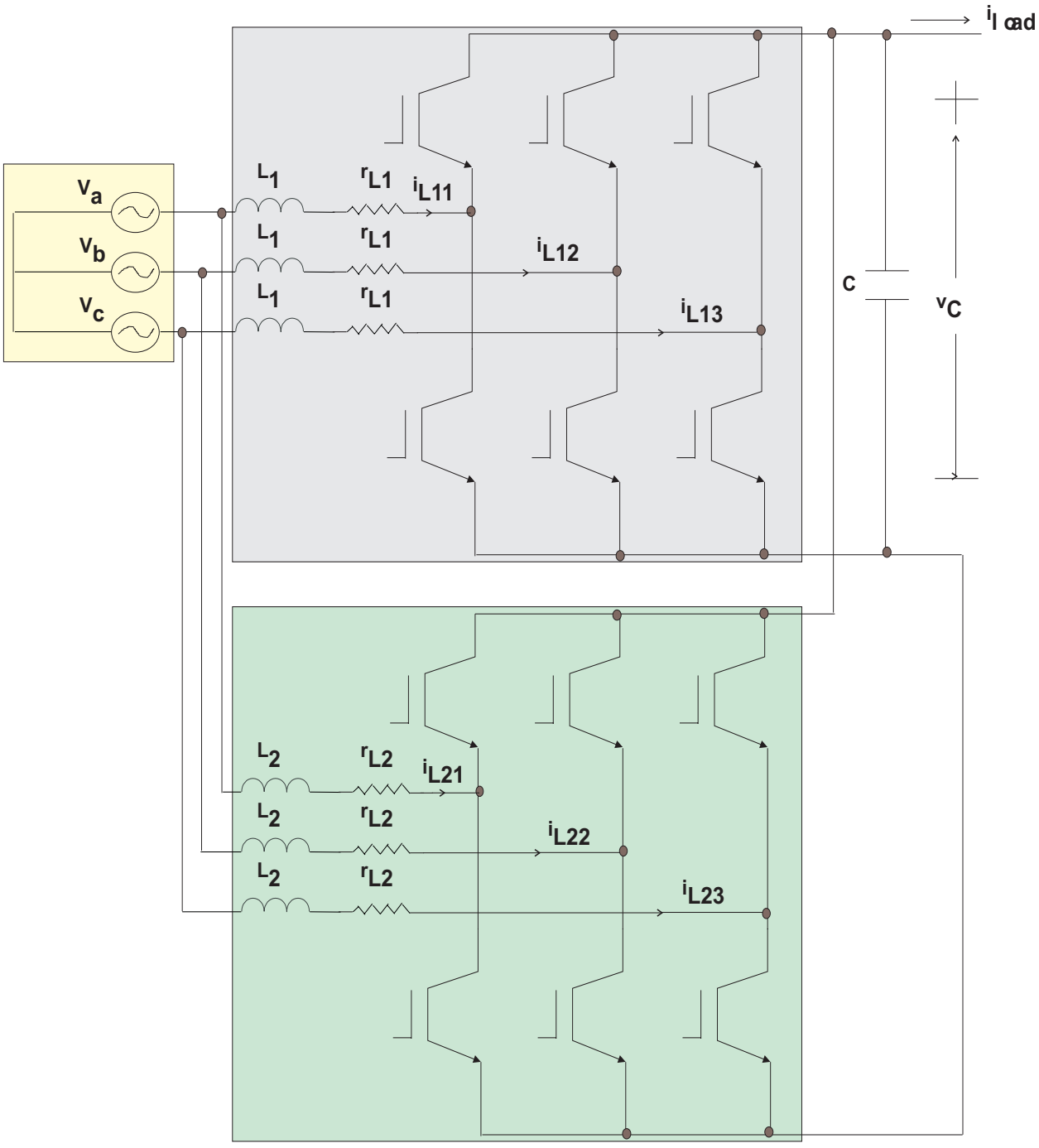

Figure 6.1: Schematic of the parallel three-phase boost converter (PTBC).

currents and switching functions of M1 and M2 are given by

$$\vec{i}_{L_k}^{abc}(t) = \left[i_{L_{k1}}(t) \;\; i_{L_{k2}}(t) \;\; i_{L_{k3}}(t) \right]^T \tag{6.2}$$

and

$$\vec{u}_k^{abc}(t) = \left[u_{k1}(t) \;\; u_{k2}(t) \;\; u_{k3}(t) \right]^T \tag{6.3}$$

respectively. In (6.1), $\vec{V}^{abc} = [V_a \; V_b \; V_c]^T$ and the matrices P_{ki} $(i = 1, 2, \cdots 5)$ are given by

$$P_{11} = -\frac{r_{L_1}}{3L_1(L_1+L_2)} \begin{bmatrix} 3L_1+2L_2 & -L_2 & -L_2 \\ -L_2 & 3L_1+2L_2 & -L_2 \\ -L_2 & -L_2 & 3L_1+2L_2 \end{bmatrix} \tag{6.4}$$

$$P_{12} = -\frac{r_{L_2}}{3(L_1+L_2)} \begin{bmatrix} 1 & 1 & 1 \\ 1 & 1 & 1 \\ 1 & 1 & 1 \end{bmatrix} \tag{6.5}$$

$$P_{13} = \frac{1}{3L_1} \begin{bmatrix} 2 & -1 & -1 \\ -1 & 2 & -1 \\ -1 & -1 & 2 \end{bmatrix} \tag{6.6}$$

$$P_{14} = -\frac{1}{3L_1(L_1+L_2)} \begin{bmatrix} 3L_1+2L_2 & -L_2 & -L_2 \\ -L_2 & 3L_1+2L_2 & -L_2 \\ -L_2 & -L_2 & 3L_1+2L_2 \end{bmatrix} \tag{6.7}$$

$$P_{15} = \frac{1}{3L_1(L_1+L_2)} \begin{bmatrix} L_1 & L_1 & L_1 \\ L_1 & L_1 & L_1 \\ L_1 & L_1 & L_1 \end{bmatrix} \tag{6.8}$$

$$P_{21} = -\frac{r_{L_1}}{3(L_1+L_2)} \begin{bmatrix} 1 & 1 & 1 \\ 1 & 1 & 1 \\ 1 & 1 & 1 \end{bmatrix} \tag{6.9}$$

$$P_{22} = -\frac{r_{L_2}}{3L_2(L_1+L_2)} \begin{bmatrix} 3L_2+2L_1 & -L_1 & -L_1 \\ -L_1 & 3L_2+2L_1 & -L_1 \\ -L_1 & -L_1 & 3L_2+2L_1 \end{bmatrix} \tag{6.10}$$

$$P_{23} = \frac{1}{3L_2} \begin{bmatrix} 2 & -1 & -1 \\ -1 & 2 & -1 \\ -1 & -1 & 2 \end{bmatrix}$$
$$P_{24} = \frac{1}{3L_2(L_1+L_2)} \begin{bmatrix} L_2 & L_2 & L_2 \\ L_2 & L_2 & L_2 \\ L_2 & L_2 & L_2 \end{bmatrix} \tag{6.11}$$

$$P_{25} = -\frac{1}{3L_2(L_1+L_2)} \begin{bmatrix} 3L_2+2L_1 & -L_1 & -L_1 \\ -L_1 & 3L_2+2L_1 & -L_1 \\ -L_1 & -L_1 & 3L_2+2L_1 \end{bmatrix}. \tag{6.12}$$

For the PTBC, the top and bottom switches of any phase are complementary in nature. The switching functions u_{kj} ($j = 1, 2, 3$) attain a value of -1 (or 1) if the bottom (or top) switch of any phase is on. For the boost converter, $\vec{u}_1^{abc}(t)$ ($\vec{u}_2^{abc}(t)$) can attain only eight discrete values $\Big(U_0 = [-1\ -1\ -1]^T, U_1 = [1\ -1\ -1]^T, U_2 = [1\ \ 1\ -1]^T, U_3 = [-1\ \ 1\ -1]^T, U_4 = [-1\ \ 1\ \ 1]^T, U_5 = [-1\ -1\ \ 1]^T, U_6 = [1\ -1\ \ 1]^T, U_7 = [1\ \ 1\ \ 1]^T \Big)$ for feasible operation, as shown in Figure 6.2. Two of these $\Big(U_0$ and $U_7\Big)$ are the zero vectors, while the other six are the active vectors. For convenience, we will drop the notation of time from now on.

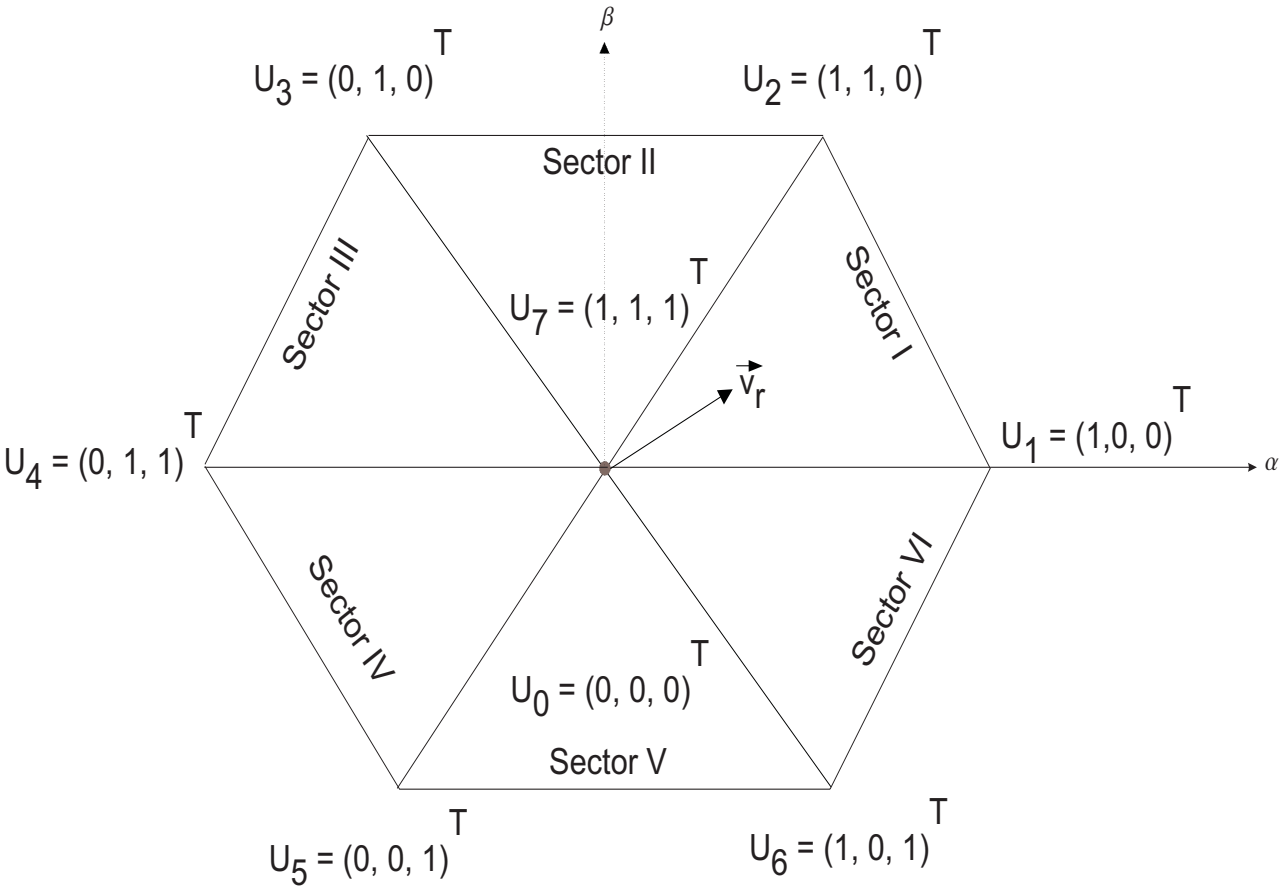

Figure 6.2: Distribution of the space vectors in the $\alpha\beta$ frame.

If we define the zero-sequence component of the two modules as

$$i_{L_{ko}} = \frac{1}{3}\sum_{j=1}^{3} i_{L_{kj}} \tag{6.13}$$

then we rewrite (6.1) as

$$\dot{\vec{i}}_{L_k}^{abc} - P_{ko}\dot{i}_{L_{ko}} = -\frac{r_{Lk}}{L_k}(\vec{i}_{L_k}^{abc} - P_{ko}i_{L_{ko}}) + P_{k3}\vec{V}^{abc} - P_{k3}\vec{u}_k^{abc}v_C \tag{6.14}$$

where $P_{ko} = \begin{bmatrix}1 & 1 & 1\end{bmatrix}^T$. Equation (6.14) shows that, if the zero-sequence currents of M1 and M2 are zero, then the PTBC behaves as two independent three-phase boost converters. However, for all practical purposes, the two modules will not be identical, and hence $i_{L_{1o}}$ and $i_{L_{2o}}$ are not equal to zero. However, based on Figure 6.1 and Kirchoff's current law, the zero-axis currents must satisfy the constraint

$$\sum_k i_{L_{ko}} = 0. \tag{6.15}$$

Next, we consider the generic transformation

$$\vec{\chi}^{abc} = [T(\theta)]^{-1}\vec{\chi}^{dqo} \tag{6.16}$$

where $\vec{\chi}^{dqo} = [\chi_d\ \chi_q\ \chi_o]^T$ and $[T(\theta)]^{-1}$ is the following non-singular matrix:

$$[T(\theta)]^{-1} = \begin{bmatrix} \cos(\theta) & -\sin(\theta) & 1 \\ \frac{1}{2}(-\cos(\theta) + \sqrt{3}\sin(\theta)) & \frac{1}{2}(\sqrt{3}\cos(\theta) + \sin(\theta)) & 1 \\ \frac{1}{2}(-\cos(\theta) - \sqrt{3}\sin(\theta)) & \frac{1}{2}(-\sqrt{3}\cos(\theta) + \sin(\theta)) & 1 \end{bmatrix}. \tag{6.17}$$

The components χ_d, χ_q, and χ_o are referred to as the active, reactive, and zero-axis components of $\vec{\chi}^{dqo}$. Using (6.16) and

$$\theta = \theta(t_0) + \int_0^t \omega d\tau \tag{6.18}$$

where ω is the line frequency, we rewrite (6.1) as

$$\begin{aligned}
\dot{v}_C &= -\tfrac{1}{C} i_{load} + \tfrac{1}{C}(i_{L_{kd}} u_{kd} + i_{L_{kq}} u_{kq} + i_{L_{ko}} u_{ko}) \\
\dot{\vec{i}}_{L_k}^{dqo} &= T(\theta)\Big(P_{k1} + P_{k2}\Big)[T(\theta)]^{-1} \vec{i}_{L_k}^{dqo} + T(\theta) P_{k3} [T(\theta)]^{-1} \vec{V}^{dqo} + \\
&\quad T(\theta) P_{k4} [T(\theta)]^{-1} \vec{u}_1^{dqo} v_C + T(\theta) P_{k5} [T(\theta)]^{-1} \vec{u}_2^{dqo} v_C - T(\theta) \tfrac{d}{d\theta} [T(\theta)]^{-1} \vec{i}_{L_k}^{dqo}.
\end{aligned} \tag{6.19}$$

In (6.19),

$$\begin{aligned}
T(\theta) &= \tfrac{2}{3} \begin{bmatrix} \cos(\theta) & \cos(\theta - \frac{2\pi}{3}) & \cos(\theta - \frac{4\pi}{3}) \\ -\sin(\theta) & -\sin(\theta - \frac{2\pi}{3}) & -\sin(\theta - \frac{4\pi}{3}) \\ \frac{1}{2} & \frac{1}{2} & \frac{1}{2} \end{bmatrix} \\
\tfrac{d}{d\theta}[T(\theta)]^{-1} &= \omega \begin{bmatrix} -\sin(\theta) & -\cos(\theta) & 0 \\ \frac{1}{2}(\sin(\theta) + \sqrt{3}\cos(\theta)) & \frac{1}{2}(-\sqrt{3}\sin(\theta) + \cos(\theta)) & 0 \\ \frac{1}{2}(\sin(\theta) - \sqrt{3}\cos(\theta)) & \frac{1}{2}(\sqrt{3}\sin(\theta) + \cos(\theta)) & 0 \end{bmatrix}
\end{aligned} \tag{6.20}$$

and

$$\begin{aligned}
\vec{i}_{L_k}^{dqo} &= [i_{L_{kd}} \; i_{L_{kq}} \; i_{L_{ko}}]^T \\
\vec{V}^{dqo} &= [V_d \; V_q \; V_o]^T \\
\vec{u}_k^{dqo} &= [u_{kd} \; u_{kq} \; u_{ko}]^T
\end{aligned} \tag{6.21}$$

where $V_q = V_o = 0$ because we have assumed that the line voltages are balanced.

Using (6.4)-(6.12), (6.17), and (6.20), we simplify (6.19) to obtain (6.22). Equation (6.22) shows that, for each module, the dynamical equations governing the currents on the dq axes depend only on u_{1d} (u_{2d}) and u_{1q} (u_{2q}). The differential equations describing the zero-axis currents (for both the modules) involve a cross-coupling control term. However, if we treat u_{2o} (u_{1o}) as a disturbance for $\dot{i}_{1o}$ ($\dot{i}_{2o}$), then the dynamics of the three currents are governed by three fictitious but independent controls on the dqo axes.

$$
\begin{aligned}
\dot{v}_C &= -\tfrac{1}{C} i_{load} + \tfrac{1}{C}\textstyle\sum_{k=1}^{2}(i_{L_{kd}}u_{kd} + i_{L_{kq}}u_{kq} + i_{L_{ko}}u_{ko}) \\
\overset{\cdot dqo}{i}_{L_1} &= \begin{bmatrix} \dot{i}_{L_{1d}} \\ \dot{i}_{L_{1q}} \\ \dot{i}_{L_{1o}} \end{bmatrix} = \begin{bmatrix} -\frac{r_{L1}}{L_1} & \omega & 0 \\ -\omega & -\frac{r_{L1}}{L_1} & 0 \\ 0 & 0 & -\frac{r_{L1}+r_{L2}}{L_1+L_2} \end{bmatrix} \begin{bmatrix} i_{L_{1d}} \\ i_{L_{1q}} \\ i_{L_{1o}} \end{bmatrix} + \frac{1}{L_1}\begin{bmatrix} V_d \\ V_q \\ V_o \end{bmatrix} \\
&\quad -\frac{v_C}{L_1}\begin{bmatrix} 1 & 0 & 0 \\ 0 & 1 & 0 \\ 0 & 0 & \frac{L_1}{L_1+L_2} \end{bmatrix}\begin{bmatrix} u_{1d} \\ u_{1q} \\ u_{1o} \end{bmatrix} - \frac{v_C}{L_1}\begin{bmatrix} 0 \\ 0 \\ -\frac{L_1}{L_1+L_2}u_{2o} \end{bmatrix} \\
\overset{\cdot dqo}{i}_{L_2} &= \begin{bmatrix} \dot{i}_{L_{2d}} \\ \dot{i}_{L_{2q}} \\ \dot{i}_{L_{2o}} \end{bmatrix} = \begin{bmatrix} -\frac{r_{L2}}{L_2} & \omega & 0 \\ -\omega & -\frac{r_{L2}}{L_2} & 0 \\ 0 & 0 & -\frac{r_{L1}+r_{L1}}{L_1+L_2} \end{bmatrix} \begin{bmatrix} i_{L_{2d}} \\ i_{L_{2q}} \\ i_{L_{2o}} \end{bmatrix} + \frac{1}{L_2}\begin{bmatrix} V_d \\ V_q \\ V_o \end{bmatrix} \\
&\quad -\frac{v_C}{L_2}\begin{bmatrix} 1 & 0 & 0 \\ 0 & 1 & 0 \\ 0 & 0 & \frac{L_2}{L_1+L_2} \end{bmatrix}\begin{bmatrix} u_{2d} \\ u_{2q} \\ u_{2o} \end{bmatrix} - \frac{v_C}{L_2}\begin{bmatrix} 0 \\ 0 \\ -\frac{L_2}{L_1+L_2}u_{1o} \end{bmatrix}.
\end{aligned}
\tag{6.22}
$$

We note that $\dot{i}_{L_{1d}}$ ($\dot{i}_{L_{2d}}$) and $\dot{i}_{L_{1q}}$ ($\dot{i}_{L_{2q}}$) are not affected by $i_{L_{1o}}$ ($i_{L_{2o}}$). If $u_1^{abc} = U_7$ and $u_2^{abc} = U_0$ or vice-versa, then using (6.16), (6.22), and

$$\cos(\theta) + \cos(\theta - \frac{2\pi}{3}) + \cos(\theta - \frac{4\pi}{3}) = 0, \;\; \sin(\theta) + \sin(\theta - \frac{2\pi}{3}) + \sin(\theta - \frac{4\pi}{3}) = 0 \tag{6.23}$$

we can show that a pure zero-sequence current flows from one module to the other and u_{1d} (u_{2d}) and u_{1q} (u_{2q}) are equal to zero. During this time, the utility is isolated from the bus. For all other switching configurations, the zero-sequence current exists but u_{1d} (u_{2d}) and u_{1q} (u_{2q}) are not equal to zero.

6.2 Control Schemes

The objectives of the control are three fold. First, we want to regulate the bus voltage at 400 volts. Second, the phase currents of each module should be synchronous with the input

phase voltages. Third, M1 and M2 should share the power consumed by the load equally. However, these objectives have to be met by controlling the two modules as independently as possible. The only common feedback to both modules is the d-axis reference current ($i^*_{L_{kd}}$) obtained from the outer voltage loop, which serves as the master. We use a common voltage loop because both M1 and M2 are connected over a common dc bus. The reference currents for the q-axis ($i^*_{L_{kq}}$) and the o-axis ($i^*_{L_{ko}}$) are maintained equal to zero to obtain unity-power-factor operation and to minimize the zero-axis interaction between the two modules.

As shown in Figure 6.3, the controllers for M1 and M2 have a multi-loop structure, with an outer voltage loop and an inner current loop. The current loops are designed to be fast so that the closed-loop system can reject the feedforward and feedback disturbances and regulate the output voltage. The outer voltage loop is designed to be slow and is based on a linear lag-lead controller with an integrator (Xing et al., 1998, 1999; Hiti, 1995). Based on these control objectives and structure, we develop three different kinds of discontinuous control schemes in the following subsections. While the first two control schemes are synthesized in the continuous domain, the third control scheme is developed in the discrete domain. However, the results for all of the controllers are based on digital implementation. The nominal switching frequency of M1 and M2 is set at 32 kHz to emulate the actual system (Lee et al., 1997; Xing et al., 1998, 1999). We, however, test the control when the modules are not synchronized and their switching frequencies are different.

6.2.1 Schemes in the Continuous Domain

Equation (6.22) shows that the open-loop PTBC is a seventh-order dynamical system. There are two sets of three differential equations that describe the dynamics of the current for M1 and M2 on the *dqo* axes and one additional differential equation for describing the dynamics of the bus voltage. One approach for implementing the current loops of M1 and

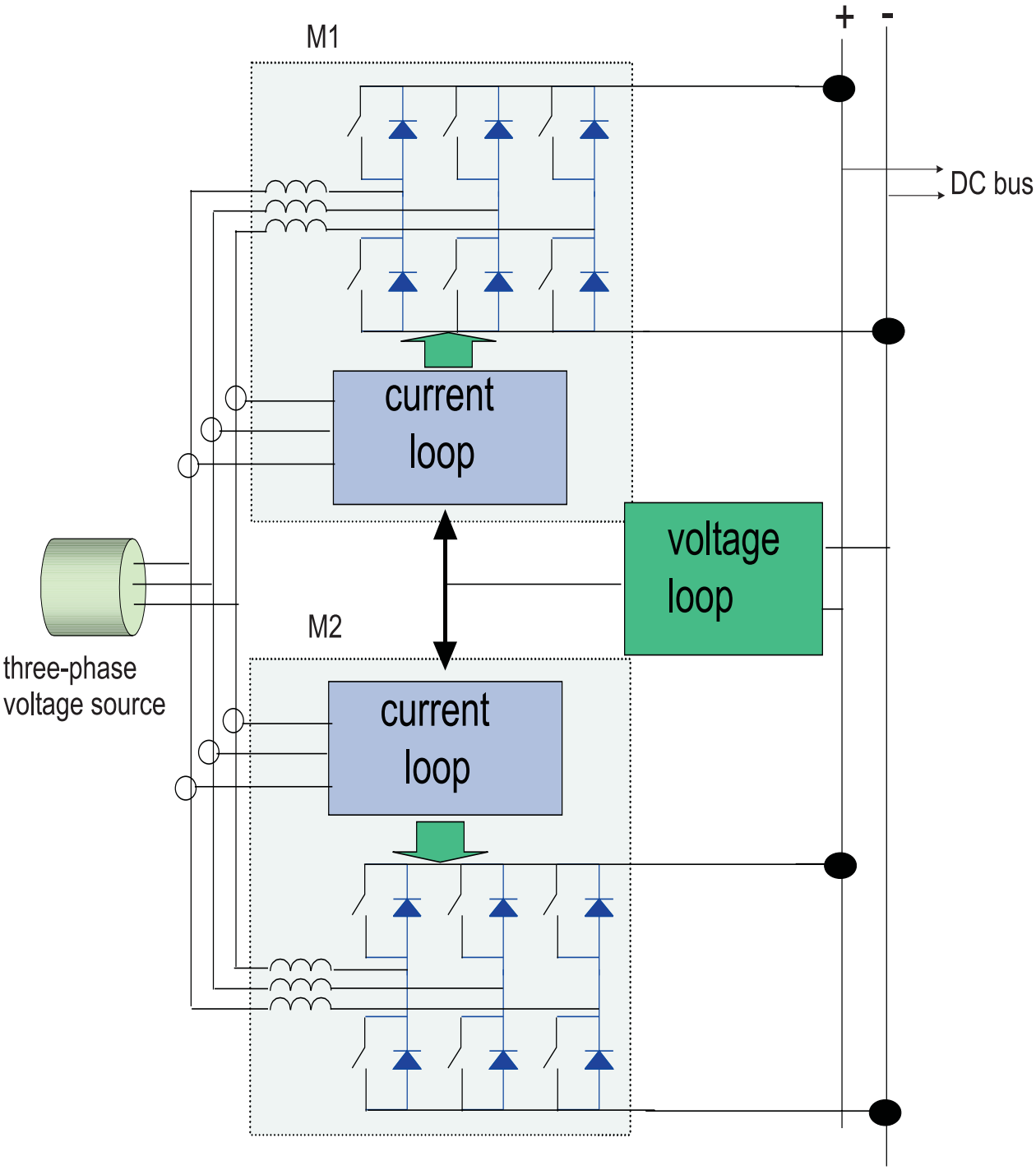

Figure 6.3: The structure of the controllers for the parallel three-phase boost converter.

M2 independently is to define the following six sliding surfaces:

$$\sigma_{kd} = i^*_{L_{kd}} - i_{L_{kd}} = 0, \;\; \sigma_{kq} = i^*_{L_{kq}} - i_{L_{kq}} = 0, \;\; \sigma_{ko} = i^*_{L_{ko}} - i_{L_{ko}} = 0 \tag{6.24}$$

and synthesize controls that will reduce $\|\sigma_{kd} + \sigma_{kq} + \sigma_{ko}\|$ to zero. Equation (6.22) shows that, if we treat the fourth terms of $\dot{\vec{i}}^{dqo}_{L_1}$ and $\dot{\vec{i}}^{dqo}_{L_2}$ as time-varying disturbances, then these two sets of dynamical equations have independent control in the *dqo* coordinates. The rank of the control matrix $\vec{u}^{dqo}_1$ ($\vec{u}^{dqo}_2$) in $\dot{\vec{i}}^{dqo}_{L_1}$ ($\dot{\vec{i}}^{dqo}_{L_2}$) is three. However, the rank of the control matrix $[\vec{u}^{dqo}_1 \;\; \vec{u}^{dqo}_2]^T$ in $[\dot{\vec{i}}^{dqo}_{L_1} \dot{\vec{i}}^{dqo}_{L_2}]^T$ is five. The physical meaning of this rank deficiency is that it is impossible to control all of the six currents ($\vec{i}^{dqo}_{L_1}$ and $\vec{i}^{dqo}_{L_2}$) independently. This follows from (6.15) as well, which shows that $i_{L_{10}} = -i_{L_{20}}$.

One way to avoid the redundancy problem is to control the sliding manifold

$$(\sigma_{1d} = 0) \bigcap (\sigma_{1q} = 0) \bigcap (\sigma_{1o} = 0) \bigcap (\sigma_{2d} = 0) \bigcap (\sigma_{2q} = 0). \tag{6.25}$$

If $\sigma_{1o} = 0$ (or $i_{L_{1o}} = 0$), then we obtain $i_{L_{2o}} = 0$ using (6.15). A simple way to achieve the stability of the sliding manifold (6.25) is to ensure the stability of the individual sliding surfaces. The conditions for the stability of these sliding surfaces are (Filippov, 1988; Utkin, 1992; Behilovic et al., 1993; Mazumder et al., 2000b, 2001a)

$$\sigma_{kd}\dot{\sigma}_{kd} < 0, \;\; \sigma_{kq}\dot{\sigma}_{kq} < 0 \tag{6.26a}$$

$$\sigma_{1o}\dot{\sigma}_{1o} < 0. \tag{6.26b}$$

It follows from (6.22) that the stability conditions in (6.26a) are satisfied provided

$$\begin{aligned} u_{kd} &= -\gamma_{kd}\text{sgn}(\sigma_{kd}), \quad |\gamma_{kd}| > |\dot{i}^*_{L_{kd}} - f_{kd}(i_{L_{kd}}, i_{L_{kq}}, V_d)|\tfrac{L_k}{v_C} \\ u_{kq} &= -\gamma_{kq}\text{sgn}(\sigma_{kq}), \quad |\gamma_{kq}| > |\dot{i}^*_{L_{kq}} - f_{kq}(i_{L_{kd}}, i_{L_{kq}}, V_q)|\tfrac{L_k}{v_C} \end{aligned} \tag{6.27}$$

where

$$\begin{aligned} f_{kd}(i_{L_{kd}}, i_{L_{kq}}, V_d) &= -\tfrac{r_{Lk}}{L_k} i_{L_{kd}} + \omega i_{L_{kq}} + \tfrac{1}{L_k} V_d - \tfrac{v_C}{L_k} u_{kd} \\ f_{kq}(i_{L_{kd}}, i_{L_{kq}}, V_q) &= -\omega i_{L_{kd}} - \tfrac{r_{Lk}}{L_k} i_{L_{kq}} + \tfrac{1}{L_k} V_q - \tfrac{v_C}{L_k} u_{kq}. \end{aligned} \tag{6.28}$$

Table 6.1: Possible values of u_{1o} for a given u_{2o} to satisfy $\dot{\sigma_{1o}}\sigma_{1o} < 0$

$i_{L_{1o}} > 0$		$i_{L_{1o}} < 0$	
$\frac{1}{\beta}u_{2o} = u_{21} + u_{22} + u_{23}$	$\frac{1}{\beta}u_{1o} = u_{11} + u_{12} + u_{13}$	$\frac{1}{\beta}u_{2o} = u_{21} + u_{22} + u_{23}$	$\frac{1}{\beta}u_{1o} = u_{11} + u_{12} + u_{13}$
-3	3/1/-1/-3	-3	-3
-1	3/1/-1	-1	-1/-3
1	3/1	1	1/-1/-3
3	3	3	3/1/-1/-3

The inequality (6.26b) requires special attention because $\dot{\sigma}_{1o}\sigma_{1o}$, which can be expressed as

$$\dot{\sigma_{1o}}\sigma_{1o} = -i_{L_{1o}}\Big(\tfrac{v_C}{2(L_1+L_2)}(u_{1o} - u_{2o}) + \tfrac{r_{L1}+r_{L2}}{L_1+L_2}i_{L_{1o}}\Big) \tag{6.29}$$

contains a term which involves u_{2o}. This term serves as a discontinuous, time-varying disturbance on M1. In addition, this disturbance is not measurable because we want to control each converter independently. For all practical purposes, the converters are not identical, and hence $u_{1o} \neq u_{2o}$ all the time. To determine the stability of the sliding surface $\sigma_{1o} = 0$, we use Table 6.1 and the following relations:

$$\begin{aligned} u_{1o} &= \tfrac{\sqrt{2}}{3}\left(u_{11} + u_{12} + u_{13}\right) \\ u_{2o} &= \tfrac{\sqrt{2}}{3}\left(u_{21} + u_{22} + u_{23}\right). \end{aligned} \tag{6.30}$$

Table 6.1 shows all possible values of u_{1o} for a given u_{2o} that satisfy (6.26b). It is obvious from Table 6.1 that it is not possible to satisfy (6.26b) using a single space vector in a single switching cycle. We now consider the stability of the sliding manifold (6.25) using the positive-definite Lyapunov function

$$V(\sigma_{1d}, \sigma_{1q}, \sigma_{1o}, \sigma_{2d}, \sigma_{2q}) = \tfrac{1}{2}\Big(\sigma_{1d}^2 + \sigma_{1q}^2 + \sigma_{1o}^2 + \sigma_{2d}^2 + \sigma_{2q}^2\Big). \tag{6.31}$$

which has a quadratic form. For the manifold to be stable

$$\dot{V}(\sigma_{1d}, \sigma_{1q}, \sigma_{1o}, \sigma_{2d}, \sigma_{2q}) = \dot{\sigma}_{1d}\sigma_{1d} + \dot{\sigma}_{1q}\sigma_{1q} + \dot{\sigma}_{1o}\sigma_{1o} + \dot{\sigma}_{2d}\sigma_{2d} + \dot{\sigma}_{2q}\sigma_{2q} < 0. \tag{6.32}$$

We have already shown that $\dot{\sigma}_{kd}\sigma_{kd} < 0$ and $\dot{\sigma}_{kq}\sigma_{kq} < 0$ are satisfied using (6.27), and it is not possible to satisfy $\dot{\sigma_{1o}}\sigma_{1o}$ using a single switching vector in a single switching cycle because of the zero-axis disturbance. The nonvanishing disturbance eliminates the possibility of satisfying (6.32) for all values of σ_{1o}. However, depending on the values of σ_{kd}, σ_{kq}, and σ_{1o}, we can always establish a bound beyond which (6.32) holds. This bound is minimized if the zero-axis disturbance is reduced.

A quick look at $\dot{i}_{L_{1o}}$ shows that the zero-axis disturbance can be reduced by increasing the size of the line inductors or the switching frequency because u_{2o} depends on the switching vectors. However, we can not increase either of them arbitrarily to avoid making the converter bulky and inefficient. For the PTBC shown in Figure 6.4, the worst disturbance occurs when $\vec{u}_1^{abc} = U_7$ and $\vec{u}_2^{abc} = U_0$ and vice-versa. During this switching configuration, a pure zero-axis current flows from M1 to M2 or vice-versa that is not reflected on the dq axes. This is because the path of this zero-sequence current involves the output capacitor and the top (or bottom) switches of M1 and M2. So, if we eliminate this possible switching configuration, then we can reduce the impact of the disturbance significantly. Although the zero-axis disturbance exists for other switching configurations, it is reflected on the dq axes, and hence the impact of this disturbance can be minimized by having a fast current loop on the dq axes (Xing et al., 1998, 1999; Hiti et al., 1994; Hiti, 1995). Therefore, it is obvious that, if we control the two modules independently, then it is impossible to have a true sliding surface. However, depending on the switching frequency, switching configuration, and inductor size (which limits the zero-axis disturbance), we can operate in a close vicinity of the sliding manifold. We should note that because the controllers are implemented in a digital domain (with finite sampling frequency), we can not have a true sliding surface anyway. Based on the above discussion, we devise the following two control schemes.

6.2.1.1 Scheme One

This scheme is implemented in the synchronous (dq) frame. We outline two approaches for scheme one. The objectives of both approaches are to control the error trajectories

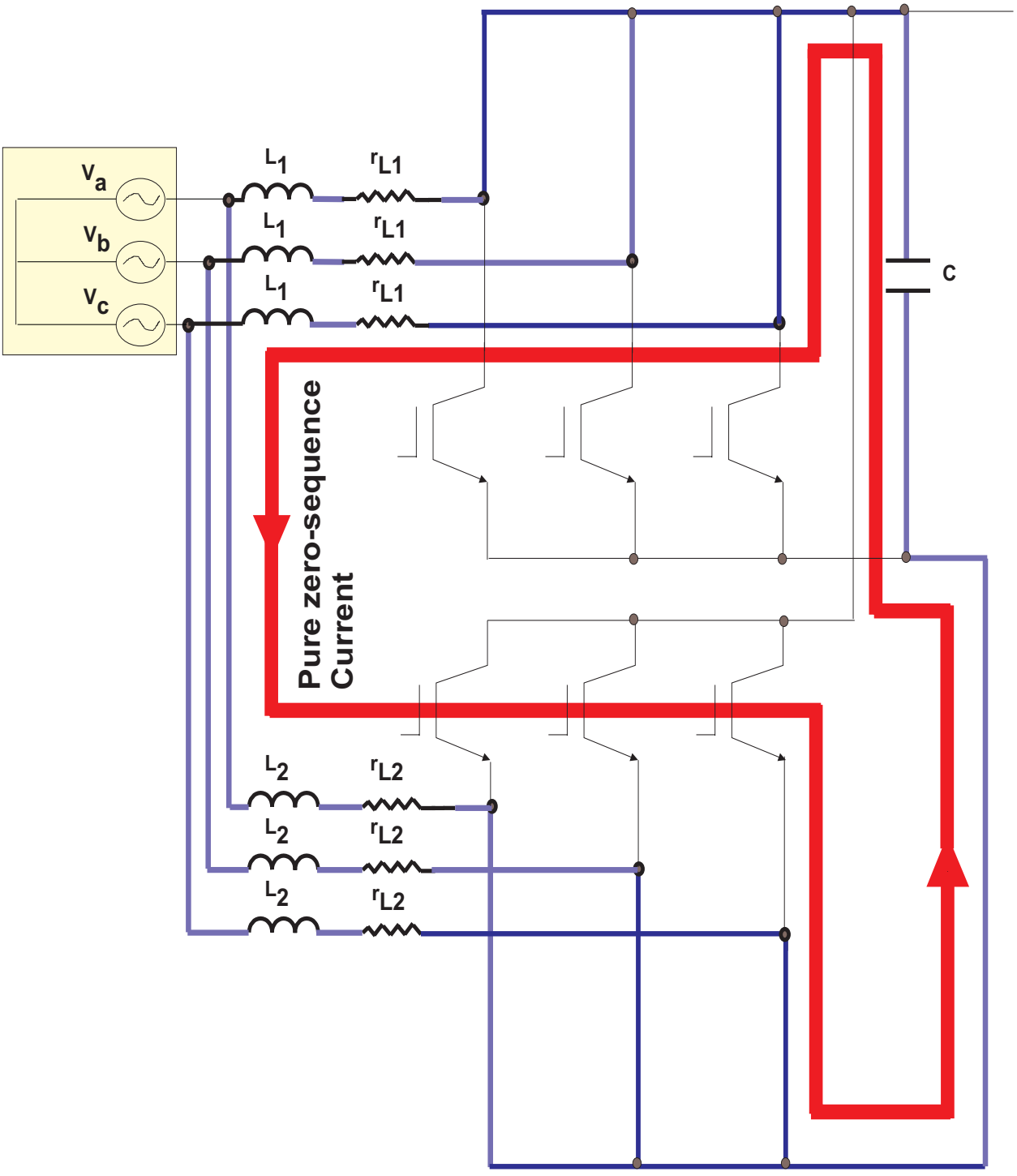

Figure 6.4: Path of the pure zero-sequence current in the parallel three-phase boost converter.

defined by the sliding surfaces σ_{kd}, σ_{kq}, and σ_{1o}. In the first approach, we control σ_{kd} and σ_{kq} using (6.27) and (6.28) and limit the zero-axis disturbance by preventing the flow of the zero-axis current from M1 to M2 or vice-versa. Using the transformation (6.16), we can then transform the controls in the *dqo* axes to the *abc* axes.

In the second approach, we first compute σ_{kd}, σ_{kq}, and σ_{1o} using (6.24), and then use (6.16) to transform the errors to the abc coordinates (σ_k^{abc}). The controls $\vec{u}_k^{abc}$ are determined from σ_k^{abc} using

$$\vec{u}_k^{abc} = -\text{sgn}(\sigma_k^{abc}) \tag{6.33}$$

to ensure the stability of (6.26a) in the absence of a zero-axis disturbance. This can be explained using an argument similar to that used to describe the stability of the control in (6.27). However, in the presence of the disturbance, the bound on σ_{1o} depends on the sizes of the inductors of M1 and M2 and their switching frequencies. This is also a limitation for approach one as well.

6.2.1.2 Scheme Two

The second scheme is a variation of the first scheme; it uses hysteresis to control the switching frequency. First, we compute σ_{kd} and σ_{kq} using (6.24) and then transform the errors to the $\alpha\beta$ coordinates using

$$\begin{bmatrix} \sigma_{k\alpha} \\ \sigma_{k\beta} \end{bmatrix} = \begin{bmatrix} \cos(\theta) & -\sin(\theta) \\ \sin(\theta) & \cos(\theta) \end{bmatrix} \begin{bmatrix} \sigma_{kd} \\ \sigma_{kq} \end{bmatrix}. \tag{6.34}$$

The selection of the switching vectors is such that

$$\dot{\sigma}_{k\alpha}\sigma_{k\alpha} < 0, \;\; \dot{\sigma}_{k\beta}\sigma_{k\beta} < 0. \tag{6.35}$$

and $\|\sigma_{1o}\|$ is bounded for a given frequency and inductor size. The latter is achieved by using an appropriate zero vector based on the direction of $i_{L_{ko}}$. For example, if $i_{L_{1o}} < 0$ and

the space vector needed to satisfy $\dot{\sigma}_{1\alpha}\sigma_{1\alpha} < 0$ and $\dot{\sigma}_{1\beta}\sigma_{1\beta} < 0$ is U_7, then we implement U_0 instead. This simple change will not affect the stability of the sliding surfaces on the $\alpha\beta$ axes but will reduce the zero-axis disturbance. Equation (6.29) and Table 6.1 confirm this claim. In addition, to achieve a compromise between the dynamic response and the harmonic distortion, we use a two-level hysteretic comparator for each axis that has two thresholds (h_i and h_o). Figure 6.5 shows a flowchart that illustrates the procedure for selecting the appropriate switching vector for either M1 or M2.

The advantage of this scheme is that we can limit the switching frequency and keep a balance between the distortion of the line currents and the transient response. Although the pure zero-sequence current is eliminated, the impact of the overall zero-sequence disturbance is still determined by the switching frequency and the inductor size.

6.2.2 Schemes in the Discrete Domain

The dynamical equations for $i_{L_{1o}}$ (or $i_{L_{2o}}$) in (6.22) show that, if $u_{1o} - u_{2o}$ (or $u_{2o} - u_{1o}$) is positive or zero, then we have a damped first-order differential equation that is stable. However, in the preceding section, we have shown that, for an independent control of M1 and M2, it is impossible to attain this objective in a single switching cycle using only one space vector. Therefore, in this section we look for stability on a reduced-order manifold, where instead of controlling $u_{1o} - u_{2o}$ (or $u_{2o} - u_{1o}$), we control their averages; that is, $\overline{u}_{1o} - \overline{u}_{2o}$ ($\overline{u}_{2o} - \overline{u}_{1o}$). An additional problem that we found in the preceding section is related to the switching frequency. Sliding-mode control tries to optimize the magnitude of switching (Utkin, 1992; Mazumder et al., 2000b), and hence it can not guarantee that the switching frequency is constant. However, using hysteresis (as in our analog schemes), the switching frequency can be kept reasonably constant under steady state (Nagy, 1994). On other hand, the control of three-phase boost converters using space-vector modulation (SVM) schemes (Broeck et al., 1988; Ogasawara et al., 1989; Habetler et al., 1992; Holtz et al., 1993; Stefanovic and Vukosavic, 1994) ensures a fixed switching frequency. However, the

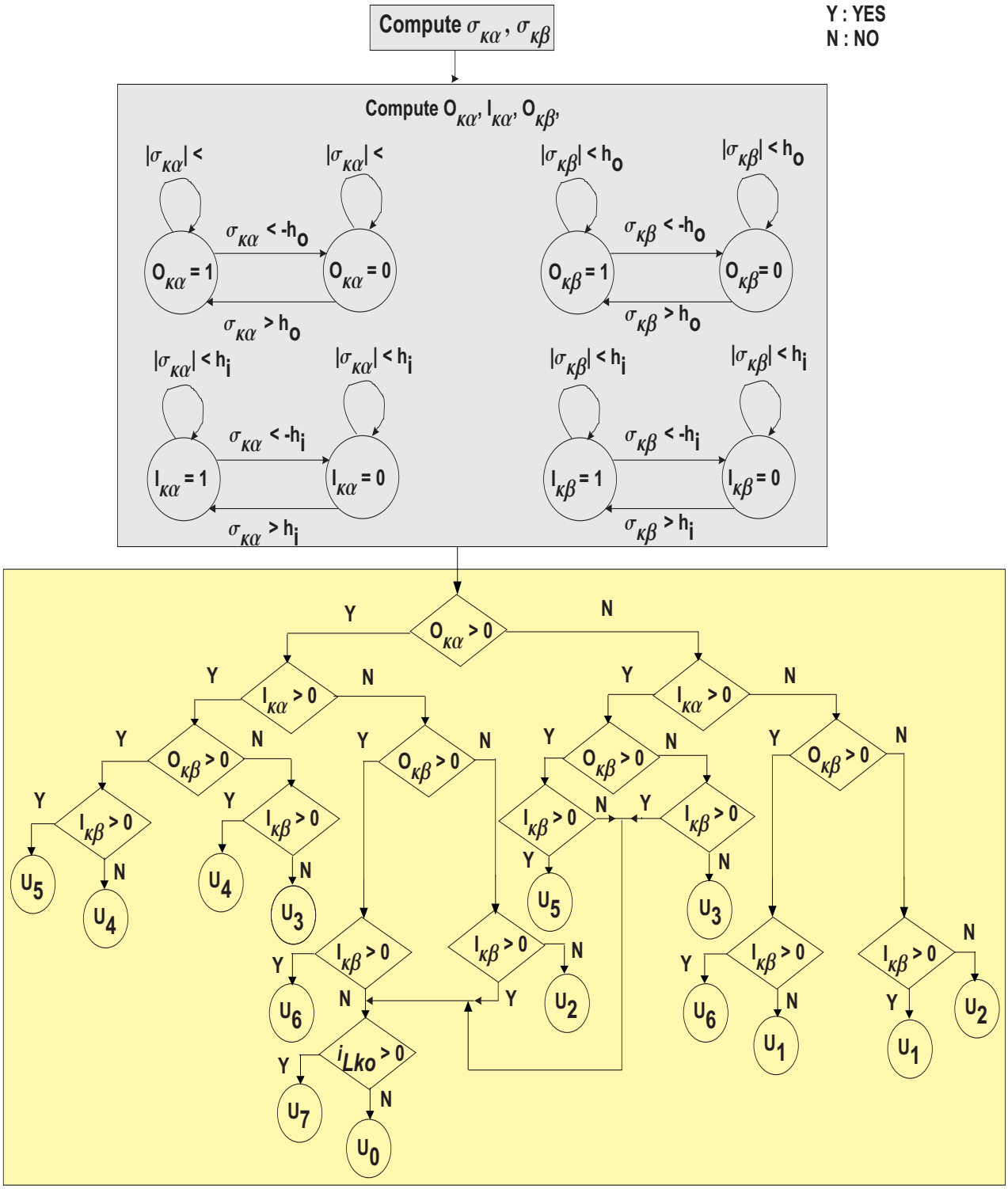

Figure 6.5: Flowchart for the implementation of the second control scheme.

stability of these controllers, developed based on small-signal analysis, can not be guaranteed except in the vicinity of the equilibrium solution.

In this section, we develop a discrete variable-structure control (DVSC) for the current-loop of the PTBC. The objective of the current loop is to stabilize the PTBC on the *dq* axes and keep the zero-axis disturbance bounded. The outer loop of the overall control system that regulates the bus voltage is designed using a linear controller such that the impact of the higher-order line frequencies on the closed-loop system is minimized.

An important feature of the DVSC is that it keeps the switching frequency constant by combining VSC with SVM techniques. The DVSC scheme can be combined with any SVM scheme. However, not all of the SVM techniques can be used to reject the disturbance due to the zero-axis currents (Xing et al., 1999). We, therefore, chose the SVM scheme outlined in (Xing et al., 1998 , 1999; Ye et al., 2000) to control the zero-axis current. In any given switching cycle, this SVM scheme synthesizes a reference voltage vector ($\vec{v}_r$) (see Figure 6.2) using two zero vectors and two active vectors. For example, if $\vec{v}_r$ is in Sector I, then it is synthesized as (Broeck et al., 1988; Ogasawara et al., 1989; Habetler et al., 1992; Holtz et al., 1993; Stefanovic and Vukosavic, 1994)

$$\vec{v}_r = \frac{v_C}{2T}(t_1U_0 + t_2U_1 + t_3U_2 + t_4U_7 + t_5U_2 + t_6U_1 + t_7U_0) \tag{6.36}$$

where $T = t_1 + t_2 + t_3 + t_4 + t_5 + t_6 + t_7$.

Having selected the SVM scheme, we need to express $i_{L_{kd}}$ and $i_{L_{kq}}$ in discrete form to implement the current loop using the DVSC. The discrete form of $\vec{i}_{L_k}^{dq}$ is a map of the form

$$\vec{i}_{L_k}^{dq}(n+1) = F_k\Big(\vec{i}_{L_k}^{dq}(n), \vec{V}^{dq}(n), \vec{t}_k^{dq}(n)\Big) \tag{6.37}$$

where $\vec{i}_{L_k}^{dq} = [i_{L_{kd}} \;\; i_{L_{kq}}]^T$, $\vec{V}^{dq} = [V_d \;\; V_q]^T$, and $\vec{t}_k^{dq} = [t_{kd} \;\; t_{kq}]^T$. To obtain the map (6.37), we first solve for $\vec{i}_{L_k}^{dq}$ (using (6.22)) in each time interval of the space-vector modulated waveform. One such waveform is shown in Figure 6.6, which is valid only for Sector I. We start by solving for $i_{L_{kd}}$ and $i_{L_{kq}}$ in Sector I for each interval of time. Once we obtain all of

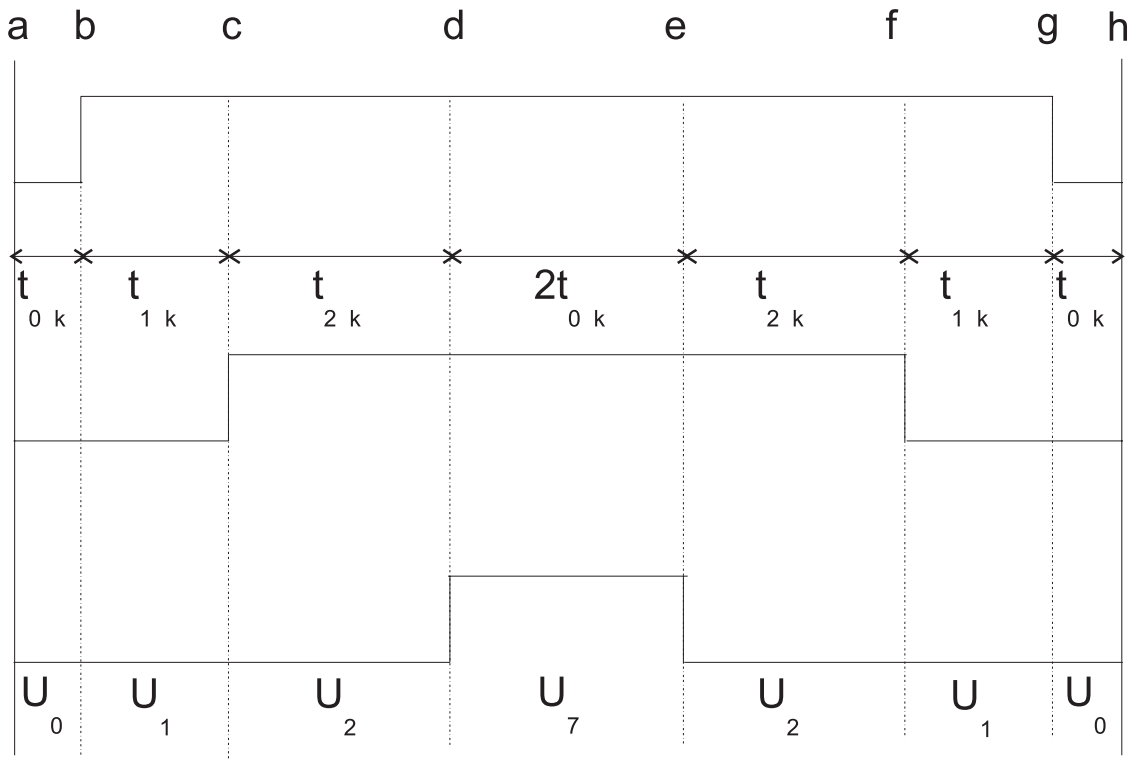

Figure 6.6: A sample space-vector modulated waveform to synthesize the reference voltage vector in Sector I.

the solutions, we obtain a map that relates $i_{L_{kd}}$ and $i_{L_{kq}}$ at the end of a switching cycle with those at the beginning. Subsequently, using this map, which is valid only for Sector I, we obtain the generalized map (6.37).

Figure 6.6 shows that, although there are seven intervals of time in a given switching cycle, only three of them are distinct. Using (6.22) and (6.23) and noting that (6.17) relates $\vec{u}_k^{dq}$ to $\vec{u}_k^{abc}$, we rewrite the dynamical equations for $i_{L_{kd}}$ and $i_{L_{kq}}$ in each of these distinct intervals of time as

{time interval a-b, d-e, and g-h}

$$\dot{\vec{i}}_{L_k}^{dq} = \begin{bmatrix} \dot{i}_{L_{kd}} \\ \dot{i}_{L_{kq}} \end{bmatrix} = \begin{bmatrix} -\frac{r_{L_k}}{L_k} & \omega \\ -\omega & -\frac{r_{L_k}}{L_k} \end{bmatrix} \begin{bmatrix} i_{L_{kd}} \\ i_{L_{kq}} \end{bmatrix} + \frac{1}{L_k} \begin{bmatrix} V_d \\ V_q \end{bmatrix} \qquad (6.38)$$
$$= A_k \vec{i}_{L_k}^{dq} + B_k \vec{V}^{dq}$$

{time interval b-c and f-g}

$$\begin{aligned}\dot{\vec{i}}^{dq}_{L_k} = \begin{bmatrix} \dot{i}_{L_{kd}} \\ \dot{i}_{L_{kq}} \end{bmatrix} &= \begin{bmatrix} -\frac{r_{L_k}}{L_k} & \omega \\ -\omega & -\frac{r_{L_k}}{L_k} \end{bmatrix} \begin{bmatrix} i_{L_{kd}} \\ i_{L_{kq}} \end{bmatrix} + \frac{1}{L_k} \begin{bmatrix} V_d \\ V_q \end{bmatrix} \\ &\quad -\frac{v_C}{L_k} \begin{bmatrix} \frac{4}{3} \\ 0 \end{bmatrix} \cos(\theta) - \frac{v_C}{L_k} \begin{bmatrix} 0 \\ -\frac{4}{3} \end{bmatrix} \sin(\theta) \qquad (6.39) \\ &= A_k \vec{i}^{dq}_{L_k} + B_k \vec{V}^{dq} + v_C C_{k1} \cos(\theta) + v_C C_{k2} \sin(\theta)\end{aligned}$$

{time interval c-d and e-f}

$$\begin{aligned}\dot{\vec{i}}^{dq}_{L_k} = \begin{bmatrix} \dot{i}_{L_{kd}} \\ \dot{i}_{L_{kq}} \end{bmatrix} &= \begin{bmatrix} -\frac{r_{L_k}}{L_k} & \omega \\ -\omega & -\frac{r_{L_k}}{L_k} \end{bmatrix} \begin{bmatrix} i_{L_{kd}} \\ i_{L_{kq}} \end{bmatrix} + \frac{1}{L_k} \begin{bmatrix} V_d \\ V_q \end{bmatrix} \\ &\quad -\frac{v_C}{L_k} \begin{bmatrix} \frac{2}{3} \\ \frac{2}{\sqrt{3}} \end{bmatrix} \cos(\theta) - \frac{v_C}{L_k} \begin{bmatrix} \frac{2}{\sqrt{3}} \\ -\frac{2}{3} \end{bmatrix} \sin(\theta) \qquad (6.40) \\ &= A_k \vec{i}^{dq}_{L_k} + B_k \vec{V}^{dq} + v_C D_{k1} \cos(\theta) + v_C D_{k2} \sin(\theta).\end{aligned}$$

The closed-form solution of (6.38) is (Mazumder et al., 2001c, d)

$$\begin{aligned}\vec{i}^{dq}_{L_k}(m+1) &= e^{A_k t_{0k}} \vec{i}^{dq}_{L_k}(m) + \left(e^{A_k t_{0k}} - I\right) A_k^{-1} B_k \vec{V}^{dq} \\ &= \Phi_{k1} \vec{i}^{dq}_{L_k}(m) + \Gamma_{k1} \vec{V}^{dq} + \Omega_{k1} v_C(n)\end{aligned} \qquad (6.41)$$

where m represents the m^{th} sub-sampling period in the n^{th} sampling period, $\vec{i}^{dq}_{L_k}(m)$ is the initial value of $\vec{i}^{dq}_{L_k}$ at the beginning of the sub-interval, and t_0 is the duration of the sub-interval. A closed-form solution of (6.39) is not possible.

To proceed further, we assume that the bus voltage is constant through out a sampling interval. Then the solution of (6.39) is given by

$$\begin{aligned}\vec{i}^{dq}_{L_k}(m+1) &= e^{A_k t_{1k}} \vec{i}^{dq}_{L_k}(m) + \left(e^{A_k t_{1k}} - I\right) A_k^{-1} B \vec{V}^{dq} + \\ &\quad v_C(n) \int_{t_k(m)}^{t_k(m)+t_{1k}} e^{A_k\left(t_k(m)+t_{1k}-\xi\right)} C_{k1} \cos(\omega\xi) d\xi + \qquad (6.42) \\ &\quad v_C(n) \int_{t_k(m)}^{t_k(m)+t_{1k}} e^{A_k\left(t_k(m)+t_{1k}-\xi\right)} C_{k2} \sin(\omega\xi) d\xi.\end{aligned}$$

To obtain the closed-form solution of (6.42), we let

$$\psi = t_k(m) + t_{1k} - \xi \qquad (6.43)$$

which implies that

$$\begin{aligned} d\psi &= -d\xi \\ \xi &= t_k(m) + t_{1k} - \psi. \end{aligned} \tag{6.44}$$

Using (6.43) and (6.44), we rewrite (6.42) using hyperbolic functions as

$$\begin{aligned} \vec{i}_{L_k}^{dq}(m+1) &= e^{A_k t_{1k}} \vec{i}_{L_k}^{dq}(m) + \Big(e^{A_k t_{1k}} - I\Big) A_k^{-1} B_k \vec{V}^{dq} + \\ & v_C(n) \int_0^{t_{1k}} e^{A_k \psi} C_{k1} \Big(\tfrac{e^{i\omega\left(t_k(m)+t_{1k}-\psi\right)} + e^{-i\omega\left(t_k(m)+t_{1k}-\psi\right)}}{2} \Big) d\psi + \\ & v_C(n) \int_0^{t_{1k}} e^{A_k \psi} C_{k2} \Big(\tfrac{e^{i\omega\left(t_k(m)+t_{1k}-\psi\right)} - e^{-i\omega\left(t_k(m)+t_{1k}-\psi\right)}}{2i} \Big) d\psi. \end{aligned} \tag{6.45}$$

Now, the eigenvalues of A_k $(= -\frac{r_{L_k}}{L_k} \pm i\omega)$ are distinct, and hence we can write $e^{A_k\psi}$ as

$$e^{A_k \psi} = M_k e^{\Lambda_k \psi} M_k^{-1} \tag{6.46}$$

where M_k is the modal matrix whose columns are the eigenvectors of A_k. The matrix Λ_k is diagonal and its elements are the eigenvalues of A_k. As such, $e^{\Lambda_k}\psi$ is also a diagonal matrix. Using (6.46), we rewrite (6.45) as

$$\begin{aligned} \vec{i}_{L_k}^{dq}(m+1) &= e^{A_k t_{1k}} \vec{i}_{L_k}^{dq}(m) + \Big(e^{A_k t_{1k}} - I\Big) A_k^{-1} B_k \vec{V}^{dq} + \\ & v_C(n) e^{i\omega\left(t_k(m)+t_{1k}\right)} M_k \int_0^{t_{1k}} \Big(\tfrac{e^{\left(\Lambda_k - i\omega I\right)\psi} + e^{\left(\Lambda_k + i\omega I\right)\psi}}{2} \Big) M_k^{-1} C_{k1} d\psi + \\ & v_C(n) e^{i\omega\left(t_k(m)+t_{1k}\right)} M_k \int_0^{t_{1k}} \Big(\tfrac{e^{\left(\Lambda_k - i\omega I\right)\psi} - e^{\left(\Lambda_k + i\omega I\right)\psi}}{2i} \Big) M_k^{-1} C_{k2} d\psi \end{aligned} \tag{6.47}$$

where I is the identity matrix having the same dimension as A_k. Finally, we obtain the closed-form solution of (6.47) as

$$\begin{aligned} \vec{i}_{L_k}^{dq}(m+1) &= e^{A_k t_{1k}} \vec{i}_{L_k}^{dq}(m) + \Big(e^{A_k t_{1k}} - I\Big) A_k^{-1} B \vec{V}^{dq} + \\ & v_C(n) \Bigg(\tfrac{e^{i\omega\left(t_k(m)+t_{1k}\right)}}{2} M_k \Big(e^{\left(\Lambda_k - i\omega I\right)t_{1k}} - I\Big) \Big(\Lambda_k - i\omega I\Big)^{-1} M_k^{-1} C_{k1} + \\ & \tfrac{e^{-i\omega\left(t_k(m)+t_{1k}\right)}}{2} M_k \Big(e^{\left(\Lambda_k + i\omega I\right)t_{1k}} - I\Big) \Big(\Lambda_k + i\omega I\Big)^{-1} M^{-1} C_{k1} \Bigg) + \\ & v_C(n) \Bigg(\tfrac{e^{i\omega\left(t_k(m)+t_{1k}\right)}}{2i} M_k \Big(e^{\left(\Lambda_k - i\omega I\right)t_{1k}} - I\Big) \Big(\Lambda_k - i\omega I\Big)^{-1} M_k^{-1} C_{k2} - \\ & \tfrac{e^{-i\omega\left(t_k(m)+t_{1k}\right)}}{2i} M_k \Big(e^{\left(\Lambda_k + i\omega I\right)t_{1k}} - I\Big) \Big(\Lambda_k + i\omega I\Big)^{-1} M_k^{-1} C_{k2} \Bigg). \end{aligned} \tag{6.48}$$

The solution of (6.40) can be found directly from (6.48) by replacing C_{k1} with D_{k1} and C_{k2} with D_{k2}.

If the switching frequency of the PTBC is high, then we can assume that during one switching cycle θ is constant. Therefore, (6.48) simplifies to

$$\begin{aligned}\vec{i}_{L_k}^{dq}(m+1) &= e^{A_k t_{1k}}\vec{i}_{L_k}^{dq}(m) + \Big(e^{A_k t_{1k}} - I\Big)A_k^{-1}B\vec{V}^{dq} + \Big((e^{A_k t_{1k}} - I)A_k^{-1}C_{k1}\cos\left(\theta(n)\right)+ \\ &\quad (e^{A_k t_{1k}} - I)A_k^{-1}C_{k2}\sin\left(\theta(n)\right)\Big)v_C(n) \\ &= \Phi_{k2}\vec{i}_{L_k}^{dq}(m) + \Gamma_{k2}\vec{V}^{dq} + \Omega_{k2}v_C(n).\end{aligned} \tag{6.49}$$

Then, using (6.49), we obtain the solution of (6.40) as

$$\begin{aligned}\vec{i}_{L_k}^{dq}(m+1) &= e^{A_k t_{2k}}\vec{i}_{L_k}^{dq}(m) + \Big(e^{A_k t_{2k}} - I\Big)A_k^{-1}B_k\vec{V}^{dq} + \Big((e^{A_k t_{2k}} - I)A_k^{-1}D_{k1}\cos\left(\theta(n)\right)+ \\ &\quad (e^{A_k t_{2k}} - I)A_k^{-1}D_{k2}\sin\left(\theta(n)\right)\Big)v_C(n) \\ &= \Phi_{k3}\vec{i}_{L_k}^{dq}(m) + \Gamma_{k3}\vec{V}^{dq} + \Omega_{k3}v_C(n).\end{aligned} \tag{6.50}$$

Using (6.41), (6.49), and (6.50) and knowing that

$$\begin{aligned}&t_{3k} = 2t_{0k},\ t_{5k} = t_{1k},\ t_{4k} = t_{2k},\ t_{7k} = t_{0k} \\ &\Omega_{k_1} = \Omega_{k_4} = \Omega_{k_7} = 0 \\ &\Omega_{k_2} = \Omega_{k_6},\ \Omega_{k_3} = \Omega_{k_5}\end{aligned} \tag{6.51}$$

we obtain the map

$$\vec{i}_{L_k}^{dq}(n+1) = \Phi_k\vec{i}_{L_k}^{dq}(n) + \Gamma_k\vec{V}^{dq} + \Omega_{ka}t_{k1}(n)v_C(n) + \Omega_{kb}t_{k2}(n)v_C(n) \tag{6.52}$$

where

$$\begin{aligned}\Phi_k &= e^{A_k T} \\ \Gamma_k &= (e^{A_k T} - I)A_k^{-1}B_k \\ \Omega_{ka} &= 2C_{k1}\cos(\theta(n)) + 2C_{k2}\sin(\theta(n)) \\ \Omega_{kb} &= 2D_{k1}\cos(\theta(n)) + 2D_{k2}\sin(\theta(n)).\end{aligned} \tag{6.53}$$

Using

$$\begin{aligned} t_{kd} &= \tfrac{1}{2}(\cos(\theta) + \sqrt{(}3)\sin(\theta))2t_{2k} + \cos(\theta)2t_{1k} \\ t_{kq} &= \tfrac{1}{2}(\sqrt{(}3)\cos(\theta) - \sin(\theta))2t_{2k} - \sin(\theta)2t_{1k} \end{aligned} \tag{6.54}$$

we convert (6.52) to the following form:

$$\begin{aligned} \vec{i}_{L_k}^{dq}(n+1) &= F_k\Big(\vec{i}_{L_k}^{dq}(n), \vec{V}^{dq}(n), \vec{t}_k^{dq}(n)\Big) \\ &= \Phi_k \vec{i}_{L_k}^{dq}(n) + \Gamma_k \vec{V}^{dq} + \Omega_k \vec{t}_k^{dq}(n) \end{aligned} \tag{6.55}$$

where Ω_k is a diagonal matrix. Using the procedure described above, we obtain maps similar to (6.55) for Sectors II-VI.

Now that we have obtained the discrete form of $\vec{i}_{L_k}^{dq}$, we define the following sliding surfaces to control the currents on the dq axes:

$$\vec{\sigma}_k^{dq}(n) = \vec{i^*}_{L_k}^{dq}(n) - \vec{i}_{L_k}^{dq}(n), \;\; \vec{\sigma}_k^{dq} = [\sigma_{kd} \;\; \sigma_{kq}]^T. \tag{6.56}$$

The stability of the sliding surfaces $\vec{\sigma}_k^{dq}(n)$ is determined using the discrete Lyapunov function

$$V(\sigma_{kd}(n), \sigma_{kq}(n)) = \frac{1}{2}\vec{\sigma}_k^{dq}(n)^T \vec{\sigma}_k^{dq}(n). \tag{6.57}$$

For stability (Miloslavljevic, 1985; Sarpturk et al., 1987; Kotta, 1989; Furutta, 1990),

$$\begin{aligned} & V_{k+1}(\sigma_{kd}(n+1), \sigma_{kq}(n+1)) - V_k(\sigma_{kd}(n), \sigma_{kq}(n)) \leq 0 \\ & \Rightarrow \sigma_{kd}(n)(\sigma_{kd}(n+1) - \sigma_{kd}(n)) + \sigma_{kq}(n)(\sigma_{kq}(n+1) - \sigma_{kq}(n)) \leq 0. \end{aligned} \tag{6.58}$$

Map (6.55) shows that the sliding surfaces $\sigma_{kd}(n)$ and $\sigma_{kq}(n)$ have independent control, and hence the stability condition (6.58) is simplified to

$$\vec{\sigma}_k^{dq}(n)^T(\vec{\sigma}_k^{dq}(n+1) - \vec{\sigma}_k^{dq}(n)) \leq 0. \tag{6.59}$$

Condition (6.59) is satisfied if we chose

$$\vec{\sigma}_k^{dq}(n+1) - \vec{\sigma}_k^{dq}(n) = \left(-\lambda_{kd}\text{sgn}(\sigma_{kd}(n)) \quad -\lambda_{kq}\text{sgn}(\sigma_{kq}(n))\right)^T \tag{6.60}$$

and determine $\vec{t}_k^{dq}(n)$ based on (6.60). In (6.60), λ_{kd} and λ_{kq} are scalar parameters that determine how fast the closed-loop system reaches the quasi-sliding surface. Substituting (6.56) into (6.60), we obtain

$$\begin{aligned}\vec{\sigma}_k^{dq}(n+1) - \vec{\sigma}_k^{dq}(n) &= (\vec{i^*}_{L_k}^{dq}(n+1) - \vec{i}_{L_k}^{dq}(n+1)) - \vec{\sigma}_k^{dq}(n) \\ &= (\vec{i^*}_{L_k}^{dq}(n+1) - \Phi_k\vec{i}_{L_k}^{dq}(n) - \Gamma_k\vec{V}^{dq} - \Omega_k\vec{t}_k^{dq}(n)) - \vec{\sigma}_k^{dq}(n) \\ &= \left[-\lambda_{kd}\text{sgn}(\sigma_{kd}(n)) \quad -\lambda_{kq}\text{sgn}(\sigma_{kq}(n))\right]^T\end{aligned} \tag{6.61}$$

and then determine $\vec{t}_k^{dq}(n)$. We then use (6.54) to obtain t_{1k}, t_{2k}, and t_{0k} $(=\frac{1}{2}(\frac{T}{2} - t_{1k} - t_{2k}))$ from $\vec{t}_k^{dq}(n)$.

While deriving the duration of the zero vectors, we did not distinguish between the vectors U_7 and U_0. However, to control the zero-axis current, such a distinction is necessary. Let us rewrite the total duration of the zero vectors in a given switching cycle as

$$4t_{0k} = (1-\beta_k)4t_{0k} + \beta_k(4t_{0k}). \tag{6.62}$$

It has been shown by Ye et al. (2000) that for the PTBC, if $\beta_2 = 0.5$, then by assigning $(1-\beta_1)4t_{01}$ to U_0 and $\beta_1(4t_{01})$ to U_7, one can minimize the effect of the zero-axis current. The parameter β_1 is the output of a feedback loop of M1 that regulates the zero-axis current to zero (Ye et al., 2000). If, however, assigning $\beta_2 = 0.5$ is not possible (for reasons of flexibility), then one still can obtain the zero vectors as a combination of the active vectors. For example, one can synthesize a reference vector $\vec{v}_r$ (for M1) in Sector I as

$$\begin{aligned}\vec{v}_r &= \tfrac{v_C}{2T}(t_{01}U_0 + t_{11}U_1 + t_{21}U_2 + 2t_{01}U_7 + t_{21}U_2 + t_{11}U_1 + t_{01}U_0) \\ &= \tfrac{v_C}{2T}\Big(\tfrac{1}{2}t_{01}(U_4+U_1) + t_{11}U_1 + t_{21}U_2 + t_{01}(U_2+U_5) + t_{21}U_2 + t_{11}U_1 + \\ &\quad \tfrac{1}{2}t_{01}(U_1+U_4)\Big).\end{aligned} \tag{6.63}$$

Although this scheme increases the flexibility of operation, it can not completely control the circulation of the zero-axis current. Further reduction of the zero-axis currents is obtained by varying the size of the line inductor and the switching frequency of the converter.

6.3 Results

We present simulation results obtained by closing the PTBC using five different controllers. The first one is a conventional *dq* controller, which is described in (Hiti et al., 1994; Hiti, 1995; Xing et al., 1998, 1999). The second control scheme is due to Ye et al (CS_{Ye}) (Ye et al., 2000). The other three control schemes, which are described in Sections 6.2.1 and 6.2.2, will be referred as CS_1 (for scheme one), CS_2 (for scheme two), and CS_3 (for scheme three), respectively. The values of the nominal parameters for the PTBC are listed in Table 6.2. The outer voltage loop, which regulates the bus voltage at 400 volts, has been chosen to have a slower dynamic response compared to that of the inner current loops to ensure stability of the overall system (Mazumder et al., 2000b, 2001a). The choice of the parameters for the voltage loop are based on the results of Hiti (1995). The load is chosen to be resistive in nature and has a magnitude of R. However, the proposed control schemes CS_1, CS_2, and CS_3 can be applied to systems that involve other types of loads because they are independent of the load type.

Using a conventional *dq* controller (Hiti et al., 1994; Hiti, 1995; Xing et al., 1998, 1999) operating with the bus-clamped SVM (Prasad et al., 1996; Mazumder, 1997b; Xing et al., 1999), we show in Figure 6.7 the steady-state responses obtained for the case in which the parameters of M1 and M2 are equal to the nominal values and the switching instants of the two modules are half a switching cycle apart (interleaved operation) (Xing et al., 1998, 1999). Clearly, the phase currents are balanced. The two modules operate with interleaving to minimize the ripple in the output voltage. We chose the bus-clamped SVM scheme (Xing et al., 1999) to reduce the switching loss of the PTBC and increase its efficiency. In addition,

Table 6.2: Nominal parameters of the PTBC.

Parameter	Nominal Value
$V_{ab} = V_{bc} = V_{ca} = V_n$	208 V (rms)
v_C (regulated)	400 V
Switching frequency ($= \frac{1}{T}$)	32 kHz
$L_1 = L_2 = L_n$	500 μH
$r_{L_1} = r_{L_2} = r_{L_n}$	0.5 Ω
C	1200 μF
R	4 Ω

for power-factor-correction (PFC) applications, the bus-clamped SVM scheme is the most favorable because, in a given sector, the phase carrying the highest current is connected to the bus permanently (Prasad et al., 1996; Mazumder, 1997b).

In practice, it is impossible to manufacture two identical modules. In fact, it is not uncommon to have variations in the circuit parameters of the order of 5%. To simulate one such scenario, we reduce L_1 by 5% from its nominal value, but keep the values of all of the other parameters of M1 equal to their nominal values. Moreover, we keep the values of the parameters of M2 equal to their nominal values. Furthermore, the two modules operate with interleaving and use the same SVM scheme (Xing et al., 1999). In Figure 6.8, we show that, even though there is only a minor difference in one of the parameters of the two modules, the phase currents in each module are no more balanced.

In Figure 6.9, we show projections of the averaged values of the unbalanced phase currents (of M1) in the *dqo* frame onto the $\alpha\beta$o axes. It show that, while the d and q components on the $\alpha\beta$ plane still rotate in a circle, the zero-axis component oscillates up and down. The flow of the zero-sequence current causes a strong oscillation in the phase currents of the two modules. Consequently, the load sharing between M1 and M2 is poor. Thus,

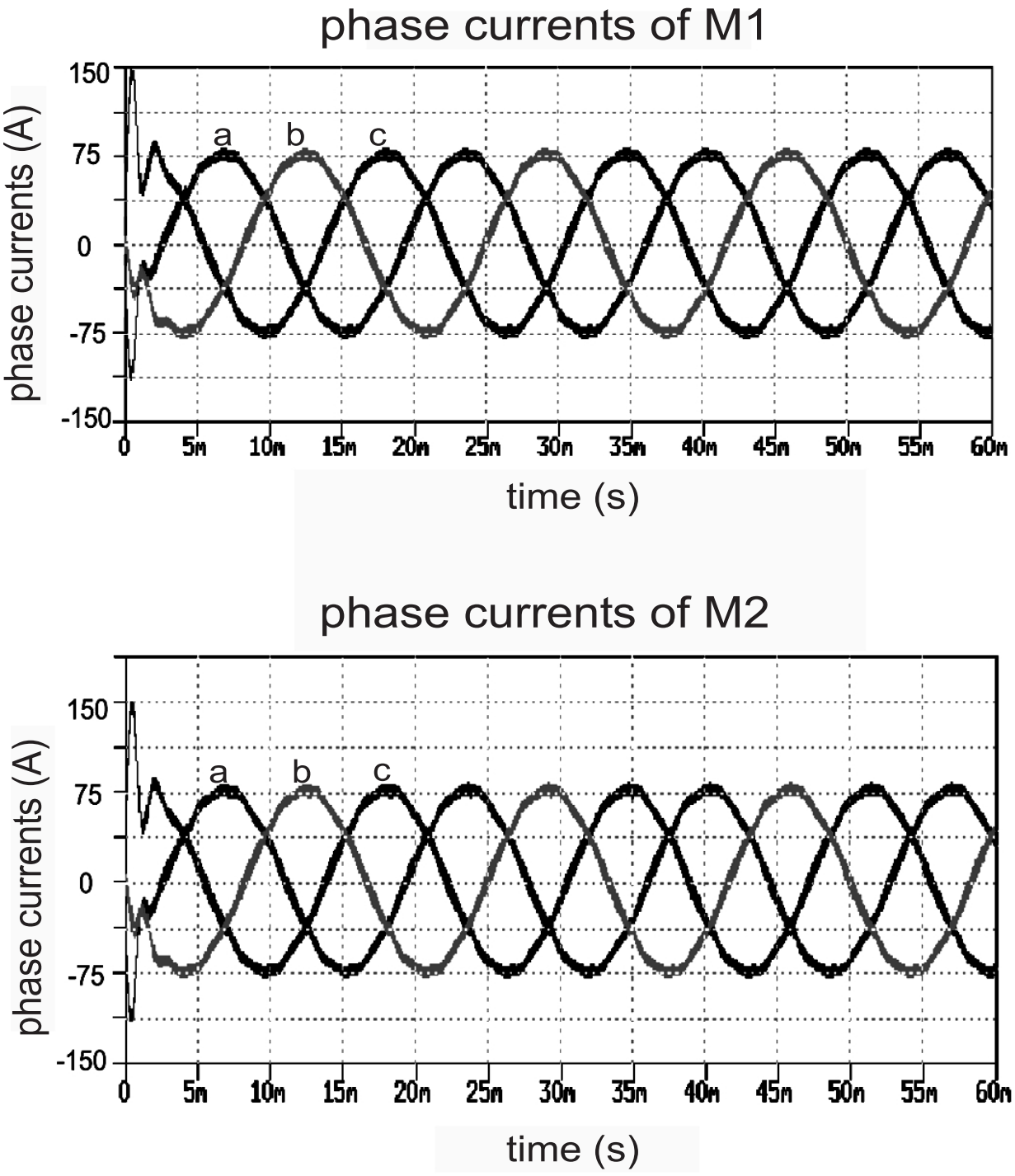

Figure 6.7: The results obtained using a conventional *dq* controller for two similar modules (i.e., the values of the parameters of M1 and M2 are identical). Clearly, the phase currents are balanced.

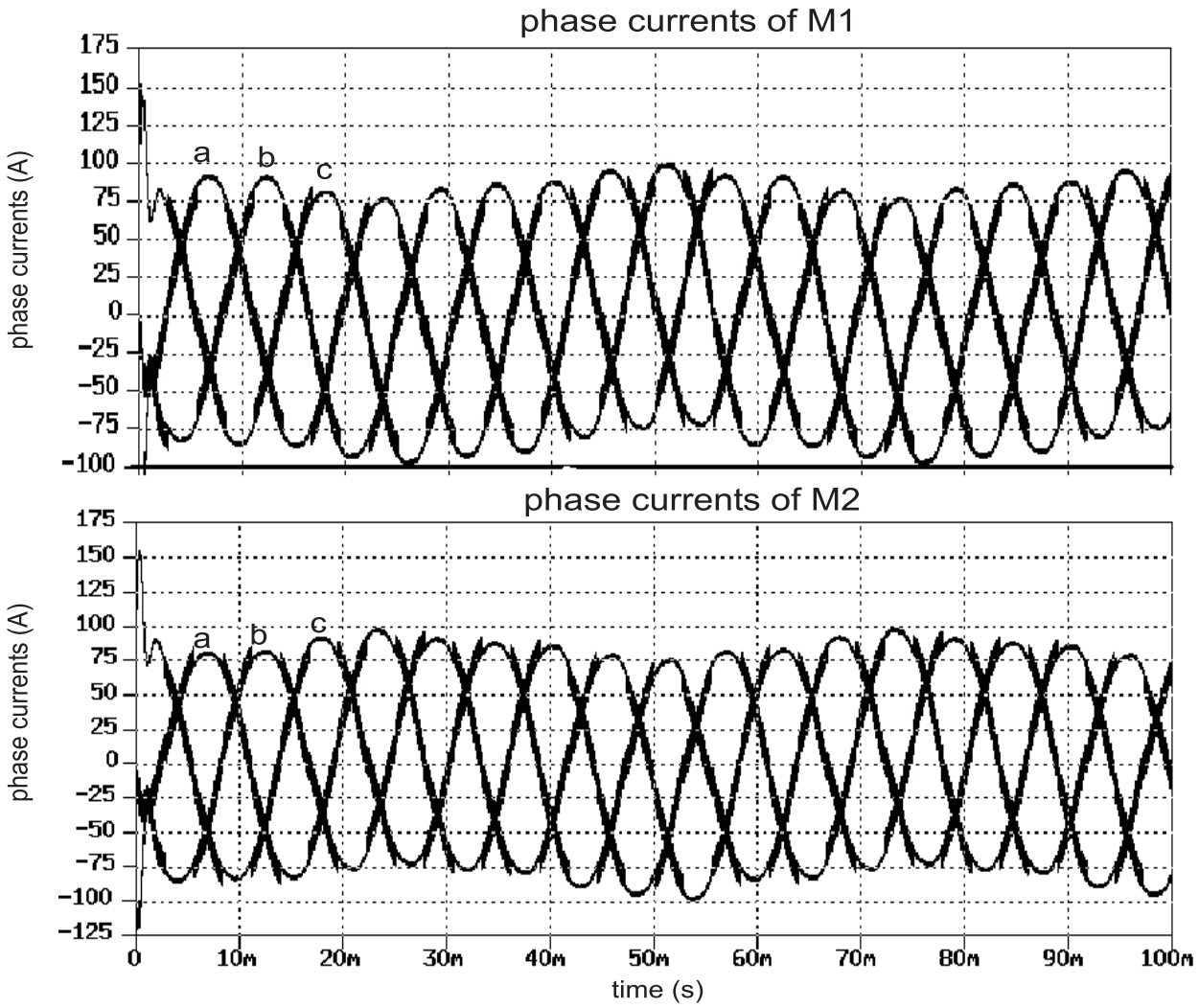

Figure 6.8: The phase currents of M1 and M2 using a conventional controller when the parameters of the modules are the same, except L_1 is 95% of L_2. The result shows the limitation of a conventional *dq* controller in ensuring even-load distribution when the two modules have parametric variations.

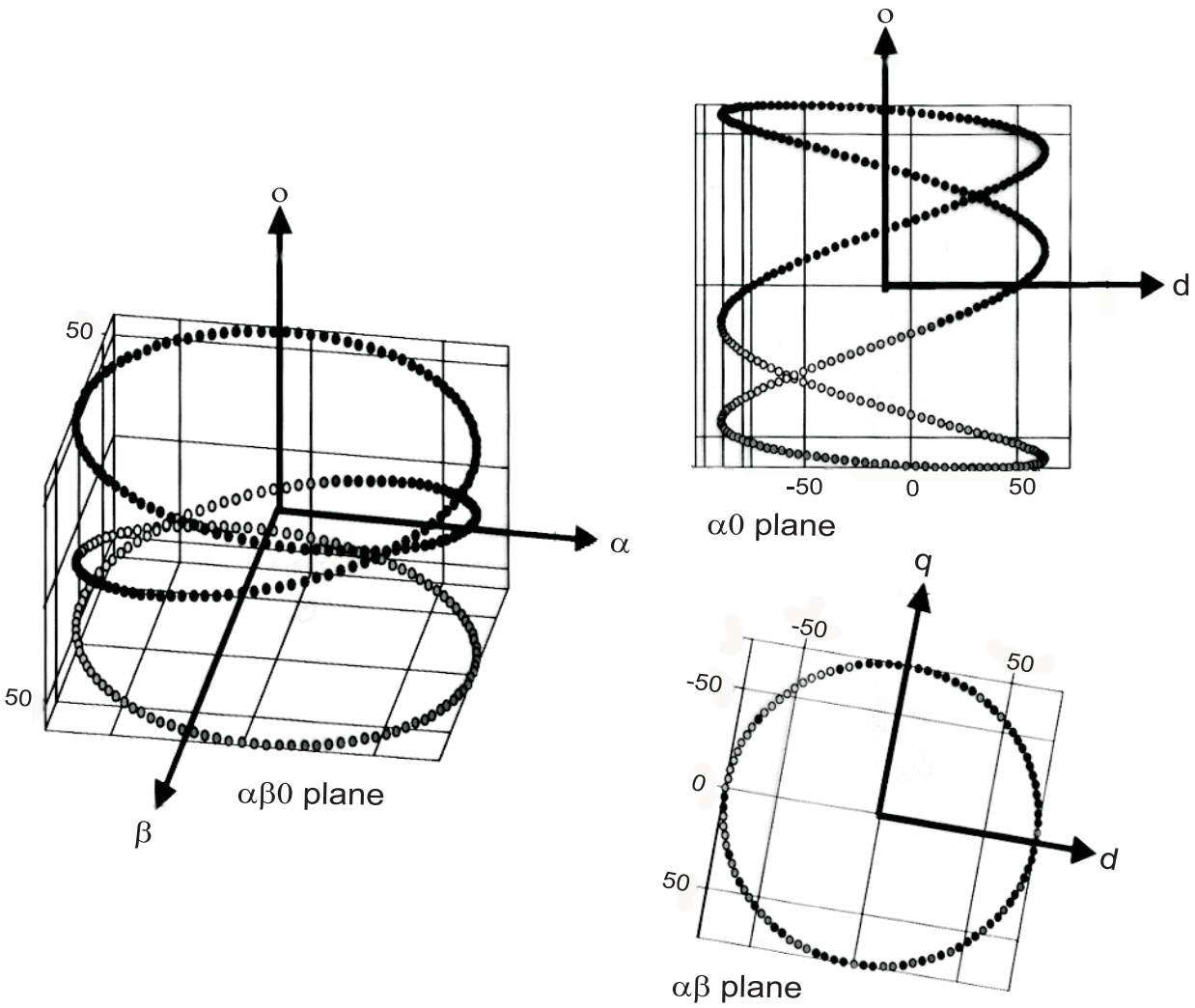

Figure 6.9: Three-dimensional view of the unbalanced phase currents of M1 in the $\alpha\beta o$ frame. It shows that a conventional dq controller can not see the zero-sequence current because it lies on a perpendicular axis.

the performance of a conventional dq control scheme is not satisfactory even under small parametric variations.

In Figure 6.10, we demonstrate the steady-state performance of the PTBC operating with CS_{Ye} (Ye et al., 2000). The values of the parameters are the same as those used to obtain Figures 6.8 and 6.9. We see that, by controlling the zero-sequence current in addition to the

dq currents, the steady-state performance becomes satisfactory. Although the zero-sequence current is not eliminated, its overall effect is minimized.

Next, we explore the dynamic performances of the PTBC using our three proposed control schemes (CS_1, CS_2, and CS_3) and CS_{Ye} under further variations in the parameters of the two modules. The switching frequencies of M1 and M2 are set at 16 kHz and 32 kHz, respectively, to replicate the conditions in Ye et al. (2000). In real life, the two modules will be physically apart, and hence synchronization of the clocks is expensive and not reliable (Lee et al., 1997; Xing et al., 1999). Hence, to increase the redundancy of operation, we switch M1 and M2 asynchronously. To test the robustness of CS_{Ye} under parametric variation, we reduce L_1 by 5% from its nominal value. We test the robustness of CS_1, CS_2, and CS_3 by reducing L_1 by 5% and 15%, an even larger variation in its nominal value. The larger variation in L_1, which makes paralleling M1 and M2 even more difficult (Xing et al., 1999), is chosen to test the robustness of the nonlinear controller under extreme conditions. For all of the control schemes, the values of all of the other parameters are kept equal to their nominal values. We found that, using the proposed control schemes, the performance for smaller variations in L_1 is excellent. Due to the limitation in space and to avoid duplication, we only demonstrate the performance of CS_1, CS_2, and CS_3 for the larger (15%) variation in L_1. If the closed-loop system performs satisfactorily for large parametric variations, it will certainly perform satisfactorily for small parametric variations.

Having set the operating parameters, we determine the response of the PTBC (using CS_1, CS_2, CS_3, and CS_{Ye}) under small- and large-signal feedforward and feedback disturbances: four cases are considered. For all cases, we investigate the performance of the PTBC by determining the drop in its bus voltage, the change in its reactive and active currents, the power factor, and the current sharing between the modules.

For case one, we subject the PTBC, operating in steady-state, to a sudden change in the input voltage. Initially, the input voltage is set equal to its nominal value, and after the transient, it is assumed to decrease to 30% of its nominal value. We begin by investigating

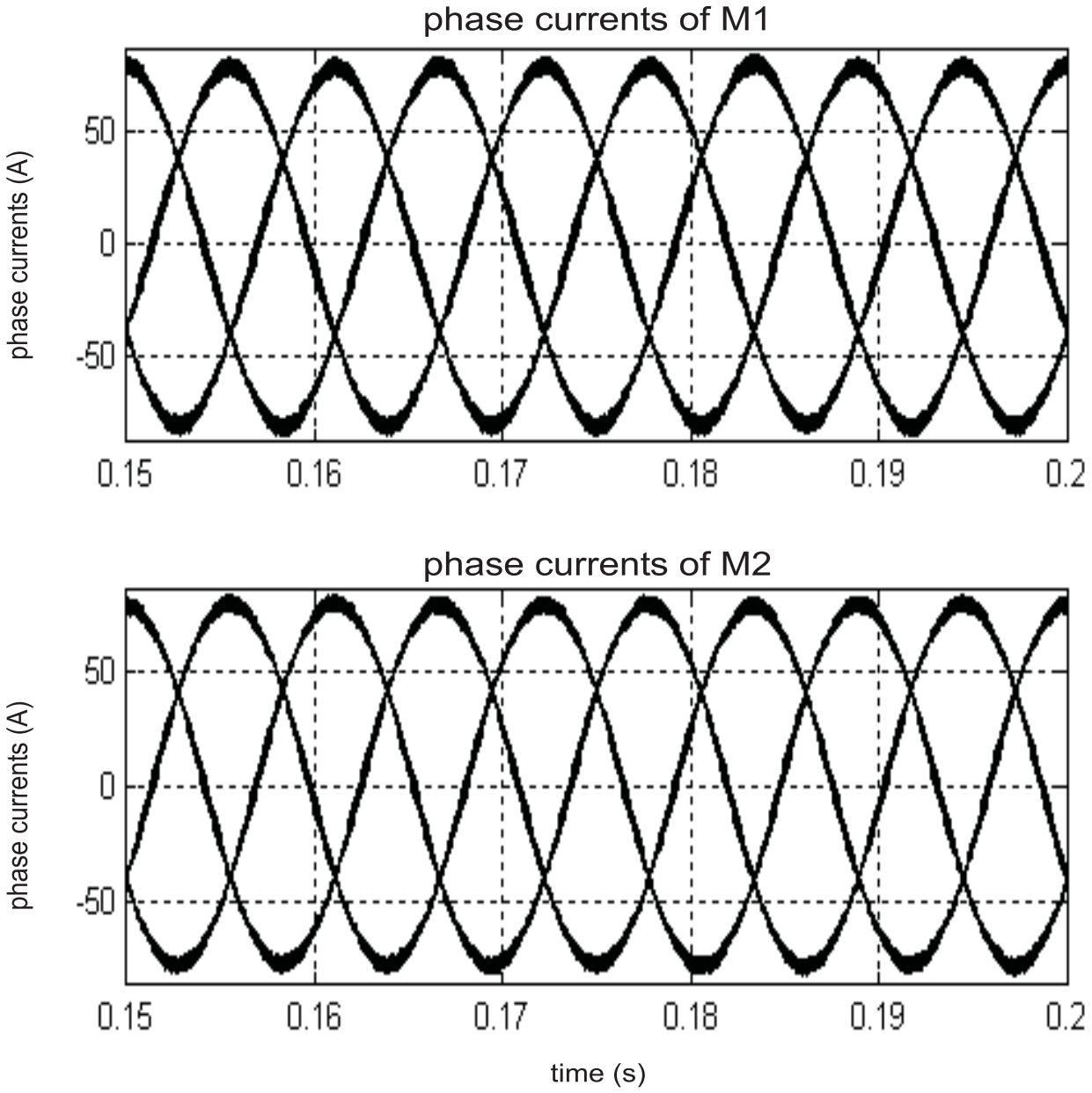

Figure 6.10: The phase currents of M1 and M2 obtained using CS_{Ye} when the parameters of the modules are the same, except L_1 is 95% of L_2. By adding a zero-sequence controller, the effect of the overall unbalance as seen in Figure 6.8 has been minimized.

the drop in the bus voltage. The results are shown in Figures 6.11(a), 6.11(c), 6.11(e), and 6.11(g). We find out that the dip in the bus voltage is maximum when the PTBC is operated using CS_{Ye}. In addition, for this control scheme, the recovery time for the bus voltage is longer. Among CS_1, CS_2, and CS_3, the latter has a slightly more sluggish response. The performances of CS_1 and CS_2 are close. The drop in the bus voltage using CS_3 is about 3V more than those obtained using CS_1 and CS_2. We note that the ripple in the bus voltage obtained using CS_1, CS_2, and CS_3 is marginally higher than that obtained with CS_{Ye} because they operate with $L_1 = 0.85L_n$ and $L_2 = L_n$ compared to $L_1 = 0.95L_n$ and $L_2 = L_n$ for CS_{Ye}. Thus, even with a larger parametric variation, the performances of the proposed control schemes are better than that obtained using the control scheme proposed by Ye et al (2000).

Case two is similar to case one, except that the drop in the input voltage is larger, 50% of its nominal value. We plot the changes in the bus voltage obtained with all of the control schemes. Figures 6.11(b), 6.11(d), 6.11(f), and 6.11(h) show that, with a larger feedforward disturbance, the dip in the bus voltage is larger and the recovery time is longer for all of the control schemes. However, the drop in the bus voltage and the recovery time obtained with CS_{Ye} are, respectively, larger and longer than those obtained with CS_1, CS_2, and CS_3, even though CS_{Ye} is implemented for a smaller variation in L_1.

For case three, we subject the PTBC, operating in steady-state, to a sudden change in the load resistance from 6 Ω to 4 Ω (nominal value). Figures 6.12(a), 6.12(c), 6.12(e), and 6.12(e) show that the changes in the bus voltage obtained using CS_1, CS_2, and CS_3 are smaller than that obtained with CS_{Ye}. Moreover, the recovery time obtained using CS_{Ye} is longer.

Finally, for case four, we subject the PTBC to an even larger change in the load resistance from 400 Ω (almost no load) to full load (4Ω). The results are shown in Figures 6.12(b), 6.12(d), 6.12(f), and 6.12(h), respectively. We see that the regulation of the bus voltage, immediately after the disturbance, is the poorest when the PTBC is controlled using CS_{Ye}.

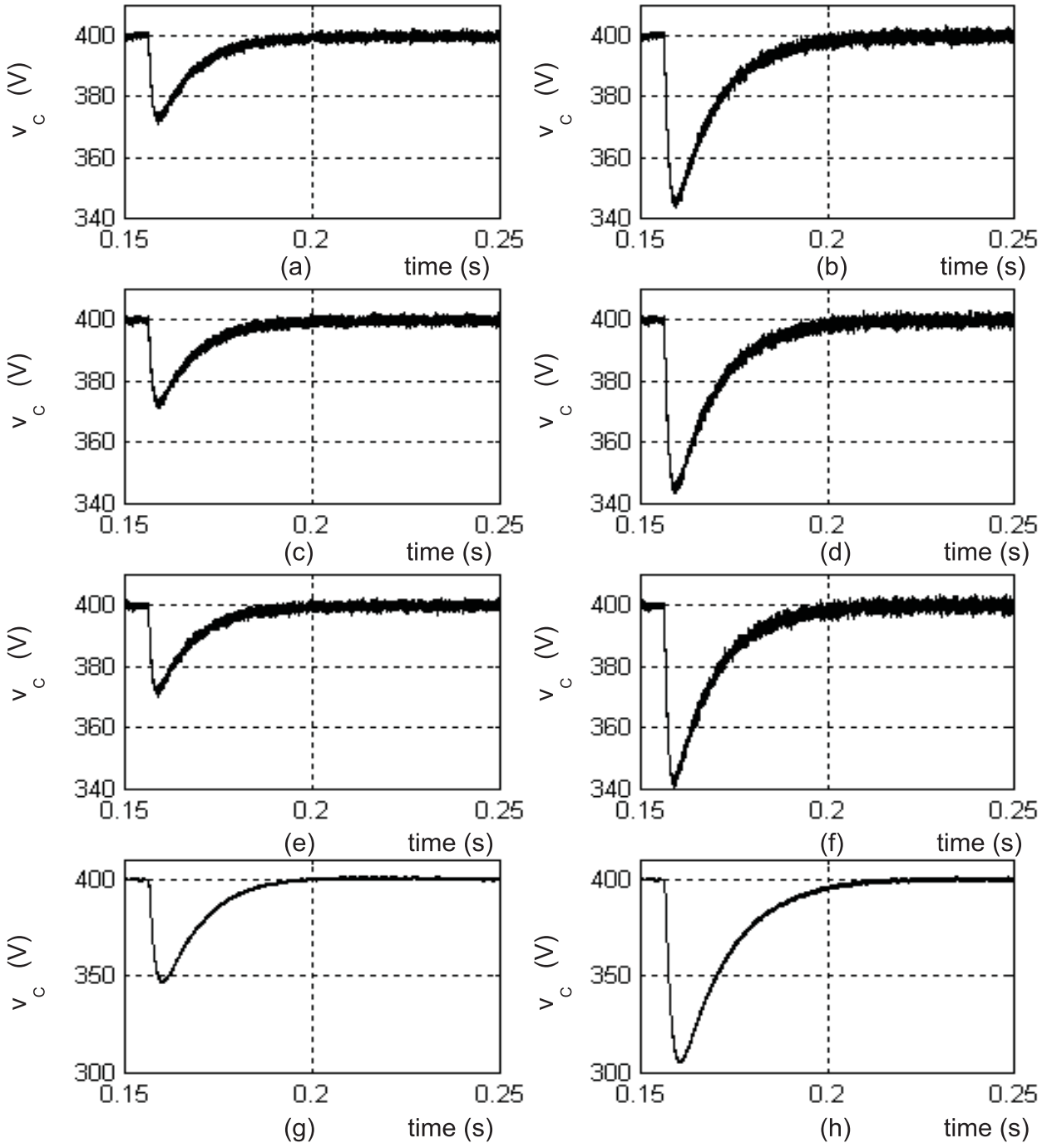

Figure 6.11: Change in the bus voltage obtained using CS_1 (a-b), CS_2 (c-d), CS_3 (e-f), and CS_{Ye} (g-h) for case one (figures on the left) and case two (figures on the right). For either case, the drop in the bus voltage is larger when using CS_{Ye}, even though it is implemented for a smaller variation (5%) L_1 as compared to the proposed control schemes (15%).

Moreover, the recovery time of the bus voltage obtained with CS_{Ye} is the longest.

Next, we investigate the performances of the inner (dq) current loops for all cases under feedforward and feedback disturbances. The higher the disturbance rejection capability of these loops is, the lesser the impact of these disturbances on the bus voltage is. Using the same procedure as described above, we first investigate the response of the d-axis (active) current using all of the control schemes. Figures 6.13(a), 6.13(c), 6.13(e), and 6.13(f) show the response of the active current of M1 (i.e., i_{L1d}) for case one. Later on, we will show the currents of both modules. We see from the figures that, using the proposed control schemes, the PTBC does not have any undershoot after the feedforward disturbance. However, the parallel converter shows a significant drop in the i_{L1d} when using CS_{Ye}. Because of this undershoot, the drops in the bus voltage obtained using CS_{Ye}, as shown in Figures 6.11 and 6.12, are higher.

For case two, the i_{L1d} obtained using CS_1, CS_2, CS_3, and CS_{Ye} are shown in Figures 6.13(b), 6.13(d), 6.13(f), and 6.13(h), respectively. The overall responses are similar to those obtained in case one. However, the recovery times using all schemes increase. Moreover, when the PTBC operates with CS_{Ye}, there is a further increase in the undershoot of i_{L1d}. The ripples in the i_{L1d} using CS_1, CS_2, and CS_3 are higher because they operate with $L_1 = 0.85L_n$ and $L_2 = L_n$ as compared to $L_1 = 0.95L_n$ and $L_2 = L_n$ for CS_{Ye}. The ripple in the i_{L1d} obtained with CS_3 is lower than that obtained with CS_1 and CS_2 because the former combines a symmetrical SVM with VSC within the boundary layer. The responses of i_{L1d} for cases three and four, shown in Figures 6.14(a)-6.14(h), are self explanatory and similar to those obtained for cases one and two. We see that the performance of the PTBC operating with CS_{Ye} suffers considerably for large load disturbances. No such shortcoming was observed for the proposed control schemes. Therefore, even with larger parametric variations, the disturbance rejection capabilities of the proposed control schemes are better than that of CS_{Ye}.

We then investigate the response of the q-axis (reactive) current of the PTBC for all

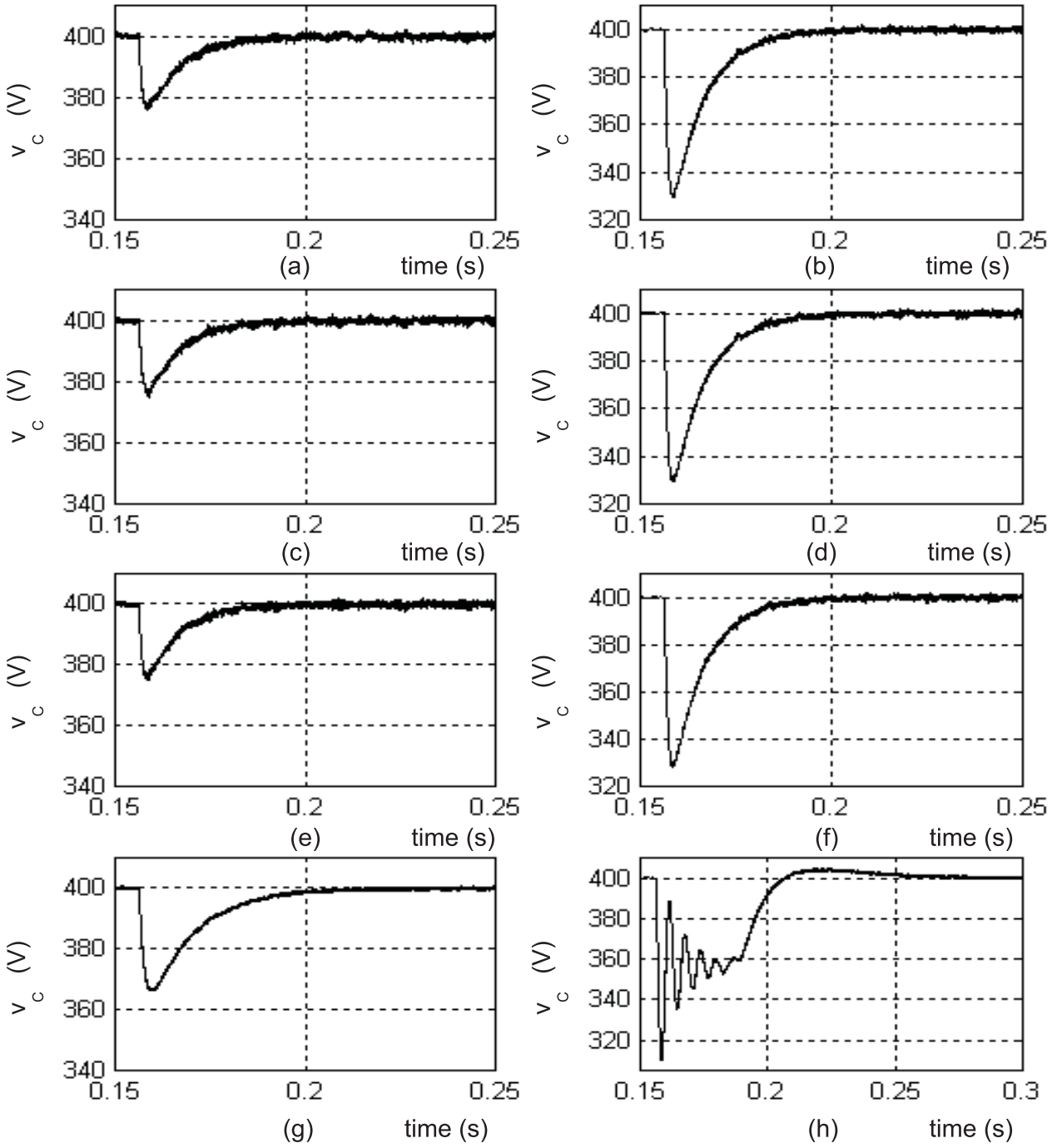

Figure 6.12: Drop in the bus voltage obtained using CS_1 (a-b), CS_2 (c-d), CS_3 (e-f), and CS_{Ye} (g-h) for cases three (figures on the left) and four (figures on the right). For both cases, the drop in the bus voltage is larger when using CS_{Ye}, even though it is implemented for a smaller variation (5%) L_1 as compared to the proposed control schemes (15%).

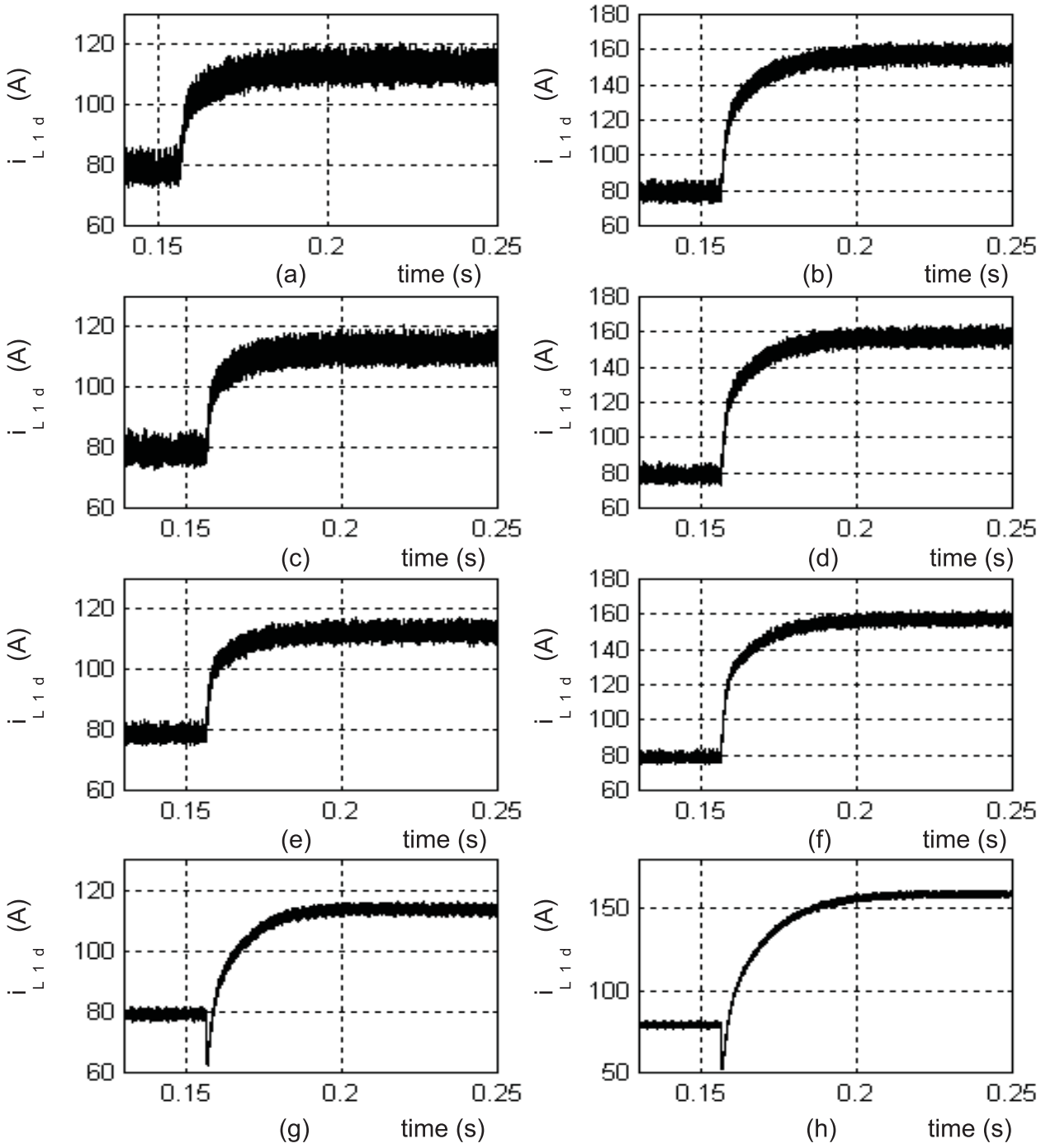

Figure 6.13: Change in the active current of M1 obtained using CS_1 (a-b), CS_2 (c-d), CS_3 (e-f), and CS_{Ye} (g-h) for case one (figures on the left) and case two (figures on the right). Although CS_1, CS_2, and CS_3 operate with a larger variation in L_1, their performances are good. Using CS_{Ye}, there is more than a 30% undershoot in i_{L1d} immediately after the disturbances.

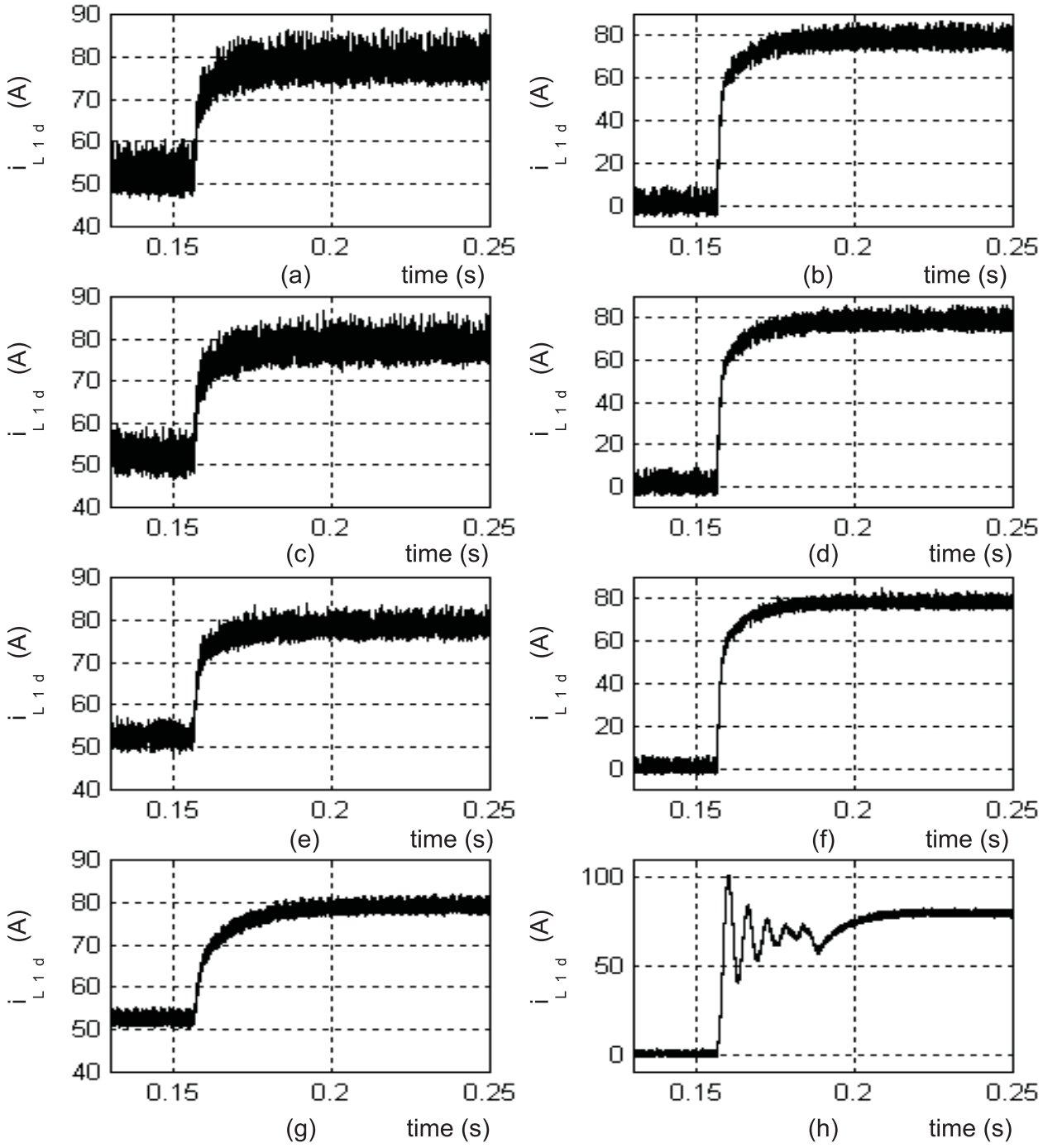

Figure 6.14: Change in the active current of M1 using CS_1 (a-b), CS_2 (c-d), CS_3 (e-f), and CS_{Ye} (g-h) for case three (figures on the left) and case four (figures on the right). The performances of the proposed control schemes are satisfactory, even though they operate with a larger variation in L_1. The performance of CS_{Ye}, for case four, is not satisfactory. Besides, CS_{Ye} has a slower recovery time for case three.

cases. The results are shown in Figures 6.15 and 6.16 for M1. We see that, under steady-state conditions, the average of i_{L1q} obtained using all control schemes is about zero. As such, the input power factor of the PTBC is close to unity, as shown in Figures 6.17 and 6.18. However, for either a large disturbance in the load or the input voltage, CS_{Ye} is unable to maintain the average of i_{L1q} at zero immediately after the disturbance. As such, the perfect decoupling between i_{L1d} and i_{L1q} is lost (Hiti, 1995) and the rate of transfer of power from the input to the load deteriorates (Hiti, 1995). For CS_1, CS_2, and CS_3, i_{L1q} does not have any undershoot after the disturbances. Therefore, it follows from Figures 6.13-6.16 that, unlike CS_{Ye}, the proposed control schemes maintain decoupling even under severe feedforward or feedback disturbances and hence are more robust (Hiti, 1995).

Next, we investigate the sharing of the line currents between M1 and M2 when the PTBC is subjected to a large disturbance in either the voltage (case two) or the load (case four). Figures 6.19(a), 6.19(c), 6.19(e), and 6.19(g) show the performance of the PTBC for case two using CS_1, CS_2, CS_3, and CS_{Ye}, respectively. For this case, we see that the best transient response is achieved using CS_1. The recovery times obtained using CS_2 and CS_3 are slightly more than that obtained with CS_1. The recovery time of the PTBC obtained with CS_{Ye} is the slowest. Moreover, immediately after the change in the voltage, there is an undershoot and an overshoot in two of the phase currents, which are not evident in the responses obtained with the proposed control schemes.

Figures 6.19(b), 6.19(d), 6.19(f), and 6.19(h) show the performance of the PTBC for case four using CS_1, CS_2, CS_3, and CS_{Ye}, respectively. Among the three proposed control schemes, CS_3 achieves the best compromise between the response time and current sharing. The recovery times of CS_1 and CS_2 are smaller than that of CS_3. The response of the PTBC obtained with CS_{Ye} is significantly inferior to those obtained with the proposed control schemes, both in terms of the response time and current sharing. Thus, even with a larger parametric variation, the performances of CS_1, CS_2, and CS_3 are better than that of CS_{Ye}.

Finally, we show the impact of the control schemes CS_1, CS_2, and CS_3, and CS_{Ye} on the steady-state ripples of the phase currents (in the $\alpha\beta$ frame) and on the zero-axis current

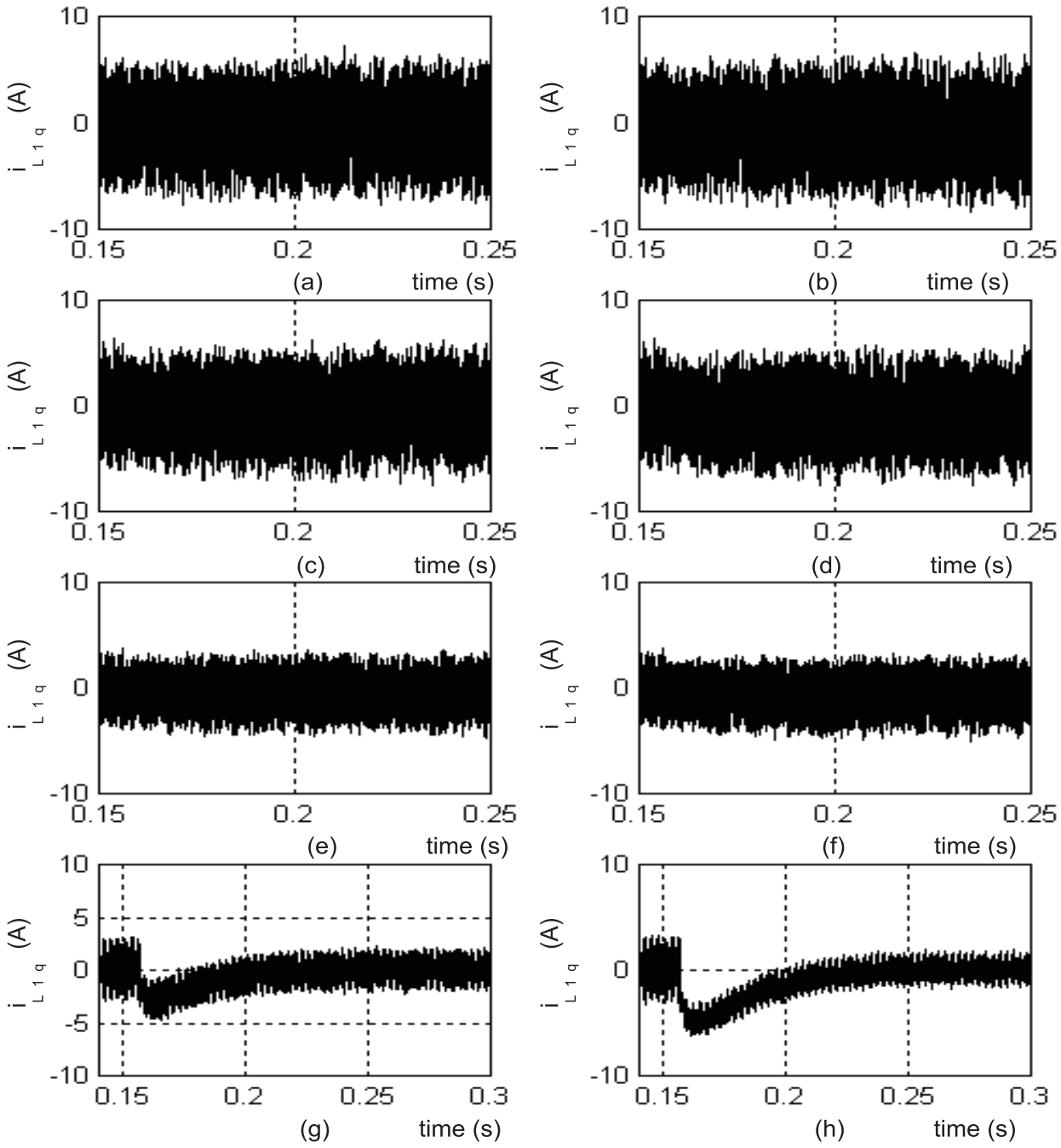

Figure 6.15: Change in the reactive current of M1 obtained using CS_1 (a-b), CS_2 (c-d), CS_3 (e-f), and CS_{Ye} (g-h) for case one (figures on the left) and case two (figures on the right). The performances of the proposed control schemes are good, even though they operate with a larger variation in L_1. However, CS_{Ye} fails to maintain the average of i_{L1q} at zero immediately after the disturbance. This weakens the decoupling between i_{L1d} and i_{L1q} and hence the dynamic response of the PTBC suffers.

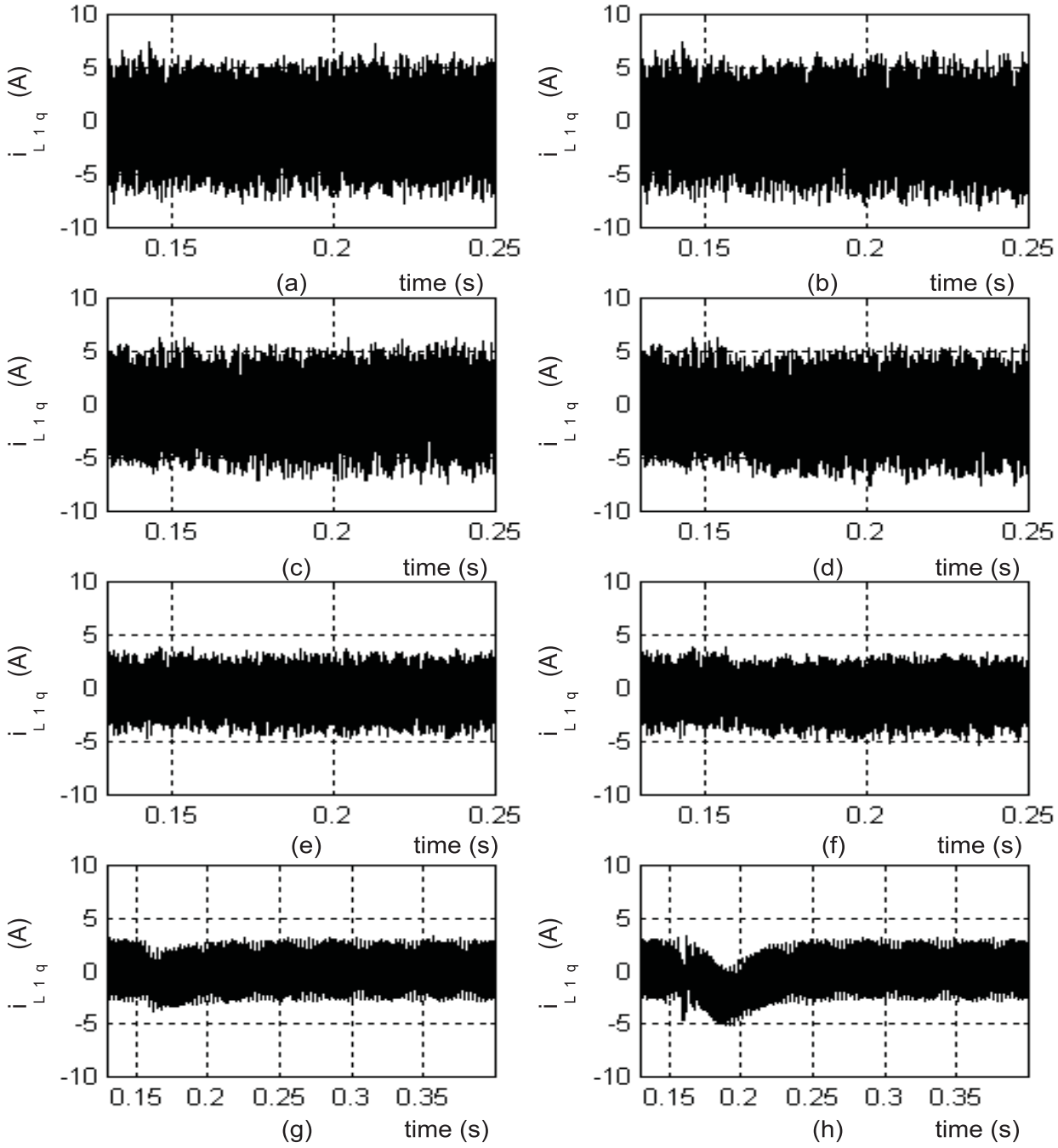

Figure 6.16: Change in the reactive current of M1 obtained using CS_1 (a-b), CS_2 (c-d), CS_3 (e-f), and CS_{Ye} (g-h) for case three (figures on the left) and case four (figures on the right). The performances of the proposed control schemes are good, even though they operate with a larger variation in L_1. For case four, CS_{Ye} fails to maintain the average of i_{L1q} at zero immediately after the disturbance. This weakens the decoupling between i_{L1d} and i_{L1q} and hence the dynamic response of the PTBC suffers.

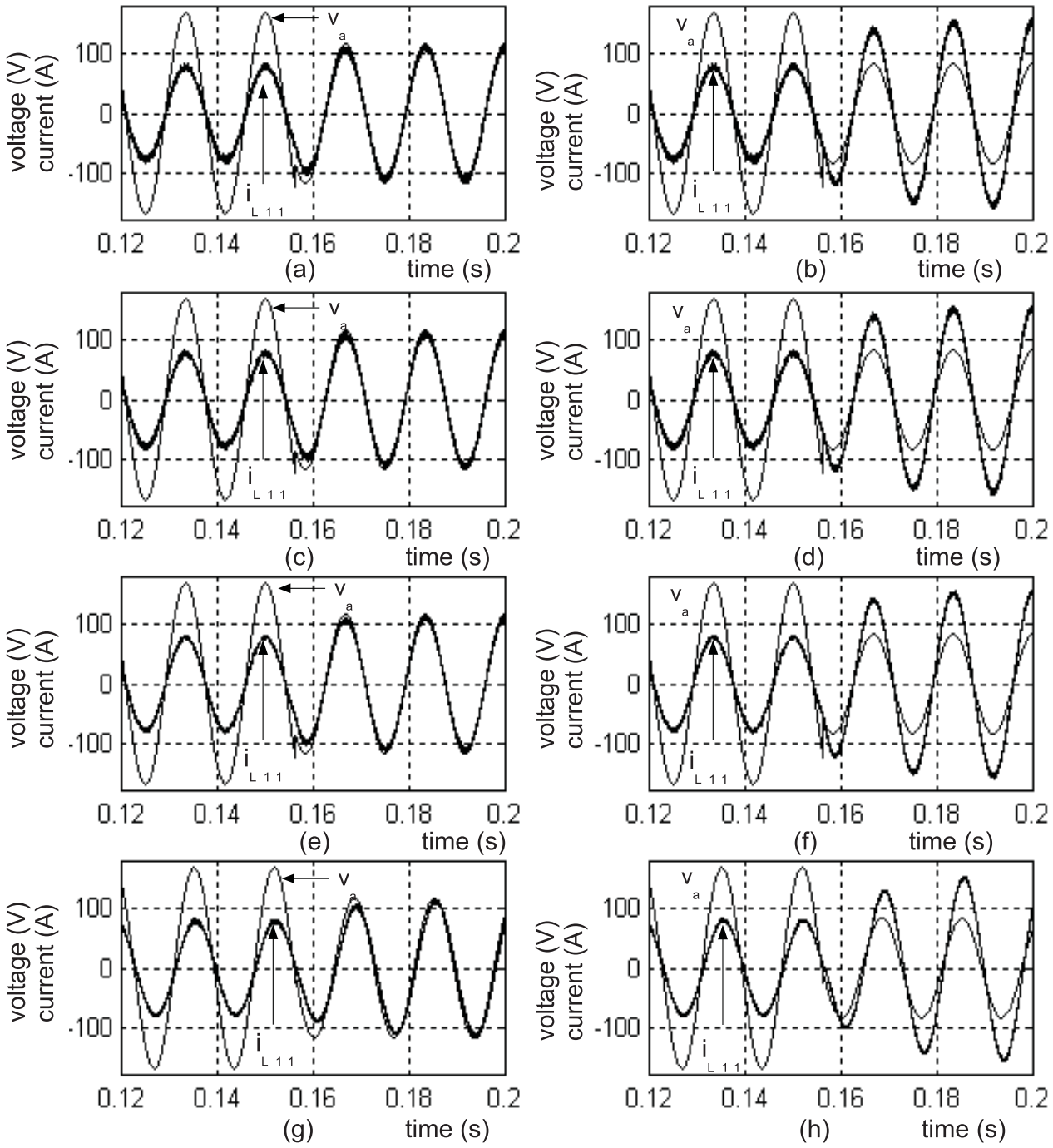

Figure 6.17: Input power factor of M1 obtained using CS_1 (a-b), CS_2 (c-d), CS_3 (e-f), and CS_{Ye} (g-h) for case one (figures on the left) and case two (figures on the right).

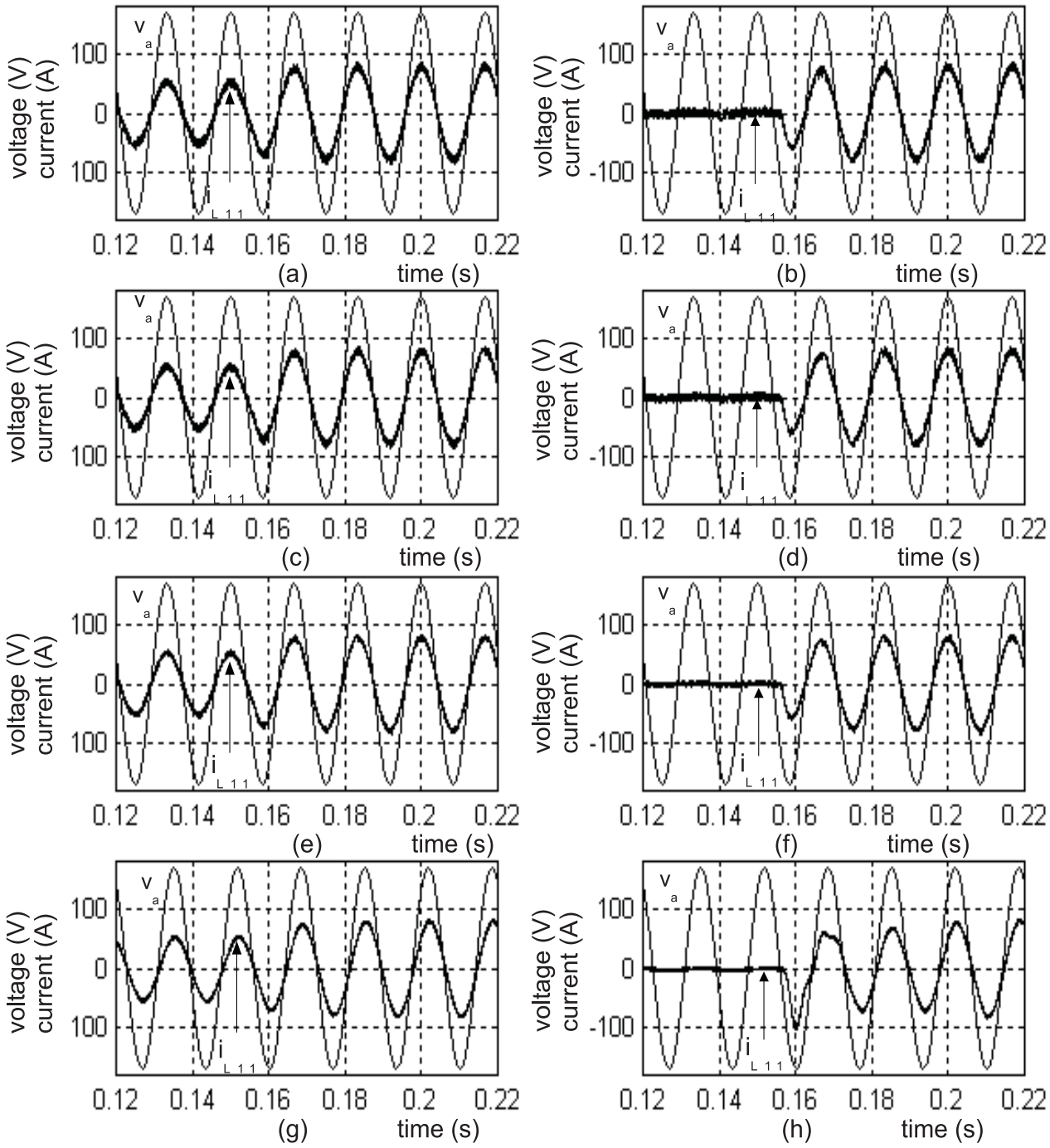

Figure 6.18: Input power factor of M1 obtained using CS_1 (a-b), CS_2 (c-d), CS_3 (e-f), and CS_{Ye} (g-h) for case three (figures on the left) and case four (figures on the right).

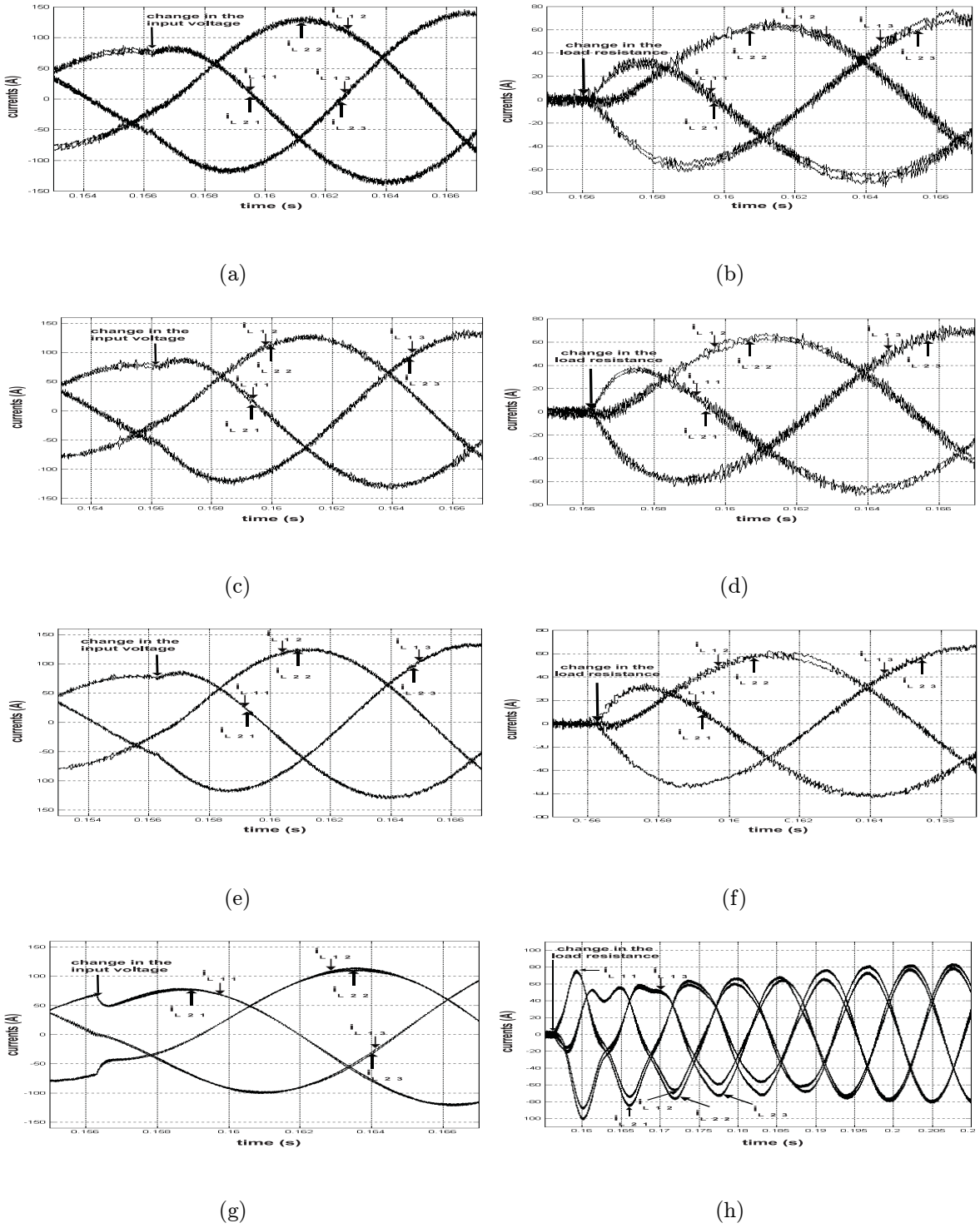

Figure 6.19: Distribution of the line currents between M1 and M2 obtained using CS_1 (a-b), CS_2 (c-d), CS_3 (e-f), and CS_{Ye} (g-h) when the PTBC is subjected to a large disturbance in the input voltage (case two) and the load (case four). The proposed control schemes and CS_{Ye} operate with $L_1 = 85\%L_n$ and $L_1 = 95\%L_n$, respectively.

that circulates between the two modules in Figures 20(a)-20(b), Figures 6.20(c)-6.20(d), Figures 6.20(e)-6.20(f), and Figures 6.20(g)-6.20(h), respectively. For all of these plots, we chose $L_1 = 0.85L_n$ and $L_2 = L_n$. All other parameters are kept the same as before. We note that the smaller the magnitude of the zero-axis current is, the more effective the load sharing between the two modules is. Figures 6.20(c) and 6.20(d) show that using CS_2 yields a negligible improvement in the steady-state ripple and a marginal reduction in $i_{L_{1o}}$ as compared to those shown in Figures 6.20(a) and 6.20(b) (which are obtained using CS_1). However, the steady-state ripple obtained with CS_3 is better than those obtained using CS_1 and CS_2. More importantly, the zero-axis current obtained with CS_3 has a smaller magnitude compared to the previous cases. The steady-state results obatined using CS_3 and CS_{Ye} are close. Therefore, CS_3 attains the best compromise between the dynamic and steady-state performances.

6.4 Extension to Other Applications

While CS_1, CS_2, and CS_3 can be used to control a PTBC with more than two modules or other multi-phase and multi-leg converters, in this section, we demonstrate these extensions only for the discrete control scheme CS_3.

6.4.1 Control of A Parallel Three-Phase Boost Converter with More Than Two Modules

The design of the control scheme CS_3 for a PTBC (operating with two modules) is described in detail in Section 6.2.2. In this section, we show how one can apply the control scheme to a parallel three-phase boost converter with more than two modules. Figure 6.21 shows one such parallel converter operating with three modules. The dynamics of the converter is described by

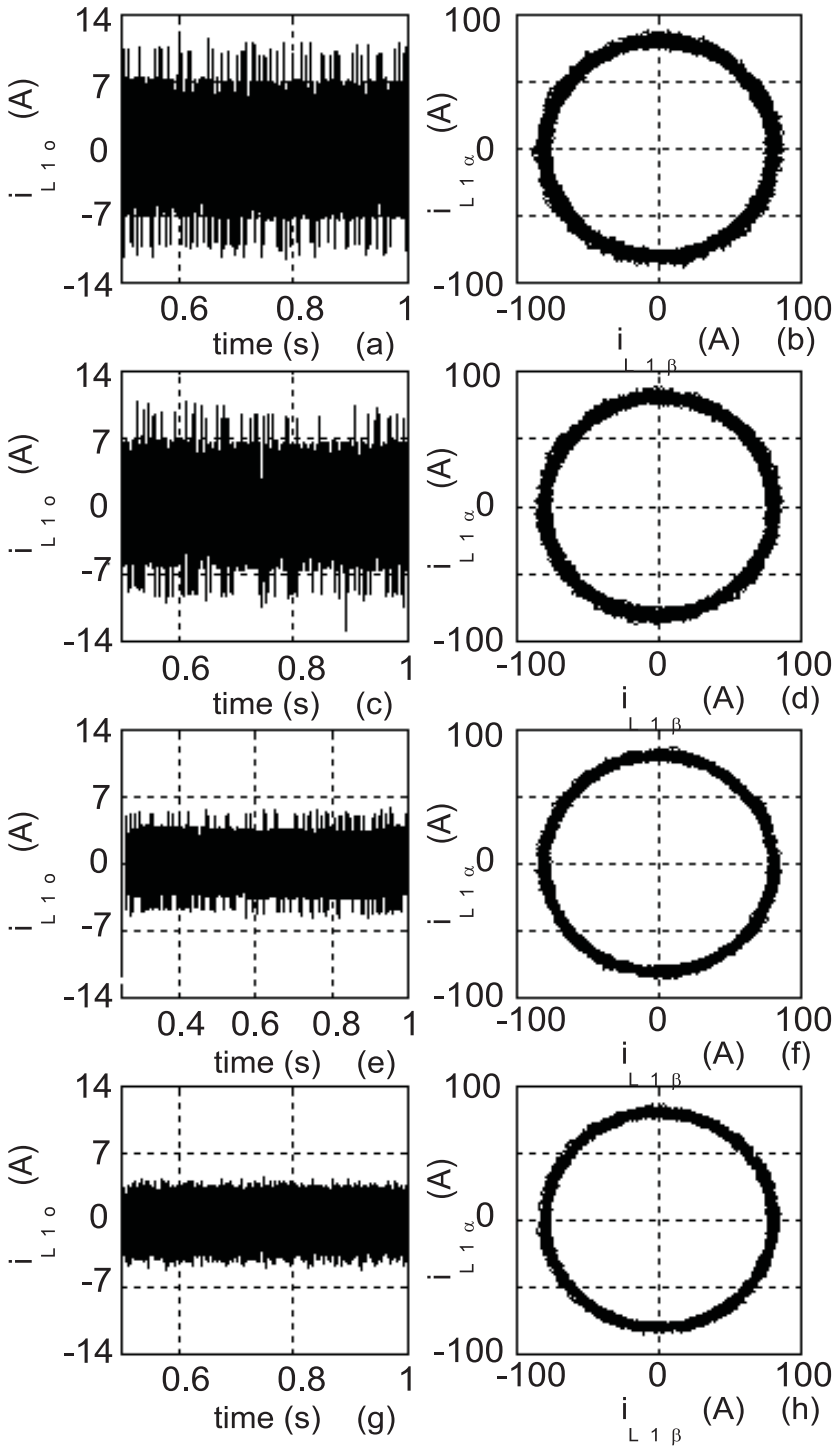

Figure 6.20: Steady-state currents on the zero axis and the $\alpha\beta$ axes for M1 obtained using CS_1 (a-b), CS_2 (c-d), CS_3 (e-f), and CS_{Ye} (g-h). All of the cases have the same parametric variations. As such, the harmonic distortion and the zero-sequence current of CS_3 and CS_{Ye} are close.

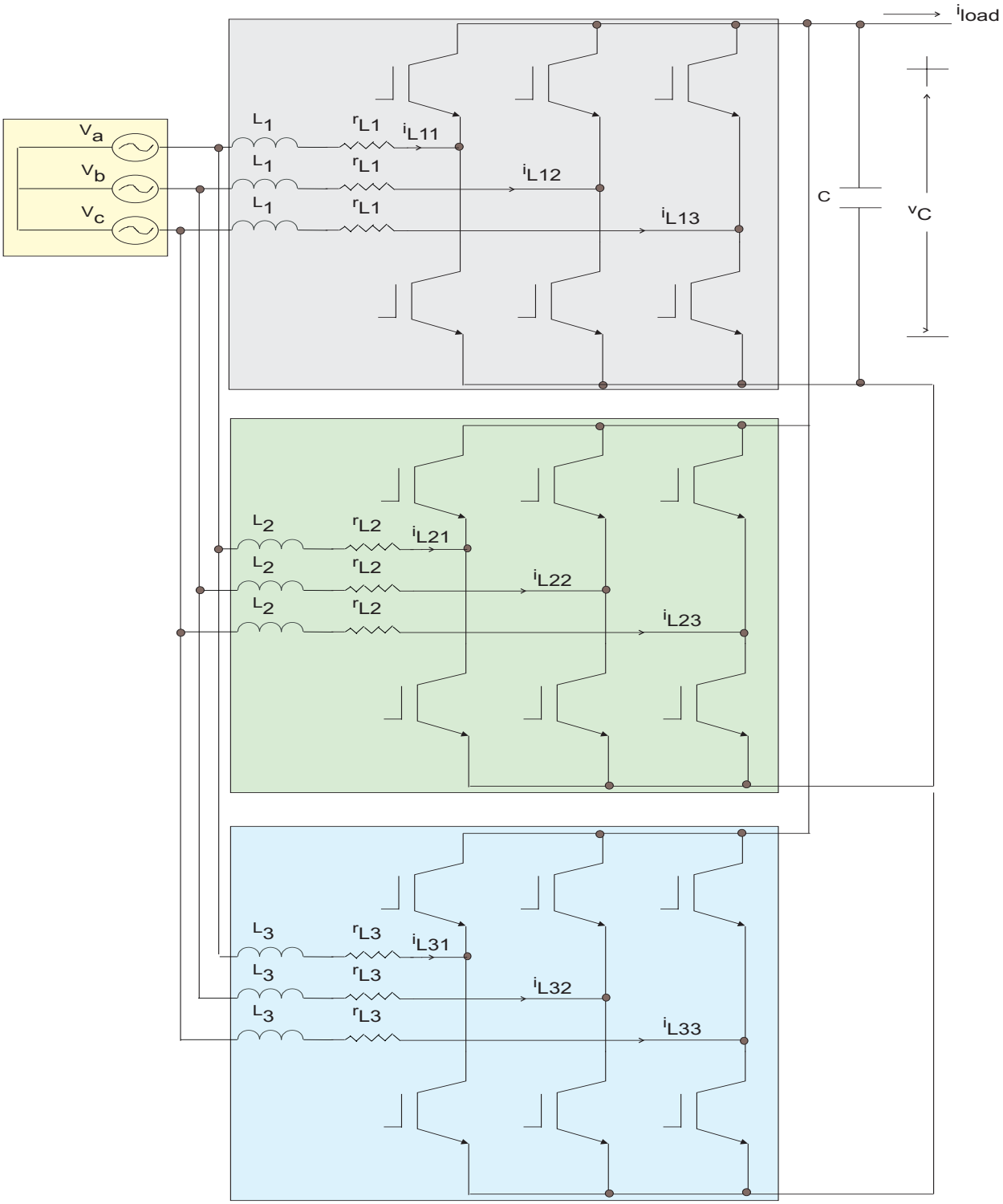

Figure 6.21: Schematic of a parallel three-phase boost converter with three modules.

$$\begin{aligned} \dot{v}_C &= -\tfrac{1}{C} i_{load} + \tfrac{1}{C} \textstyle\sum_{k=1}^{3} \sum_{j=1}^{3} i_{L_{kj}} u_{kj} \\ \dot{\vec{i}}^{abc}_{L_k} &= \textstyle\sum_{j=1}^{3} P_{kj} \vec{i}^{abc}_{L_j} + P_{k4} \vec{V}^{abc} + v_C \sum_{j=5}^{7} P_{kj} \vec{u}^{abc}_{j-4} \end{aligned} \tag{6.64}$$

where $\vec{u}_1^{abc} = [u_{11}\ u_{12}\ u_{13}]^T$, $\vec{u}_2^{abc} = [u_{21}\ u_{22}\ u_{23}]^T$, and $\vec{u}_3^{abc} = [u_{31}\ u_{32}\ u_{33}]^T$ and the matrices P_{11}, P_{12}, P_{13}, P_{14}, P_{15}, P_{16}, and P_{17} are defined as

$$P_{11} = -\tfrac{r_{L_1}}{3L_1(L_1L_2+L_1L_3+L_2L_3)} * \begin{bmatrix} 3L_1(L_2+L_3)+2L_2L_3 & -L_2L_3 & -L_2L_3 \\ -L_2L_3 & 3L_1(L_2+L_3)+2L_2L_3 & -L_2L_3 \\ -L_2L_3 & -L_2L_3 & 3L_1(L_2+L_3)+2L_2L_3 \end{bmatrix} \tag{6.65}$$

$$P_{12} = \tfrac{r_{L_2}}{3(L_1L_2+L_1L_3+L_2L_3)} \begin{bmatrix} L_3 & L_3 & L_3 \\ L_3 & L_3 & L_3 \\ L_3 & L_3 & L_3 \end{bmatrix} \tag{6.66}$$

$$P_{13} = \tfrac{r_{L_3}}{3(L_1L_2+L_1L_3+L_2L_3)} \begin{bmatrix} L_2 & L_2 & L_2 \\ L_2 & L_2 & L_2 \\ L_2 & L_2 & L_2 \end{bmatrix} \tag{6.67}$$

$$P_{14} = \tfrac{1}{3L_1} \begin{bmatrix} 2 & -1 & -1 \\ -1 & 2 & -1 \\ -1 & -1 & 2 \end{bmatrix} \tag{6.68}$$

$$P_{15} = -\tfrac{1}{3L_1(L_1L_2+L_1L_3+L_2L_3)} * \begin{bmatrix} 3L_1(L_2+L_3)+2L_2L_3 & -L_2L_3 & -L_2L_3 \\ -L_2L_3 & 3L_1(L_2+L_3)+2L_2L_3 & -L_2L_3 \\ -L_2L_3 & -L_2L_3 & 3L_1(L_2+L_3)+2L_2L_3 \end{bmatrix} \tag{6.69}$$

$$P_{16} = \tfrac{1}{3(L_1L_2+L_1L_3+L_2L_3)} \begin{bmatrix} L_3 & L_3 & L_3 \\ L_3 & L_3 & L_3 \\ L_3 & L_3 & L_3 \end{bmatrix} \tag{6.70}$$

$$P_{17} = \frac{1}{3(L_1L_2+L_1L_3+L_2L_3)} \begin{bmatrix} L_2 & L_2 & L_2 \\ L_2 & L_2 & L_2 \\ L_2 & L_2 & L_2 \end{bmatrix}. \tag{6.71}$$

The matrices P_{21}, P_{22}, P_{23}, P_{24}, P_{25}, P_{26}, and P_{27} and P_{31}, P_{32}, P_{33}, P_{34}, P_{35}, P_{36}, and P_{37} can be obtained similarly. Using (6.17), (6.20), (6.64)-(6.71), and

$$\begin{aligned} \dot{\vec{i}}^{dqo}_{L_k} &= T(\theta)\sum_{j=1}^{3} P_{kj}[T(\theta)]^{-1}\vec{i}^{dqo}_{L_j} + T(\theta)P_{k4}[T(\theta)]^{-1}\vec{V}^{dqo} + \\ &\quad v_C T(\theta)\sum_{j=5}^{7} P_{kj}[T(\theta)]^{-1}\vec{u}^{dqo}_{j-4} \end{aligned} \tag{6.72}$$

we obtain

$$\begin{aligned} \dot{\vec{i}}^{dqo}_{L_1} = \begin{bmatrix} \dot{i}_{L_{1d}} \\ \dot{i}_{L_{1q}} \\ \dot{i}_{L_{1o}} \end{bmatrix} &= \begin{bmatrix} -\frac{r_{L1}}{L_1} & \omega & 0 \\ -\omega & -\frac{r_{L1}}{L_1} & 0 \\ 0 & 0 & -\frac{r_{L1}+r_{L2}+r_{L3}}{L_1+L_2+L_3} \end{bmatrix} \begin{bmatrix} i_{L_{1d}} \\ i_{L_{1q}} \\ i_{L_{1o}} \end{bmatrix} + \frac{1}{L_1} \begin{bmatrix} V_d \\ V_q \\ V_o \end{bmatrix} \\ &\quad -\frac{v_C}{L_1} \begin{bmatrix} \frac{1}{2} & 0 & 0 \\ 0 & \frac{1}{2} & 0 \\ 0 & 0 & \frac{L_1}{L_1+L_2+L_3} \end{bmatrix} \begin{bmatrix} u_{1d} \\ u_{1q} \\ u_{1o} \end{bmatrix} - \frac{v_C}{L_1} \begin{bmatrix} 0 \\ 0 \\ -\frac{L_1}{L_1+L_2+L_3}u_{2o} \end{bmatrix} \\ &\quad -\frac{v_C}{L_1} \begin{bmatrix} \frac{1}{2} & 0 & 0 \\ 0 & \frac{1}{2} & 0 \\ 0 & 0 & \frac{L_1}{L_1+L_2+L_3} \end{bmatrix} \begin{bmatrix} u_{1d} \\ u_{1q} \\ u_{1o} \end{bmatrix} - \frac{v_C}{L_1} \begin{bmatrix} 0 \\ 0 \\ -\frac{L_1}{L_1+L_2+L_3}u_{3o} \end{bmatrix} \end{aligned} \tag{6.73}$$

which is similar to (6.22). Expressions for $\dot{\vec{i}}^{dqo}_{L_2}$, $\dot{\vec{i}}^{dqo}_{L_3}$, and $\dot{v}_C$ can be obtained similarly. Using (6.73), assigning $\beta_1 = 0.5$, and following the argument in Section 6.2.2, we can implement the control scheme CS_3 for the converter shown in Figure 6.21. Furthermore, using the same procedure, one can extend the control scheme to a parallel three-phase boost converter with N (> 3) number of modules.

6.4.2 Control of A PTBC Driving A Constant-Power Load

Figure 6.22, shows a parallel three-phase boost converter, which is driving a constant-power load P_o ($= v_C\ i_{load}$). We test the dynamic performance of the discrete-control scheme CS_3 by subjecting the PTBC to a sudden and extreme change in the value of the constant-power load. Initially, P_o is equal to 400 W (almost no load) and then it is changed to 40 kW (full load). Subsequently, we change the value of P_o back to 400 W. Figure 6.23, shows the transient performance of CS_3. It shows that, even under these extreme conditions, the change in the bus voltage is only about 12%. Figure 6.24, shows that unity power factor is maintained at full load.

6.4.3 Control of A Front-End PTBC Driving and An Inverter-Based Motor Drive

Figure 6.25 shows a motor-drive system. The front end of the system is the PTBC while its back end is an inverter, which drives a squirrel-cage induction motor. The nonlinear seventh-order model of the induction motor in synchronous frame is given by

$$\dot{i}^s_{qs} = \frac{1}{l_{sm}l_{rm}-l_M^2}\Big(- l_{rm}r_s i^s_{qs} - (l_{sm}l_{rm} - l_m^2)\,\omega_s i^s_{ds} + l_M r_r i^s_{qr} - l_m\,(l_M i^s_{ds} + l_{rm} i^s_{dr})\,\omega_r + l_{rm}V^s_{qs} - l_M V^s_{qr}\Big) \tag{6.74}$$

$$\dot{i}^s_{ds} = \frac{1}{l_{sm}l_{rm}-l_M^2}\Big(- l_{rm}r_s i^s_{ds} + (l_{sm}l_{rm} - l_M^2)\,\omega_s i^s_{qs} + l_M r_r i^s_{dr} + l_M\left(l_M i^s_{qs} + l_{rm} i^s_{qr}\right)\omega_r + l_{rm}V^s_{ds} - l_M V^s_{dr}\Big) \tag{6.75}$$

$$\dot{i}^s_{os} = \frac{1}{l_{ls}}\left(-r_s i^s_{os} + V^s_{os}\right) \tag{6.76}$$

$$\dot{i}^s_{qr} = \frac{1}{l_{sm}l_{rm}-l_M^2}\Big(- l_{sm}r_r i^s_{qr} - (l_{sm}l_{rm} - l_M^2)\,\omega_s i^s_{dr} + l_M r_s i^s_{qs} + l_{sm}\,(l_M i^s_{ds} + l_{rm} i^s_{dr})\,\omega_r + l_{sm}V^s_{qr} - l_M V^s_{qs}\Big) \tag{6.77}$$

$$\dot{i}^s_{dr} = \frac{1}{l_{sm}l_{rm}-l_M^2}\Big(- l_{sm}r_r i^s_{dr} + (l_{sm}l_{rm} - l_M^2)\,\omega_s i^s_{qr} + l_M r_s i^s_{ds} - l_{sm}\left(l_M i^s_{qs} + l_{rm} i^s_{qr}\right)\omega_r + l_{sm}V^s_{dr} - l_M V^s_{ds}\Big) \tag{6.78}$$

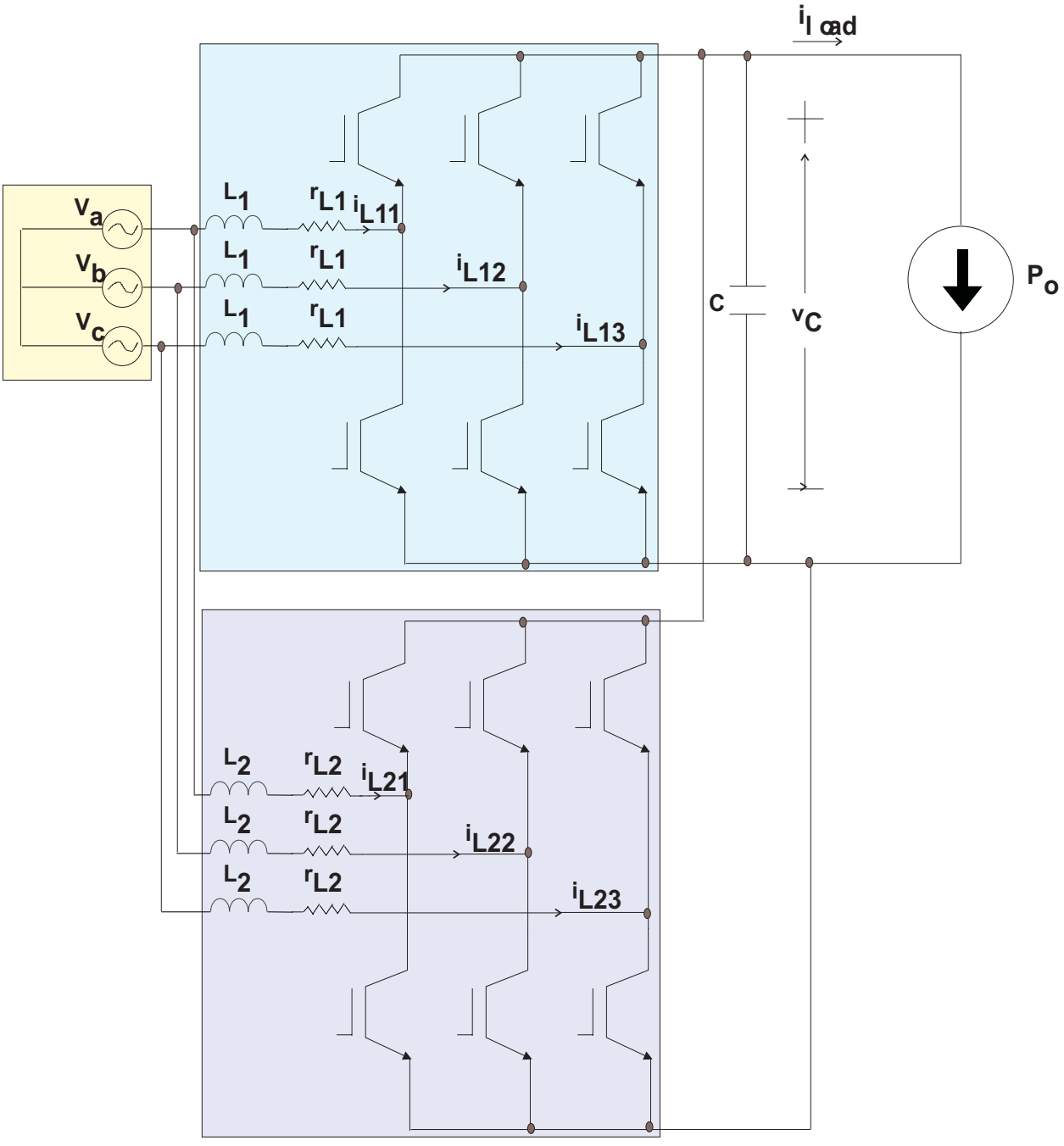

Figure 6.22: Schematic of a PTBC driving a constant-power load.

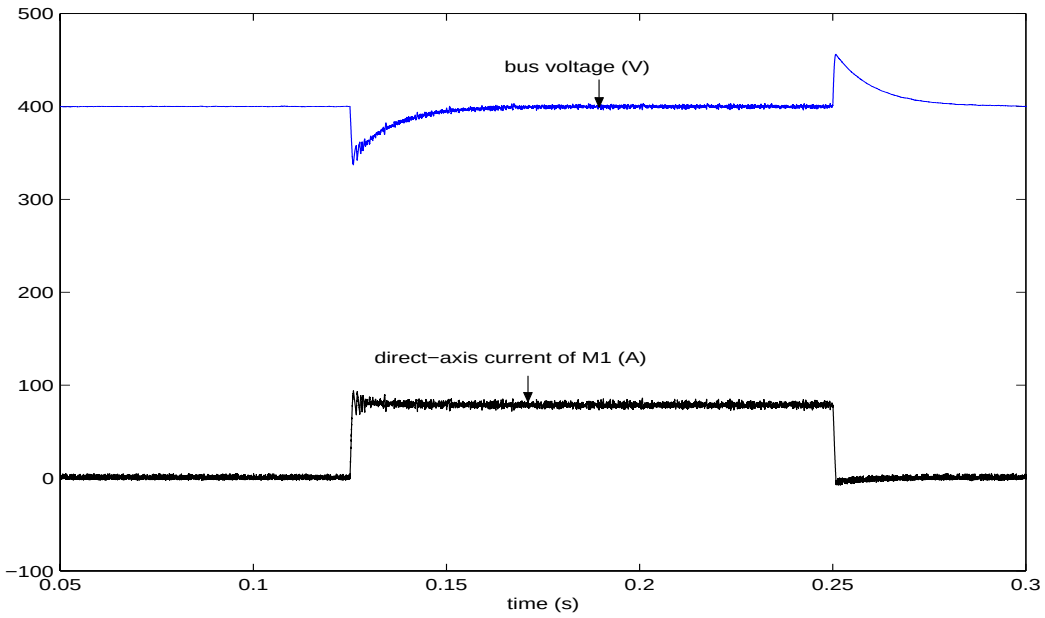

Figure 6.23: Transient performance of one of the modules of the PTBC when P_o changes from almost no load (400 W) to full load (40 kW) and vice-versa.

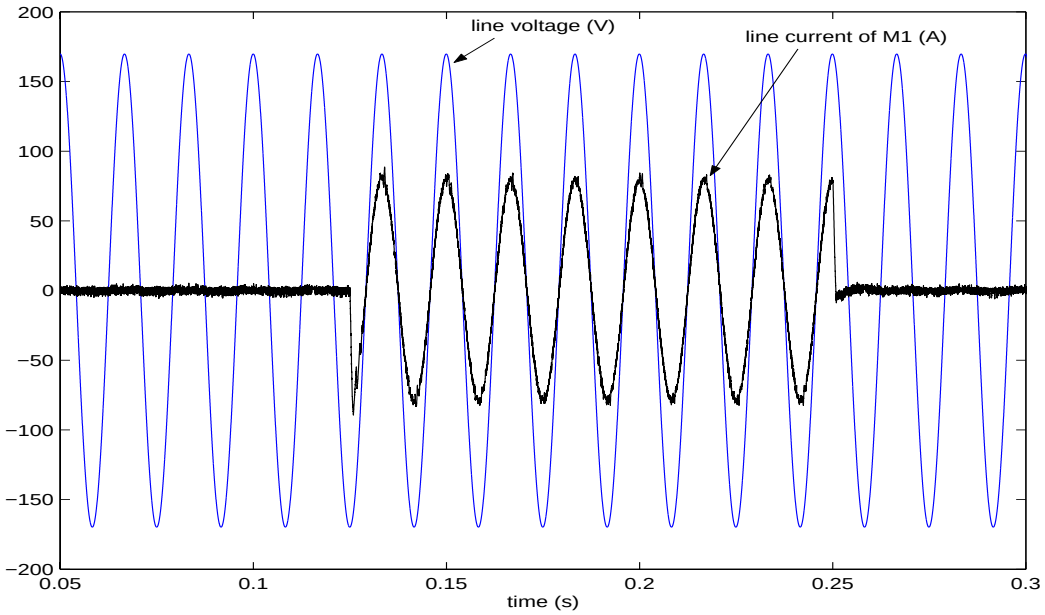

Figure 6.24: Power factor of one of the modules of the PTBC under transient conditions. The constant-power load changes from almost no load (400 W) to full load (40 kW) and vice-versa.

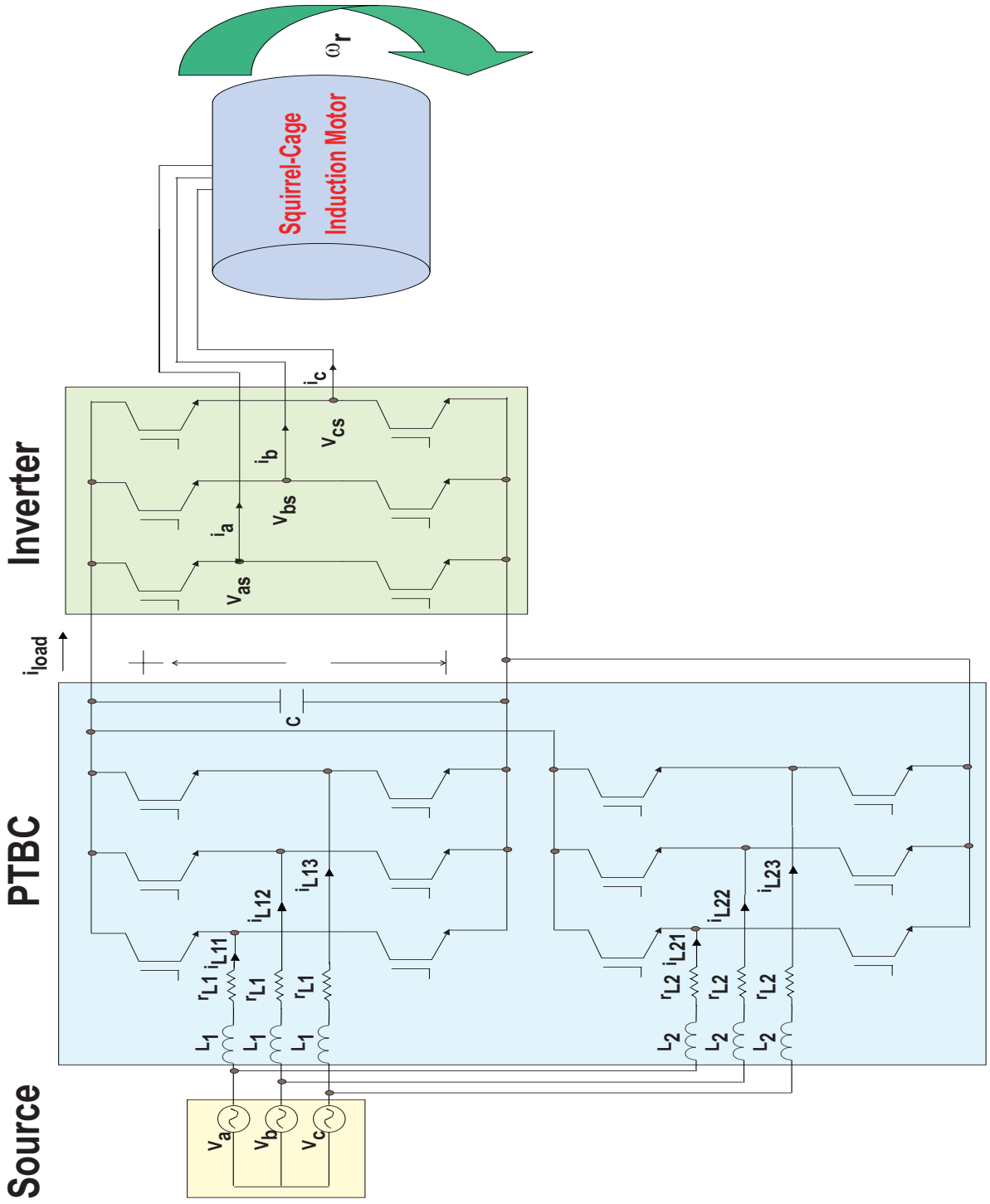

Figure 6.25: Schematic of a motor-drive system: Front end is a parallel three-phase boost converter with two modules; the back-end is an inverter, which drives a squirrel-cage induction motor.

$$\dot{i}^s_{or} = \frac{1}{l_{lr}}\left(-r_r i^s_{or} + V^s_{or}\right) \tag{6.79}$$

$$\dot{\omega}_r = \frac{3P^2}{8J} l_M \left(i^s_{qs} i^s_{dr} - i^s_{ds} i^s_{qr}\right) - \frac{B_m}{J}\omega_r - \frac{P}{2J} T_l \tag{6.80}$$

$$\dot{\theta}_r = \omega_r \tag{6.81}$$

where $l_{sm} = l_s + l_M$, $l_{rm} = l_r + l_M$, $l_M = 1.5 l_m$, and $\omega_s = \omega_r$+slip frequency (ω_{sl}) and the superscript s denotes the synchronous reference frame. Furthermore, i^s_{qs}, i^s_{ds}, and i^s_{os} are the stator currents; i^s_{qr}, i^s_{dr}, and i^s_{or} are the rotor currents; V^s_{qs}, V^s_{ds}, and V^s_{os} and V^s_{qr}, V^s_{dr}, and V^s_{or} are the stator and rotor voltages; ω_r and ω_s are the rotor and the synchronous angular velocity; r_s and r_r are the stator and rotor resistances; l_s and l_r are the stator and rotor leakage inductances; l_m is the stator magnetizing inductance; P, J, and T_l are the number of poles, the moment of inertia of the rotor, and the load torque, respectively. The relationship between the stationary-frame variables, that is X_{abc} (defined in Section 6.1), and the synchronous-frame variables (X^s_{qdo}) is given by

$$X^s_{qdo} = T_1(\theta) X_{abc} \tag{6.82}$$

where

$$T_1 = \frac{2}{3}\begin{bmatrix} \cos(\theta) & \cos(\theta - \frac{2\pi}{3}) & \cos(\theta + \frac{2\pi}{3}) \\ \sin(\theta) & \sin(\theta - \frac{2\pi}{3}) & \sin(\theta + \frac{2\pi}{3}) \\ \frac{1}{2} & \frac{1}{2} & \frac{1}{2} \end{bmatrix} \tag{6.83}$$

and $\theta = \int \omega_s d\tau$. For a balanced system, $\dot{i}_{os} = \dot{i}_{or} = 0$; furthermore, for a squirrel-cage motor $V^s_{qr} = V^s_{dr} = V^s_{or} = 0$.

To test the performance of the PTBC-based motor-drive system, we chose an induction motor with the following parameters: $l_s = 0.0699$ H, $l_r = 0.0699$ H, $l_m = 0.0699$ H, $r_s = 0.18$ Ω, $r_s = 0.15$ Ω, rated rotor speed = 220 rad/s, rated flux = 1.3 Wb, $P = 2$, $J = 0.0586$ Kgm^2, and $B_m = 0$. To control the induction motor, we select the direct-torque control

(DTC) scheme defined by Takahashi and Noguchi (1986). The block diagram of the stator-flux oriented direct-torque-control scheme is shown in Figure 6.23. The PTBC is controlled using CS_3, which is explained in Section 6.2.2. Figure 6.27, shows the performance of the motor drive during startup. The induction motor operates with a full-load torque and its reference speed is set at 100 rad/s. We see that although the rotor ramps up to to the reference speed, the bus voltage is well regulated by the PTBC during that interval.

6.4.4 Control of Parallel Voltage-Source Inverters

Figure 6.28 shows a parallel three-phase voltage-source inverter with N modules. The input to the converter is a dc voltage source v_{in}. The output of the converter is a passive three-phase load. We assume that the converter has ideal switches and that the values of all of the line inductors and their esls in any module are the same. Then, the model of the converter is described by

$$L_j \dot{i}_{L_{jk}} dt = (v_{jk} - v_n) - r_{Lj} i_{L_{jk}} - (v_k - v_n) = v_{jk_n} - r_{Lj} i_{L_{jk}} - v_{k_n} \tag{6.84}$$

$$C_k \dot{v}_{k_n} = i_k - i_{load_k} \tag{6.85}$$

$$v_{jk_n} = v_{in} u_{jk} - \frac{1}{3N} v_{in} \sum_{q=1}^{N} \sum_{r=1}^{3} u_{qr} \tag{6.86}$$

$$v_{k_n} = v_k - v_n \tag{6.87}$$

$$i_k = \sum_{q=1}^{N} i_{L_{qk}} \tag{6.88}$$

$$i_{load_k} = \frac{1}{R_k} v_{k_n} \tag{6.89}$$

where $j = 1, N$, $k = 1, 2, 3$. The control functions u_{11}, u_{12},...,u_{N3} have a value of 0 or 1. As such, (6.84) represents a set of $3N$ discontinuous differential equations.

For simplicity, we outline the application of CS_3 to this converter when $N = 2$. Using the same argument outlined in Section 6.4.1, one can extend the control scheme to the converter with more than two modules. Expanding v_{jk_n} for all j and k, we obtain (6.90):

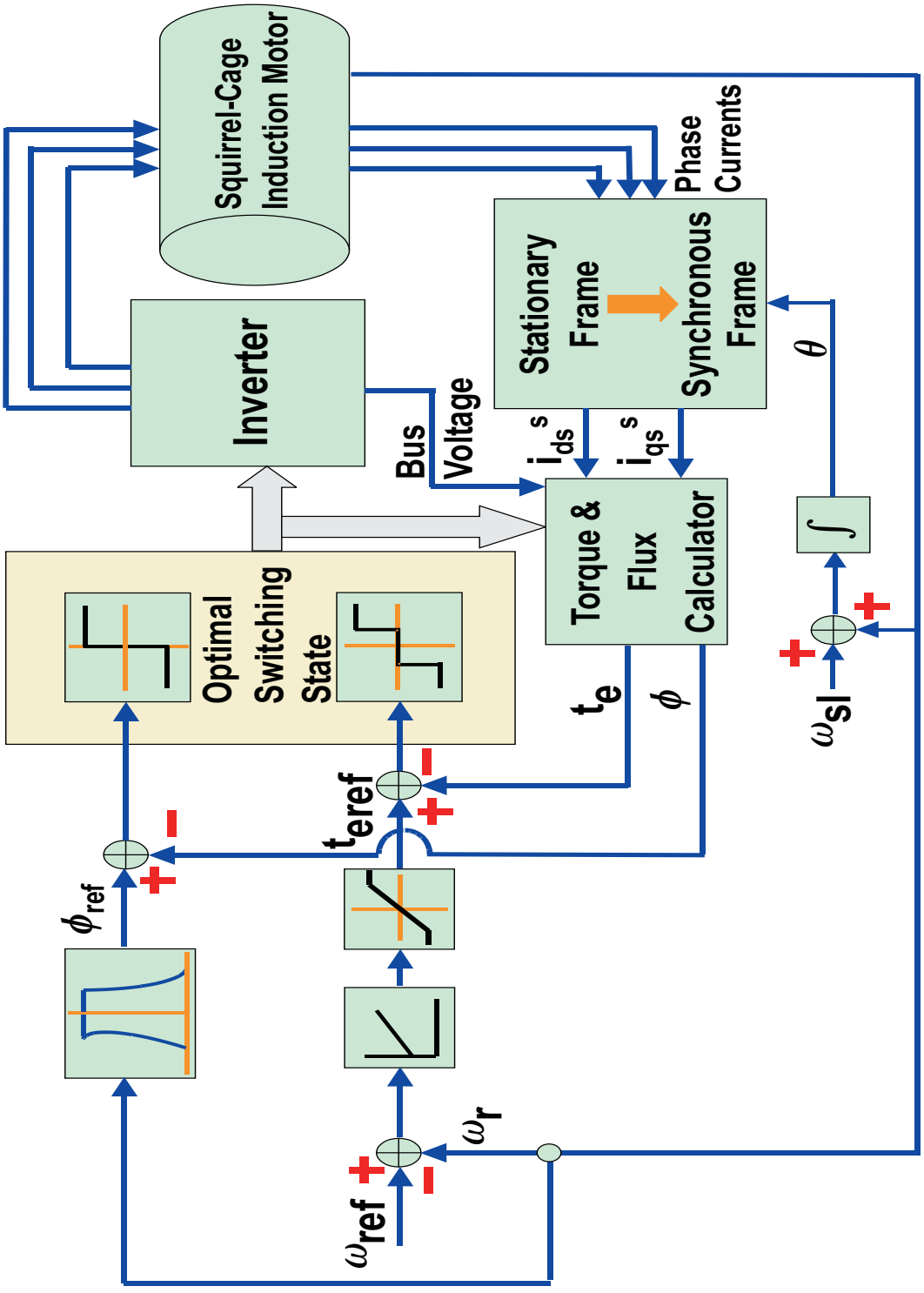

Figure 6.26: A stator-flux oriented direct-torque-control scheme for the induction motor.

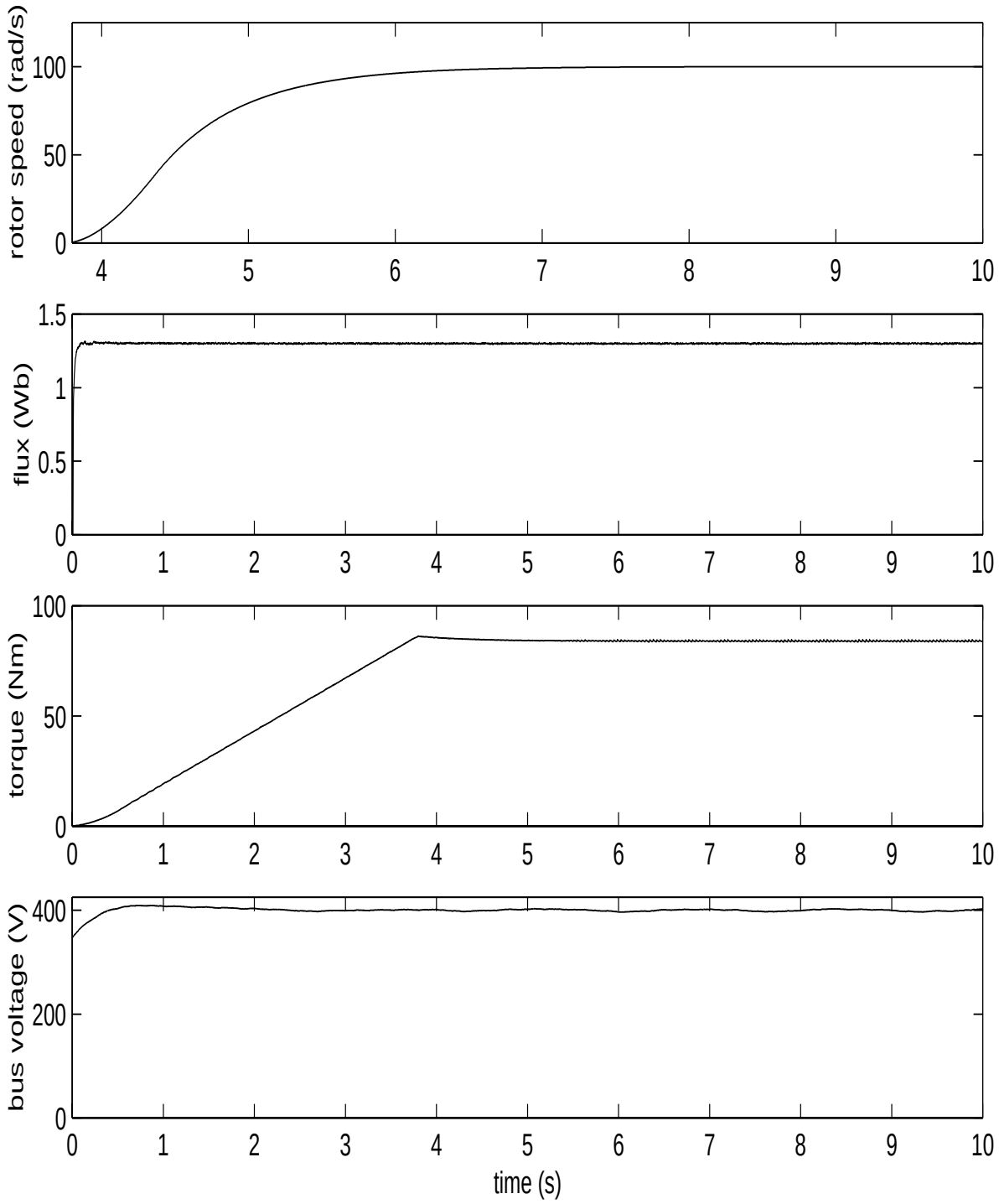

Figure 6.27: Startup performance of the induction-motor drive. The PTBC regulates the bus voltage satisfactorily during the transient condition.

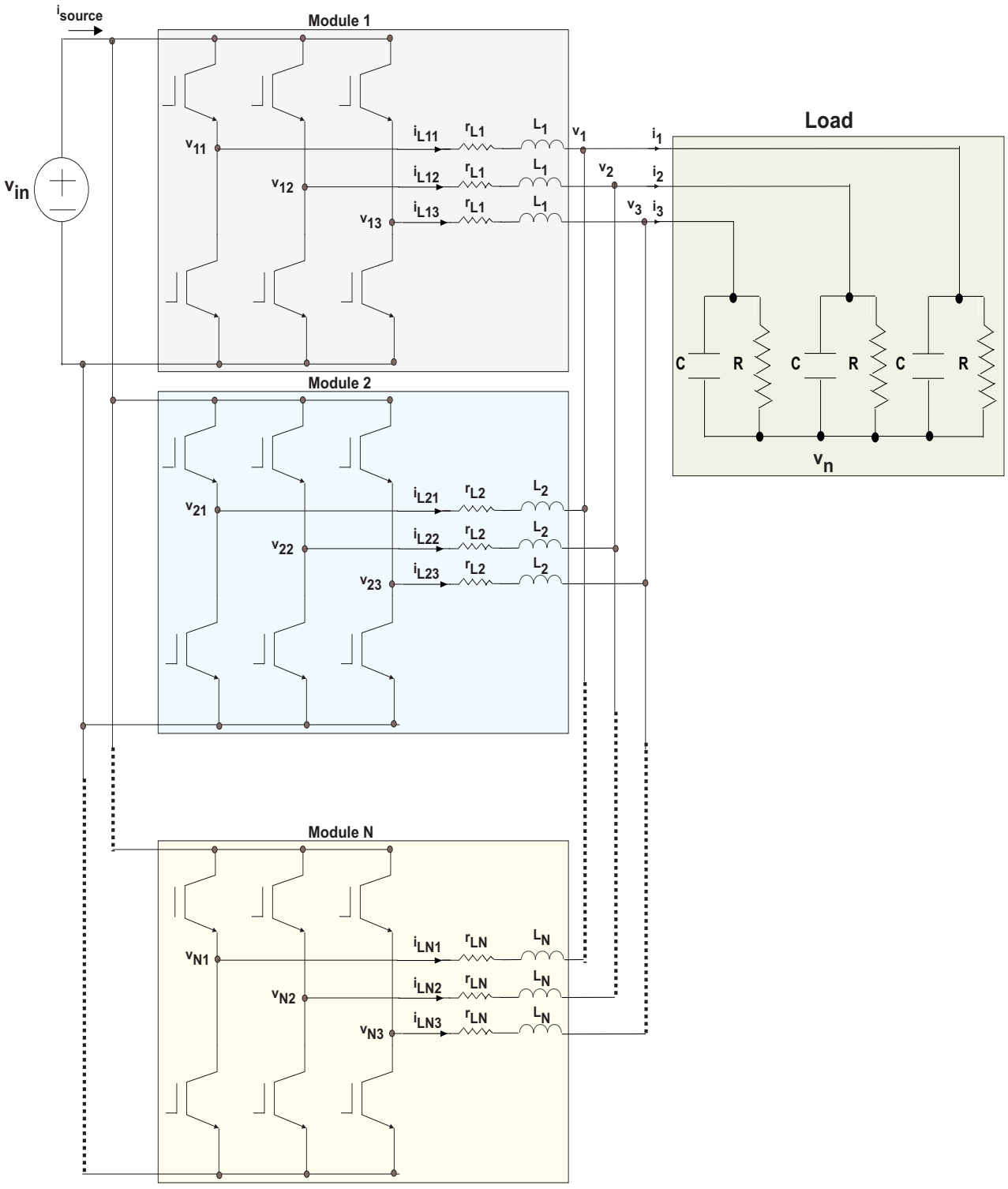

Figure 6.28: Schematic of a parallel three-phase three-leg voltage-source inverter with N modules.

$$\begin{pmatrix} v_{11_n} \\ v_{12_n} \\ v_{13_n} \\ v_{21_n} \\ v_{22_n} \\ v_{23_n} \end{pmatrix} = P \begin{pmatrix} u_{11} \\ u_{12} \\ u_{13} \\ u_{21} \\ u_{22} \\ u_{23} \end{pmatrix} = \frac{1}{6} \begin{pmatrix} 5 & -1 & -1 & -1 & -1 & -1 \\ -1 & 5 & -1 & -1 & -1 & -1 \\ -1 & -1 & 5 & -1 & -1 & -1 \\ 5 & -1 & -1 & 5 & -1 & -1 \\ -1 & -1 & -1 & -1 & 5 & -1 \\ -1 & -1 & -1 & -1 & -1 & 5 \end{pmatrix} \begin{pmatrix} u_{11} \\ u_{12} \\ u_{13} \\ u_{21} \\ u_{22} \\ u_{23} \end{pmatrix}. \tag{6.90}$$

The rank of the matrix P in (6.90) is five, which implies that only five states in (6.84) are controllable. Using (6.16), (6.17), and (6.20), we then transform (6.84) to the form (6.19). Subsequently, we define five sliding surfaces given by (6.25). Using these sliding surfaces, we design a current controller based on CS_3. The references for the currents in (6.25) can be calculated offline or can be obtained from an outer voltage-loop controller. The objective of the voltage-loop controllers is to obtain balanced sinusoidal voltages v_1, v_2, v_3. Because the output line currents have been transfomed to the *dqo* coordinates, we transform (6.85) to the same coordinates using (6.16), (6.17), and (6.20). Then, we close the voltage loops in the *dq* coordinates.

Next, we test the performance of the control scheme CS_3. We select a converter and a passive load, which have the following parameters: $C = 350$ μF, $R = 1$ Ω, $L_1 = 500$ μH, $r_{L1} = 0.5$ Ω, $L_2 = 550$ μH, $r_{L2} = 0.55$ Ω, $v_{in} = 400$ V. The switching frequencies of the two modules of the parallel converter are set at 32 and 16 kHz, respectively. Furthermore, the two modules switch asynchronously. Figure 6.29, shows that using the control scheme, we obtain balanced output voltages and currents even though the two modules have different parameters.

Using (6.84) and (6.85) and the ideas outlined for the control of a parallel three-phase, three-leg converter, one can apply the control scheme for higher-leg converters. For example, the dynamics of the parallel three-phase four-leg converter (shown in Figure 6.30) is obtained by substituting $N = 4$ in (6.84) and (6.85). To apply the control CS_3 to this model, first, one needs to transform the states from a stationary frame to a synchronous frame. Although, the

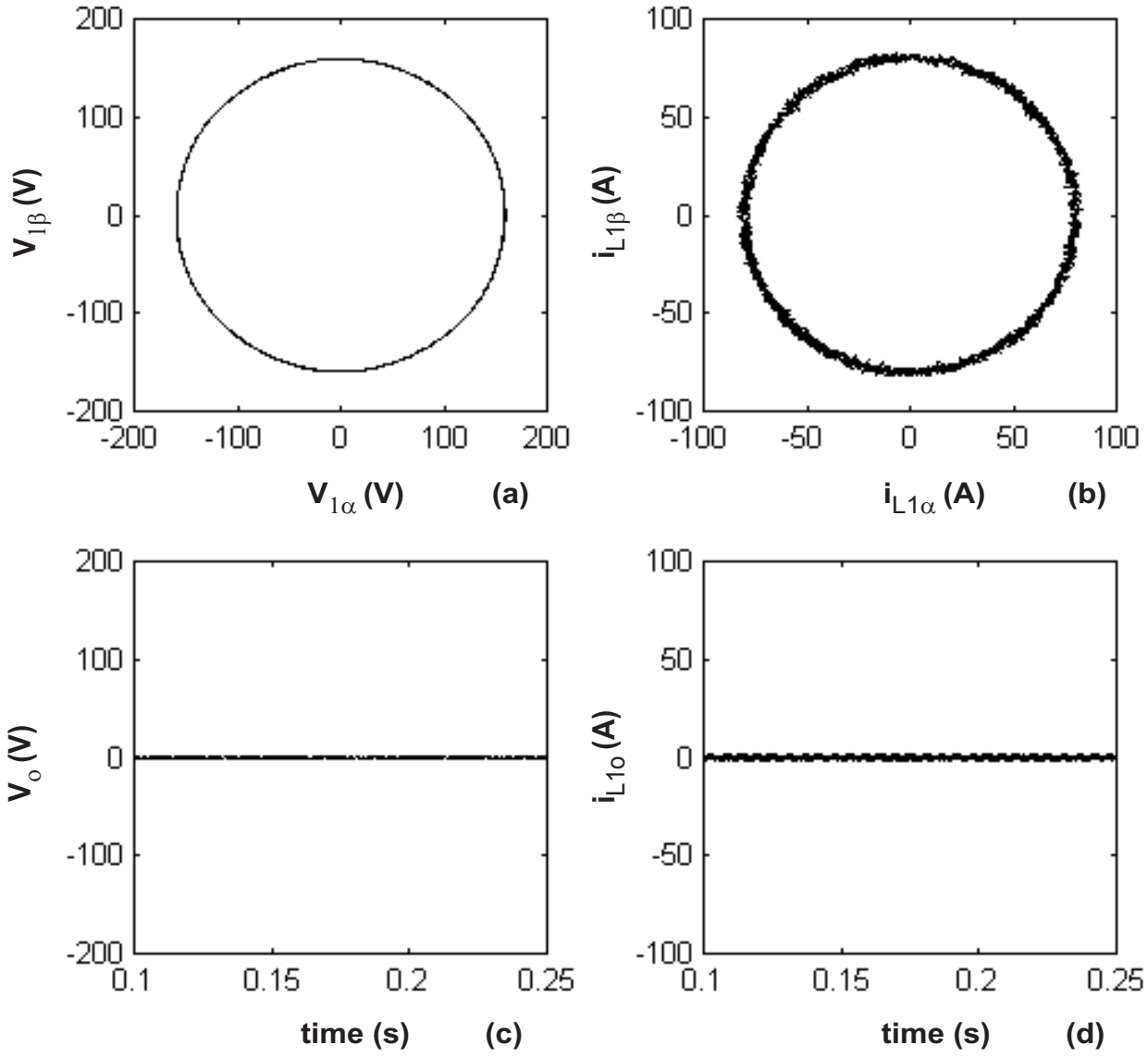

Figure 6.29: Steady-state waveforms of a three-phase parallel voltage-source inverter operating with two modules: (a) output voltages in the α-β frame of reference, (b) line currents of module one in the α-β frame of reference, (c) zero-axis output voltage, (d) zero-axis current of module one.

procedure remains the same as before, there are few modifications. First, the transformation matrix ($T(\theta)$) is different:

$$T(\theta) = \frac{2}{3}\begin{bmatrix} \cos(\theta) & \cos(\theta - \frac{2\pi}{3}) & \cos(\theta - \frac{4\pi}{3}) & 0 \\ -\sin(\theta) & -\sin(\theta - \frac{2\pi}{3}) & -\sin(\theta - \frac{4\pi}{3}) & 0 \\ \frac{1}{2} & \frac{1}{2} & \frac{1}{2} & \frac{-3}{2} \\ \frac{\sqrt{3}}{2} & \frac{\sqrt{3}}{2} & \frac{\sqrt{3}}{2} & \frac{\sqrt{3}}{2} \end{bmatrix}. \tag{6.91}$$

Second, instead of 8 feasible switching states, there are now 16 feasible switching states (as shown in Figure 6.31). Third, due to the fourth leg, there is an additional degree of freedom for each module. As such, the space-vector waveform in Figure 6.6 changes to that in Figure 6.32. Fourth, the duration of the additional switching state in a switching cycle has to be calculated. The procedure to calculate this time duration is the same as that in Section 6.2.2. Fifth, the structure of the closed-loop controller for the four-leg converter remains the same as that for the three-leg converter except that it will have an additional axis.

6.5 Summary and Conclusion

We model a parallel three-phase boost converter (PTBC) with discontinuous vector differential equations (that can be extended to more than two modules) and transform the model to a synchronous (dqo) frame. Based on this transformed model and the fact that the sum of the zero-axis currents is zero, we show that, for a two-module PTBC, independent control of the sliding surfaces on the dqo axes is impossible. We, therefore, modify the control problem to that of controlling the sliding surfaces on the dq axes ($\vec{\sigma}_k^{dq}$) and on the zero (o) axis of one of the modules (σ_{1o}). However, based on our analysis, we find that, if we control the two modules independently (with no communication between them), then even this control objective can not be satisfied in a single switching cycle using a single space vector. The best that can be done is to control $\vec{\sigma}_k^{dq}$ and bound the error on the zero axis.

We then propose three different control schemes to attain the objectives. The first two

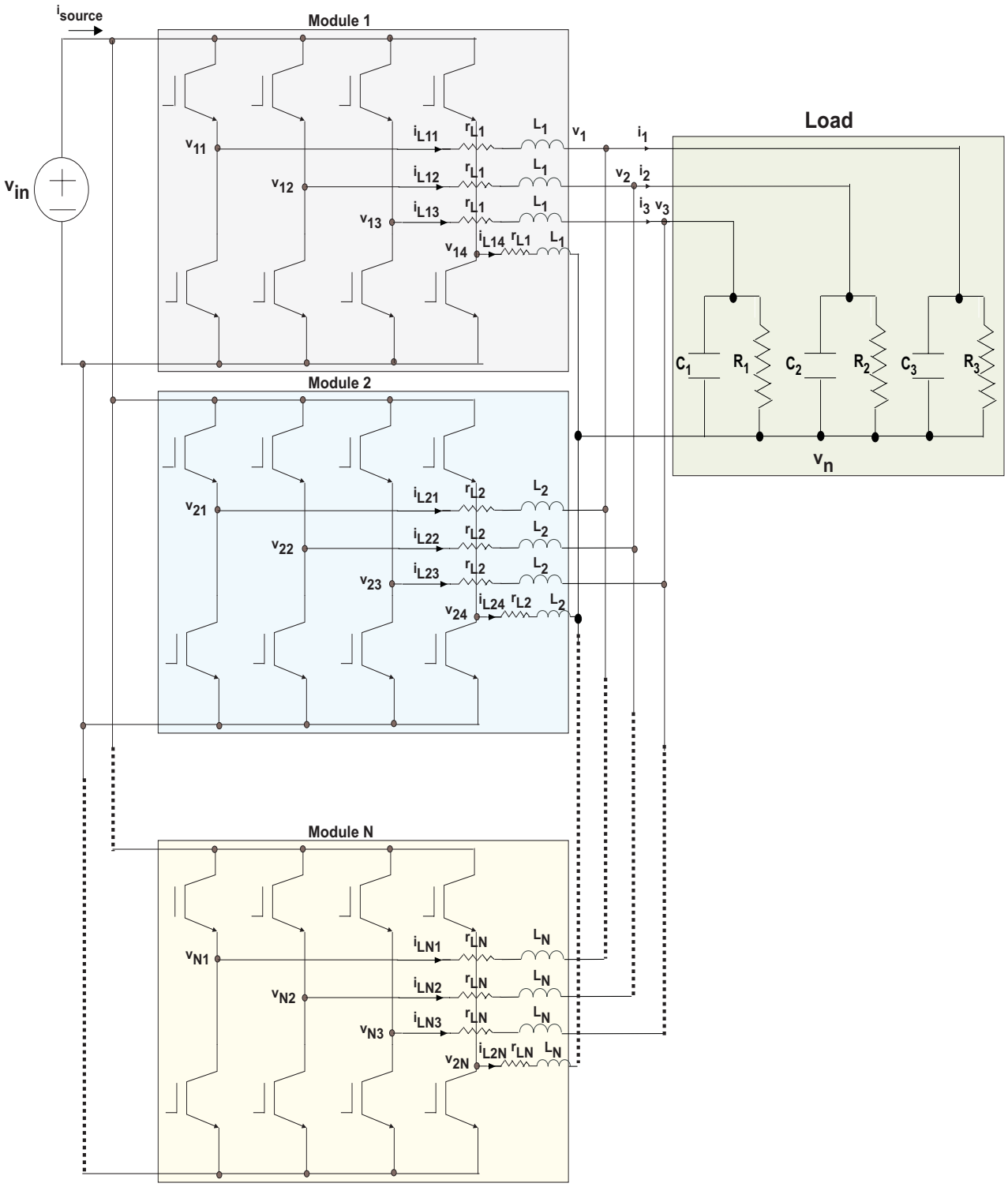

Figure 6.30: Schematic of a parallel three-phase, four-leg voltage-source inverter with N modules.

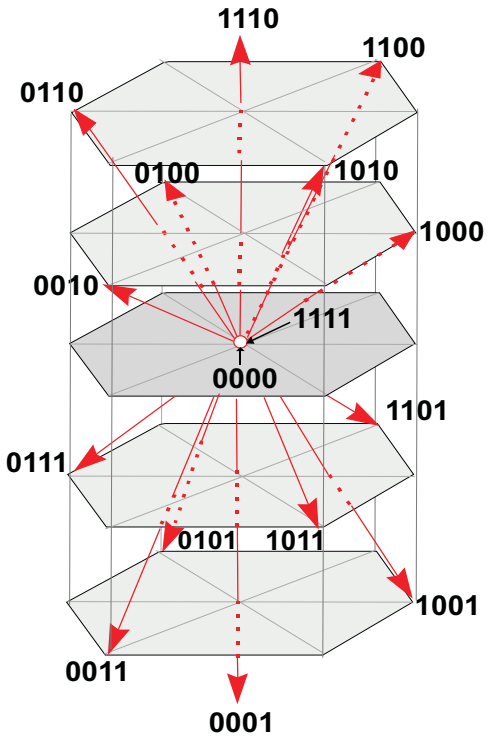

Figure 6.31: Feasible switching of a four-leg voltage-source inverter.

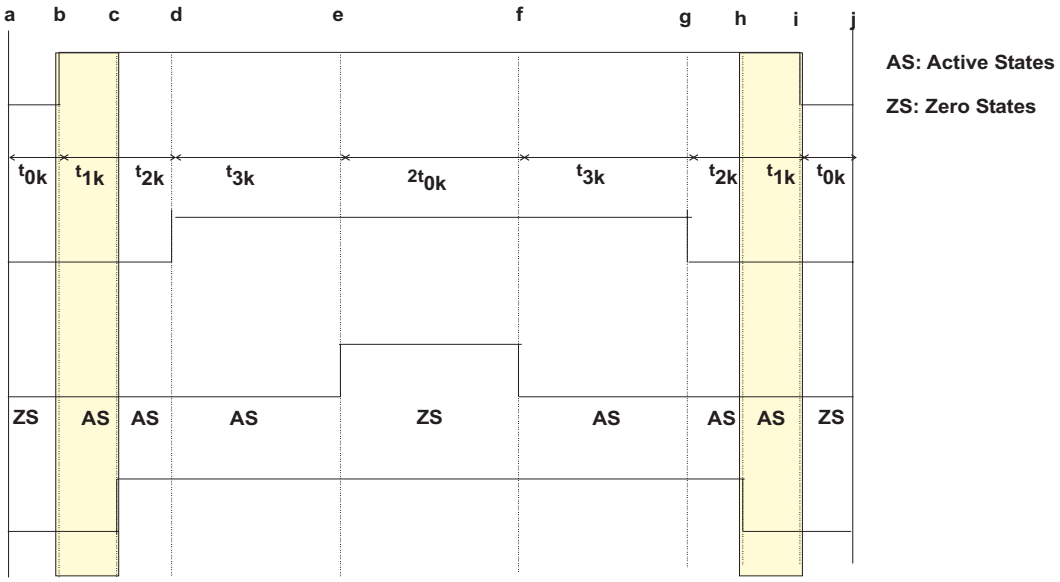

Figure 6.32: A sample space-vector modulated waveform for a four-leg converter in a given sector. As compared to Figure 6.6, it shows the introduction of two additional switching intervals (b-c) and (h-i).

control schemes (CS_1 and CS_2) are developed in the continuous domain, whereas the third scheme (CS_3) is developed in the discrete domain. The former control schemes stabilize the errors on the sliding surfaces of the *dq*-axes and rely on blocking the pure zero-sequence current path, the inductor size, and the switching frequency to bound the errors on the sliding surfaces of the zero axis. Simulation results show that the dynamic performances of the PTBC using these two schems are good. The steady-state ripple of the PTBC obtained using CS_2 is slightly better than that obtained using CS_1 because the former uses a hysteretic comparator that has an inner and an outer hysteretic band.

The steady-state ripple of the PTBC obtained with CS_3 is better than those obtained with the other two control schemes because it combines SVM and nonlinear control and also stabilizes the zero-axis disturbance. Hence, the steady-state ripple has a constant frequency, and the deviation of the zero-axis current from its reference value (= 0) is minimized. We believe that this is the first time that a scheme like CS_3, which combines space-vector modulation with a discontinuous control has been developed for a PTBC.

We also compare the performances of the three proposed controllers with a conventional *dq* controller (Takahashi and Yamane, 1986; Ogasawara et al., 1987; Sato and Kataoka, 1995; Matsui, 1985) and the recently proposed controller (CS_{Ye}) by Ye et al (2000). We find that the conventional *dq* controller fails to stabilize the PTBC even for slight parametric variations of the two modules. This is because it does not control the current on the zero axis, which is perpendicular to the *dq* axes.

The controller proposed by Ye et al. (2000) performs better than the conventional *dq* controller. However, its transient reponse, when the input voltage and the load drop to about 30% of their nominal values, is inferior to the proposed control schemes. For even larger disturbances, the dynamic performances of the controller proposed by Ye et al. (2000) suffers considerably. We find that, if the input voltage drops to 50% of its rated value, then the dips in the bus voltage and the active current are about 25% and 35%, respectively, of their nominal values. For the same disturbance, using the proposed control schemes, the

drop in the bus voltage is about 15%. The active currents do not show any undershoot. When the PTBC is subjected to a change in the load from almost no load to full load, the control scheme propsed by Ye et al (2000) barely stabilizes the system. The undershoot and the overshoot in the bus voltage and the active currents are about 25% and 28%, respectively. Furthermore, the recovery time is considerably longer than those obtained with the proposed control schemes. The drop in the bus voltage, using the proposed control schemes, is about 16% of its nominal value. Besides, the active currents do not show any undershoot.

Finally, we used the controller CS_3 to demonstrate how, with minor modifications, it can be applied to other parallel multiphase converters.

Conclusions

We investigated the dynamics and stability of standalone, integrated, and parallel PWM converters using new and existing modeling techniques. In addition, we developed robust nonlinear controllers for the stabilization of parallel dc-dc and parallel multi-phase converters. Based on this work, we came up with several conclusions.

First, conventional analyses of power converters based on state-space averaged models assume ideal sliding surfaces and hence ignore the impact of switching. Therefore, such models can not predict anything about the fast-scale dynamics. Because the averaged models do not account for the finite delay, their predictions of the stability boundaries may not always be accurate. Besides, validity of the averaged models may vary with the switching frequency even for the same topological structure.

In reality, the switching frequency is finite, and therefore a sliding surface is not possible; instead the existence of a quasi-sliding surface or boundary layer has to be sought. Using nonlinear maps and switching models, one can investigate the fast-scale dynamics within this finite layer. The mechanisms of fast-scale instabilities, for the same converter, can vary, depending on the bifurcation parameter and initial conditions of the states. Furthermore, the instability mechanisms in such discontinuous systems can be completely different from those known for smooth systems. For example, a bifurcation analysis on a dc-dc buck converter showed that the onset of chaos occurs immediately after a period-doubling bifurcation of the nominal solution.

The analyses of multi-phase converters is even more involved. These systems have two fundamental frequencies: the line frequency and switching frequencies. As such, the dynamics of these converters within the boundary layer evolve on a torus. If the two frequencies are incommensurate, then a combination of a second-order Poincare map and Lyapunov's method is used to determine the complete stability of the fundamental orbit.

Second, for high-frequency converters, the prediction of stability should be preferably done based on nominal and high-frequency models. At high frequencies, the parasitics and the device nonlinearities may have significant impact. For example, such nonideal effects may lead to an earlier onset of chaos.

Third, even a slow-scale averaged model may have more than one equilibrium solution or more than one stable orbit. However, a linearized small-signal analysis ignores the presence of these other solutions. Therefore, a small-signal analysis can not predict anything about the domain of attraction of the nominal solution. For example, the averaged model of a multi-loop dc-dc boost converter or a filter-converter system may have quadratic or cubic nonlinearities. In other words, these systems may have more than one equilibrium solution. If more than one of these solutions are stable, then the system will have multiple operating points, one of which is the nominal solution. This possibility is completely ignored in linearized averaged models. Consequently, the small-signal model can not predict the post-instability dynamics. The knowledge of the post-instability dynamics can lead to a less conservative design of a closed-loop converter.

Fourth, the prevalent procedure for analyzing the stability of switching converters is based on linearized averaged (small-signal) models that require smooth averaged models. Yet there are systems (e.g., boost power-factor-correction circuit), which yield non-smooth averaged models. The stability analyses of these systems can only be done by treating them as hybrid systems.

Fifth, averaged models assume that, when power is fed to a converter, the trajectories of the system are already on the sliding surface. In other words, the sliding surface is

assumed to always exist. This may not be true, even for systems that are linear with respect to control. These systems may have a stable equilibrium solution or a stable orbit in the saturated region. As such, global existence of the hypersurface may not be possible.

Considering the shortcomings of small-signal models, we conclude that many of the industrial controllers, which are designed based on them, may be conservative and non-optimal and may not stabilize the closed-loop converters except in the vicinity of an operating point. To address some of these issues, we developed robust nonlinear controllers for the stabilization of parallel dc-dc and parallel multi-phase converters.

The controller for the parallel dc-dc converters combines the concepts of multi-sliding-surface control (MSSC) and integral-variable-structure control (IVSC). The choice of variable-structure controllers (VSC) for power converters is natural because both of the plant and the controller are discontinuous. Moreover, it optimizes the switching frequency to attain the control objectives. The main concern with VSC is that it varies the switching frequency, and hence dealing with the design of filters and electromagnetic-interference issues become more involved. To keep the frequency constant and to stabilize the system, we found that a hybrid control strategy, like the one proposed in this Dissertation, is a viable alternative.

Combination of MSSC and IVSC has several advantages. First, the controller is easier to design because each sliding surface is independently controlled. As such, the operation of a parallel converter with N modules is not hampered even if a module fails. Second, the controller yields good transient responses even under parametric variations. Third, due to the integral action, the controller eliminate bus-voltage and line-current errors under steady-state conditions with reduced effort. Fourth, the integrators in the control scheme can reduce the impact of very high-frequency dynamics due to parasitics on an experimental closed-loop system. Fifth, the control scheme within the boundary layer enables operation of the converter with a finite switching frequency. Sixth, the converter modules can be operated in interleaving or synchronicity modes. Finally, the control scheme can also be applied to nonminimum-phase converters.

We then, developed three nonlinear controllers for the stabilization a parallel three-phase boost converter (PTBC) and compared their performances with a conventional *dq* controller and another controller (CS_{Ye}), which was recently proposed by Ye et al. (2000). Two of the proposed controllers (CS_1 and CS_2) are developed in the continuous domain; the other (CS_3) is developed in the discrete domain. We found that, the conventional *dq* controller fails to stabilize the PTBC even for slight parametric variations of the two modules. This is because it does not control the current on the zero axis, which is perpendicular to the *dq* axes.

The controller proposed by Ye et al. (2000) performs better than the conventional *dq* controller. However, its transient response is inferior to the proposed control schemes for moderate disturbances. For larger disturbances, the dynamic performances of the controller proposed by Ye et al. (2000) suffers considerably. This is because, unlike the proposed schemes, CS_{Ye} is developed based on a small-signal model of the PTBC.

Among the proposed controllers, the CS_3 achieves the best compromise between the transient and steady-state performances. This is because CS_3 combines space-vector modulation with variable-structure control. However, under saturated conditions, the effectiveness of this controller will diminish because the zero vectors can not be applied. We note that CS_Ye has the same limitation. However, unlike CS_{Ye}, CS_3 guarantees global stability within the boundary layer. This is why its transient performances are better. The proposed control schemes, developed in the continuous domain, do not have any such limitations, but create more harmonic distortions. Between CS_1 and CS_2, the latter gives lower ripple because it uses a three-level hysteretic comparator.

To obtain a balance between steady-state and transient performances and to operate the PTBC in saturated conditions, we recommend a combination of CS_1 or CS_2 (outside the boundary layer) and CS_3 (inside the boundary layer). Implementation of such a hybrid control scheme on a digital signal processor is fairly straightforward. However, if the worst-case disturbances are not large enough to saturate the PTBC, then CS_3 provides the best

alternative. Furthermore, the structure of this controller is general, and hence it can be used with little modifications to control other parallel multi-phase and multi-leg converters.

Future Work

- Modeling and analyses of the stability and dynamics of resonant, soft-switched, and thyristor- and diode-based standalone and parallel multi-phase converters.
- Development of a unified methodology for modeling and stability analyses of any power-electronic converter by incorporating the effect of temporal and spatial variations and generate newer design guidelines for distributed-power systems and their building blocks.
- Investigation of the impact of the variation of more than one parameters on the stability of a power-electronic converter using bifurcation analyses with a co-dimension of more than one.
- Exploration of the feasibility of operating a switching converter in a chaotic region.
- Extension of the analyses and control methodologies developed in this Disertation for parallel dc-dc converters to the case when each module is driven by a separate source.
- Development of control methods for parallel multi-phase boost converters, which integrate the problem of current and voltage control.
- Development of an optimization technique for multi-phase converters, which will ensure the best possible space-vector-modulation strategy given all of the constraints.
- Development of optimization methodology to automate the procedure to synthesize a power-electronic converter based on design specifications.

Bibliography

Abed, E. H., Wang, H. O., and Chen, R. C., 1992, "Stabilization of period doubling bifurcation and implications for control of chaos", *IEEE Decision and Control Conference*, pp. 2119-2124.

Alderfer, R. B. and Starrs, T. J., 2000, *Making connections: Case studies of interconnection barriers and their impact on distributed power projects*, NREL/SR-200-28053, National Renewable Energy Laboratory, Colorado.

Alfayyoumi, M., 1998, *Nonlinear dynamics and interactions in power electronic systems*, MS Thesis, Department of Electrical and Computer Engineering, Virginia Polytechnic Institute and State University, Blacksburg, Virginia.

Alfayyoumi, M., Nayfeh, A. H., and Boroyevich, D., 1999, "Input filter interactions in dc-dc switching regulators", *IEEE Power Electronic Specialists Conference*, pp. 926-932.

Alfayyoumi, M., Nayfeh, A. H., and Borojević, D., 2000, "Modeling and analysis of switching-mode dc-dc regulators," *International Journal of Bifurcation and Chaos.* vol. 10, no. 2.

Andreycak, B., 1997, "Advanced power factor correction control ICs", *Unitrode Inc.*, Design Note DN-44.

Angulo-Nunez, M. I. and Sira-Ramirez, H., 1998, "Flatness in the passivity based control of dc-to-dc power converters", *IEEE Conference on Decision and Control*, vol. 4, pp.

4115-4120.

Aubin, J. and Cellina, A., 1984, *Differential inclusions: set-valued maps and viability theory*, Springer-Verlag, New York.

Aubin, J., 1999, *Impulse and hybrid control systems: a viability approach*, Lecture notes for a mini-course, Department of Electrical Engineering, University of California at Berkeley.

Bainov, D. and Milusheva, S., 1981, "Justification of the averaging method for a system of differential equations with fast and slow variables with impulses", *Z Angew Mathematical Physics*, vol. 32, pp. 237-254.

Balachandra, M. and Sethna, P. R., 1975, "A generalization of the method of averaging for systems with two time scales", *Archive for Rational Mechanics and Analysis*, vol. 58, no. 3, pp. 261-283.

Balestrino, A., Eisinberg, A., and Sciavicco, L., 1974, "A generalized approach to the stability analysis of PWM feedback control systems" *Journal of the Franklin Institute*, vol. 298, no. 1, pp. 45-58.

Ball, J. and Helton, J. W., 1998, "Factorizaion of nonlinear systems: toward a theory for nonlinear H_∞ control", *IEEE Conference on Decision and Control*, vol. 3, pp. 2376-2381.

Banda, J. and Siri, K., 1995, "Improved central-limit control for parallel-operation of dc-dc power converters", *IEEE Power Electronics Specialists Conference*, pp. 1104-1110.

Banerjee, S. and Grebogi, C., 1999, "Border collision bifurcations in two dimensional piecewise smooth maps", *Physical Review E*, vol. 59, no. 4, pp. 4052-4061.

Banerjee, S., Ott, E., Yorke, J. A., and Yuan, G. H., 1997, "Anomalous bifurcations in dc-dc converters: borderline collisions in piecewise smooth maps", *IEEE Power Electronic Specialists Conference*, pp. 1337-1344.

Banerjee, S. and Verghese, G. C. (Editors), 2001, *Nonlinear phenomena in power electronics: bifurcations, chaos, control and applications*, Wiley-IEEE Press.

Barbosa, P., Canales, F., and Lee, F. C., 2000, "A front-end distributed power system for high-power applications", *Proceedings of Industry Applications Society*, pp. 2546-2551.

Barmish, B. R. and Leitmann, G., 1982, "On ultimate boundedness control of uncertain systems in the absence of matching assuptions" *IEEE Transactions on Automatic Control*, vol. 27, no. 1, pp. 153-158.

Bass, R. M. and Sun, J., 1998, "Large-signal averaging methods under large ripple conditions (for power convertors)" *IEEE Power Electronics Specialists Conference*, pp. 630-632.

Batarseh, I., Siri, K., and Banda, J., 1994a, "An alternative approach for improving current-sharing in parallel-connected dc-dc converter systems", *High Frequency Power Conversion Conference*, pp. 17-21.

Batarseh, I., Siri, K., and Lee, H., 1994b, "Investigation of the output droop characteristics of parallel-connnected dc-dc converters", *IEEE Power Electronics Specialists Conference*, pp. 1342-1351.

Batham, M., Bining, A., Birkinshaw, K., Hatfield, D., and Soinski, A. J., 1999, *Draft plan for research in environmentally preferred advanced generation technologies*, Report on Public Interest Energy Research submitted to California Energy Commission.

Bauer, P. and Klaassens, J. B., 1993, "Dynamic modeling of ac power converters", *IEEE Power Conversion Conference*, pp. 502-507.

Behilovic, N. S., Ninomiya, T., Sabanovic, A., and Perunicic, B., 1993, "Control of three-phase switching converters: a sliding mode approach", *IEEE Power Electronic Specialists Conference*, pp. 630-635.

Belkhayat, M., 1997, *Stability criteria for ac power systems with regulated loads*, Ph.D. Dissertation, Department of Electrical and Computer Engineering, Purdue University, West Lafayette, Indiana.

Belkhayat, M., Cooley, R., and Abed, E. H., 1995, "Stability and dynamics of power systems with regulated converters", *IEEE International Symposium on Circuits and Systems*, pp. 143 -145.

Bernardo, M. D., Garofalo, F., and Vasca, F., 1998, "Switchings, bifurcations, and chaos in dc-dc converters", *IEEE Transactions on Circuits and Systems-1: Fundamental Theory and Applications*, vol. 45, no. 2, pp. 133-141.

Bogoliubov, N. N. and Mitropolski, Y. A., 1961, *Asymptotic methods in the theory of nonlinear oscillations*, Gordon and Breach, New York.

Bowman, W. and Young, C., 2001, "Tools to design and evaluate the stability of highly complex distributed power architectures", Professional Seminar, *IEEE Applied Power Electronics Conference.*

Branicky, M.S., Borkar, V. S., and Mitter, S. K., 1998, "A unified framework for hybrid control: model and optimal control theory", *IEEE Transactions on Automatic Control*, vol. 43, no. 1, pp. 31-45.

Brockett, R. W. and Wood, J. R., 1984, "Understanding power converter chaotic behavior mechanisms in protective and abnormal modes", *Proceedings of the Powercon*, vol. 11, no. 4, pp. 1-15.

Broeck, V. D., Skudelny, H. C., and Stanke, G., 1988, "Analysis and realization of a pulse width modulator based on voltage space vectors", *IEEE Transactions on Industry Applications*, vol. 24, no. 1, pp. 142-150.

Brogliato, B., 1996, *Nonsmooth impact mechanics: models, dynamics and control*, Springer-Verlag, New York.

Brogliato, B., 1999, *Nonsmooth mechanics*, Springer-Verlag, London.

Brown, A.R. and Middlebrook, R.D., 1981, "Sampled-data modelling of switching regulators", *IEEE Power Electronic Specialists Conference*, pp. 346-369.

Burlacu, C. and Masada, E., 1996, "Bilinear approach for the parallel connected multiconverter and the respective control", *International Power Electronics and Motion Control Conference*, pp. 201-209.

Burlacu, C., Ohsaki, H., and Masada, E., 1997, "Combined optimality and robustness assessments for interconnected power converters - theoretical and experimental results", *Power Conversion Conference*, pp. 445-450.

Burns, J., Riel, J., and DiBene, A., 1994, "An intelligent, fault tolerant, high power, distributed power system for massively parallel processing computers" *IEEE Applied Power Electronics Conference*, pp. 795-800.

Campos, A., Joos, G., Ziogas, P. D., and Lindsay, J. F., 1994, "Analysis and design of a series voltage unbalance compensator based on a three-phase VSI operating with unbalanced switching functions", *IEEE Transactions on Power Electronics*, vol. 9, no. 3, pp. 269-274.

Canales, F., Barbosa, P. M., and Lee, F. C., 2000, "A zero voltage and zero current switching three level dc-dc converter", *IEEE Applied Power Electronics Conference*, pp. 314-320.

Capel, A., Ferrante, J. G., and Prajoux, R., 1975, "State-variable stability of multi-loop PWM controlled dc-dc regulators in light and heavy mode", *IEEE Power Electronics Specialists Conference*, pp. 91-103.

Carsten, B., 1987, "Distributed power system of the future utilizing high frequency converter", *High Frequency Power Conversion Conference.*

Chan, W. C. Y. and Tse, C. K., 1996a, "Studies of routes to chaos for current-programmed dc-dc converters", *IEEE Power Electronics Specialists Conference*, pp. 789-795.

Chan, W. C. Y. and Tse, C. K., 1996b, "Bifurcation in bifurcation from a current-programmed dc-dc boost converter", *IEEE International Symposium on Circuits and Systems*, pp. 249-252.

Chandrasekaran, S., 2000, *Optimization tools for subsystem design in aircraft power distribution systems*, Ph.D. Dissertation, Department of Electrical and Computer Engineering, Virginia Polytechnic Institute and State University, Blacksburg, Virginia.

Chandrasekaran, S., Lindner, D. K., and Boroyevich, D., 1999, "Analysis of subsystem integration in aircraft power distribution systems", *IEEE International Symposium on Circuits and Systems*, vol. 5, pp. 82-85.

Chang, L. W., 1990, "A MIMO sliding control with a second order sliding condition", *ASME WAM*, Paper No. 90-WA/DSC-5, Dallas, TX.

Chang, M. Y., Lin, J. Y., and Tzou, Y. Y., 1990, "DSP-based fully digital control of a ac-dc converter with a nonlinear digital current mode control".

Chen, J. H., Chau, K.T., and Chan, C.C., 2000, "Analysis of chaos in current-mode-controlled dc drive systems", *IEEE Transactions on Industrial Electronics*, vol. 47, no. 1, pp. 67-76.

Chau, K. T., Chan, C. C., and Yao Jianming, 1997, "Nonlinear modeling and spectral analysis of Cuk converters", *IEEE International Conference on Industrial Electronics, Control and Instrumentation*, pp. 605 -610.

Chen, Q., 1995, "Stability analysis of paralleled rectifier systems", *International Telecommunications Energy Conference*, pp. 35-40.

Choi, B., 1992, *Dynamics and control of switching power conversion in distributed power systems*, Ph.D. Dissertation, Department of Electrical Engineering, Virginia Polytechnic Institute and State University, Blacksburg, Virginia.

Choi, B., Cho, B. H., Ridley, R. B., and Lee, F. C., 1990, "Control strategy for multi-module parallel converter system", *IEEE Power Electronics Specialists Conference*, pp. 225-234.

Clarke, F. C., 1995, *Optimization and nonsmooth analysis*, John Wiley and Sons, New York.

Corless, M. and Leitmann, G., 1981, "Continuous state feedback guarantees uniform ultimate boundedness for uncertian dynamical systems", *IEEE Transactions on Automatic Control*, vol. 26, pp. 1139-1144.

Crutchfield, J., Nauenberg, M., and Rudnick, J., 1981, "Scaling for external noise at the onset of chaos", *Physical Review Letters*, vol. 46, no. 14, pp. 933-939.

Crutchfield, J. and Huberman, B. A., 1980, "Fluctuations and the onset of chaos", *Physical Letters*, vol. 77A, no. 6, pp. 407-410.

Deane, J. H. B., 1992, "Chaos in a current-mode controlled boost dc-dc converter", *IEEE Transactions on Circuits and Systems I: Fundamental Theory and Applications*, vol. 39, no. 8, pp. 680-683.

Deane, J. H. B. and Hamill, D. C., 1990, "Analysis, simulation and experimental study of chaos in the buck converter", *IEEE Power Electronics Specialists Conference*, pp. 491-498.

DeCarlo, R. A., Branicky, M. S., Pettersson, S., and Lennartson, B., 2000, "Perspectives and results on the stability and stabilizability of hybrid systems", *Proceedings of the IEEE*, vol. 88, no. 7, pp. 1069-1082.

Dennis, J. E. (Jr.) and Schnabel, R. B., 1983, *Numerical methods for unconstrained optimization and nonlinear equations*, Prentice Hall, New Jersey.

Dixon, J.W. and Ooi, B.T., 1988, "Dynamically stabilized indirect current controlled SPWM boost type 3-phase rectifier", *Proceedings of IEEE Industry Applications Society*, pp. 700-705.

Dixon, J.W. and Ooi, B.T., 1989, "Series and parallel operation of hysterisis current-controlled PWM rectifiers", *IEEE Transactions on Industry Applications*, vol. 25, no. 4, pp. 644-651.

Drakunov, S. V., Izosimov, D. B., Lukajanov, A. G., Utkin, V., and Utkin, V. I., 1990a, "Block control principle: part I", *Automation and Remote Control*, vol. 51, no. 5, pp. 38-46.

Drakunov, S. V., Izosimov, D. B., Lukajanov, A. G., Utkin, V., and Utkin, V. I., 1990b, "Block control principle: part II", *Automation and Remote Control*, vol. 51, no. 6, pp. 20-31.

Drobnik, J., Huang, L., Jain, P., and Steigerwald, R., 1999, "PC platform power distribution system-past application, today's challenge and future direction", *IEEE Telecommunication Energy Conference.*

Elmali, H. and Olgac, N., 1992, "Robust output tracking control of nonlinear MIMO systems via sliding mode technique", *Automatica* vol. 28, pp. 145-151.

Enjeti, P. and Choudhury, S. A., 1991, "A new control strategy to improve the performance of a PWM ac to dc converter under unbalanced operating conditions", *IEEE Power Electronics Specialists Conference*, pp. 381-387.

Enjeti, P. and Ziogas, P. D., 1990, "Analysis of a static power converter under unbalance", *IEEE Transactions on Industrial Electronics*, pp. 91-93.

Erickson, R.W., Ćuk, S., and Middlebrook, R.D., 1982, "Large-signal modelling and analysis of switching regulators", *IEEE Power Electronics Specialists Conference*, pp. 240-250.

Escobar, G., Ortega, R., Sira-Ramirez, H., and Ludvigsen, H., 1998, "A hybrid passivity based controller design for a three phase voltage sourced reversible boost type rectifier", *IEEE Conference on Decision and Control.*

Fang, C-C. and Abed, E. H., 1999, "Sampled-data modeling and analysis of closed-loop PWM dc-dc converters", *IEEE International Symposium on Circuits and Systems*, pp. 110-115.

Feigin, M. I., 1974, "On the structure of C-bifurcation boundaries of piecewise-continuous systems", *PMM*, vol. 38, no. 5, pp. 810-818.

Feigin, M. I., 1995, "The increasingly complex structure of the bifurcation tree of a piecewise-smooth system", *Journal of Applied Mathematics and Mechanics*, vol. 59, no. 6, pp. 853-863.

Feng, X., Ye, Z., Xing, K., Lee, F. C., and Boroyevich, D., 1999, "Individual load impedance specification for a stable dc distributed power system", *IEEE Applied Power Electronics Conference*, pp. 923-929.

Filippov, A. F., 1988, *Differential equations with discontinuous righthand sides*, Kluwer, Netherlands.

Fossas, E. and Olivar, G., 1996, "Study of chaos in the buck converter", *IEEE Transactions on Circuits and Systems-I*, vol. 43, no. 1, pp. 13-25.

Freeman, R. A., and Kokotović, P. V., 1996, *Robust nonlinear control design: state-space and Lyapunov techniques*, Birkhäuser, Boston.

Furuta, K., 1990, "Sliding mode control of a discrete system", *System and Control Letters*, vol. 14, pp. 145-152.

Garabandic, D. S. and Petrovic, T. B., 1995, "Modeling parallel operating PWM dc-dc power supplies", *IEEE Transactions on Industrial Electronics*, vol. 42, no. 5, pp. 545-550.

Garabandic, D. S., Dunford, W., and Petrovic, T., 1998, "Robust decentralized control of parallel dc-dc converters", *IEEE Power Electronics Specialists Conference*, pp. 911-915.

Gauger, D., 1986, "A three-phase off line switching power supply with unity power factor and low TIF", *International Telecommunications Energy Conference*, pp. 115-121.

Gelig, A. K. and Churilov, A. N., 1987, "Study of q-periodic modes in pulse-width modulated systems", *Avtomatika i Telemekhanika*, pp. 30-39.

Gelig, A. K. and Churilov, A. N., 1998, *Stability and oscillations of nonlinear pulse-modulated systems* Birkhauser, Boston.

Gerdes, J. C., 1996, *Decoupled design of robust controllers for nonlinear systems: as motivated by and applied to coordinated throttle and brake control for automated highways*, Ph.D. Dissertation, Department of Mechanical Engineering, University of California, Berkeley.

Gholdston, E. W., Karimi, K., Lee, F. C., Rajagopalan, J., Panov, Y., and Manners, B., 1996, "Stability of large dc power systems using switching converters, with application to the international space station", *Intersociety Energy Conversion Engineering Conference*.

Glaser, J. S. and Witulski, A. F., 1992, "Application of a constant-output-power converter in multiple-module converter systems", *IEEE Power Electronics Specialists Conference*, pp. 909-916.

Glennon, T. F., 1998, "Fault tolerant generating and distributing system architecture", *IEE Colloquium on All Electric Aircraft*, pp. 4/1-4/4.

Gollu, A. and Varaiya, P. O., 1989, "Hybrid dynamical systems", *IEEE Decision and Control Conference*, pp. 2708-2712.

Green, J. H. and Hedrick, K., 1990, "Nonlinear speed control of automative engines", *IEEE American Control Conference*, pp. 2891-2897.

Gupta, M. M. (editor) and Yamakawa, T. (editor), 1988, *Fuzzy computing: theory, hardware, and applications*, Elsevier Science.

Gutman, S., 1979, "Uncertain dynamical systems - A Lyapunov min-max approach", *IEEE Transactions on Automatic Control*, vol. 24, pp. 437-443.

Habetler, T. G., 1991, "A space-vector based rectifier regulator for ac-dc/ac converters", *European Conference on Power Electronics and Applications*, vol. 2, pp. 101-107.

Habetler, T. G., Perfumo, F., Pastorelli, M., and Tolbert, L. M., 1992, "Direct torque control of induction machines using space vector modulation", *IEEE Transactions on Industry Applications*, vol. 28, no. 5, pp. 1045-1053.

Hahn, W., 1963, *Theory and application of Liapunov's direct method*, Prentice-Hall, New Jersey.

Hamill, D. C., 1995, "Power electronics: A field rich in nonlinear dynamics", *International Specialists' Workshop on Nonlinear Dynamics of Electronic Systems*, pp. 165-178.

Hamill, D. C. and Deane, J. H. B., 1992, "Modeling of chaotic dc-dc converters by iterated nonlinear mappings", *IEEE Transactions on Power Electronics*, vol. 7, pp. 25-36.

Hamill, D. C. and Jefferies, D. J., 1988, "Subharmonics and chaos in a controlled switched-mode power converter", *IEEE Transactions on Circuits and Systems*, vol. 35, no. 8, pp. 1059-1061.

Hedel, K., 1980, "High-density avionic power supply", *IEEE Transactions on Aerospace and Electronic Systems*, pp. 615-619.

Henze, C.P. and Mohan, N., 1986, "Digitally controlled ac to dc power conditioner that draws sinusoidal input current", *IEEE Power Electronics Specialists Conference*, pp. 531-540.

Hingorani, N. G., 1990, "FACTS: flexible ac transmission systems", *Electric Power Research Institute Conference on Flexible AC Transmission System.*

Hingorani, N. G., 1993, "Flexible ac transmission", *IEEE Spectrum*, vol. 30, no. 4, pp. 40-45.

Hingorani, N. G. and Gyugyi, L., 1996, *Understanding FACTS*, IEEE Press, New York.

Hirschberg, W. J., 1985, "Current-sharing of parallel power supplies", *IEEE Power Electronics Specialists Conference*, pp. 76-84.

Hiti, S., 1995, *Modeling and control of three-phase PWM converters*, Ph.D. Dissertation, Department of Electrical and Computer Engineering, Virginia Polytechnic Institute and State University, Blacksburg, Virginia.

Hiti, S., Boroyevich, D., and Cuadros, C., 1994, "Small signal modeling and control of three-phase PWM converters", *Proceedings of IEEE Industry Applications Society*, pp. 1143-1150.

Holtz, J. H., 1992, "Pulsewidth modulation - a survey", *IEEE Transactions on Industrial Electronics*, vol. 39 no. 5., pp. 410-420.

Holtz, J. H., Lotzkat, W., and Khambadkone, A. M., 1993, "On continuous control of PWM inverters in the overmodulation range including the six step mode", *IEEE Transactions on Power Electronics*, vol. 8, no. 4, pp. 546-553.

Hua, G. C., Tabisz, W. A., Leu, C. S., Dai, N., Watson, R., and Lee, F. C., 1994, "Development of a dc distributed power system", *IEEE Applied Power Electronics Conference*, pp. 763-769.

Huliehel, F.A., Lee, F. C., and Cho, B.H., 1992, "Small-signal modeling of the single-phase boost high factor converter with constant frequency control", *IEEE Power Electronics Specialists Conference*, pp. 475-482.

Hur, N. and Nam, K., 2000, "A robust load-sharing control scheme for parallel-connected multisystems", *IEEE Transactions on Industrial Electroncis*, vol. 47, no. 4., pp. 871-879.

Huth, S., 1996, "DC-DC converters in parallel operation with digital load distribution control", *IEEE International Symposium on Industrial Electronics*, pp. 808-813.

Huynh, P., 1994, *Stability analysis of large-scale power electronics systems*, Ph.D. Dissertation, Department of Electrical Engineering, Virginia Polytechnic Institute and State University, Blacksburg, Virginia.

Isidori, A., 1995, *Nonlinear Control Systems*, Springer-Verlag, New York.

Ivanov, A. P., 1993, "Analytical methods in the theory of vibro-impact systems", *Journal of Applied Mathematics and Mechanics*, vol. 57, no. 3, pp. 221-236.

Jacobina, C. B., Correa, M. B. R., Oliveira, T. M., Lima, A. M., da Silva, E. R. C, 1999, "Vector modeling and control of unbalanced electrical systems", *Proceedings of IEEE Industry Applications Society*, vol. 2, pp. 1011-1017.

Jacobina, C. B., de Rossiter Correa, M. B., Oliveira, T. M., Nogueira Lima, A. M., and da Silva, E. C., 2001, "Current control of unbalanced electrical systems", *IEEE Transactions on Industrial Electronics*, vol. 48, no. 3, pp. 517-525.

Jamerson, C., Long, T., and Mullett, C., 1993, "Seven ways to parallel a magamp", *IEEE Applied Power Electronics Conference*, pp. 469-474.

Jamerson, C. and Mullett, C., 1994, "Paralleling supplies via various droop methods", *High Frequency Power Conversion Conference*, pp. 68-76.

Jamshidi, M., Titli, A., Zadeh, L., and Boverie, S., 1997, "Applications of fuzzy logic: towards high machine intelligency quotient systems", Prentice Hall.

Jefferies, D. J., Deane, J. H. B., and Johnstone, G. G., 1989, "An introduction to chaos", *Electronics and Communication Engineering Journal*, vol. 1, no. 3, pp. 115-123.

Jensen, U. B., Blaabjerg, F., and Pedersen, J. K., 2000a, "A new control method for 400-Hz ground power units for airplanes", *IEEE Transactions on Industry Applications*, vol. 36, no. 1, pp. 180-187.

Jensen, U. B., Blaabjerg, F., and Enjeti, P. N., 2000b, "Sharing of nonlinear load in parallel connected three-phase converters", *Proceedings of Industry Applications Society*, pp. 2338-2344.

Jinjun Liu, Xiaogang Feng, Lee, F. C., and Boroyevich, D., 2001, "Stability margin monitoring for dc distributed power systems via current/voltage perturbation", *IEEE Applied Power Electronics Conference*, pp. 745-751

Jordan, M., 1991, "UC3907 load share IC simplfies parallel power supply design", Unitrode Application Note U-129.

Jordan, M., 1991, "Load share IC simplifies power supply design", *High Frequency Power Conversion Conference*, pp. 65-76.

Jovanovic, M. M., 1996, "A novel, low-cost implementation of "democratic" load-current sharing of parallel converter modules", *IEEE Transactions on Power Electronics*, vol. 11, no. 4, pp. 604-611.

Julian, A. L., Lipo, T. A., and Oriti, G., 1999, "Elimination of common-mode voltage in three-phase sinusoidal power converters", *IEEE Power Electronics Specialists Conference*, pp. 1968-1972.

Kaas-Petersen, C., 1986, "Computation of quasi-periodic solutions of forced dissipative systems", *Journal of Computational Physics*, vol. 58, pp. 395-408.

Kassakian, J. G. and Perreault, D. J., 1994, "An assessment of cellular architectures for large converter system", *International Conference on Power Electronics and Motion Control*, pp. 70-79.

Kawabata, T. and Higashino, S., 1988, "Parallel operation of voltage source inverters" *IEEE Transactions on Industry Applications*, vol. 24, no. 2, pp. 281-287.

Khalil, H.K., 1996, *Nonlinear systems*, Prentice-Hall, New Jersey.

Khan, I. A., 1999, "Automotive electrical systems: architecture and components", *Digital Avionics Systems Conference*, pp. 8.C.5-1-8.C.5-10.

Kipnis, M. M., 1989, "Phase portraits of pulse-width systems", *Avtomatika i Telemekhanika*, no. 12, pp. 105-115.

Kipnis, M. M., 1991, "Application of discrete convolution equations for checking stability of periodic processes in pulse-width systems", *Avtomatika i Telemekhanika*, no. 4, pp. 86-93.

Kohama, T., Ninomiya, T., Shoyama, M., and Ihara, F., 1994, "Dynamic analysis of parallel-module converter system with current balance controllers", *International Telecommunications Energy Conference*, pp. 190-195.

Kokotovic, P. V., 1992, "The joy of feedback: nonlinear and adaptive", *IEEE Control Systems Magazine*, vol. 12, no. 3, pp. 7-17.

Komatsuzaki, Y., 1994, "Cross current control for parallel operating three-phase inverter", *IEEE Power Electronics Specialists Conference*, pp. 943-950.

Korondi, P., Nagi, L., and Nemeth, G., 1991, "Control of a three phase ups inverter with unbalanced and nonlinear load", *European Conference on Power Electronics Firenze*, vol. 3, pp. 180-184.

Kotta, U., 1989, Comments on "On the stability of discrete-time sliding mode control systems", *IEEE Transactions on Automatic Control*, vol. 34, no. 9, pp. 1021-1022.

Kourjanski, M. and Varaiya, P., 1996, "Stability of hybrid systems", *Hybrid Systems III*, Springer-Verlag.

Krein, P. T. and Bass, R. M., 1989, "Multiple limit cycle phenomena in switching power converters", *IEEE Applied Power and Electronics Conference*, pp. 143-148.

Krein, P. T. and Bass, R. M., 1990, "Types of instability encountered in simple power electronic circuits: unboundedness, chattering, and chaos", *IEEE Applied Power Electronics Conference and Exposition*, pp. 191-194.

Kugi, A. and Schlacher, K., 1999, "Nonlinear H_∞-controller design for a dc-dc power converter", *IEEE Transactions on Control Systems Technology*, vol. 7, no. 2, pp. 230-237.

Kuznetsov, I. A., 1998, *Elements of applied bifurcation theory*, Springer-Verlag, New York.

Langholz G. and Kandel, A. (editors), 1993, *Fuzzy control systems*, CRC Press.

Lee, F. C., 1990, *Modeling, analysis, and design of PWM converter*, Virginia Power Electronic Center Publications Series, vol. 2, Blacksburg, Virginia.

Lee, F. C., 1995, *Converters and distributed power systems*, Virginia Power Electronic Center Publications Series, Blacksburg, Virginia.

Lee, F. C., 2000a, *Low voltage power conversion and distributed power systems*, Center for Power Electronics Systems Publications Series, Blacksburg, Virginia.

Lee, F. C., 2000b, *Integrated power electronics module- a building block concept for system integration*, Center for Power Electronics Systems Publications Series, Blacksburg, Virginia.

Lee, F. C., Boroyevich, D., Xing, K., **Mazumder, S. K.**, Dai, H., Milosavljevic, I., Ye, Z., Zhu, H., Choi, J., Lin, R., Lipo, T., Vinod, J., Sinha, G., Oriti, G., Baliga, B. J.,

Ramamurthy, A., Kelley, A. W., and Armstrong, K., 1997, *Power electronics building blocks and system integration*, Project Report Submitted to Office of Naval Research, Virginia Power Electronics Center, Blacksburg, Virginia.

Lee, F. C. Y., Iwens, R. P., and Yu, Y., 1979, "Generalized computer-aided discrete time-domain modeling and analysis of dc-dc converters," *IEEE Transactions on Industrial Electronics and Control Instrumentation*, vol. 26, no. 2, pp. 58-69.

Lee, C. Q., Siri, K., and Wu, T. F., 1991, "Dynamic current distribution controls of a parallel connected converter system", *IEEE Power Electronics Specialists Conference*, pp. 875-881.

Lehman, B. and Bass, R., 1996a, "Switching frequency dependent averaged models for PWM dc-dc converters", *IEEE Transactions on Power Electronics*, vol. 11, no. 1, pp. 89-98.

Lehman, B. and Bass, R., 1996b, "Extensions of averaging theory for power electronic systems", *IEEE Transactions on Power Electronics*, vol. 11, no. 4, pp. 542-553.

López, M., de Vicuña, L. G., Castilla, M., López, O., and Majó, J., 1998, "Interleaving of parallel dc-dc converters using sliding-mode control", in *Proceedings of the IEEE Industrial Electronics Society*, vol. 2, pp. 1055-1059.

Luo, S., Ye, Z., Lin, R., and Lee, F. C., 1998, "A classification and evaluation of paralleling methods for power supply modules", *Proceedings of Annual Seminar of Virginia Power Electronics Center*, pp. 221-231.

Lyshevski, S. E., 2000, "Resonant converters: nonlinear analysis and control", *IEEE Transactions on Industrial Electronics*, vol. 47, no. 4 , pp. 751-758.

Malesani, L., Rossetto, L., Spiazzi, G., and Zuccato, A., October 1996, "An ac power supply with sliding-mode control", *IEEE Industry Applications Magazine*, pp. 32-37.

Mammano, B., 1993, "Distributed power system", *Unitrode Seminar*, SEM-900.

Marino, R. and Tomei, P., 1995, *Nonlinear control design: geometric, adaptive, and robust*, Simon and Schuster International Group.

Marple, W. P., 1979, "Low distortion three-phase power regulator", *IBM Technical Disclosure Bulletin*, vol. 22, no. 3, pp. 970-971.

Marrero, J. L. R., Font, J. M., and Verghese, G. C., 1996, "Analysis of the chaotic regime for dc-dc converters under current-mode control", *IEEE Power Electronics Specialists Conference*, pp. 1477-1483.

Matakas, L. (Jr.), Burlacu, C., and Masada, E., 1995, "High power, high performance parallel connected multi-convertes: analysis and control", *International Symposium on Industrial Electronics*, pp. 121-126.

Matakas, L. (Jr.) and Masada, E., 1993, "Multi-converter implementation by parallel association of K voltage-source converters-control method", *European Power Electronic Conference*, pp. 35-40.

Matakas, L. (Jr.) and Masada, E., 1995, "Analysis of the parallel connection three-phase VSC converters", *International Power Electronics Congress*, pp. 854-859.

Matsui, K., 1985, "A pulsewidth modulated inverter with parallel-connected transistors by using current sharing reactors", *Proceedings of Industry Applications Society*, pp. 1015-1019.

Mattavelli, P., Escobar, G., and Stankovic, A. M., 2001, "Dissipativity-based adaptive and robust control of UPS", *IEEE Transactions on Industrial Electronics*, vol. 48, no. 2, pp. 334-343.

Mattavelli, P., Rossetto, L., Spiazzi, G., and Tenti, P., 1995, "General-purpose fuzzy controller for dc-dc converters", *IEEE Power Electronics Specialists Conference*, pp. 723-730.

Mazumder, S. K., 1997a, "DSP based implementation of a PWM ac-dc-ac converter using space-vector-modulation with primary emphasis on the analysis of the practical problems involved", *IEEE Applied Power Electronics Conference*, pp. 306-312.

Mazumder, S. K., 1997b, "Complete mathematical analysis of ripple current as a function of the modulation index for direct-indirect and bus-clamped space-vector-modulation techniques", *IEEE International Electric Machines and Drives Conference*, pp. TC2 10.1-10.3.

Mazumder, S. K. and Nayfeh, A. H. and , 2001, "A new approach to the stability analysis of boost power-factor-correction circuits", *Journal of Vibration and Control: Special Issue on Nonlinear Dynamics and Control* (accepted).

Mazumder, S. K., Alfayyoumi, M., Nayfeh, A. H., and Boroyevich, D., 2000a, "A theoretical and experimental investigation of the nonlinear dynamics of dc-dc converters", *IEEE Power Electronics Specialists Conference*, pp. 729-734.

Mazumder, S. K., Nayfeh, A. H., and Boroyevich, D., 2000b, "Development of integral-variable-structure control schemes for parallel-buck and parallel-boost dc-dc converters", *IEEE International Telecommunications Energy Conference*, pp. 82-89.

Mazumder, S. K., Nayfeh, A. H., and Boroyevich, D., 2001a, "Robust control of parallel dc-dc buck converters by combing the concepts of integral-variable-structure- and multiple-sliding-surface control schemes", *IEEE Transactions on Power Electronics* (provisionally accepted).

Mazumder, S. K., Nayfeh, A. H., and Boroyevich, D., 2001b, "Independent discontinuous control of parallel three-phase ac-dc PWM converters: solutions and limitations", *IEEE Transactions on Power Electronics* (in review).

Mazumder, S. K., Nayfeh, A. H., and Boroyevich, D., 2001c, "Theoretical and experimental investigation of the fast- and slow-scale instabilities of a dc-dc converter", *IEEE Transactions on Power Electronics*, vol. 16, no. 2, pp. 201-216.

Mazumder, S. K., Nayfeh, A. H., and Boroyevich, D., 2001d, "Nonlinear dynamics and stability analysis of parallel dc-dc converters including the effect of saturation", *Journal of Vibration and Control: Special Issue on Nonlinear Dynamics and Control* (unpublished).

Mazumder, S. K., Nayfeh, A. H., and Boroyevich, D., 2001e, "A novel approach to the stability analysis of boost power-factor-correction circuits", *IEEE Power Electronics Specialists Conference* (in press).

Mazumder, S. K., Nayfeh, A. H., and Boroyevich, D., 2001f, "A nonlinear approach to the analysis of stability and dynamics of standalone and parallel dc-dc converters", *IEEE Applied Power Electronics Conference*, pp. 784-790.

McLyman, W. T., 1993, *Designing magnetic components for high-frequency dc-dc converters*, K G Magnetics.

Meyer, M. and Sonnenmoser, A., 1993, "A hysterisis current control for parallel connected line-side converters of an inverter locomotive", *European Power Electronics Conference*, pp. 102-109.

Michel, A. N. and Bo, Hu., 1997, "Toward a general stability theory for hybrid dynamical systems", *IEEE Conference on Decision and Control.*

Middlebrook, R. D., 1976, "Input filter considerations in design and application of switching regulators", *Proceedings of the IEEE Industry Applications Society*, pp. 91-107.

Middlebrook, R. D. and Cuk, S., 1977a, "A general unified approach to modeling switching-converter power stages", *IEEE Power Electronics Specialists Conference*, pp. 521-550.

Middlebrook, R. D. and Cuk, S., 1977b, "A general unified approach to modelling switching dc to dc converters in discontinuous conduction mode", *IEEE Power Electronic Specialists Conference*, pp. 36-57.

Milosavljevic, D., 1985, "General conditions for the existence of a quasi-sliding mode on the switching hyperplane in discrete variable structure systems", *Automation and Remote Control*, vol. 46, pp. 307-314.

Miroslav, K., Kanellakopoulos, I., and Kokotovic, P. V., 1995, *Nonlinear and adaptive control design*, Wiley, New York.

Miwa, B., Otten, D. M., and Schlecht, M. F., 1992, "High efficiency power factor correction using interleaving techniques", *IEEE Power Electronic Specialists Conference*, pp. 557-568.

Miyashita, O., Nishida, Y., Ohnuki, T., Ohtsuji, E., and Haneyoshi, T., 1994, "High power factor PWM rectifiers with an analog pulse-width predictor", *IEEE Power Electronic Specialists Conference*, pp. 563-568.

Mohan, N., Undeland, T.M., and Ferraro, R.J., 1984, "Sinusoidal line current rectification with a 100 kHz B-SIT step-up converter", *IEEE Power Electronics Specialists Conference* pp. 92-98.

Nagy, I., 1994, "Novel adaptive tolerance band based PWM for field-oriented contro of induction machines", *IEEE Transactions on Industrial Electronics*, vol. 41, no. 4, pp. 406-417.

Nayfeh, A. H., 1973, *Perturbation methods*, Wiley, New York.

Nayfeh, A. H., 1993, *Method of normal forms*, John Wiley Interscience, New York.

Nayfeh, A. H., 1998, *MURI nonlinear active control of dynamical systems*, end of fiscal year letter submitted to the Office of Naval Research.

Nayfeh, A. H. and Balachandran, B., 1995, *Applied nonlinear dynamics*, Wiley, New York.

Nayfeh, A. H. and **Mazumder, S. K.**, 2001, "Power-electronics converters: a field rich in discontinuities", Invited Paper, *ASME Conference* (in press).

Nayfeh, A. H. and Mook, D. T., 1979, *Nonlinear oscillations*, Wiley, New York.

Needham, B. R., Eckerling, P. H., and Siri, K., 1994, "Simulation of large distributed DC power systems using averaged modelling techniques and the Saber simulator", *IEEE Applied Power Electronics Conference*, pp. 801-807.

Ngo, K. D. T., 1984, *Topology and analysis in PWM inversion, rectification, and cycloconversion*, Ph.D. Dissertation, Department of Electrical Engineering, California Institute of Technology, Pasadena, California.

Ngo, K. D. T., 1986, "Low frequency characterization of PWM converters", *IEEE Transactions on Power Electronics*, vol. 1, pp. 223-230.

Nordmark, A. B., 1997, "Universal limit mapping in grazing bifurcations", *Physical Review*, vol. 55, no. 1, pp. 266-270.

Nusse, H. E., and York, J. A., 1992, "Border-collision bifurcations including period two to period three for piecewise smooth systems", *Physica D*, vol. 57, pp. 39-57.

Ogasawara, S., Takagaki, J., Akagi, H., and Nabae, A., 1987, "A novel control scheme of duplex current-controlled PWM inverters", *Proceedings of IEEE Industry Applications Society*, pp. 330-337.

Ogasawara, S., Akagi, H., and Nabae, A., 1989, "A novel pwm scheme of voltage source inverters based on space vector theory", *European Power Electronics Conference*, pp. 1197-1202.

Ojo, O. and Bhat, I., 1994, "Influence of input supply voltage unbalances on the performance of ac-dc buck rectifiers", *IEEE Power Electronics Conference*, vol. 2, pp. 777-784.

Pan C. T. and Chen, T. C., 1993, "Modeling and design of an ac to dc converter", *IEEE Transactions on Power Electronics*, vol. 8, no. 4, pp. 501-508.

Panov, Y., Rajagopalan, J., and Lee, F. C., 1996, "Design-oriented analysis of paralleled dc-dc converters with master-slave current-sharing control", *Proceedings of the Annual Seminar of Virginia Power Electronics Seminar*, pp. 83-89.

Panov, Y., Rajagopalan, J., and Lee, F. C., 1997, "Analysis and design of N paralleled dc-dc converters with MS current-sharing control", *IEEE Applied Power Electronics Conference*, pp. 436-442.

Parker, T. S. and Chua, L. O., 1989, *Practical numerical algorithms for chaotic systems*, Springer-Verlag, New York.

Patil, A. R., Cho, B. H., Sable, D. M., and Lee, F. C., 1992, "Design and test hardware for a solar array switching unit", *Intersociety Energy Conversion Engineering Conference.*

Perkinson, J., 1995, "Current sharing of redundant dc-dc converters in high availability systems- a simple approach", *IEEE Applied Power Electronics Conference*, pp. 952-956.

Perreault, D. J., Kassakian, J. G., and Verghese, G. C., 1997, "Stability analysis of nonlinear current-sharing techniques", *IEEE Power Electronics Specialists Conference*, pp. 665-671.

Perreault, D. J., Selders, R. L., and Kassakian, J. G., 1996a, "Frequency-based current-sharing techniques for paralleled power converters", *IEEE Power Electronics Specialists Conference*, pp. 1073-1079.

Perreault, D. J., Selders, R. L., and Kassakian, J. G., 1996b, "Implementation and evaluation of a frequency-based current-sharing technique for cellular converter systems", *IEEE AFRICON*, pp. 682-686.

Petry, C., 1995, "Shipboard electrical power architecture" *Control Technology Workshop*, pp. 100-110.

Petruzziello, F., Ziogas, P. D., and Joos, G., 1990, "A novel approach to paralleling of converter units with true redundancy", *IEEE Power Electronics Specialists Conference*, pp. 808-813.

Pinheiro, J. R. and Barbi, I., 1995, "Three-level zero-voltage-switching PWM dc-dc converters-a comparison", *IEEE Power Electronics Specialists Conference*, pp. 914-919.

Poddar, G., Chakrabarty, K., and Banerjee, S., 1998, "Control of chaos in dc-dc converters", *IEEE Transactions on Circuits and Systems I: Fundamental Theory and Applications*, vol. 45, no. 6, pp. 672-676.

Prajoux, R., Marpinard, J. C., and Jalade, J., 1976, "Etablissement de modeles mathematiques pour regulateurs de puissance a modulation de largeur d'impulsions (pwm)", *ESA Scientific and Technical Review*, vol. 2, pp. 25-42.

Prasad, A. R., Ziogas, P. D., and Manias, S., 1989, "An active power factor correction technique for three-phase diode rectifiers", *IEEE Power Electronics Specialists Conference*, pp. 58-66.

Prasad, V. H., Borojevic, D., and Dubovsky, S., 1996, "Comparison of high frequency PWM algorithms for voltage source inverters", *Proceedings of the Virginia Power Electronics Center Seminar*, pp. 115-122.

Qu, Z., 1998, *Robust control of nonlinear uncertain systems*, Wiley, New York.

Rajagopalan, J., Xing, K., Guo, Y., and Lee, F. C., 1996, "Modeling and dynamic analysis of paralleled dc-dc converters with master-slave current sharing control", *IEEE Applied Power Electronics Conference*, pp. 678-684.

Ridley, R.B., 1986, *Small-signal analysis of parallel power converters*, MS Thesis, Department of Electrical and Computer Engineering, Virginia Polytechnic Institute and State University, Blacksburg, Virginia.

Ridley, R.B., 1989, "Average small-signal analysis of the boost power factor correction circuit", *Proceedings of the Virginia Power Electronics Center Seminar*, pp. 108-120.

Ridley, R.B., 1991, "A new continuous-time model for current-mode control", *IEEE Transactions on Power Electronics*, vol. 6, no. 2, pp. 271-280.

Rim, C. T., Hu, D. Y., and Cho, G. H., 1990, "Transformers as equivalent circuits for switches: general proofs and d-q transformation-based analyses", *IEEE Transactions on Industrial Applications*, vol. 26, no. 4, pp. 777-785.

Rios-Bolivar, M., Sira-Ramirez, H., and Zinober, A. S. I., 1995, "Output tracking control via adaptive input-output linearization: a backstepping approach", *IEEE Conference on Decision and Control*, vol. 2, pp. 1579-1584.

Rios-Bolívar, M., Zinober, A. S. I., and Sira-Ramirez, H., 1996, "Dynamical sliding mode control via adaptive input-output linearization: a backstepping approach", *Lecture notes in control and information sciences: robust control via variable structure and Lyapunov techniques*, Springer-Verlag, New York.

Rioual, P., Pouliquen, H., and Louis, J. P., 1993, "Regulation of a PWM rectifier in the unbalanced network state", *IEEE Power Electronics Specialists Conference*, pp. 641-647.

Rostek, P. M., 1994, "Power system design for massive parallel computer systems", *IEEE Applied Power Electronics Conference*, pp. 808-814.

Royden, H. L., 1988, *Real analysis*, Prentice Hall, New Jersey.

Ryan, M. J., 1997, *Analysis, modeling and control of three-phase, four-wire sine wave inverter systems*, Ph.D. Dissertation, Department of Electrical and Computer Engineering, University of Wisconsin at Madison.

Sabanovic, A., Behilovic, N. S., and Ninomiya, T., 1994, "PWM in three-phase switching converters - sliding mode solution", *IEEE Power Electronics Specialists Conference*, pp. 560-565.

Sable, D. M., Noon, J., Gur, Z., Patil, A. R., Butler, S. J., Mang, X., Lee, F. C., and Cho, B. H., 1991, "Design and development of a testbed for the space platform power system", *Proceedings of Annual Seminar of Virginia Power Electronics Center*, pp. 63-68.

Sakharuk, T. A., Lehman, B., Stankovic, A. M., and Tadmor, G., 2000, "Effects of finite switching frequency and delay on PWM controlled systems", *IEEE Transactions on Circuits and Systems I: Fundamental Theory and Applications*, vol. 47, no. 4, pp. 555-567.

Salon, S. J., 1993, *Computer methods in electrical power engineering*, Class notes, Department of Electrical Power Engineering, Rensselaer Polytechnic Institute, Troy, New York.

Sanders, J. A., 1985, *Averaging methods in nonlinear dynamical systems*, Springer-Verlag, New York.

Sanders, S. R., 1989, *Nonlinear control of switching power converters*, Ph.D. Dissertation, Department of Electrical and Computer Engineering, Massachusetts Institute of Technology, Cambridge, Massachussetts.

Sanders, S. R., 1993, "On limit cycles and the describing function method in periodically switched circuits", *IEEE Transactions on Circuits and Systems I: Fundamental Theory and Applications*, vol. 40, no. 9, pp. 564-572.

Sanders, S. R., Noworolski, J. M., Liu, X. J., and Verghese, G. C., 1991, "Generalized averaging method for power conversion circuits", *IEEE Transactions on Power Electronics*, vol. 6, no. 2, pp. 251-259.

Sanders, S. R. and Verghese, G. C., 1990, "Lyapunov-based control for switching power converters", *IEEE Power Electronics Specialists Conference*, pp. 51-58.

Sarpturk, S. Z., Istefanopulos, Y., and Kaynak, O., 1987, "On the stability of discrete-time sliding mode control systems", *IEEE Transactions on Automatic Control*, vol. 32, no. 10, pp. 930-932.

Sastry, S., 1999, *Nonlinear systems: analysis, stability, and control*, Springer-Verlag, New York.

Sato, Y. and Kataoka, T., 1995, "Simplified control strategy to improve ac input-current waveform of parallel connected current-type PWM rectifiers", *Proceedings of Institute of Electrical Engineers*, vol. 142, pp. 246-254.

Scheffer, M., Bellini, A., Rovatti, R., Zafarana, A., and Diazzi, C., 1996, "A fuzzy analog controller for high performance microprocessor power supply", *Proceedings of EUFIT*.

Shevitz, D. and Paden, B., 1994, "Lyapunov stability theory of nonsmooth systems", *IEEE Transactions on Automatic Control*, vol. 39, pp. 1910-1914.

Short, D. J. and Lee, F. C., 1983, "Improved switching converter model using discrete and averaging techniques", *IEEE Transactions Aerospace Electronic Systems*, vol. 19, no. 2, pp. 190-202.

Simonetti, D., Sebastiań, J., Cobos, J.A., and Uceda, J., 1995, "The continuous-discontinuous conduction boundary of a boost PFP fed by universal input", *CIEP*, pp. 20-24.

Sira-Ramirez, H., 1989, "Sliding regimes in pulse-width-modulation systems design", *IEEE Conference on Decision and Control*, pp. 2199-2204.

Sira-Ramirez, H., Escobar, G., and Ortega, R., 1996, "On passivity-based sliding mode control of switched dc-to-dc power converters" *IEEE Conference on Decision and Control*, vol. 3, pp. 2525-2526.

Siri, K., 1991, *Analysis and design of distributed power systems*, Ph.D. Dissertation, Department of Electrical Engineering, University of Ilinois, Chicago, Illinois.

Siri, K. and Banda, J., 1995, "Analysis and evaluation of current-sharing control for parallel-connected dc-dc converters taking into account cable resistance", *IEEE Aerospace Applications Conference*, pp. 29-48.

Siri K., Wu, T. F., and Lee C. Q., 1991, "Maximum power tracking in parallel connected converter systems", *Intersociety Energy Conversion Engineering Conference*, pp. 4-9.

Siri, K., Lee, C. Q., and Wu, T. F., 1992a, "Current distribution control for parallel-connected converters", I, *IEEE Transactions on Aerospace and Electronic Systems*, vol. 28, no. 3, pp. 829-840.

Siri, K., Lee, C. Q., and Wu, T. F., 1992b, "Current distribution control for parallel-connected converters", II, *IEEE Transactions on Aerospace and Electronic Systems*, vol. 28, no. 3, pp. 841-850.

Siri, K. and Truong, C., 1998, "Performance limitations of random current-sharing parallel-connected converter systems and their solution", *IEEE Applied Power Electronics Conference*, pp. 860-866.

Small, K. T., 1988, "Single wire current share paralleling of power supplies", U. S. Patent 4717833.

Stankovic, A. M., Mattavelli, P., Caliskan, V., and Verghese, G. C., 2000, "Modeling and analysis of FACTS devices with dynamic phasors", *Proceedings of IEEE Power Engineering Society*, pp. 1440-1446.

Stankovic, A. M., Perreault, D. J., and Sato, K., 1999, "Synthesis of dissipative nonlinear controllers for series resonant dc-dc converters", *IEEE Transactions on Power Electronics*, vol. 14, no. 4, pp. 673-682.

Stankovic, A. M., Sanders, S. R., and Aydin, T., 1998, "Analysis of unbalanced ac machines with dynamic phasors", *Naval Symposium on Electric Machines*, pp. 219-224.

Stefanovic,V.R. and Vukosavic, S. N., 1994, "Space vector PWM voltage control with optimized switching strategy", *IEEE Transactions on Industry Applications*, pp. 1025-1035.

Stotsky, A. A., Hedrick, J. K., and Yip, P. P., 1999, "The use of sliding modes to simplify the backstepping control method", *Applied Mathematics and Computational Science*, vol. 8, no. 1, pp. 123-133.

Sun, J., 2000, "Unified averaged switch models for stability analysis of large distributed power systems", *IEEE Applied Power Electronics Conference*, pp. 249-255.

Sun, J. and Mehrotra, V., 2001, "Unified analysis of half-bridge converters with current-doubler rectifier", *IEEE Applied Power Electronics Conference*, pp. 514-520.

Sun, J., Wu, W-C., and Bass, R. M., 1998, "Large-signal characterization of single-phase PFC circuits with different types of current control", *IEEE Applied Power Electronics Conference*, pp. 655-661.

Swaroop, D., Gerdes, J. C., Yip, P. P., and Hedrick, J. K., 1997, "Dynamic surface control of nonlinear systems", *IEEE American Control Conference*, pp. 3028-3034.

Tabisz, W. A., Jovanović, M. M., and Lee, F. C., 1992, "Present and future of distributed power systems", *IEEE Applied Power Electronics Conference*, pp. 11-18.

Takahashi, I. and Noguchi, T., 1986, "A new quick response and high efficiency control strategy for the induction motor", *IEEE Transactions on Industry Applications*, vol. 22, pp. 820-827.

Takahashi, I. and Yamane, M., 1986, "Multiparallel asymmetrical cycloconverter having improved power factor and waveforms", *IEEE Transactions on Industry Applications*, vol. 22, no. 6, pp. 1007-1016.

Tanaka, H., 1988, "Method for centralized voltage control and balancing for parallel operation of power supply equipment", *International Telecommunications Energy Conference*, pp. 434-440.

Tavernini, L., 1987, "Differential automata and their discrete simulators", *Nonlinear Analysis Theory, Methods, Applications*, vol. 11, no. 6, pp. 665-683.

Thandi, G. S., 1997, *Modeling, control and stability analysis of a PEBB based dc distribution power system*, Ph.D. Dissertation, Department of Electrical Engineering, Virginia Polytechnic Institute and State University, Blacksburg, VA.

Thandi, G. S., Zhang, R., Xing, K., Lee, F. C., and Boroyevich, D. 1999, "Modeling, control and stability analysis of a PEBB based dc DPS", *IEEE Transactions on Power Delivery*, vol. 14, no. 2, pp. 497-505.

The Office of the Director of Defense Research and Engineering (ODDR&E) and Electric Power Research Institute (EPRI), 1998 *Complex interactive networks/systems initiative*, Research Announcement DAAG55-98-R-RA08.

Thiyagarajah, K., Ranganathan, V. T., and Iyengar, B. S., 1991, "A high switching frequency IGBT PWM rectifier/inverter system for ac motor drives operating from single phase suppply", *IEEE Transactions on Power Electronics*, vol. 6, no. 4, pp. 576-584.

Thottuvelil, V.J. and Verghese, G.C., 1996, "Stability analysis of paralleled dc-dc converters with active current sharing", *IEEE Power Electronics Specialists Conference*, pp. 1080-1086.

Thottuvelil, V. J. and Verghese, G. C., 1998, "Analysis and control design of paralleled dc-dc converters with current sharing", *IEEE Transactions on Power Electronics*, vol. 13, no. 4, pp. 635-644.

Thunes, J., Kerkman, R., Schlegel, D., and Rowan, T., 1999 "Current regulator instabilities on parallel voltage-source inverters", *IEEE Transactions on Industry Applications*, vol.

35, no. 1, pp. 70-77.

Todd, P., 1999, "UC3854 controlled power factor correction circuit design", Application Note U-134, Unitrode Inc.

Tolbert, L. M., Peng, F. Z., and Habetler, T. G., 1999, "A multilevel converter-based universal power conditioner", *IEEE Power Electronics Specialists Conference*, pp. 393-399.

Tomescu, B. and VanLandingham, H. F., 1998, "Improved large signal performance of parallel dc-dc converters current sharing using fuzzy logic control", *IEEE Applied Power Electronics Conference*, pp. 867-873.

Tse, C. K., 1994a, "Flip bifurcation and chaos in three-state boost switching regulators", *IEEE Transactions on Circuits and Systems-1: Fundamental Theory and Applications*, vol. 41, pp. 16-23.

Tse, C. K., 1994b, "Flip bifurcation and chaos in three-state boost switching regulators", *IEEE Transactions on Circuits and Systems I: Fundamental Theory and Applications*, vol. 41, no. 1, pp. 16-23.

Tse, C. K., 1994c, "Chaos from a buck switching regulator operating in discontinuous mode", *International Journal of Circuit Theory and Applications*, vol. 22, no. 4, pp. 263-278.

Tse, C. K. and Adams, K.M., 1990, "Qualitative analysis and control of a dc to dc boost converter operating in discontinuous mode", *IEEE Transactions on Power Electronics*, vol. 5, no. 3, pp. 323-330.

Tse, C. K. and Adams, K. M., 1991, "A nonlinear large-signal feedforward-feedback control for two-state dc-dc converters", *IEEE Power Electronics Specialists Conference*, pp. 722-729.

Tuladhar, A., Jin, H., Unger, T., and Mauch, K., 2000, "Control of parallel inverters in distributed ac power systems with consideration of line impedance effect", *IEEE Transactions on Industrial Applications*, vol. 36, no. 1., pp. 131-138.

Tymerski, R., Vorperian, V., Lee, F. C., and Baumann, W., 1988, "Nonlinear modeling of the PWM switch", *IEEE Power Electronics Specialists Conference*, pp. 968-975.

Ueno, F., Inoue, T., Oota, I., and M. Sasaki, 1991, "Regulation of Cuk converters using fuzzy controllers", *IEEE International Telecommunications Energy Conference*, pp. 261-267.

Utkin, V., 1992, *Sliding modes in control optimization*, Springer-Verlag, New York.

Utkin, V., Guldner, Jü., and Shi, J., 1999, *Sliding mode control in electromechanical systems*, Taylor & Francis.

Van der Schaft, A. J., 1996, *L_2-gain and passivity techniques in nonlinear control*, Springer-Verlag, New York.

Verghese, G. C., Elbuluk, M. E., and Kassakian, J. G., 1986, "A general approach to sampled-data modelling for power electronic circuits", *IEEE Transactions on Power Electronics*, vol. 1, no. 2, pp. 76-89.

Vincenti, D. and Jin, H., 1994, "A three-phase regulated PWM rectifier with on-lie feed-forward iput unbalance correction", *IEEE Transactions on Industrial Electronics*, vol. 41, no. 5, pp. 526-532.

Vlatkovic, V., Borojevic, D., and Lee, F. C., 1996, "Input filter design for power factor correction circuits", *IEEE Transactions on Power Electronics*, vol. 11, no. 1, pp. 199-205.

Vorperian, V., 1990a, "Simplified analysis of pwm converters using model of PWM switch. I. Continuous conduction mode", *IEEE Transactions on Aerospace Electronic Systems*, vol. 26, pp. 490-496.

Vorperian, V., 1990b, "Simplified analysis of pwm converters using model of PWM switch. II. Discontinuous conduction mode", *IEEE Transactions on Aerospace Electronic Systems*, vol. 26, pp. 497-505.

Wang, X., 1997, *Analytical methods of nonsynchronous response and bifurcation in nonlinear rotordynamics with applications*, Ph.D. Dissertation, Department of Mechanical Engineering, Texas A&M University, College Station, Texas.

Watson, L. T., 1990, "Globally convergent homotopy algorithms for nonlinear systems of equations", *Nonlinear Dynamics*, vol. 1, pp. 143-191.

Watson, R. W., Chen , W., Hua, G., and Lee, F. C., 1995, "Component development for a high-frequency ac distributed power system", *Proceedings of Annual Seminar of Virginia Power Electronics Center.*

Watson, R. W. and Lee, F. C., 1999, "High-frequency ac distributed power systems, part III: dc and ac distributed power system comparison", *Proceedings of Annual Seminar of Center for Power Electronics Systems*, pp. 27-33.

Wester, G. W. and Middlebrook, R. D., 1972, "Low-frequency characterization of switched dc-dc converters", *IEEE Transactions on Aerospace and Electronic Systems*, vol. 9, no. 3, pp. 376-85.

White, R. W., 1995, "Fault tolerance in distributed power systems", *European Power Electronics Conference*, pp. 851-857.

Wiggins, S., 1990, *Introduction to applied nonlinear dynamical systems and chaos*, Springer-Verlag, New York.

Wildrick, C. M., 1993, *Stability of distributed power supply systems*, M.S. Thesis, Department of Electrical Engineering, Virginia Polytechnic Institute and State University, Blacksburg, Virginia.

Wildrick, C. M., Yang, E., Choi, B., Tang, W., Cho, B., and Lee, F. C., 1992, *Modeling and analysis of distributed power system*, Final Report submitted to General Electric Corporation (Schenectady), Center for Power Electronics Systems, Blacksburg, Virginia.

William, H. J., 1999, *Extending H_∞ control to nonlinear systems: control of nonlinear systems to achieve performance objectives*, Society for Industrial and Applied Mathematics.

Williams J. B., 1989, "Design of feedback loop in unity power factor ac to dc converter", *IEEE Power Electronics Specialists Conference*, pp. 959-967.

Wills, R. H., 1994, *The interconnection of photovoltaic power systems with the utility grid: An overview for utility engineers*, Report (#SAND94-1057) submitted to the Sandia National Laboratory, Solar Design Associates, Inc., Harvard, Massachusetts.

Witsenhausen, H. S., 1966, "A class of hybrid-state continuous-time dynamic systems", *IEEE Transactions on Automatic Control*, vol. 11, no. 2, pp. 161-167.

Wood, J. R., 1989, "Chaos: a real phenomenon in power electronics", *IEEE Applied Power Electronics Conference and Exposition*, pp. 115-124.

Wolf, D.M. and Sanders, S.R., 1994, "Multi-parameter homotopy for finding periodic solutions of power electronic circuits", *IEEE International Symposium on Circuits and Systems*, pp. 137-140.

Wolf, D. M., Verghese, G. C., and Sanders, S. R., 1994, "Bifurcation of power electronic circuits", *Journal of Franklin Institute*, pp. 957-999.

Wu, Q., Onyshko, S., Sepehri, N., and Thornton-Trump, A. B., 1998, "On construction of smooth Lyapunov functions for non-smooth systems", *International Journal of Control*, vol. 69, pp. 443-457.

Wu, R., Dewan, S. B., and Slemon, G. R., 1990, "Analysis of a PWM ac to dc voltage source converter under the predicted current control with a fixed switching frequency", *IEEE Transactions on Industry Applications*, vol. 26, pp. 880-885.

Wu, R., Dewan, S. B., and Slemon, G. R., 1991, "Analysis of an ac-to-dc voltage source converter using PWM with phase and amplitude control", *IEEE Transactions on Industry Applications*, vol. 27, pp. 355-363.

Wu, R. H., Kohama, T., Kodera, Y., Ninomiya, T., and Ihara, F., 1993, "Load-current-sharing control for parallel operation of dc-to-dc converters", *IEEE Power Electronics Specialists Conference*, pp. 101-107.

Wu, T. F., Huang, Y. H., Chen, Y. K., and Liu, Z. R., 1998, "A 3C strategy for multi-module inverters in parallel operation to achieve an equal current distribution", *IEEE Power Electronics Specialists Conference*, pp. 186-192.

Wu T. F., Siri K., and Banda J., 1994, "The central-limit control and impact of cable resistance in current distribution for parallel-connected dc-dc converters", *IEEE Power Electronics Specialists Conference*, vol. 1, pp. 694-702.

Wu, T. F., Siri, K., Lee, C. Q., and Burns, J. R., 1991, "A fault-tolerant parallel connected power system", *Intersociety Energy Conversion Engineering Conference*, pp. 156-161.

Wu, T. F., Siri, K., and Lee, C. Q., 1992a, "Current-mode control for load sharing converter systems with dynamic current distribution", *IEEE Conference on Systems, Man and Cybernetics*, pp. 459-464.

Wu, T. F., Siri, K., and Lee, C. Q., 1992b, "Comparison among three types of dynamic current distribution control strategies" *International Conference on Power Electronics and Motion Control*, pp. 289-294.

Xing, K., 1999, *Modeling , analysis, and design of distributed power electronics system based on building block concept*, Ph.D. Dissertation, Department of Electrical and Computer

Engineering, Virginia Polytechnic Institute and State University, Blacksburg, Virginia.

Xing, K., Lee, F. C., Boroyevich, D., Ye, Z., and **Mazumder, S. K.**, 1999, "Interleaved PWM with discontinuous space-vector modulation", *IEEE Transactions on Power Electronics*, vol. 14, no. 5, pp. 250-256.

Xing, K., **Mazumder, S. K.**, Ye, Z., Boroyevich, D., and Lee, F. C., 1998, "The circulating current in paralleled three-phase boost PFC rectifiers", *IEEE Power Electronics Specialists Conference*, pp. 783-789.

Xing, K., Thandi, G., Zhu, H., Mihailovic, Z., Prasad, V. H., Lee, F. C., and Boroyevich, D., 1996, *Nonlinear modeling, control and stability analysis of PEBB-base power system*, Project Report Submitted to The Office of Naval Research, Virginia Power Electronics Center, Blacksburg, Virginia.

Ye, Z., 2000, *Modeling and control of parallel three-phase PWM converters*, Ph.D. Dissertation, Department of Electrical and Computer Engineering, Virginia Polytechnic Institute and State University, Blacksburg, Virginia.

Ye, Z., Boroyevich, D., Choi, J. Y., and Lee, F. C., 2000, "Control of circulating current in parallel three-phase boost converters", *IEEE Applied Power Electronics Conference*, pp. 506-512.

Ye, Z., Xing, K., **Mazumder, S. K.**, Boroyevich, D., and Lee, F. C., 1998, "Modeling and control of parallel three-phase PWM boost rectifiers in PEBB-based dc distributed power systems", *IEEE Applied Power Electronics Conference*, pp. 1126-1132.

Zafrany, I. and Ben-Yaakov, S., 1995, "A chaos model of subharmonic oscillations in current mode PWM boost converters", *IEEE Power Electronic Specialists Conference*, pp. 1111-1117.

Zafrany, I. and Ben-Yaakov, S., 1998, "Average modeling, analysis and simulation of current shared dc-dc converters", *IEEE Power Electronics Specialists Conference*, pp. 640-646.

Zhang, R., 1998a, *High performance power converter systems for nonlinear and unbalanced load/source*, Ph.D. Dissertation, Department of Electrical and Computer Engineering, Virginia Polytechnic Institute and State University, Blacksburg, Virginia.

Zhang, W., 1998b, *Integrated EMI/thermal design for switching power supplies*, M.S. Thesis, Department of Electrical Engineering, Virginia Polytechnic Institute and State University, Blacksburg, Virginia.

Zhang, Z. and Ooi, B., 1993, "Multimodular current-source SPWM converters for superconducting a magnetic energy storage system", *IEEE Transactions on Power Electronics*, vol. 8, no. 3, pp. 250-256.

Zhou, C. and Jovanović, M. M., 1992, "Design trade-offs in continuous current-mode controlled boost power factor correction circuits", *High-Frequency Power Conversion Conference*, pp. 209-220.

Zhou, C., Ridley, R.B., and Lee, F. C., 1990, 'Design and analysis of a hysteretic boost power factor correction circuit', *IEEE Power Electronics Specialists Conference*, pp. 800-807.

Zhu G., Iannello, C., Kornetzky, P., and Batarseh, I., 2000, "Large-signal modeling of a single-switch power factor correction converter", *IEEE Power Electronics Specialists Conference*, pp. 1351-1357.

Zhu, G., Wei, H., Iannello, C., and Batarseh, I., 1999, "Large-signal simulation of a distributed power supply system with power factor correction", *IEEE International Symposium on Circuits and Systems*, pp. 258-261.

Zinober, A. S. I. (editor), 1990, *Deterministic control of uncertain systems*, INSPEC.

Vita

Sudip K. Mazumder received his Bachelor's in Electrical Engineering from University of Delhi (India) and M. S. in Electrical Power Engineering (with specialization in Power Electronics) from Rensselaer Polytechnic Institute (Troy, New York) in 1993. Sudip began his Doctoral career in 1997, when he joined the Center for Power Electronics Systems, Department of Electrical and Computer Engineering, Virginia Polytechnic Institite and State University.

He has eight years of professional experience in the area of power electronics, motor drives, and motion control. His areas of expertise and interests include nonlinear analysis and nonlinear control of standalone, integrated, and parallel dc-dc and multiphase converters, hybrid systems, DSP/RISC-based high-performance standalone and multi-axis drives, and multi-phase converters, electric/hybrid vehicles, multilevel converters, active filters, soft- and hard-switching topologies and techniques for power converters.

Currently, he has twenty refereed international journal and conference papers and one invited paper, and he has received the invitation for lectures in two international conferences. A monograph based on his Ph.D. work is under preparation. Sudip was selected as a Session Chair on "Inverter Control Techniques" at the IEEE Power Electronics Specialists Conference (June, 2001), held at Vancouver, Canada. He is the reviewer for six international journals and conferences. He is currently a member of the Phi Kappa Phi honor society and a student member of the IEEE.

After graduation, Sudip will join the Department of Electrical Engineering, University of Illinois as an Assistant Professor.